

# **RESEARCH EXPERIENCES FOR UNDERGRADUATES PROGRAM**



## **1999 PROGRAM REPORT**

NATIONAL RADIO ASTRONOMY OBSERVATORY





# **Research Experiences for Undergraduates Program 1999 Program Report**

National Radio Astronomy Observatory

# Table of Contents

## Overview

..... 2

## Appendix

### Student Presentations at the 195<sup>th</sup> AAS Meeting

..... 3

## Project Reports

### 1999 REU Students

..... 4

## Papers to be Published

..... 5

## Student Questionnaires 1999

### (GB and CV Students)

..... 6

## 1999 Summer Research Symposium

### Program (CV)

..... 7

# National Radio Astronomy Observatory

## REU Program Report

### Overview

Fifteen undergraduates participated in the 1999 Research Experiences for Undergraduates Program sponsored by the National Science Foundation, at the NRAO. These students were joined by graduating seniors and graduate students paid for by other funds, to bring the total number of students to 24. 1999 was the fortieth year of the NRAO Summer Research Program, which has graduated over 800 students during its tenure. During that period, many NRAO summer students have gone on to become astronomers, among them winners of the AAS Warner and Pierce Prizes. During the period 1992-1996, NRAO REU students published 27 refereed papers; one third went on to obtain an astronomy degree. Three of the six 1992 REUs have obtained their astronomy Ph. D. and are currently employed in the field. Research initiated in previous years by some students and their mentors continues, giving the program a continuing impact even for students who have departed. In this report we divide the narrative into four main sections, each of which covers activities in the program and research conducted at one of the four main NRAO sites; Charlottesville, Socorro, Green Bank and Tucson. In an Appendix, we include the reports which many of the students wrote as part of their experience. Eight of the research projects will be presented at the 195<sup>th</sup> meeting of the American Astronomical Society in Atlanta, Georgia in January, 2000. All of these presentations are expected to be published in astronomical journals during 2000.

Several students were supported by non-REU funds--graduate students, graduating seniors, or foreign students. They are included in this report for completeness. Specifically, these students include: T. Cheung, J. Durbin, S. Hicks, N. Mohan, D. Osgood, C. Power and C. Schwartz.

There were 94 applicants to the 1999 program, of whom 36 (37%) were women. There were 24 positions which were filled, of which 15 were funded from under REU guidelines. Of these 24 positions, 10 (44%) were filled by women. Of the REU positions, 8 (53%) were filled by women.

# **1999 Research Experiences for Undergraduates Program**



**National Radio Astronomy Observatory**

## **1999 is the 40th Anniversary of the NRAO Summer Student Program!**

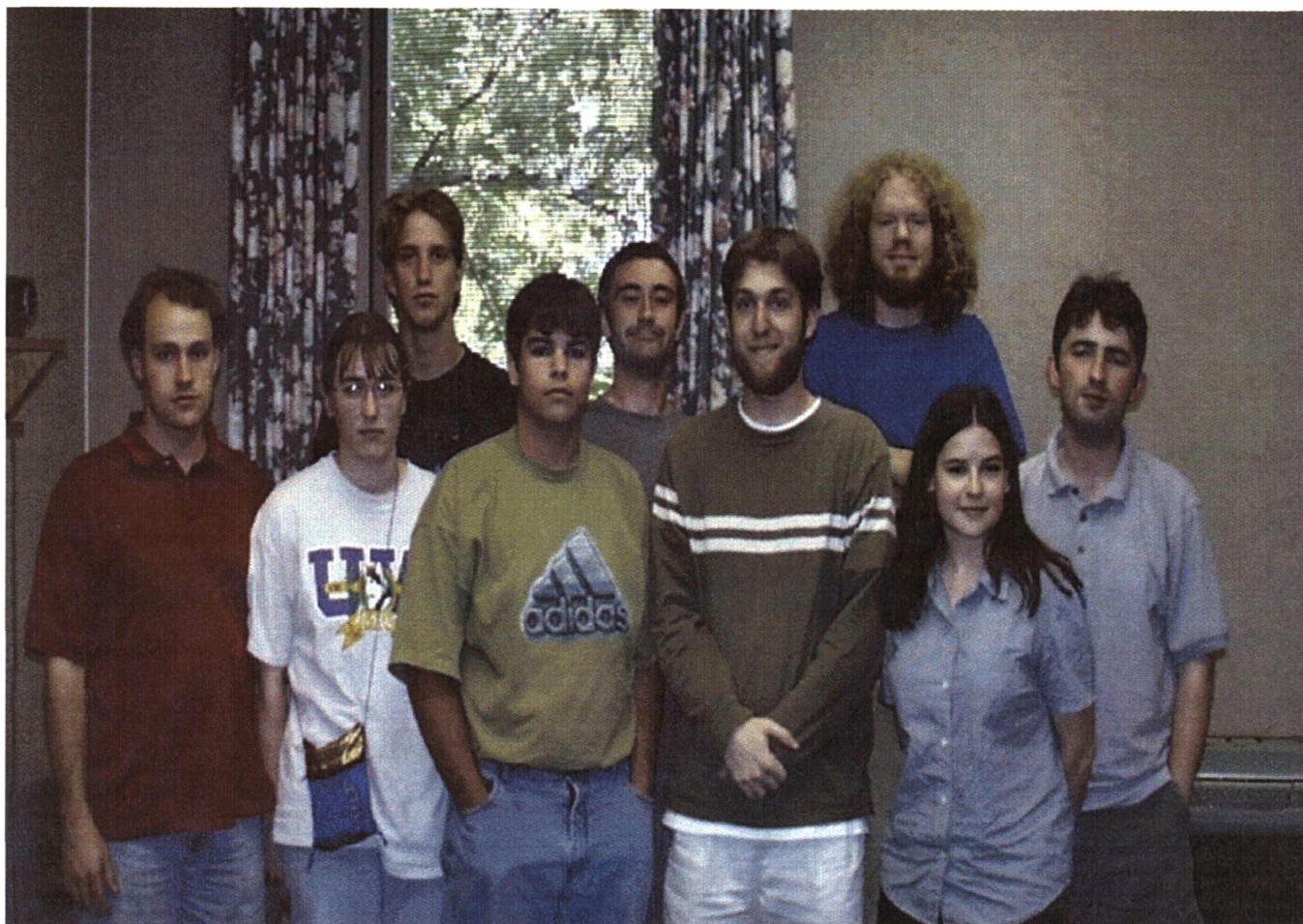
Research Projects by NRAO Site

- Charlottesville
- Socorro
- Green Bank
- Tucson

### **Charlottesville, Virginia (NRAO Headquarters)**

---

There were five students in the 1999 Summer Student Research Program, three of them under the NSF Research Experience for Undergraduates (REU) program at NRAO-Charlottesville. Highlights of the program included a series of introductory level lectures on aspects of astronomy, particularly radio astronomy, spread over a few weeks. These lectures are intended to acquaint the students with the research which various staff members carry out. The lectures are listed below.



1999 Summer students from Green Bank and Charlottesville met at a get-together with mentors and lecturers in Charlottesville.

Many of the students in the NRAO-Green Bank program visited Charlottesville for a tour of the Central Development Laboratory, and of the University of Virginia's facility for the fabrication of the Semiconductor-Insulator-Semiconductor detectors used in millimeter wave receivers, the Semiconductor Device Laboratory.





The 1999 students enjoy an informal get-together with astronomers from the University of Virginia and NRAO at lunch. followed by a visit with graduate students from the University's Astronomy Department.



The students wrote a Target of Opportunity proposal to measure OH in a comet which was awarded time. As a consequence, they observed at the 43m telescope in Green Bank, which closed this summer. They observed OH in C/1999 H1 (Lee) (above, seen on 20 May by Seiichi Yoshida). Water is the dominant constituent of comets but is unobservable owing to the earth's atmosphere. However, its photodissociation product OH can be observed with the 43m telescope. From that, the water production rate may be measured. We did this and published the result in the IAU Circular No. 7233:

#### Comet C/1999 H1 (Lee)

P. Mason, C. Murray, D. Bambic, J. Durbin and A. Wootten (NRAO) report that the OH 18-cm transitions were detected toward comet C/1999 H1 (Lee) at the NRAO 140-ft telescope in Green Bank, WV on 1999 May 25th. The 1667 MHz line was measured with a line area of  $0.062 \pm 0.007$  K km/s in antenna temperature; the 1665 MHz line was measured at  $0.026 \pm 0.008$  K km/s. The 1667/1665 ratio of 2.4 reasonably matches the expected line ratio of 1.8. Assuming an OH lifetime of  $2 \times 10^{-5}$  s, the line measurements give a water production rate of  $5.5 \times 10^{28} \text{ s}^{-1}$ .

Later in the summer, the Charlottesville students visited Green Bank again to tour the NRAO telescopes located there, to meet members of the Green Bank staff, and to attend the annual picnic.

One highlight was the placing of the panels onto the Green Bank telescope (GBT), the world's largest steerable telescope. It is an offset paraboloid, 110m across the longest axis, incorporating 16 million lbs of steel in the moving structure. The surface is more than half complete on the structure; during the rest of the year it will be completed. In Green Bank for observations, the students got to watch the process.

The 40 ft telescope there is a student telescope, open for any project which students would like to carry



out on it (though its instrumentation is limited). If there is interest, we may carry out, probably remotely, a project on the VLA or 12m telescope in Tucson.

We're very excited about the Atacama Large Millimeter Array, which was selected as the top priority for a new astronomical instrument in the 90s back at the beginning of the decade by the Astronomy Survey Committee. Students got to see it take shape as the second year of design and development gets underway.

The students gave a series of 15 minute talks on their projects during a lunch symposium in Charlottesville before they begin leaving for the summer. They produced short reports describing their summer research.



1999 Summer students from Charlottesville and their mentors at the 1999 Summer Student Research Symposium. Left to right: John Hibbard, Chris Power, Jack Gallimore, Jonathan Durbin, Dustin Bambic, Cristina Murray, Porter Mason, Michele Thornley and Barry Turner.



On August 11, 1999, the last total eclipse of the millennium occurred. Although totality was most easily viewed over the Atlantic through Europe to India, the path began over the Eastern Shore of Maryland and Virginia about 20 minutes before sunrise. Reliving eclipse expeditions of old, we decided to see if we could see any effects of totality before the shadow actually hit the Earth. Possibilities included a delayed twilight followed by sudden dawn and the rise of the partially eclipsed sun. The interpretations of our observations was somewhat muddled by the passage of a line of strong thundershowers just before 'totality'. However, we convinced ourselves that we had, in fact, seen a delayed twilight. On the return, we took a scenic route through historic Oxford and St. Michaels Maryland.



Students (l-r) Dustin Bambic, Chris Power and Cristina Murray on the auto ferry from Oxford to Bellaire cross the Tred Avon River (about half water and half stinging nettles at this time of year).

## **CV Summer Student Schedule, Summer 1999**

--

Date	Person	Item	Location	Time
17 May	open	Students begin arriving		
19 May	R2D2	Star Wars Opens	Carmike	12am
19 May	Wootten	Welcome	NRAO,Room 317, Stone Hall	9am
21 May	Wootten	Radiotelescopes and Radioastronomical Jargon	NRAO,Room 317, Stone Hall	9am
21 May	open	Public Night at McCormick Observatory	at the Observatory	9pm
24 May	Wootten	Preparation for Observing--From Antenna Temperature to Science	NRAO,Room 317, Stone Hall	9am
25 May	Wootten	Leave for Observing	NRAO,Room 317, Stone Hall	9am
25 May	Wootten	Observing, 43m telescope	Green Bank, W. Va.	1pm
25 May	Wootten	Observing ends, 43m telescope	Green Bank, W. Va.	9pm
26 May	Wootten	Return to Charlottesville	Green Bank, W. Va.	8am
28 May	Kellerman	The Development of Radio Astronomy	NRAO,Room 317, Stone Hall	9am
2 June	Condon	Radio Sources	NRAO,Room 317, Stone Hall	9am
4 Jun	open	Public Night at McCormick Observatory	at the Observatory	9pm
9 June	Turner	Interstellar Chemistry	NRAO,Room 317, Stone Hall	9am
14 June	Beasley	Interferometry	NRAO,Room 317, Stone Hall	9am
16 June	Liszt	The Interstellar Medium	NRAO,Room 317, Stone Hall	9am
18 June	Matthews	HI in Nearby Galaxies	NRAO,Room 317, Stone Hall	9am

18 Jun	open	Public Night at McCormick Observatory	at the Observatory	9pm
19 June	All	NRAO Summer Picnic	McIntire Park Shelter No. 3	1:30 pm
21 June (tent)	Wells	The Green Bank Telescope	NRAO, Room 317, Stone Hall	9am
23 June	Hogg	Radio Stars	NRAO, Room 317, Stone Hall	9am
25 June	Thornley	Molecules in Normal Galaxies	NRAO, Room 317, Stone Hall	9am
28 June	McMullin	Interstellar Molecules	NRAO, Room 317, Stone Hall	9am
30 June	Gallimore	Active Galactic Nuclei	NRAO, Room 317, Stone Hall	9am
2 Jul	open	Public Night at McCormick Observatory	at the Observatory	9pm
7 Jul	Garwood	AIPS++	NRAO, Room 317, Stone Hall	9am
12 Jul	Wootten	Star Formation	NRAO, Room 317, Stone Hall	9am
16 Jul	open	Public Night at McCormick Observatory	at the Observatory	9pm
TBD	Bradley	Central Development Lab Introduction	Rm 228 Ivy Road	9am
TBD	Bradley	Tour of Central Development Lab	Rm 228 Ivy Road	10am
TBD		Lunch with U. Va.	NRAO, Room 317, Stone Hall	12pm
TBD	Bradley	Tour of U. Va. Device Fabrication Facility	U. Virginia	1:20pm
TBD	Wootten	BBQ for CV, GB REUs and mentors	Wootten Home	6pm
24 July	All	CV REUs -> Green Bank Picnic	Green Bank, W. Va.	noon



28 July	van den Bout	TBD	NRAO, Room 317, Stone Hall	9am
3 Aug	Students	REU research presentations	Rm 317,	high noon
4 Aug	Hibbard	TBD	NRAO, Room 317, Stone Hall	9am
6 Aug	Hibbard	TBD	NRAO, Room 317, Stone Hall	9am
6 Aug	open	Public Night at McCormick Observatory	at the Observatory	9pm
20 Aug	open	Public Night at McCormick Observatory	at the Observatory	9pm

>



**Cristina M. Murray of University of New Mexico  
works with Jack Gallimore  
on**

## **Black Holes in Active Galaxies**

Active galaxies (AGNs) are thought to be powered by accretion onto a central, massive black hole. Seyfert galaxies are the nearest AGNs that show all of the classic signs of activity, including radio jets, broad optical line emission, hard X-ray emission, and rapid variability. They are indistinguishable from quasars except that they are nearer and less luminous. Recent VLBA observations have demonstrated that the radio emission from a Seyfert nucleus is, however, peculiar. The nuclear radio properties may owe to thermal processes in gas located very near the massive black hole (i.e., a few light years from the AGN).

I have several projects investigating peculiar radio sources in Seyfert nuclei, two of which are naturally suited for summer student research. One is a VLA survey of high frequency (22 and 43~GHz) emission from Seyfert nuclei. The goal is to locate potential flat-spectrum sources and address the effects of thermal free-free absorption (or possibly emission). There are currently data for 13 sources in hand, and we anticipate having an additional 15 sources this summer (TAC-willing). The other is a VLBI survey of nearby Seyfert galaxies. The main goal of the VLBI project is to investigate the Seyfert radio jets at a

spatial resolution of  $\sim 1$  light year. We will be receiving snapshot VLBI data for 8 sources this spring.

Both programs are technically challenging, and the summer student can expect to come away with an advanced understanding of aperture synthesis techniques. The student might choose either to concentrate on complete reduction of the survey data, in which case he or she will receive co-authorship on the survey paper, or to focus on the analysis and interpretation of a specific source and assume lead authorship.



**Dustin Bambic, of Western Kentucky University  
will work with Michele Thornley  
on**

## **NGC 7331: Characterizing the contribution of spiral density waves in flocculent galaxies**

My summer with NRAO in Charlottesville began as smoothly as one could hope, even though I was completely unfamiliar with our subject, flocculent galaxies. I had just finished school a week earlier, allowing little preparation time. Michele began the summer with discussion of our project, data, goals, and motivation. In short, galaxies with large-scale spiral structure are thought to contain spiral density waves. A spiral density wave is a compression wave that is able to organize a galaxy's constituents, forming spiral arms. However, not all galaxies have a large scale spiral design. Another galaxy type, flocculent galaxies, has a disc like the grand-design spirals, but no arms are visible in optical light. Due to their lack of organization, flocculent galaxies have been assumed by some of the astronomical community to not contain spiral density waves. In addition, the topic draws very little attention, and little data is available to those who wish to investigate the matter. So, Michele made this her doctoral thesis topic, investigated several flocculents, including the prototypical flocculent galaxy, NGC 5055, and found conclusive evidence for density wave presence in a few of them. She wished to continue this work, and turned the telescopes toward another flocculent, NGC 7331. Michele was granted 15 hours of observing time with NRAO's Very Large Array, and the data was safe in hand well before the summer. She soon turned her efforts toward new topics, with the NGC 7331 data set unreduced.

As an undergraduate interested in astronomy, I applied to NRAO's summer REU program, and other REU programs, in January 1999. In March, NRAO offered me a position in Charlottesville, and I quickly accepted. I had been chosen by Michele to help reduce her aforementioned data set.

I immediately began my background readings, consisting mostly of astrophysical and astronomical journals, spanning the spiral galaxy formation process, spiral form maintenance, galactic surveys, galactic kinematics, galactic interactions and mergers, and of course an introduction to radio astronomy.



In addition, the other summer students and I attended a few lectures a week concerning other astronomical topics, each about an hour long, and each by a different NRAO scientist. This introductory time was focused yet unhurried, and perhaps the most learningful period of my life. After only a few weeks, my view of the universe had changed considerably. Suddenly galaxies were dynamical, evolving systems, and the cosmos was much more exciting.

Soon, however, it was back to earth and into the world of AIPS and LINUX. UNIX is an operating system. Prior to NRAO, I may have thought the whole world was either Windows or Mac. However, my eyes were shown additional operating systems, UNIX/LINUX and SUN OS, and my digital adventure was underway. But, not before I was shown AIPS, and opened to what real radio astronomy consists of. AIPS is the data reduction program used for reduction of data collected by NRAO telescopes. Data from observations is stored onto DAT tape, and AIPS enters when you're ready to read and/or edit the data. AIPS consists of tasks and verbs used to configure your data, and with AIPS, bytes are turned into actual images of your object. Initially, I was very intimidated by both AIPS and LINUX, but as my stay at NRAO advanced, I became much more confident in my understanding of both, or at least the parts of each we used.

The data set came in three main sets, each corresponding to a different antenna configuration used to obtain the data. Different configurations provide information on different size scales. However, the reduction process is basically the same for each. Michele and I went through the first data set together, taking notes the entire time so that I could repeat the process by myself. However, it was not thoughtless replication. Each data set is different, almost taking on a character. Each had its own problems, requiring data interpretation and troubleshooting until the final image was satisfactory. The first eight of my twelve week stay at NRAO consisted of this reduction process, until three final images were obtained, one from each configuration.

These three images served as the base of all our further investigations. The three images were combined to create one "mother image." From this image, we were able to create velocity maps, density maps, major and minor axis velocity slices, and zooms of each, corresponding to different regions of NGC 7331. Again, we used each to look for density wave signatures in NGC 7331. We were not the first to look at NGC 7331 with density wave detection in mind. A previous group had used optical means to search for density waves, and claimed to detect density wave perturbations along the western side of the galaxy. We investigated the same region, and the rest of the galaxy. Interestingly, we could not confirm the wave detection along the western side of NGC 7331, but found more significant perturbations along the southeastern side of the galaxy. This final analysis process, along with my preparation for the final presentation of our research to the NRAO staff, occupied the last four weeks of my stay in Charlottesville, and before I knew it, the summer was over.

My summer at NRAO was as pleasing an experience as I could have imagined. I formed great friendships during my stay. I experienced the reality of astronomical research. I saw what astronomers do all day, what they eat, what they talk about, and even how they drive. My plans before NRAO included attending an astronomical graduate program. After my summer at NRAO, these plans have solidified. In fact, I plan to pursue astronomy more than ever. Perhaps I'll have a summer student working under me some day.

---



**Porter Mason , of Duke University**

**works with Barry Turner  
on**

## **The 2mm Spectral Survey**

Mr. Mason worked on preparing Turner's 2mm survey for presentation on the WWW. The input to the problem is (i) the observed spectra in tabular form (the form to be determined); (ii) and catalog of computed spectral lines including Lovas, JPL, and my own calculations; (iii) tables of spectral line parameters measured by me from the spectra. The problem will be to provide a WEB setup that allows the user to click on a given spectrum, and obtain several features including (i) a plot which with cursor control may be scaled in both axes, over a chosen frequency range; (ii) may be linked to the atlas of computed lines with which any selected line on the plot may be searched and labelled if a match is found; (iii) contain most of the elementary features of Unipops or AIOS++ such as rms (requiring designation of baseline parameters); perhaps gaussian fitting; 0th moment measures, etc.

The result may be viewed [here](#).



**Jonathan Durbin , of  
Valdosta State University  
works with Richard Bradley  
on**

## **Wideband Balanced Amplifiers**

Mr. Durbin helped to design wideband balanced amplifiers for operation in the 1-6 GHz band. Specifically, we need to develop multi-octave hybrid couplers. The student will learn about the operation of such components and then use computer-aided design tools to simulate their performance.

Test structures will be fabricated and evaluated.

---



**Chris Power, of Trinity College, Dublin**  
**works with John Hibbard and J. Barnes (IfA)**  
**on**

## **N-body Simulation of "The Antennae"**

Collisions between galaxies can be dealt with analytically only in very specific cases. Unfortunately, the conditions that are prevalent in the bulk of galaxy interactions rarely satisfy these idealisations and so, when considering such situations, the researcher must make use of N-Body simulations to model the encounters. In general, pictorial representations of the time evolution of such encounters is desired.

In this report, I will discuss my work in this area; in particular I will concentrate on how I developed a means to convert observational and simulation data into a form that is readable by the interactive 3 dimensional visualization tool, Geomview. I will also describe my work on the matching of simulation and observational data for the case of NGC 4038/9, the "Antennae", as well as the motivation for such model matching and the characteristic features of a system that are particularly suited to such fitting.

As an interesting aside, I indulged myself and present brief discussions on The History of Mergers and previous attempts to model the "Antennae" in Numerical Models of NGC 4038/9. My work may be reviewed here.

---

## **NRAO/Socorro 1999 Research Experience for Undergraduates (REU) Program**





1999 Summer students from Socorro visit the NRAO-Kitt Peak 12m telescope. (left to right, standing) Allison Coil, Liz McGrath, Bryan Jones, Niruj Mohan, Crystal Brogan, Chad Young, Colleen Schwartz, Makenzie Lystrup, Hannah Smith, (sitting) Darrell Osgood, and Teddy Cheung at the 12-meter NRAO telescope.

---

The summer REU program at NRAO/Socorro in 1999 consists of 4 main categories of activity:

- 1 - student research projects, in collaboration with an NRAO advisor
- 2 - lectures to the students by NRAO staff members
- 3 - a joint student project, involving observations with the Very Large Array (VLA)
- 4 - guided tours of the VLA, given by the students on weekends

The 1999 REU program at NRAO/Socorro is under the direction of Liese van Zee , Chris Fassnacht and Greg Taylor. Drs. van Zee and Fassnacht are Jansky Postdoctoral Researchers at NRAO/Socorro, and Dr. Taylor is a member of the scientific research staff. Please visit the NRAO/Socorro Summer Student Page.

---

## Lectures, etc...

Several lectures about radio astronomy and interferometry will be presented, allowing the students to obtain a good understanding of the technique. Talks were also given on general topics in astronomy, presented by members of the scientific staff. The astronomy talks were designed to give the students an understanding of what sort of research goes on at NRAO, and in radio astronomy in general. The detailed list of lectures and events for the summer is in the following table.

## 1999 Calendar of Events -- New Mexico

This is the list of 1999 student lectures and other organized events for the summer students.

---

## 1999 Summer Student Calendar of Events

### June 1999

June 8, 10:00 am: "Interferometry" by R. Perley  
June 10, 10:00 am: "Gamma Ray Bursts" by D. Frail  
June 11, 1:30 pm: Safety Lecture by Jon Spargo  
June 14, 10:00 am: "Fourier Transform" by B. Butler  
June 17, 10:00 am: "Imaging and Deconvolution" by T. Cornwell  
June 17, 11:00 am: VLA tour by G. Taylor (site)  
June ??, 10:00 am: VLA Public information lecture by D. Finley  
June 18, 11:00 am: Colloquium by Phil Gregory (UBC)  
June 21-23: field trip to KPNO/Tucson  
June 24, 10:00 am: "Radio Astronomy Instrumentation and Telescopes" by P. Napier  
June 25, 11:00 am: Colloquium by Miller Goss (NRAO)  
June 29, 10:00 am: "Radio Emission from Exotic Binary Stars" by R. Hjellming

### July 1999

July 1, 9:30 am: "Gravitational Lenses" by C. Fassnacht  
July 1, 11:00 am: Colloquium by Eric Richards (NRAO-CV)

July 6, 10:00 am: "Radio Galaxies and Jets" by G. Taylor  
July 8, 10:00 am: "A Supermassive Blackhole in the Galactic Center" by G. Bower  
July 9, 11:00 am: Colloquium by Phil Hardee (Univ. of Alabama)  
July 9, 2:00 pm: "Brown Dwarfs and the Search for Extrasolar Planets" by S. Kulkarni  
July 13, 10:00 am: "Recombination Lines" by Anantha (3rd floor conference room)  
July 15, 10:00 am: "Radio Evidence for Black Holes in Nearby Galactic Nuclei" by J. Wrobel (3rd floor conference room)  
July 19, 11:00 am: Colloquium by Amy Barger (IfA)  
July 20, 10:00 am: "Getting into Graduate School and other post-graduate plans"  
July 20, 2:00 pm: "Science with VLBI" by C. Walker  
July 22, 10:00 am: "Planetary Science" by B. Butler  
July 26, 7:00 pm: (public talk) "A Universe of Colour" by David Malin (AAO)  
July 27, 11:00 am: Colloquium by David Malin (AAO)  
July 27, 2:00 pm: "Space VLBI" by J. Ulvestad  
July 29, 12:00 pm: Student presentations: Niruj, Chad, and Andreea


## August 1999

August 5, 10:00 am: "Normal Galaxies" by M. Rupen  
August 5, 12:00 pm: Student presentations: Darrell, Bryan, Elizabeth, and Teddy  
August 10, 10:00 am: "Interstellar Fog" by K. Desai  
August 12, 12:00 pm: Student presentations: Crystal, Makenzie, Colleen, and Hanna  
August 13, 11:00 am: Colloquium by Vikram Dwarkadas (Univ. of Sydney)

Last update: July 18, by LvZ

---

---



The VLA is in A configuration this summer. Three hours of telescope time have been allocated to the summer students to pursue group projects.

A Study of Water Masers

HI Absorption towards PDS 456

Last Modified on Aug 11, 1999

## Planned Trips



Kitt Peak/Tucson - June 21-23.

The NRAO/AOC summer students embarked on a trip to Kitt Peak, where they visited the NRAO 12m telescope, the NRAO/Tucson REU students, and the NOAO facilities and summer students.

## Trip Itinerary

0700, June 21 - leave Socorro  
1100, June 21 - lunch in Lordsburg  
1430, June 21 - tour of NRAO 12-m antenna (by Jeff Mangum)  
1630, June 21 - dinner @ KP cafeteria  
1700, June 21 - tour of optical telescopes (by Nigel Sharp)

1000, June 22 - KP-VLBA antenna tour (by Nick Jesch)  
1130, June 22 - leave for Tucson  
1300, June 22 - lunch  
1430, June 22 - tour of NRAO Tucson (by Jeff Mangum)  
1600, June 22 - free time to explore Tucson/U of A  
1900, June 22 - dinner at Caruso's Italian restaurant

1000, June 23 - breakfast, check out of hotel  
1100, June 23 - tour of UA mirror lab  
1230, June 23 - lunch at Eric's  
1400, June 23 - leave Tucson for Socorro  
1900, June 23 - short walk along the Catwalk, Glenwood, NM  
2300, June 23 - arrive in Socorro

---

[Click here to see pictures of this year's trip.](#)

## Other Stuff

A Basic Information Letter is available from the WWW pages.

A more complete picture page on the WWW shows snap-shots from the summer.



## **Student Research Projects**

Each of the REU students will work with one or more advisors on one or more projects throughout the summer. This is the main focus of the program, and the majority of the students' time will be spent on these research endeavors. These projects involved observing, data reduction and analysis, equipment development, and theoretical studies. At the end of the program, each student gave a lunch talk explaining the main project(s) he or she worked on during the summer. The possibility exists for the students to present their original research at scientific meetings deemed appropriate by their advisor(s). Following is a detailed list of the specific projects carried out by the NRAO/Socorro REU students:

---

**Darrell Osgood of New Mexico Institute of Mining and Technology**  
works with Frazer Owen  
on

### **Evolution of Populations of Radio Galaxies in Clusters**

Using the existing deep VLA radio images for 6 clusters of galaxies with  $z$  between 0.25 and 0.41 and existing optical imaging (ground-based and HST), the student would make the optical identifications. The student would use these data, along with existing optical spectroscopy to estimate size of the radio populations in each of these clusters and whether the radio galaxies were likely star-formation driven or AGN's. These data would then be compared with lower redshift results to evaluate the evolution of these populations with redshift and other cluster properties.

---

**Teddy Cheung of Brandeis**  
works with Jim Ulvestad  
on

### **ARISE Imaging**

Space VLBI missions have unique imaging requirements relative to ground VLBI. For the highest resolutions, there typically are large holes in the  $(u,v)$  plane, both due to the high spacecraft orbit and to intermittent tracking. Also, high sensitivity is required, but the space telescope cannot nod back and forth between sources due to a limited slewing capability, making phase referencing impossible for the space element. These two issues should be addressed in order to provide better imaging for the future ARISE mission. Either problem is reasonably well-defined, and could be completed in a summer term, assuming a well-prepared student with some AIPS and radio interferometry background. The proposed approaches are outlined below, with the final selection to be made based on the student's and advisor's negotiation. Item (1) is probably a more tractable problem for a summer, although item (2) might also be possible. (1) Explore techniques in AIPS and/or DIFMAP for imaging of ARISE data having large holes in the  $(u,v)$  plane. The approach would be to take on-hand VSOP data from my projects or other

observations, then create (u,v) holes of varying sizes by deleting antennas giving long ground spacings (e.g., use the southwestern VLBA stations plus HALCA). The data would be used to examine techniques for fringe-fitting, self-calibration, and data weighting in order to find the best range of parameters, the limitations to dynamic range, and the inflection points at which the images begin to degrade rapidly. Simulated data might also be used.

(2) Investigate the possibility of phase-referencing the ground telescopes at high frequencies, while keeping ARISE pointed at the program source, in order to increase the coherent integration time and the detection threshold. There are two possible approaches, either through the acquisition of VLBA test data with most (but not all) of the antennas phase referencing, or by generation of simulated data with such an observing strategy. Currently, the latter strategy is favored, because real test data would still have an atmosphere above the VLBA antenna that is not phase referencing; the whole point of the project would be to test phase referencing for an antenna that cannot slew, but also has NO atmosphere.

---

**Colleen Schwartz of Colby College**  
**works with Joan Wrobel**  
**on**

## **SYMMETRIZATION OF THE RELATIVISTIC JETS IN M84**

The elliptical galaxy M84 hosts an FR I radio continuum source and a dusty, warped optical emission line “disk”. HST imaging shows that the inner dust distribution is not relaxed, but filamentary and complex. We have a VLA image of M84 at 4.9 GHz with a resolution of 500 mas (36 pc) FWHM, showing that the two large-scale jets in M84 are initially asymmetric: the ratio  $R_I$  of the intensity of the northern main jet to the southern counterjet exceeds unity. However, these jets symmetrize ( $R_I$ ) by a projected nuclear offset  $r_p$  (950 pc). Is this VLA symmetrization trend consistent with Doppler boosting in a decelerating, but initially relativistic, jet characterized by a (slowing) jet fluid velocity and a (constant) line-of-sight viewing angle? To test this, we obtained VLBA images of M84 at 1.7 GHz and 8.4 GHz, with resolutions of 11 mas (0.80 pc) and 1.9 mas (0.14 pc), respectively, and used them to evaluate  $R_I$  on pc scales for comparison with  $R_I$  on 100-pc (VLA) scales. These comparisons imply: (a)  $R_I > 15$  at pc and pc, requiring and at these locations. (b)  $R_I$  drops gradually between pc and pc, as expected if twin relativistic jets smoothly decelerate. (c)  $R_I$  drops rapidly between pc and pc, suggesting an abrupt slowing of the jet at this distance. Indeed, the main jet morphology at pc resembles an oblique shock. Furthermore, although the main jet is not initially perpendicular to the dust layer seen by HST, a clockwise deflection of the jet at pc brings it into closer alignment with the normal to the layer. This hints that the optical line-emitting gas and the dust in M84 trace the medium initially entrained across the jet’s boundary layer, both abruptly slowing the jet and deflecting it toward the normal to the gas/dust layer. These preliminary results were reported at IAU Symp. 175 in 1995 October.

---

**Andreea Petric, of Columbia University and NMIMT**  
**works with Michael Rupen**



on

## **Multi-object Spectroscopy of the Cluster CL0939+47**

Multi-object spectroscopy of objects in this  $z=0.4$  cluster was undertaken to determine how important dust extinction is in moderate redshift clusters, and to clarify galaxy type in clusters at 0.3

---

**Niruj Mohan , of Raman Research Institute, Bangalore**

**works with K. Anantharamiah**

on

## **Recombination Line Emission from Starbursts**

Niruj will work mainly on VLA spectral line data from two proposals AN81 and AM614. This will form the basis of his Ph.D. thesis. If time permits, he will also work on VLBA continuum data on PKS 1830-211 (at 90 and 50 cm) from the project BA031.

AN81 is a VLA proposal to study Recombination line emission near 8.5 GHz from a variety of starburst galaxies: a Wolf-Rayet Galaxy (He 2-10), a blue compact Dwarf (NGC 5253), an interacting system (NGC 1808) and two merging systems (NGC 4038 and VV 114). This proposal was awarded a total of 38 hours of VLA time (14 hrs in CnB, 4 hrs in C, 16 hrs in DnC and 4 hrs in D configurations). The CnB and C array observations were made in Nov/Dec 98 and is awaiting data reduction. The remaining observations will be made sometime during Mar-Jun 99. These proposals were prepared by Niruj and the observe files were also made by him.

AM614 is a VLA proposal that Niruj wrote to followup our earlier detection of RRLs from two well known starburst systems, IC694 and NGC 3628. Models for line emission that were made based on the detections at 8.5 GHz, predicted a strong variation of line strength with frequency. It is crucial to study higher frequency RRLs to constrain the models. This proposal is for observations of RRLs at 2 cm and has been awarded a total of 16 hours of VLA time in the D-configuration. I expect that these observations will be made when Niruj is visiting Socorro and thus he will take care of all aspects of these observations.

Another project that Niruj is involved in, and which is only peripherally related to the main theme of his thesis, is search for RRLs at 20cm from the gravitational lens system PKS1830-211 (VLA proposal AA220). To study the effect of intervening ionized gas (due to free-free absorption and scattering) on the continuum structure of PKS 1830-211, we have obtained a 10 hr VLBA observation (Program BA031) at 90 cm and 50 cm. If time permits, I will ask Niruj to work on this data as well while he is here. This will provide him (and me) valuable experience with low-frequency VLBA data.

Niruj is already proficient in preparing VLA observe files and spectral line data reduction using AIPS. I therefore expect him to get started as soon as he arrives. A large amount of data, all produced through his proposals and which will become part his Ph.D thesis, will be waiting for him when he arrives. He will greatly benefit from a summer studentship in 1999.

---

**Crystal Brogan , of The University of Kentucky  
works with Dale Frail  
on**

## **1720 MHz Zeeman Observations of OH Masers Toward SNRs**

Ms Brogan will be working with Drs D. A. Frail and W. M. Goss on an effort to perform 1720 MHz Zeeman observations of OH masers toward galactic supernova remnants. The 1720 MHz transition has proven to be a powerful probe of supernova remnant interactions with molecular clouds. The 1720 MHz line also exhibits the Zeeman effect, allowing for the magnetic field strength to be measured in these regions for the first time. The goal of this project will be to increase significantly the small number of such measurements in order to accurately model the role of magnetic fields in molecular shocks.

---

**Chad Young of Mississippi State University,  
works with Dale Frail  
on**

## **Afterglows from Gamma-ray Bursters**

The goal is the detection of long-lived afterglows from gamma-ray bursters at radio wavelengths. The study of these afterglows in the radio yields unique diagnostics not obtainable by any other means. In particular radio observations give the size and allow one to infer the expansion of the relativistic fireball that is produced in the burst.

A student might be expected to work on several things including (1) the monitoring of known radio afterglows (2) searching for radio emission from new bursts, (3) modeling the flux evolution of the synchrotron-emitting fireball, (4) developing observing/reduction code to simplify the process of obtaining radio data on GRBs. Depending on the student's talents I can see this as a pure observing project, a theory project or a partial software project. The detection of an afterglow would almost certainly involve the publication of paper.

---

**Hanna Smith , of Smith College,  
works with Greg Taylor  
on**

## **Compact Symmetric Object 1946+708**

The Compact Symmetric Object 1946+708 was the first extragalactic source in which bi-directional motions were directly observed (Taylor & Vermeulen 1997, ApJL, 485, L9). This offers a unique chance to measure  $H_0$ . Along with Rene Vermeulen, I have obtained multi-epoch VLBA observations of 1946+708 at 8 and 15 GHz. Our program will also measure the advance speeds of the hot spots, from which we will obtain the age of the source. The past year has seen the first such direct



measurements of the hotspot advance speed in extragalactic radio sources (Owsianik, Conway & Polatidis 1998, A&A, 336, L37; Owsianik & Conway 1998, A&A, 337, 69). The high reported velocities (0.25 c) in the Compact Symmetric Objects 0108+388 and 0710+439, give ages of order 1000 years, reinforcing the idea that these objects are compact by virtue of their youth and are not confined ("frustrated") by a dense environment. A velocity of 0.25 c (0.06 mas/yr) will be readily detectable by our monitoring observations. The basic work for a summer student would be to calibrate and image four VLBA epochs at 8 and 15 GHz on 1946+708 and to determine the motions of the jet components and especially the hot spots. A summer student working on this project would learn about the physics of Compact Symmetric Objects, and about the reduction and analysis of phase-referenced VLBI data. The goal for the student would be the publication of a paper in the ApJ and presentation of the results at a AAS meeting or other suitable conference.

---

**Elizabeth McGrath of Vassar**  
**works with Miller Goss**  
**on**

## **Water and HII in the Giant HII Region W49**

Miller Goss: Chris De Pree and I have started a program to determine the relative positions of H<sub>2</sub>O and continuum components in the giant HII regions Sgr B2 and W49. The observing technique is to do simultaneous continuum and H<sub>2</sub>O observations ( both IF's ). We self cal on the strong H<sub>2</sub>O masers and then can detect the weak 1.3 cm continuum components at high resolution ( 0.2 arc sec or so in the B array). The data reduction is complete for Sgr B2 and just started for W49. The relative positions can be determined at the level of 0.001 arc sec or so due to the favorable signal to noise. An REU student can bring this program to completion.

---

**Makenzie Lystrup of Portland State University**  
**works with Craig Walker**  
**on**

## **Phase Referencing with the VLBA: Structure and Motion of 3C120**

I would have the summer student work on a test of some aspect of phase referencing with the VLBA. Phase referencing is, of course, critical to high sensitivity on the VLBA. It is one of the two main focus areas in VLBA testing at the moment (the other is 3mm). The exact details of the project may vary depending on what others do between now and then and on the status of some old phase referencing tests. But my current idea would be to test various aspects of the use of multiple calibrators to improve the quality of reference results. Very early in the summer, or perhaps before the student gets here, a test project would be observed and correlated. In the test, several calibrators in a cluster, plus a few others around the sky, would be observed. All would be strong sources with very well known positions. Using

those data, we would look for the most effective, and easiest, scheme to use to improve the accuracy of referenced phases.

---

**Bryan Jones, of  
works with Rick Perley  
on**

## **Ionospheric Correction Using A Dual Frequency GPS Unit**

I think I have a cool project for an REU student -- working with our brand new dual frequency GPS unit. It looks as though the software support promised by the software group will be a little late in showing up. We could probably use a student to help us learn how to use the device. It is run from a PC running Windows NT, and does lots of cool things. So, I think we can offer this as a project. Once we get the receiver up, and the software loaded, more experiments with polarized pulsars will be needed to finish the project.

---

## **Green Bank, West Virginia (NRAO 43m and 100m Telescopes)**

Students conducting their research at the NRAO Green Bank Site in West Virginia included the students in the list below, along with others. The program at Green Bank is under the direction of Dr. Ron Maddalena.



1998 Summer and co-op Students (L-R): Marc Apgar, Jennifer Lockman, Steve Hicks, Naomi Bates, Lisa Wray, and Nicole Wiersgalla



1998 Summer and co-op Students and NRAO staff members after a caving trip (L-R): Frank Ghigo, Jennifer Lockman, Pat Matheny, Ron Maddalena, Nicole Wiersgalla, and Steve Hicks.

---

## 1998 Calendar of Events -- West Virginia

The following lists the scheduled activities for the GB students:  
May 7, 12, and June 2 -- Student Orientation and tours

### June 1998

June 1 - 5 -- Future VLBI Missions from Space (workshop)  
June 14 - 27 -- Teacher's Institute  
June 12: Mark Clark: M&C architecture  
June 17: Toney Minter: Turbulence  
June 26: Lisa Wray: Radio Astronomy Receivers  
June 29: Frank Ghigo: Earth Wobble

### July 1998

July 1: Dan Pedtke: OVLBI



July 7: Jim Braatz: Active Galactic Nuclei  
July 9: Rick Fisher: Antennae  
July 14: Dana Balser: Radiative Processes  
July 16: Joe McMullin: Spectroscopy  
July 21: Ron Maddalena: Holography  
July 22: Jay Lockman: HI in the Milky Way  
July 23: Gary Anderson: History of Radio Technology  
July 27 - 29 -- Workshop on Science with the Green Bank Telescope (workshop)

The dates might vary slightly from the above. The time and place might also vary but will usually be at 3:00 in the conference room in the new wing.

---

**Scott Zmerick, of West Virginia University**  
**works with Ron Maddalena and Sue Ann Heatherly**  
**on**

## **A 40 Foot Upgrade**

We are currently updating the control interface and receiver system for the 40-ft educational telescope. A programming student is needed to complete the graphical user interface to the telescope system.

---

**Steve Hicks, of**  
**works with Dan Pedtke**  
**on**

## **An OVLBI Controller**

OVLBI and NRAO is to complete the design of our new Peltier controller. This is a 90% hardware and 10% software project, so it would be good to have an EE as opposed to a CE. I think it could be finished in a summer and would help all on the site. There are a few other small things as well, one would be capturing schematics, updating our documentation - pretty boring for most people but a student might be into it.

---

**Christopher S Deyoung , of University of Houston**  
**works with Steve White**  
**on**

## **Test Dewars for Radioastronomy Instrumentation**

A project in the cryogenics lab. An automated system for characterizing and logging the cooling capacity of the various refrigerator needs to be designed built and tested. This would be a nice summer

long project which could be carried through from design to completion during the summer months. What I have in mind is a test dewar(s) with variable loads on the first and second stages of the refrigerators. A computer controls the energy applied to each load and graphs a load diagram for the particular refrigerator. This project entails thermodynamics, electrical engineering and writing code for the PC.

---

**Jill C. Kamienski , of University of Colorado, Boulder**  
works with Frank Ghigo  
on

## **Green Bank Interferometer Upgrades**

The project will involve programming in C or C++ for the Green Bank Interferometer project. It can involve either 1. Developing software for control of two 85-foot telescopes, in a vxWorks environment. The software would generate commands for moving the telescope to desired positions, would monitor the positions and other status information, and would write the status data in a log file. or 2. Developing a system for on-line editing and analysis of data from the Interferometer. Perhaps this will include an automated way of identifying radio sources that are flaring or exhibiting unusual behavior, and of identifying hardware problems.

---

**David Sand, of UCLA,**  
works with Jim Braatz  
on

## **Distant Megamasers**

The student and I will address the question of whether water megamaser sources are preferentially detected in AGNs with highly inclined galactic disks. Such a trend was detected at early stages of the maser surveys, and it can now be updated with survey results from the past two years, and the question addressed more confidently. The project will involve collecting, cataloguing, and analyzing properties of galaxies which have been observed for water. Statistical comparisons of the detected and undetected populations will then be pursued.

---

**Jeanine Wilson , of The University of Washington,**  
works with Dana Balser and Toney Minter  
on

## **Diffuse Ionized Gas in Galaxies**

The summer student will work on modelling the diffuse ionized gas of galaxies. Models of ionization levels of different atoms will be computed using the program CLOUDY for many different types of stars and differing ISM characteristics around these stars. The results from the CLOUDY models will then be



used to model a galactic disk. These models will then be compared to the galactic disk of the Milky Way and other galaxies with extended emission from diffuse ionized gas such as NGC 891.

---

## **Tucson, Arizona (NRAO 12m, ALMA and VLBA Telescopes)**

Two REU students conducted research at the NRAO Tucson site in Arizona during the summer of 1999. The program in Tucson is under the direction of Jeff Mangum. As the NRAO offices are across the street from KPNO/NOAO offices, the REU group shares in the activities of the NOAO REU program there.



1999 Summer students get a tour of the 12m from Jeff Mangum.

In addition to the general activities carried out at the KPNO/NOAO offices, the NRAO and KPNO/NOAO REU students participated in two group activities organized by the NRAO staff. The first was a night at the 12 Meter Telescope, where the REU students spent a day at the 12 Meter Telescope. Following a tour of the telescope and lab facilities, where the students were introduced to the instrumentation used in millimeter wavelength astronomy, the students were given the opportunity to participate in some actual millimeter wave astronomical observations. With this experience the students got an introduction to the observing techniques used in millimeter wavelength astronomy.

The second general activity was a lecture series on millimeter wavelength astronomy given by members of the NRAO scientific staff. Three lectures were given. Jeff Mangum gave a presentation on millimeter wavelength research into the properties of objects in the Solar System and molecular clouds. Darrel Emerson gave a lecture on millimeter wavelength observing techniques. Finally, to complete the survey of millimeter astronomy, Simon Radford gave a lecture on extragalactic astronomy at millimeter wavelengths.



1999 Summer students get a tour of the 12m from Jeff Mangum.

The following are detailed reports describing the work done by each REU student at NRAO Tucson.

---

**Sean Andrews, of Northwestern University**



**works with Jonathan Williams**  
**on**

## **Molecular Clouds and Star Formation in the Outer Galaxy**

My project was a study of star formation and molecular clouds using data from the Five College Radio Astronomy Observatory's CO Outer Galaxy Survey (Heyer et al. 1998, ApJ Suppl, 115, 241) and the IRAS point source catalog. The CO survey contains more than 2 million spectra and is the most detailed millimeter spectral line map ever made. It covers approximately 300 square degrees of sky in the outer Perseus arm of the Galaxy.

The beginning of the project consisted of a general overview of the properties of molecular clouds in the outer Galaxy, including analysis of their masses, volume densities, sizes, dynamics, and temperatures. As a familiarity with these characteristics was developed, the project shifted into an examination of star formation within the clouds of the survey.

Using the IRAS point source catalog, I created images of the clouds and embedded stars using IDL. After thorough analysis of the IRAS sources' spectra, two samples of clouds were compiled: one of clouds with embedded stars and the other of clouds without embedded stars. Many comparisons between these two samples were made to bring out any characteristics that are indicative of star formation. Specifically, I found a relationship between the samples that suggests that most of the integrated mass of clouds with embedded stars is in a much higher mass range than that of the clouds without embedded stars. Additionally, comparing the column densities of the two samples revealed signs that clouds with embedded stars are more compact than those clouds without stars. These results affirm that molecular clouds that are more massive and compact are likely to have greater star formation efficiencies.

---

**Andria Schwartz , of Alfred University**  
**works with Jeff Mangum**  
**on**

## **Methyl Cyanide as a Probe of Kinetic Temperature in Dense Molecular Clouds**

Historically, the inversion transition of ammonia ( $\text{NH}_3$ ) has been used as the primary temperature indicator in dense molecular clouds. However, the physical approximation typically used for this method assumes that only three energy levels are populated. This model breaks down when the temperature becomes high enough, about 50K. Recent investigations designed to determine the temperatures of the cores of molecular clouds have found that many of them to be at about 70-150K. As these temperatures are beyond the range of accuracy of the  $\text{NH}_3$  inversion transition method, these numbers have significant inaccuracies. We propose a different temperature probe which retains its accuracy at higher temperatures than the probes previously used. This probe uses the rotational transitions of methyl cyanide ( $\text{CH}_3\text{CN}$ ), a symmetric rotor. Using measurements of the J=6-5, 8-7, and 12-11 rotational transitions of  $\text{CH}_3\text{CN}$  obtained with the IRAM 30m Telescope, we have derived the kinetic temperature within a sample of molecular cloud cores. The analysis of these data used two separate analysis



methods; a statistical equilibrium technique which compared the intensities of the different K-transitions within a given J-ladder, and a rotational temperature diagram analysis. The results of this analysis has yielded good temperature and column density figures for some 24 molecular cloud cores within our galaxy. The results of this work will be presented at the AAS meeting in Atlanta, Georgia in January 2000.



[Take me to the 1998 Summer student Home Page](#)

[Take me to the 1997 Summer student Home Page](#)

[Take me to the 1996 Summer student Home Page](#)

[Take me to the 1995 Summer student Home Page](#)

[Back to the Home Page](#)

[Take me to the Shakespearean Insult Server](#)

# **Appendix**

## **Student Presentations at the 195<sup>th</sup> AAS Meeting**

### **Atlanta, Georgia**

**Bambic, Dustin (Western Kentucky U.) and Thornley, M. D. (NRAO) Session 7.07**

**Cheung, C. T. (Brandeis University) and Ulvestad, James (NRAO) Session 16.02**

**McGrath, E. J. (Vassar College), Goss, W. M. (NRAO) and DePree, C. (Agnes Scott College) Session 53.15**

**Murray, C. (U. N. M.), J.F. Gallimore (NRAO), S.A. Baum (STScI), A. Pedlar (NRAL, Jodrell Bank), A. Thean (Bologna), and M. Kukula (Edinburgh) Session 115.08**

**Sand, D. (U. C. L. A.), J. Braatz (NRAO), and L. Greenhill (CfA) Session 115.10**

**Schwartz, A. C. (Alfred University) and Mangum, J. G. (NRAO) Session 73.01**

**Wilson, J. M., (U. Washington) D. S. Balser, and A. H. Minter (NRAO) Session 51.06**

**Young, C. H. (Mississippi State University), D. A. Frail (National Radio Astronomy Observatory), S. R. Kulkarni (California Institute of Technology) Session 71.05**

**Copies of the abstracts follow.**

**AAS 195th Meeting, January 2000***Session 7. Galaxy Structures and Dynamics: Models and Observations**Display, Wednesday, January 12, 2000, 9:20am-6:30pm, Grand Hall*[\[Previous\]](#) | [\[Session 7\]](#) | [\[Next\]](#)

---

## **[7.07] NGC 7331: Examining Density Wave Contributions in Flocculent Galaxies**

*D. Bambic (Western Kentucky U.), M. D. Thornley (NRAO)*

We have used the VLA in three array configurations (B, C, and D) to produce high-resolution (10\arcsec~and 15\arcsec) HI images of NGC 7331, a nearby flocculent spiral galaxy. In this poster, we compare the distribution and kinematics of atomic hydrogen in NGC 7331 with the results of a previous kinematic analysis of H $\alpha$  Fabry-Perot data (Marcelin et al. 1994). Marcelin et al. suggest that perturbations in the velocity field of NGC 7331 are consistent with the presence of density waves, despite the lack of grand-design spiral structure in the optical. We find significant, organized velocity perturbations are present, though we do not detect velocity perturbations in the inner region Marcelin et al. indicated, likely due to our lower resolution. However, the more complete coverage of our map provides us with a more complete picture of the kinematic structures present over the optical disk of NGC 7331.

We will also compare our results with an HI kinematic study of NGC 5055, a similarly flocculent spiral galaxy which has previously been shown to exhibit density-wave-like velocity perturbations in its optically flocculent disk (Thornley & Mundy 1997). We discuss the implications of our findings on the theory of spiral density waves and the significance of separate classifications for disk galaxies with apparent flocculent and grand design spiral structure.

---

[\[Previous\]](#) | [\[Session 7\]](#) | [\[Next\]](#)

**AAS 195th Meeting, January 2000**  
*Session 16. Blazar and Quasar Variability*  
*Display, Wednesday, January 12, 2000, 9:20am-6:30pm, Grand Hall*

[\[Previous\]](#) | [\[Session 16\]](#) | [\[Next\]](#)

---

# **[16.02] Space VLBI Imaging and Simulations of the EGRET Blazar 1633+382**

*C. C. Cheung (Brandeis), J. S. Ulvestad (NRAO)*

We present our second epoch VSOP (VLBI Space Observatory Programme) observation of the EGRET blazar 1633+382 at 5 GHz. The VSOP satellite (HALCA) was used with NRAO's VLBA plus phased VLA on 4/5 August 1998 to produce projected baselines well over a factor of three over that achievable from the ground only. This image is combined with our first epoch VSOP observation on 29/30 July 1997 and an 8 GHz VLBA observation in 1995 in our proper motion study of this blazar.

We also present image simulations created from the second epoch VSOP observation. We assess the imaging capabilities of apogee heights plausible for future Space VLBI missions such as VSOP-2 and ARISE (Advanced Radio Interferometry between Space and Earth) by removing telescope data to simulate different sizes of the UV hole in the VLBI imaging plane. Our preliminary results show that image fidelity is severely compromised when the major axis of an elliptical hole in the UV plane is as large as 75% of the longest projected baseline. This technique can be utilized on other observations with HALCA to aid in the determination of a tolerable orbit for upcoming Space VLBI missions.

We thank the 1999 NSF REU/NRAO Summer Student program and its coordinators. The National Radio Astronomy Observatory is a facility of the National Science Foundation operated under cooperative agreement by Associated Universities, Inc.

---

The author(s) of this abstract have provided an email address for comments about the abstract:  
[ccc@quasar.astro.brandeis.edu](mailto:ccc@quasar.astro.brandeis.edu)

[\[Previous\]](#) | [\[Session 16\]](#) | [\[Next\]](#)



**AAS 195th Meeting, January 2000***Session 53. ISM: Ionized Gas**Display, Thursday, January 13, 2000, 9:20am-6:30pm, Grand Hall*[\[Previous\]](#) | [\[Session 53\]](#) | [\[Next\]](#)

---

**[53.15] H<sub>2</sub>O Maser Emission in W49N***E. J. McGrath (Vassar College), W. M. Goss (NRAO), C. G. De Pree (Agnes Scott College)*

We present observations from the Very Large Array (VLA) in A and B configuration at 43 GHz and 22 GHz of the energetic star forming region W49N. Maser features in this source extend between velocities -260 km/s and +270 km/s. Positions and fluxes were calculated for 312 H<sub>2</sub>O masers with resolutions between 0.045" and 0.30". The weak continuum was cross calibrated with a strong maser feature that appears at  $v=170.7$  km/s in the line data. The masers were then aligned to the continuum by using this reference line at  $v=170.7$  km/s. Alignment errors are at the level of  $\sim 0.01''$  ( $5.6 \times 10^{-4}$  pc, or 115 AU at a distance of 11.4 kpc as determined by proper motion studies of Gwinn, Moran, & Reid 1992), which is a factor of ten better than previous observations. The center of outflow of these maser features appears to be located between two ultra-compact (UC) HII regions, within 0.2" of the bright source G2.

This work was supported by the NSF sponsored REU program. The National Radio Astronomy Observatory is facility of the National Science Foundation operated under a cooperative agreement by Associated Universities, Inc.

---

The author(s) of this abstract have provided an email address for comments about the abstract:  
[elmgrath@vassar.edu](mailto:elmgrath@vassar.edu)

[\[Previous\]](#) | [\[Session 53\]](#) | [\[Next\]](#)

**AAS 195th Meeting, January 2000***Session 115. Seyferts and Other Mildly Active Galaxies**Display, Saturday, January 15, 2000, 9:20am-4:00pm, Grand Hall*[\[Previous\]](#) | [\[Session 115\]](#) | [\[Next\]](#)

---

**[115.08] VLBA Imaging of the CfA Seyferts**

*C. Murray (UNM), J.F. Gallimore (NRAO), S.A. Baum (STScI), A. Pedlar (NRAL, Jodrell Bank),  
A. Thean (Bologna), M. Kukula (Edinburgh)*

As resolved by the VLA and MERLIN, the radio structures of Seyfert galaxies commonly resemble linear outflows, or jets, that may be low-power versions of the large jets observed in radio galaxies. It is rare, however, that Seyfert galaxies show a compact radio source that can be identified unambiguously as the location of the central engine. To explore the nuclear environment of Seyfert radio jets, we have used the Very Long Baseline Array (VLBA) to image a radio flux-limited sample selected from the CfA Seyfert catalog. We identify new flat-spectrum radio sources that might be self-absorbed components near the central engine. Several Seyfert nuclei show resolved, parsec-scale jets that align well with the larger scale radio structure. Both MERLIN and the VLBA resolve out the central, flat-spectrum radio source of NGC~5929. We consider radio emission and scattering models to explain this peculiar source.

---

[\[Previous\]](#) | [\[Session 115\]](#) | [\[Next\]](#)

**AAS 195th Meeting, January 2000***Session 115. Seyferts and Other Mildly Active Galaxies**Display, Saturday, January 15, 2000, 9:20am-4:00pm, Grand Hall*[\[Previous\]](#) | [\[Session 115\]](#) | [\[Next\]](#)

---

## **[115.10] VLA Observations of Extragalactic Water Maser Sources**

*D. Sand (NRAO/UCLA), J. Braatz (NRAO), L. Greenhill (CfA)*

Extragalactic water masers are excellent tools for studying the central regions of active galactic nuclei. VLBI observations have shown that water maser emission is associated with thin, parsec-scale molecular disks located near the spout of radio continuum jets. In order to study this general model, the fifteen water maser emitting galaxies observable by the VLA were imaged in A-array in April 1998. Two IFs were used simultaneously, one tuned to the frequency of the maser emission and the other slightly offset in order to gauge the continuum emission without any low level maser contamination. Both line and continuum data were successfully imaged for six of the sources, while for one other only the continuum data was successfully imaged. The remaining seven sources were not detected, due to instrumental or atmospheric instabilities. Of the sources with both line and continuum detections, three (NGC 3079, NGC 1052, and IC 1481) had measurable separations between the maser and continuum emission peaks and three (NGC 4258, NGC 1068, and NGC 2639) had maser and continuum emission coincident to within the observational uncertainties (roughly 1 pc for each). NGC 3079 and NGC 1052 both show projected separations of about 0.3 pc, which is in agreement with previous VLBI studies. IC 1481 has a much larger projected separation of 5.4 pc. If the maser geometry in IC 1481 is similar to that in NGC 4258, it would imply a central black hole mass of  $1.7 \times 10^7$  solar masses.

---

[\[Previous\]](#) | [\[Session 115\]](#) | [\[Next\]](#)



**AAS 195th Meeting, January 2000**

*Session 73. ISM: Molecular Gas*

*Display, Friday, January 14, 2000, 9:20am-6:30pm, Grand Hall*

[\[Previous\]](#) | [\[Session 73\]](#) | [\[Next\]](#)

---

## **[73.01] Using Rotational Transitions of Methyl Cyanide (CH<sub>3</sub>CN) as a Temperature Indicator in Molecular Clouds**

*A. C. Schwartz (Alfred University), J. G. Mangum (National Radio Astronomy Observatory, Tucson)*

Traditionally, the inversion transitions of ammonia (NH<sub>3</sub>) have been used as a primary temperature indicator. However, the physical model typically used for this method assumes that only three energy levels are populated. This model breaks down when the temperature becomes high enough, about 50K. Previous investigations to determine the temperatures of the cores of molecular clouds found them to be at about 70-150K. As these temperatures are beyond the range of accuracy of the inversion transition method, these numbers have great inherent inaccuracies. We have investigated the utility of the CH<sub>3</sub>CN molecule as a temperature monitor which retains its accuracy at higher temperatures. Using CH<sub>3</sub>CN rotational transitions and two separate methods of analyzing the resultant data, we have obtained good temperature and column density figures for some 24 molecular cloud cores within our galaxy.

This project was partially supported by NRAO and the NSF REU program.

---

If you would like more information about this abstract, please follow the link to <http://heineken.tuc.nrao.edu/>. This link was provided by the author. When you follow it, you will leave the Web site for this meeting; to return, you should use the Back command on your browser.

The author(s) of this abstract have provided an email address for comments about the abstract: [schworac@hotmail.com](mailto:schworac@hotmail.com)

[\[Previous\]](#) | [\[Session 73\]](#) | [\[Next\]](#)

**AAS 195th Meeting, January 2000**  
*Session 51. ISM: Theory and Modelling*  
*Display, Thursday, January 13, 2000, 9:20am-6:30pm, Grand Hall*

[\[Previous\]](#) | [\[Session 51\]](#) | [\[Next\]](#)

---

# **[51.06] The Dissipation of Turbulence as a Heat Source in the Warm Ionized Medium**

*J. M. Wilson (U. Washington), D. S. Balser, A. H. Minter (NRAO)*

The observed properties of the diffuse warm ionized gas (WIM) in our Galaxy are not consistent with photoionization models. Photoionization models, however, can reproduce the observed properties in classical HII regions. For some time now there has been mounting evidence of an additional heating source in the WIM. This conclusion is based on the fact that the recombination lines, which are produced almost entirely by the stellar radiation field, are consistent with the models but the fine structure lines, excited primarily by collisions, are more intense than the predictions from photoionization models. Recent observations of the WIM suggest that any additional heating source must supply heat with a rate per unit volume proportional to a lower power of the electron density than the heating rate (Reynolds et al. 1999, ApJ, submitted).

A promising candidate is the dissipation of turbulence which heats the interstellar medium in our Galaxy at a rate which is approximately proportional to the density. Models which include both photoionization and heating from turbulence have had some success (Minter & Balser 1997, ApJ, 484, L133). Here we expand on these initial models using the numerical program CLOUDY (Ferland 1996). We explore a variety of physical conditions with over 10,000 different models. Models which include turbulent heating fit the observations much better than models without extra heating for a large range of the physical conditions explored (e.g., electron density, filling factor, radiation field).

This work was funded by the National Science Foundation's Research Experiences for Undergraduates program.

---

[\[Previous\]](#) | [\[Session 51\]](#) | [\[Next\]](#)

**AAS 195th Meeting, January 2000**

*Session 71. Gamma Ray Bursts (and the Swift GRB Mission)*

*Display, Friday, January 14, 2000, 9:20am-6:30pm, Grand Hall*

[\[Previous\]](#) | [\[Session 71\]](#) | [\[Next\]](#)

---

## **[71.05] Long Term Radio Observations of GRB 980329**

*C. H. Young (Mississippi State University), D. A. Frail (National Radio Astronomy Observatory),  
S. R. Kulkarni (California Institute of Technology)*

The gamma-ray burst of 1998 March 29 (GRB 980329) had an unusually dim optical afterglow despite the fact that it was readily detectable at X-ray and radio wavelengths. Taylor et al. (1998) were the first to suggest this dimness was due to a high dust content in the region where the burst originated. Other explanations, however, require that the burst have occurred at a redshift of  $\sim 5$ . Taylor et al. monitored the afterglow for a month after the burst and have already published their results. In this poster, we present follow-up observations made with the VLA at 8.46 GHz, 4.86 GHz, and 1.43 GHz for up to 500 days after the burst. We will discuss preliminary applications of models to the radio data as well as a broadband view of the afterglow to include x-ray and optical data.

---

[\[Previous\]](#) | [\[Session 71\]](#) | [\[Next\]](#)



# **Project Reports**

## **1999 Summer Research Students**

### **Individual Research Project Reports**

**D. Bambic (Western Kentucky University)**

**C. L. Brogan (University of Kentucky) (with Frail, Goss and Troland)**

**C. C. T. Cheung (Brandeis University) (with Ulvestad; three papers)**

**Bryan Jones (University of Arizona) (with Perley, Moeser, Flatters and Erickson)**

**Jill Kamienski (University of Colorado, Boulder)**

**Mackenzie Lystrup (Portland State University)**

**Elizabeth J. McGrath (Vassar College)**

**Cristina M. Murray (University of New Mexico)**

**Darrell Osgood (New Mexico Inst. Of Mining and Technology)**

**Andreea Petric (New Mexico Inst. Of Mining and Technology) (with Owen and Rupen)**

**C. Power (Trinity College Dublin)**

**Niruj Mohan Ramanujam (Raman Research Institute, India)**

**Collen Schwartz (University of California, Santa Barbara)**

**Hanna G. Smith (Smith College)**

**C. H. Young (Mississippi State University) (with D. A. Frail)**

**Scott A. Zemerick (West Virginia University)**

### **Group Research Project Reports**

**AOC Summer Students (C. Young, C. Brogan, C. Cheung, B. Jones, M. Lystrup, E. McGrath, N. Mohan, D. Osgood, A. Petric, C. Schwartz, H. Smith and Min S. Yun)**

**Charlottesville Summer Students (P. Mason, D. Bambic, C. Murray, J. Durbin, C. Power and A. Wootten)**



# OH Zeeman Magnetic Field Detections Toward Five Supernova Remnants

C. L. Brogan<sup>1</sup>, D. A. Frail<sup>2</sup>, W. M. Goss<sup>2</sup>, and T. H. Troland<sup>1</sup>

## ABSTRACT

We have observed the OH (1720 MHz) line in five galactic SNRs with the VLA to measure their magnetic field strengths using the Zeeman effect. We detected all 11 of the bright ( $S_\nu > 200$  mJy) OH (1720 MHz) masers previously detected by Frail et al. (1996) and Green et al. (1997) and measured significant magnetic fields (i.e.  $> 3\sigma$ ) in nine of them. Assuming that the “thermal” Zeeman equation can be used to estimate  $|\vec{B}|$  for OH masers, our estimated fields range from 0.2 to 2 mG. These magnetic field strengths are consistent with the hypothesis that ambient molecular cloud magnetic fields are compressed via the SNR shock to the observed values. Magnetic fields of this magnitude exert a considerable influence on the properties of the cloud with the magnetic pressures ( $10^{-7} - 10^{-9}$  erg cm<sup>-3</sup>) exceeding the pressure in the ISM or even the thermal pressure of the hot gas interior to the remnant. This study brings the number of galactic SNRs with OH (1720 MHz) Zeeman detections to ten.

*Subject headings:* ISM:clouds — ISM:individual (W51, G349.7+0.2, CTB37A, CTB33, G357.7-0.1) — ISM:magnetic fields — masers — polarization — radio lines:ISM

## 1. INTRODUCTION

Magnetic fields can moderate the impact that a shock has on a molecular cloud. In the absence of a field, a supernova blast wave will heat, compress and fragment the cloud and may ultimately destroy it (Klien, McKee & Colella 1994). The inclusion of a field ameliorates these effects, limiting compression and stabilizing it against fragmentation,

---

<sup>1</sup>University of Kentucky, Department of Physics & Astronomy, Lexington, KY 40506-0055

<sup>2</sup>National Radio Astronomy Observatory, P. O. Box O, 1003 Lopezville Road, Socorro, NM 87801



allowing the cloud to survive, perhaps to trigger a future generation of star formation (Miesch & Zweibel 1994; MacLow et al. 1994).

It has long been known that supernova remnants (SNRs) possess magnetic fields. Observations of synchrotron radiation have established that the *direction* of the magnetic field in young SNRs like Cas A is predominately parallel to the shock normal (i.e. radial), whereas for older remnants the fields are perpendicular (e.g. Dickel et al. 1991; Milne 1990). The latter geometry likely originates from the compression of the ambient interstellar field, while Rayleigh-Taylor instabilities are invoked to explain the radial fields in young SNRs (Jun & Norman 1996). Until recently, estimates of the *strength* of the magnetic fields in SNRs had to rely on the somewhat dubious equipartition approximation. This situation has changed with the re-discovery of shock-excited OH (1720 MHz) maser emission in SNRs (Frail, Goss & Slysh 1994).

In a series of recent papers, the satellite line of the OH molecule at 1720.53 MHz has been used as a powerful probe of SNR-molecular cloud interactions. OH (1720 MHz) masers are found in  $\sim 20$  SNRs, or 10% of the known SNRs in our Galaxy (see Koralesky et al 1998 and references therein). This maser line is inverted through collisions with  $H_2$  ( $n \sim \text{few} \times 10^4 \text{ cm}^{-3}$  and  $T \sim 80 \text{ K}$ ) behind C-type shocks propagating into molecular clouds (Reach & Rho 1999, Frail & Mitchell 1998). The geometry of the shock is well constrained since strong maser amplification can only occur when the shock is transverse to the line-of-sight (Claussen et al. 1997). These observational statements are well-supported by theoretical modeling of the OH (1720 MHz) excitation (Lockett, Gauthier & Elitzur 1998; Wardle, Yusef-Zadeh, & Geballe 1998; Wardle 1999).

One advantage of observing the OH (1720 MHz) maser line is that it allows for a measurement of the strength of the magnetic field via Zeeman splitting (e.g. Troland & Heiles 1982). In this case, when the observed splitting is small compared to the line width,  $V = ZC|\vec{B}|dI/d\nu$ , where  $B$  is the the magnetic field strength,  $Z$  is the Zeeman splitting coefficient, and  $C$  is a constant which depends on the angle between the line of sight and  $\vec{B}$  (the possible forms of  $C$  will be discussed in §4.1). For now we will denote the combination of  $C|\vec{B}|$  as  $B_\theta$ .

This method has already been used to successfully measure the magnetic field strength in the post-shock gas behind five SNRs (Sgr A East, W44, W28, G32.8–0.1, and G346.6–0.2), yielding values for  $B_\theta$  between 0.1 to 4 mG (Yusef-Zadeh et al. 1996, Claussen et al. 1997, Koralesky et al. 1998). With these promising results in mind, we have performed 1720 MHz Zeeman studies toward five of the 17 SNRs found in surveys by Frail

et al. (1996) and Green et al. (1997) to contain OH (1720 MHz) masers using the NRAO<sup>3</sup> VLA. Only SNRs with bright masers ( $I > 200$  mJy) and no previous high resolution Stokes V observations were chosen.

## 2. OBSERVATIONS

We observed five SNRs (W51, G349.7+0.2, CTB37A, CTB33, and G357.7–0.1) at 1720 MHz with the VLA in A configuration. The key observing parameters for each SNR are given in Table 1. All of the SNRs were observed in “2IF mode” (recording both right (RCP) and left (LCP) circular polarization) with a 0.1953 MHz bandwidth divided into 127 channels. The observations were conducted on June 22, July 6, 8, 12, and 15, 1999. The OH data were Hanning smoothed online, and the resulting velocity resolution is  $0.27 \text{ km s}^{-1}$ . We observed both senses of circular polarization simultaneously and since Zeeman observations are very sensitive to small variations in the bandpass, a front-end transfer switch was used to periodically switch the sense of circular polarization passing through each telescope’s IF system.

The AIPS (Astronomical Image Processing System) package of the NRAO was used for the calibration, imaging, and cleaning of the OH (1720 MHz) data sets. The RCP and LCP data were calibrated separately and later combined during the imaging process to make Stokes  $I = (RCP + LCP)/2$  and Stokes  $V = (RCP - LCP)/2$  data sets. Bandpass correction was applied only to the I data sets since bandpass effects cancel to first order in the V data. Line data sets were created by estimating and removing the continuum emission in the UV plane using the AIPS task UVLSF. The strongest maser channel in each line data set was then self-calibrated and the solutions were applied to each channel. Subsequent magnetic field estimates were performed using the MIRIAD (Multichannel Image Reconstruction Image Analysis and Display) processing package from BIMA. The rms noise per spectral channel obtained for each SNR is summarized in Table 1.

After imaging, each of the bright maser spots were fit with a 2-D Gaussian using the AIPS task JMFIT. None of these fits showed convincing evidence that the individual maser spots are resolved at the resolutions shown in Table 1; therefore, we regard the maximum sizes reported by JMFIT to be upper limits. The positions, peak fluxes, and an upper limit to the maser spot sizes are reported in Table 2. In addition, the Stokes I spectrum at the peak pixel of each maser spot was fit with a single Gaussian in the spectral domain

---

<sup>3</sup>The National Radio Astronomy Observatory is a facility of the National Science Foundation operated under a cooperative agreement by Associated Universities, Inc.

using GIPSY, to obtain each maser’s center velocity ( $v$ ) and linewidth ( $\Delta v_{FWHM}$ ). These estimates of  $\Delta v_{FWHM}$  were then corrected for the finite channel width of the data ( $0.27 \text{ km s}^{-1}$ ), these deconvolved  $\Delta v_{FWHM}$  and center velocities are also reported in Table 2. The absolute position errors of these data are  $\sim 0.1''$ , while the relative position errors (compared to other masers in the field) are much better with typical values of  $\sim 0.001''$  in R.A. and  $\sim 0.02''$  in Declination.

In addition, W51 was observed on August 3, 1999 in “PA mode” (recording all Stokes parameters) with a 0.1953 MHz bandwidth, and 64 channels. This correlator setup resulted in a velocity resolution of  $\sim 0.54 \text{ km s}^{-1}$  after Hanning smoothing. The details of this observation can also be found in Table 1. This data was calibrated in the same manner described above, with the exception of the polarization calibration. The absolute polarization calibration was carried out by extrapolating 3C48 data from seven previous 20 cm polarimetry observations to yield a position angle of P.A. =  $13^\circ$  for this calibrator at 1720 MHz. Note that the error in this estimate ( $\sim 5^\circ$ ) will also apply to the position angles derived from these data.

### 3. RESULTS

#### 3.1. General Maser Properties

From the five observed SNRs we detected all 11 bright OH (1720 MHz) masers ( $S > 200 \text{ mJy}$ ), previously known from the surveys of Frail et al. (1996) and Green et al. (1997). Table 2 summarizes the fitted parameters of these maser features. Of these, nine show classical S-shaped Stokes V profiles (e.g. Elitzur 1998), one shows a complicated Stokes V profile, and one shows no discernible V signal despite its  $\sim 1800 \text{ mJy}$  peak flux density. The observed masers have typical deconvolved line widths of  $\sim 0.8 \text{ km s}^{-1}$ , spanning the range from 0.3 to  $1.5 \text{ km s}^{-1}$ . In addition, none of the observed OH (1720 MHz) masers appear to have undergone significant changes in flux density or position since the detection experiments were performed in 1994. As noted in §2, none of the maser spots have been resolved at the resolutions listed in Table 1. This may be due, in part, to the low declination, and hence elliptical synthesized beam shapes observed for four of the five SNR. Using the upper limits on the maser spot sizes listed in Table 2, lower limits on the brightness temperatures of these masers range from  $4 \times 10^4 \text{ K}$  to  $10^8 \text{ K}$ .

As noted in §1,  $V = ZC|\vec{B}|dI/d\nu$  for thermal radiation when the Zeeman splitting is a small fraction of the line width ( $Z = 0.6536 \text{ Hz } \mu\text{G}^{-1}$  for OH at 1720 MHz). The validity of this thermal expression for the magnetic field in masers and the  $\theta$  dependence



and magnitude of  $C$  is discussed in §4.1. Using the thermal Zeeman expression, the derivative of Stokes I was fitted to Stokes V in a least square fitting routine as described by Claussen et al (1997), to obtain the combination  $C|\vec{B}|=B_\theta$ . Magnetic fields were detected toward all five SNR at greater than the  $3\sigma$  level. The fitted magnetic field strengths ( $B_\theta$ ), and their associated  $1\sigma$  errors are summarized in Table 3, while comments on individual sources appear in §3.2. The detected  $B_\theta$  fields span a range of values from 0.2 to 2 mG. Unlike the case found in W28 and W44, where the fields were found to be uniform in both magnitude and direction (Claussen et al. 1997), CTB37A shows a complicated magnetic field morphology. In this source  $B_\theta$  changes by a factor of seven and reverses sign on a length scale of  $\sim 3$  pc.

### 3.2. Individual Sources

#### 3.2.1. W51

W51 is composed of two H II region complexes (W51A and W51B), as well as, the SNR W51C and is located at the tangent point of the Sagittarius arm at  $\ell = 49^\circ$ . A continuum image of W51 at 330 MHz from Subrahmanyan & Goss (1995) is shown in Figure 1 with the two W51C OH (1720 MHz) masers superposed. Based on the absorption of X-ray emission from W51C toward W51B, W51C seems to be located behind W51B at a distance of  $\sim 6$  kpc (Koo, Kim, & Seward 1995). This also seems plausible based on the velocities of the masers themselves  $\sim 69$  and  $72 \text{ km s}^{-1}$  which are red-shifted with respect the recombination line velocity of G49.2-0.3 ( $66 \text{ km s}^{-1}$ ; Wilson et al. 1970; see Fig. 1), the closest W51B H II region to the 1720 OH maser locations. The spectral index of W51C is difficult to calculate due to contamination from the H II regions, but Subrahmanyan & Goss (1995) estimate that  $\alpha = -0.2$  ( $S = \nu^\alpha$ ).

Koo & Moon (1997a, 1997b) observed high velocity (HV) H I, CO(1-0), and CO(2-1) emission between  $+85$  and  $+120 \text{ km s}^{-1}$  toward W51B. They interpret this HV gas as arising from a shock interaction between W51C and a molecular cloud (presumably located between W51C and W51B, or possibly the backside of the W51B complex itself). Indeed, they show that the HV H I is located toward the western edge of the centrally bright X-ray emitting region of W51C in an arc-shape, while the shocked CO gas is located slightly east of the HV H I emission (toward the SNR). The two OH (1720 MHz) masers reported in this work (and Green et al. 1997) are located toward the northeast end of this shocked CO/H I arc structure.

Fits of  $B_\theta$  for the two W51C OH (1720 MHz) masers are shown in Figure 2. The values

of  $B_\theta$  for these masers are 1.5 and 1.9 mG for features 1 and 2, respectively (see Tables 2 and 3). The W51C masers were also observed in PA mode, providing images of all four Stokes parameters (I, V, Q, U), with half the 2IF velocity resolution as described in §2. Toward the strongest W51C OH maser (feature 2), Stokes Q and U signals were detected at the  $15\sigma$  and  $17\sigma$  levels respectively. A profile showing Stokes Q and U toward this maser is shown in Figure 3. Using Stokes Q and U values of  $Q = 0.10 \text{ Jy beam}^{-1}$  and  $U = -0.11 \text{ Jy beam}^{-1}$ , we obtain a linear polarization percentage of 3.5% and a P.A. of  $-25^\circ$ .

### 3.2.2. G349.7+0.2

G349.7+0.2 is one of the most luminous SNR's in the galaxy (after Cas A and the Crab; Shaver et al. 1985), given its distance of  $\sim 22 \text{ kpc}$  (Frail et al. 1996). The spectral index of G349.7+0.2 was estimated by Shaver et al. (1985) to be  $\sim -0.5$ , typical of shell type remnants. This SNR contains three bright maser features along with several weaker features within  $\sim 1'$  (6 pc) near the center of the remnant. The positions of the brightest masers are shown on a continuum image of G349.7+0.2 in Figure 4. This continuum map is a compilation of 18 and 20 cm data retrieved from the VLA archive, and contains data from all four configurations (A, B, C, and D). It is the most sensitive and highest resolution continuum image of this SNR to date, with a resolution of  $5'' \times 2''$  (P.A. =  $0.6^\circ$ ) and rms noise of  $\sim 1 \text{ mJy beam}^{-1}$ .

Only G349.7+0.2 OH(3) (OH maser feature 3) has a significant magnetic field detection with  $B_\theta = 0.35 \text{ mG}$ . The  $B_\theta$  fit for this feature is shown in Figure 5. Maser features 1 and 2 are the only bright ( $S > 200 \text{ mJy}$ ) OH (1720 MHz) masers in our sample for which we were unable to detect a significant  $B_\theta$ . G349.7+0.2 OH(1) exhibits a complicated Stokes V spectrum that is indicative of blending. Therefore, it is possible that improved velocity and/or angular resolution would lead to a  $B_\theta$  detection for this maser. G349.7+0.2 OH(2) shows no hint of any Stokes V signal despite its 1800 mJy flux density which allows us to place an upper limit on its magnetic field of  $B_\theta < 0.1 \text{ mG}$ . It is interesting to note that this maser is also the narrowest maser in our sample ( $\Delta v_{FWHM} = 0.3 \text{ km s}^{-1}$ ), so it is possible that the Stokes V was not resolved in velocity space.

### 3.2.3. CTB37A

CTB37A, also known as G348.5+0.1, is estimated to lie at a distance of  $\sim 11 \text{ kpc}$  (Frail et al. 1996). Kassim, Baum, & Weiler (1991) estimate its spectral index to be  $\sim -0.5$  based

on flux density measurements ranging from 80 MHz to 14.7 GHz. A 21 cm continuum map of CTB37A from Kassim et al. (1991) is displayed in Figure 6 with the OH (1720 MHz) masers superposed. CTB37A contains two kinematically distinct sets of OH (1720 MHz) masers. One group at  $\sim -22$  km s $^{-1}$  is located toward the north end of CTB37A, while the others have velocities of  $\sim -65$  km s $^{-1}$  and are located near the center and southern parts of the source. Kassim et al. (1991) propose that the extension of continuum emission seen to the east of CTB37A (see Fig. 6) is a separate SNR which they name G348.5–0.0. It was further proposed by Frail et al. (1996) that the  $\sim -22$  km s $^{-1}$  masers originate from this second SNR.

As noted at the beginning of this section, the  $B_\theta$  of the  $\sim -65$  km s $^{-1}$  OH (1720 MHz) masers have the unusual property that they change direction along the line of sight over length scales as small as  $\sim 3$  pc. In addition, the magnitude of  $B_\theta$  changes by a factor of seven between CTB37A OH(2) and CTB37A OH(4). Fits of  $B_\theta$  for these four  $\sim -65$  km s $^{-1}$  masers are shown in Figure 7.

Reynoso & Mangum (1999, private communication) have detected CO(1-0) emission toward CTB37A with  $\sim 1'$  resolution using the Kitt Peak 12m. Their maps show two distinct CO clouds, one at  $\sim -22$  km s $^{-1}$  in the northern part of CTB37A, and another at  $\sim -65$  km s $^{-1}$  which is concentrated to the northwest and middle of the source. Both CO clouds are coincident spatially and in velocity with our two groups of OH (1720 MHz) masers.

### 3.2.4. CTB33

The SNR in CTB33 is also known as G337.0–0.1, and was estimated to lie at a distance of  $\sim 11$  kpc by Sarma et al. (1997) using H I absorption data from the ATCA. These authors also find that CTB33 has a spectral index of  $\sim -0.6$ , typical of shell type SNRs. The locations of the two bright OH (1720 MHz) masers from Frail et al. (1996) are shown on Figure 8 superposed on a 1380 MHz CTB33 continuum map (Sarma et al. 1997). However, Sarma et al. (1997) present evidence that the southern most CTB33 maser is probably associated with the H II region G336.9–0.2. Our OH (1720 MHz) results corroborate their claim since this maser feature has been resolved into at least four different velocity components, each of which show complicated Stokes V spectra typical of H II region masers (i.e. no “S” shaped Zeeman pattern). For this reason only the centrally located CTB33 maser (CTB33 OH(1)) has been included in Tables 2 and 3. The  $B_\theta$  detected for this maser is 1.1 mG, but the range of channels over which the fit was performed had to be limited to obtain a reasonable fit. This indicates that this maser is likely to be blended

in velocity space (see Fig. 9).

The CTB33 SNR is coincident with the site of a recently discovered Soft Gamma ray Repeater (SGR1627–41; see for example Hurley et al. 1999). The location of the SGR has been constrained by the 3rd Interplanetary Network (IPN: *Ulysses*, KONUS-WIND and BATSE) along with the detection of a presumably related BeppoSAX X-ray source to lie within the error boxes shown in Figure 10 on a simplified contour map of CTB33 (Sarma et al. 1997; Hurley et al. 1999; Woods et al. 1999). Current theories for the nature of SGRs suggest that they arise from strongly magnetized neutron stars or ‘magnetars’, and that the outbursts are the result of crustquakes on the surface of the neutron star (Thompson & Duncan 1995). The discovery of SGR1627–41, marks only the fourth such source to be detected.

All of the previously known SGRs have been associated with young SNRs (although SNR1900+14 lies close to, but not inside its associated SNR; see Hurley et al. 1999 and references therein). For this reason, despite the inexact correspondence between the INP/BeppoSAX error boxes and the extent of CTB33 (95'') proposed by Sarma et al. (1997), SGR1627–41 has been assumed to be the progenitor of CTB33 and to have moved to its present location at a transverse speed between 200 and 2,000 km s<sup>-1</sup> (Hurley et al. 1999).

Although, these speeds are not unreasonable, the location of the maser CTB33 OH(1) suggests that CTB33 actually extends farther west as shown in Figure 10, and has a ‘blowout’ morphology toward the NE and SW. This structure is not easily visible in the low resolution 843 MHz image used by Hurley et al. (1999) from Whiteoak and Green (1996). Such a morphology would not be unexpected in a region populated by H II regions that could have effectively cleared such cavities (see Jones et al 1998). This would place the IPN/BeppoSAX error boxes and the OH (1720 MHz) maser much closer to the center of CTB33, rather than at its outskirts, with a commensurate reduction in the transverse velocity of SGR1627–41. Future molecular, or high resolution, low-frequency continuum data toward CTB33 may help resolve this issue.

### 3.2.5. G357.7–0.1 (*Tornado*)

G357.7–0.1 is an unusual SNR candidate located near the galactic center with a non-thermal spectral index in the range  $-0.5 < \alpha < -1.0$  (Stewart et al. 1994). It has been variously considered to be everything from an extragalactic head-tail or double lobed source (Weiler & Panagia 1980; Caswell et al. 1989) to a new class of galactic head-tail



object (Becker & Helfand 1985; Helfand & Becker 1985; see also Gray 1994). Another intriguing suggestion is that G357.7–0.1 is powered by an object ejected from the nearby SNR (G359.0–0.9) which lies only 1' from the symmetry axis of G357.7–0.1. This scenario, however, would require such a ‘runaway’ pulsar or X-ray binary to have a transverse velocity  $\gtrsim 2,000 \text{ km s}^{-1}$  which is considered unlikely (Gray 1994). The discovery of a OH (1720 MHz) maser coincident with G357.7–0.1 has renewed speculation that it is in fact a galactic SNR (Frail et al. 1996).

In any case the odd morphology of G357.7–0.1 has earned it the name ‘Tornado’. The reason for this moniker can be seen in the greyscale continuum images of G357.7–0.1 shown in Figure 11 (see also, Shaver et al. 1985; Becker & Helfand 1985). The data used to create the image in Figure 11b was compiled from 18 cm and 20 cm VLA archive data, and contains data from all four VLA configurations making it the most sensitive (rms  $\sim 5 \text{ mJy beam}^{-1}$ ) and one of the highest resolution ( $11.6'' \times 9.6''$ , P.A. =  $13.8^\circ$ ) images of this source to date (see also Shaver et al. 1985; Becker & Helfand 1985; Yusef-Zadeh 1999).

Figure 12 shows the same image but with continuum contours and the single G357.7–0.1 OH (1720 MHz) maser superposed. The fit of this maser’s  $B_\theta = 0.7 \text{ mG}$  is shown in Figure 13. Note that only the high velocity side of the line could be adequately fit by the derivative of Stokes I. This is most likely indicative of blending in velocity space. Yusef-Zadeh et al. (1999) also observed G357.7–0.1 at 1720 MHz with the VLA in A-configuration during an OH (1720 MHz) survey of the Galactic center. With their short integration time (rms  $\sim 12 \text{ mJy}$ ), they were able to place an upper limit on  $B_\theta$  for G357.7–0.1 OH(1) of 2 mG, in agreement with our 0.7 mG detection. In addition, these authors detected extended OH (1720 MHz) emission toward G357.7–0.1 with the VLA in D-configuration ( $114'' \times 38''$  resolution). These authors note that this extended emission may originate from low-gain masers given the lack of OH (1720 MHz) absorption toward this source.

Linear polarization images of G357.7–0.1 at 5.8 GHz by Stewart et al. (1994) show that the transverse magnetic field vectors lie circumferentially to the vertical bands of continuum emission (best seen in Fig. 11). These authors note that this morphology is suggestive of a spiral magnetic field structure in the SNR. It is also interesting to note that the Stewart et al. images show almost no linear polarization at the location of the OH (1720 MHz) maser, as might be expected if  $\vec{B}$  were nearly along the line of sight.

## 4. DISCUSSION

### 4.1. Implications from 1720 MHz Maser Theory

A recent analytical study of the polarization properties of masers by Elitzur (1998) has suggested that the usual thermal Zeeman equation (i.e.  $V = ZC|\vec{B}|dI/d\nu$ ) may not be valid for unsaturated masers. Unfortunately, a key uncertainty in the study of masers is that their degree of saturation can not be observed directly. It has recently been proposed, however, that a maser’s saturation state can be revealed by the ratio of its Stokes V profile to the derivative of Stokes I (i.e.  $\mathcal{R} = V/I'$  where the prime denotes a derivative w.r.t frequency; Elitzur 1998). This is a consequence of the fact that maser amplification during unsaturated maser growth is exponential, causing a narrowing of the maser line. Under these circumstances  $\mathcal{R}$  is not a constant (i.e.  $\neq ZC|\vec{B}|$ ) and instead assumes a Gaussian absorption shape (see Elitzur 1998). However, since the flatness of  $\mathcal{R}$  in a saturated maser is a measure of ‘goodness of fit’, only very high dynamic range observations lend themselves to this test.

This test was performed for W51C feature 2 (the highest dynamic range maser in this study) and the highest dynamic range maser in the Claussen et al. (1999) VLBI study of W28 (W28 F39 [A]). There is no evidence for unsaturated maser emission in W51C feature 2 or W28 feature F39 [A]  $\mathcal{R}$  profiles.

Another perspective on a maser’s degree of saturation can be gained from comparing an upper limit for its optical depth ( $\tau_{max}$ ) obtained by assuming that it is, in fact unsaturated, with a lower limit ( $\tau_{min}$ ) based on the flatness of its observed  $\mathcal{R}$  ratio. For unsaturated masers,  $T_b = T_x \exp(\tau_o)$  (where  $\tau_o$  is the maser’s optical depth at line center and  $T_x$  is the excitation temperature; see Elitzur 1998 for details). As mentioned above, the lower limit depends on the confidence with which a flat  $\mathcal{R}$  profile can be determined, so that  $\tau_{min} = \epsilon^{-1} \ln \mathcal{D}$  where  $\epsilon$  is the dynamic range of the observations and  $\mathcal{D}$  is  $\sigma_{B_\theta}/B_\theta$  (Elitzur 1998). Elitzur (1998) notes that whenever these two limits are inconsistent, that is  $\tau_{min} > \tau_{max}$ , the maser must be saturated. This ‘inconsistency’ was found to be true for every maser in our sample, indicating that OH (1720 MHz) masers may indeed be saturated (see also Elitzur 1998; Yusef-Zadeh et al. 1999). However, we must point out that we have only been able to estimate  $T_{b\ min}$  since the maser spots are not resolved at the present resolutions.

Even given that these masers are likely to be saturated, a second intrinsic uncertainty in performing Zeeman analysis on masers is the value that should be taken for the constant “C” in  $V = ZC|\vec{B}|I'$ . According to Elitzur, this constant is modified from its thermal value:  $C_{th} = \cos \theta$ , to  $C_m = 8/3p \cos \theta$ . This new version accounts for the fact that a

photon generated via stimulated emission has the same wavevector as the parent photon, but not necessarily the same polarization. The parameter  $p$  in this formulation depends on the geometry of the masing region, with  $p=1$  or  $2$  for filamentary or planar geometry respectively. Notice that in addition to the factor of  $8/3p$  difference between the thermal and maser equations for  $|\vec{B}|$ , they also have a completely different dependence on  $\cos \theta$ . That is, while thermal radiation samples  $B_{los}=|\vec{B}| \cos \theta$ , masers sample  $B_m=|\vec{B}| / \cos \theta$  according to the Elitzur model.

There are some constraints that can be placed on the allowed values of  $\theta$  and  $p$  from Elitzur’s maser theory. From Elitzur (1996) and the constraint that  $q^2+v^2 \leq 1$  ( $q=(Q^2 + U^2)^{1/2}/I$  and  $v=V/I$ ), the angle  $\theta$  is constrained by the equation  $1/3 \leq \sin^2 \theta \leq 1 - 32(Z|\vec{B}|/\Delta\nu_D)^2$  ( $\Delta\nu_D$  is the Doppler width in Hz; see Elitzur 1996 for details). This means that  $\theta$  must be greater than  $35^\circ$  in order for polarized emission to be observed at all. Unfortunately, the upper bound can not be determined without *a priori* knowledge of  $|\vec{B}|$ . Elitzur (1998) also notes that if a saturated maser line is observed which is narrower than its expected  $\Delta\nu_D$  it is an indication that its geometry is planar rather than filamentary (i.e.  $\Delta\nu_m = \Delta\nu_D/\sqrt{p}$ ). The Doppler width of OH for  $50 \text{ K} < T < 125 \text{ K}$  is  $0.37$  to  $0.58 \text{ km s}^{-1}$ . One of the masers in our sample, G349.7+0.2 (2) has an observed line width of  $0.3 \pm 0.03 \text{ km s}^{-1}$ , so that  $\sqrt{2} \times 0.3 = 0.4 \text{ km s}^{-1}$  well within the predicted Doppler range. That is, this narrow linewidth is evidence for planar geometry ( $p=2$ ), assuming that this maser is, in fact, saturated.

Given these new developments in the theory of maser polarization, it is possible that the magnetic field values reported in Table 3 ( $B_\theta$ ) are *overestimated* by factors of at least  $1.6$  ( $p=2$ ;  $\theta = 35^\circ$ ) and conceivably by as much as  $\sim 10$ .

For the special case of W51C (2), where we have also measured Stokes Q and U, we can calculate  $\theta$  directly and determine the 3-D geometry of the magnetic field. From Elitzur (1996; Eq. 4.14, assuming Zeeman splitting  $\ll$  linewidth)  $q = (1 - 2/3 \sin^2 \theta)$ , and therefore  $\theta \approx 56^\circ$ . But this is just the angle between the line-of-sight and  $\vec{B}$ . In addition, we know that the linear polarization is projected on the plane of the sky at an angle of  $-25^\circ$  (§3.2.1). In other words the  $\theta$  constraint defines a cone around the line-of-sight with an angle of  $56^\circ$  and the linear polarization angle constrains the location of  $\vec{B}$  on this cone. Given  $\theta$  and using the Elitzur model, we can also estimate  $|\vec{B}| \approx (400 \times p) \mu\text{G}$  in W51C OH(2).

It is important to note, however, that the conclusions reached here are not without controversy and that other maser studies have not reached the same conclusions. For example, Nedoluha & Watson (1992) find that as long as the rate for stimulated emission is much less than the Zeeman splitting divided by Planck’s constant, and the maser is not *strongly* saturated, the thermal Zeeman relationship is a good approximation. However, it is

interesting to note that Nedoluha & Watson (1990) find that it is very difficult to produce linear polarization in masers unless they are at least *partially saturated*. It is impossible to make any quantitative statements on this issue with our sample since we only observed Stokes Q and U toward one of our sources. However, the Claussen et al. (1997) OH (1720 MHz) maser study consisted of observations of all four Stokes parameters toward the SNRs W28, W44, and IC443. Their sample contained a total of 49 masers with  $S_\nu > 200$  mJy and 60% of these have positive Q and/or U detections. In addition, none of the 13 masers with  $3\sigma$   $B_\theta$  detections are lacking Stokes Q and/or U detections. These comparisons suggest that in the Nedoluha & Watson model strong OH (1720 MHz) masers are also likely to be at least partially saturated.

## 4.2. Magnetic Fields in Shocked Molecular Gas

In this study we have reported nine new measurements of OH (1720 MHz) Zeeman magnetic field strengths in five galactic SNRs. Previous studies of this type (Claussen et al. 1997; Koralesky et al. 1998; Yusef-Zadeh et al. 1996) have measured  $B_\theta$  in an additional five SNRs. The magnitude of  $B_\theta$  in all of these SNRs (including those measured here) have typical values between 0.1 and 4 mG.

Maser theory points to the conclusion that OH (1720 MHz) masers originate in shocked molecular clouds (e.g. Lockett et al. 1999; Wardle 1999) and, therefore, the measurements reported here of  $B_\theta$  (and in the references cited above) must originate in post-shock gas. These theories suggest that OH (1720 MHz) masers can only be pumped efficiently for densities in the range  $1 \times 10^4 \text{ cm}^{-3} \lesssim n_{H_2} \lesssim 5 \times 10^5 \text{ cm}^{-3}$  and temperatures in the range  $50 \text{ K} \lesssim T \lesssim 125 \text{ K}$  (see Lockett et al. 1999). Indeed when independent measurements of the conditions in the post-shock gas have been made (see Frail & Mitchell; Reach & Rho 1998, 1999) the gas properties are in agreement with these theoretical expectations.

It remains an open question how magnetic fields of these strengths are generated; i.e. shock compression vs. turbulent amplification (Jun & Norman 1996). In what follows we will show that compression of the existing ambient molecular cloud field is all that is required to produce the observed field strengths. One further argument against significant turbulent amplification of the fields is the likelihood of destroying the maser action due to loss of velocity coherence in a turbulent velocity field.

There exists a substantial body of literature and great interest in measuring magnetic fields in molecular clouds for the purpose of studying star formation. In a recent review by Crutcher (1999) of the existing data for star forming regions, the magnetic field was found



to scale with density as  $|\vec{B}| \propto n^{0.47}$ . Crutcher notes that there are two possible physical interpretations for this relationship: (1) Such a relationship between  $|\vec{B}|$  and  $n$  has been predicted by Fiedler & Mouschovias (1993) based on studies of ambipolar diffusion; (2) A similar relation is suggested by the observed invariance of the Alfvénic Mach number  $m_A = \sqrt{3}\sigma/V_A \approx 1$  in molecular clouds, where  $V_A = |\vec{B}| / 4\pi\rho^{1/2}$  and  $\sigma = \Delta v / (8 \ln 2)^{1/2}$  (see Bertoldi & McKee 1992; Zweibel & McKee 1995). Thus, this invariance implies  $|\vec{B}| \propto \Delta v \sqrt{\rho}$ .

For the range of gas densities expected to permit significant OH (1720 MHz) maser amplification ( $1 \times 10^4 \text{ cm}^{-3} \lesssim n_{H_2} \lesssim 5 \times 10^5 \text{ cm}^{-3}$ ), the range of magnetic fields predicted by the relation  $|\vec{B}| \propto n^{0.47}$  is  $75 \mu\text{G} \lesssim B \lesssim 475 \mu\text{G}$ . Clearly most of our  $B_\theta$  measurements are greater than those predicted by Crutcher’s relation (see Figure 14). However, there is a great deal of uncertainty in this statement since Crutcher is plotting  $B_{los}$  ( $B_{los} = |\vec{B}| \cos \theta$ ) which underestimates the field and we are plotting  $B_\theta$  which could substantially overestimate the field (see §4.1).

If we assume that the two types of magnetic field measurements (molecular cloud vs. OH (1720 MHz) masers) are directly comparable (i.e. the thermal Zeeman equation is valid for masers) it may not be surprising that their magnitudes are different. This is because we know that OH (1720 MHz) masers do not originate in undisturbed “normal” molecular clouds, but rather have experienced a shock. Indeed, if this is the case it would suggest that the Bertoldi & McKee interpretation for the scaling of  $|\vec{B}|$  ( $\propto \Delta v \sqrt{\rho}$ ) is the correct one, with OH (1720 MHz) maser’s  $B_\theta$  maintaining the  $|\vec{B}| \propto n^{1/2}$  relation but with larger linewidths for a given density than unshocked molecular clouds. Setting  $V_A = \sqrt{3}\sigma$ ,  $|\vec{B}| = 0.4\Delta v n_p^{1/2}$  where  $n_p$  is the proton density in  $\text{cm}^{-3}$  and the line width is in  $\text{km s}^{-1}$ . For the case of the W51C OH (1720 MHz) masers, we can take  $\Delta v = 10 \text{ km s}^{-1}$  based on the CO observations of Koo (1999), and  $n_p = 1 \times 10^5 \text{ cm}^{-3}$  from the typical density needed to excite OH (1720 MHz) masers (Lockett et al. 1999; Wardle et al. 1999). With these values,  $B = 1.3 \text{ mG}$ , in close agreement with the  $B_\theta$  magnetic field values observed toward W51.

Alternatively, if the  $B_\theta$ ’s measured in OH (1720 MHz) masers should be reduced by factors of  $\sim 5$  (i.e. Elitzur’s maser polarization model) the magnitudes of  $B_{los} \approx B_\theta$ . Hence the observed scaling of  $|\vec{B}|$  with density would seem to have its roots in the process of ambipolar diffusion. Clearly convergence on our understanding of the nature of maser polarization is needed to distinguish between the two possibilities.

In a radiative shock, compression of the gas follows the relation  $\eta = \sqrt{2}V_s/V_{Ao}$ , where  $V_{Ao}$  is the Alfvén velocity in the pre-shock gas (see Draine & McKee 1993). Using the relation  $B_o \propto n_o^{1/2}$ ,  $V_{Ao} \simeq 2 \text{ km s}^{-1}$  (see also Heiles et al. 1993). Thus for reasonable shock

velocities (10 - 50 km s<sup>-1</sup>; Lockett et al. 1999; Frail & Mitchell 1998)  $\eta = 7 - 35$ . This compression is sufficient to enhance  $B_o$  to  $B_\theta$  without invoking turbulent enhancement of the magnetic field, assuming that  $B_{ps}/B_o = \eta$  (see Chevalier 1998; Frail & Mitchell 1998). For example, if we take a typical shock speed of  $V_s \sim 25$  km s<sup>-1</sup> and typical values of  $B_o \sim 70$   $\mu$ G for molecular clouds of density  $n_o \sim 5 \times 10^3$  cm<sup>-3</sup> (Frail & Mitchell 1998; Wardle 1999; Crutcher 1999),  $\eta \approx 18$  and  $B_{ps} \sim 1.2$  mG – in close agreement with our observed values of  $B_\theta$ .

### 4.3. Energetics Implied by Observed $B_\theta$

Regardless of the origin of the OH (1720 MHz) maser magnetic fields, it is clear that  $B_\theta$  is large. This is an important finding since the magnetic field plays a key role in many aspects of the SNR/molecular cloud interaction. For one, as noted above, the magnetic field determines and, in fact, limits the amount of shock compression in the post-shock gas. Second, magnetic support may help stabilize the post-shock cloud, via the magnetic force acting on ions perpendicular to the magnetic field lines. Third, in the model of Lockett et al. (1999), heating by ambipolar diffusion is needed to extend the length of time the post-shock gas spends at temperatures favorable to OH (1720 MHz) maser inversion. Ambipolar diffusion is also thought to be the method by which subcritical clouds dissipate their magnetic energy and form stars (Ciolek & Mouschovias 1995).

The magnetic pressure in this post-shock gas  $B_{ps}^2/8\pi$  is large compared to the  $P_{ISM}$  ( $\sim 5 \times 10^{-13}$  erg cm<sup>-3</sup>) and  $P_{thermal}$  of the hot X-ray emitting gas driving the expansion, typically *a few*  $\times 10^{-10}$  erg cm<sup>-3</sup> (Kulkarni & Heiles 1988; Frail & Mitchell 1998; Claussen et al. 1997). The value of  $P_{thermal}$  for W51C can be obtained directly from the X-ray observations of Koo et al. (1995), who estimate that  $n_e = 0.3$  cm<sup>-3</sup> and  $T_e = 3 \times 10^6$  K so that  $P_{thermal} = 2n_e k T_e \approx 3 \times 10^{-10}$  erg cm<sup>-3</sup>. For the values of  $B_\theta$  shown in Table 3, the magnetic pressure ranges from  $10^{-7} - 10^{-9}$  erg cm<sup>-3</sup>. These values are relevant since the magnetic pressure in the post-shock gas should be approximately equal to the ram pressure (i.e.  $B_{ps}^2/8\pi = \rho_o V_s^2$ ). For example, using the values of  $n_o$  and  $V_s$  estimated in §4.2 ( $n_o = 5 \times 10^3$  and  $V_s = 25$ ),  $\rho_o V_s^2 = 5 \times 10^{-8}$  erg cm<sup>-3</sup>. The equivalent magnetic pressure ( $|\vec{B}|^2/8\pi$ ) for W51C OH(1) ( $B_\theta = 1.5$  mG) is  $9 \times 10^{-8}$  erg cm<sup>-3</sup>.

## 5. SUMMARY AND CONCLUSIONS

We have observed the OH (1720 MHz) line in five galactic SNRs to measure their magnetic field strengths using the Zeeman effect. We detected all 11 of the bright ( $S_\nu > 200$  mJy) OH (1720 MHz) masers previously observed by Frail et al. (1996) and Green et al. (1997) and measured significant magnetic fields (i.e.  $> 3\sigma$ ) in nine of them. Although there exists some controversy about whether the thermal Zeeman equation can be used to estimate  $|\vec{B}|$  for OH masers (see §4.1), our estimated fields using this method range from 0.2 to 2 mG (Table 3). These  $B_\theta$  values are in good agreement with those measured in the five other SNR (0.1 - 4 mG) for which Zeeman OH (1720 MHz) maser studies exist. We estimate that these magnetic field strengths are consistent with the hypothesis that ambient molecular cloud B-fields are compressed via the SNR shock to the observed values (§4.2). Indeed, field strengths of this magnitude exert a considerable influence on the properties of the shocked cloud. For example the magnetic pressures estimated from the values of  $B_\theta$  listed in Table 3 ( $10^{-7} - 10^{-9}$  erg cm $^{-3}$ ) far exceed the pressure in the ISM or even the thermal pressure of the hot gas interior to the remnant (§4.3).

In §4.2 and §4.3 we show that there is excellent agreement between our values of  $B_\theta$  and those implied by shock compression and ram pressure using typical values from the literature. It is somewhat difficult to imagine that  $B_\theta$  could be reduced by factors of  $\sim 5$  and retain such agreement (i.e. Elitzur’s maser polarization model §4.1), although there is probably sufficient uncertainty in the parameters to allow such fine-tuning. We also show that the observed values of  $B_\theta$  for OH (1720 MHz) masers are greater than those observed in molecular clouds for the same range of densities (Crutcher 1999). It is possible that this difference is due the intrinsic physical nature of the  $|\vec{B}| \propto n^{1/2}$  relation (§4.2) or may be the result of overestimating the maser B-fields (§4.1).

In the future, knowledge of the field strength could be used in conjunction with molecular data to study the physics of these molecular shocks in more detail. In one such study Frail & Mitchell (1998) imaged the distribution of molecular gas in the vicinity of several masers spots in W28 and W44 with the JCMT. These observations revealed that the OH masers are preferentially located along the edges of thin filaments or clumps of molecular gas, suggesting compression of the gas by the passing shock. In addition to this morphological evidence, the density, temperature and velocity dispersion of the gas at these locations suggested that the OH (1720 MHz) masers originate in post-shock gas. Combining the VLA and JCMT data they were able to show directly that the magnetic pressure dominates over the thermal pressure in the post-shock gas, balancing against the ram pressure of the gas entering the shock wave (i.e.  $B_{ps}^2/8\pi = \rho_o V_s^2$ ). Thus VLA measurements of  $B_\theta$  lead to constraints on the physics of these molecular shocks that are

difficult to obtain any other way. When used in conjunction with molecular observations, it should be possible to fully specify the properties (i.e. geometry, density, temperature, velocity) of C-type shocks.

C. Brogan would like to thank NASA/EPSCoR for fellowship support through the Kentucky Space Grant Consortium, as well as, summer student support from NRAO. We would also like to thank M. Elitzur and G. Nedoluha for useful discussions on maser theory and M. Claussen for providing his W28 data and useful comments on the manuscript.

## REFERENCES

- Becker, R. H., & Helfand, D. J. 1985, *Nature*, 313, 115
- Bertoldi, F., & McKee, C. F. 1992, *ApJ*, 395, 140
- Caswell, J. L., Kesteven, M. J., Bedding, T. R., & Turtle, A. J., 1989 *Proc. Astron. Soc. Aust.*, 8 184
- Ciolek, G. E. & Mouschovias, T. Ch. 1995, *ApJ*, 454, 194
- Claussen, M. J., Frail, D. A., Goss, W. M., & Gaume, R. A. 1997, *ApJ*, 489, 143
- Crutcher, R. M. 1999, *ApJ*, 520, 706
- Dickel, J. R., van Breugel, W. J. M., & Strom, R. G. 1991, *AJ*, 101, 2151
- Draine, B. T., & McKee, C. F. 1993, *ARA&A*, 31, 373
- Elitzur, M. 1996, *ApJ*, 457, 415
- Elitzur, M. 1998, *ApJ*, 504, 390
- Fiedler, R. A., & Mouschovias, T. Ch. 1993, *ApJ*, 415, 680
- Frail, D. A., Goss, W. M., Reynoso, E. M., Giacani, E. B., Green, A. J., & Otrupcek, R. 1996, *AJ*, 111, 1651
- Frail, D. A., Goss, W. M., & Slysh, V. I. 1994, *ApJ*, 424, L111
- Frail, D. A., & Mitchell, G. F. 1998, *ApJ*, 508, 690
- Gray, A. D. 1994, *MNRAS*, 270, 835
- Green, A. J., Frail, D. A., Goss, W. M., & Otrupcek, R. 1997, *AJ*, 114, 2058
- Heiles, C., Goodman, A. A., McKee, C. F., & Zweibel, E. G. 1993, *Protostars and Planets III*, ed. E.H. Levy & J. I. Lunine (Tucson: Univ. of Arizona Press), 279167-181
- Helfand, d. J. & Becker, R. H. 1985, *Nature*, 313, 118



Kulkarni & Heiles

Hurley et al.

Jun, B. & Norman, M. L. 1996, ApJ, 472, 245

Kassim, N. E., Baum, S. A., & Weiler, K. W. 1991, ApJ, 374, 212

Klein, R. I., McKee, C. F. & Colella, P. 1994, ApJ, 420, 213

Koo, B. -C., Kim, K. -T., & Seward, F. D. 1995, ApJ, 447, 211

Koo, B. -C., & Moon, D. -S., 1997, ApJ, 475, 194

Koo, B. -C., & Moon, D. -S., 1997, ApJ, 485, 263

Koralesky, B., Frail, D. A., Goss, W. M., Claussen, M. J, & Green, A. J. 1998, AJ, 116, 1323

Lockett, P., Gauthier, E., & Elitzur, M. 1999, ApJ, 511, 235

MacLow, M.-M., McKee, C. F., Klein, R. I., Stone, J. M., & Norman, M. L., 1994, ApJ, 433, 757

Miesch, M. S. & Zweibel, E. G. 1994, ApJ, 432, 622

Milne, D. K. 1990, in Proc. 140th IAU Symp., Galactic and Intergalactic Magnetic Fields, Beck, B., Kronberg, P. P., & Wielebinski, R., ed., 67

Nedoluha, G. E., & Watson, W. D. 1990, ApJ, ApJ, 354, 660

Nedoluha, G. E., & Watson, W. D. 1992, ApJ, ApJ, 384, 185

Reach, W. T., & Jeonghee, R. 1998, ApJ, 507, L93

Reach, W. T., & Jeonghee, R. 1999, ApJ, 511, 836

Shaver, P. A., Salter, C. J., Patnaik, A. R., van Gorkom, J. H. & Hunt, G. C. 1985, Nature, 313, 113

Stewart, R. T., Haynes, R. F., Gray, A. D., & Reich, W. 1994, ApJ, 432, L39

Subrahmanyam, R., & Goss, W. M. 1995, MNRAS, 275, 755

Thompson & Duncan 1995

Troland, T. H., & Heiles, C. 1982, ApJ, 260, L19

Wardle, M., Yusef-Zadeh, F. & Geballe, T. R. 1999, in The Central Parsecs, eds. H. Falcke et al. in press (astro-ph/9811090)

Wardle, M., 1999, submitted ApJ Letters (astro-ph/9908161)

Weiler, K. W., & Panagia, N. 1980, A&A, 90, 269

Whiteoak, J. B. Z. & Green, A. J. 1996, A&AS, 118, 329

Woods et al.

Yusef-Zadeh, F., Roberts, D. A., Goss, W. M., Frail, D. A., & Green, A. J. 1996, ApJ, 466, L25

Yusef-Zadeh, F., Roberts, D. A., Goss, W. M., Frail, D. A., & Green, A. J. 1999, ApJ, 512, 230

Yusef-Zadeh, F., Goss, W. M., Roberts, D. A., Robinson, B. & Frail, D. A. 1999, ApJ, in press

Zweibel, E. G., & McKee, C. F. 1995, ApJ, 439, 779

Table 1. Observational Parameters

SNR	R. A. (B1950)	Decl. (B1950)	$V_{lsr}$ (km s <sup>-1</sup> )	$t_{source}$ (hours)	Beam (" x ")	P. A. (°)	$\sigma_{rms}$ <sup>a</sup> (mJy)
W51C (2IF)	19 20 35.0	+14 09 00.0	+64.0	3.3	1.4 x 1.2	−40	6.6
(PA)	19 20 35.0	+14 09 00.0	+70.0	1.6	1.6 x 1.3	+55	6.5
G349.7+0.2	17 14 36.0	−37 22 00.0	+16.0	2.6	3.4 x 1.3	+08	7.2
CTB37A	17 11 00.0	−38 30 00.0	−64.0	4.9	3.9 x 1.2	−14	5.4
CTB33	16 32 14.0	−47 31 00.0	−70.0	2.1	8.0 x 1.1	+67	10.2
G357.7−0.1	17 36 56.0	−30 56 00.0	−12.0	5.1	3.0 x 1.2	+18	5.2

<sup>a</sup>This is the rms noise in an individual channel.

Table 2. Fitted Parameters of OH (1720 MHz) Masers

SNR	Feature	R. A. (B1950)	Decl. (B1950)	$S_{peak}^a$ (mJy)	$v_{lsr}^b$ (km s <sup>-1</sup> )	$\Delta v_{FWHM}^c$ (km s <sup>-1</sup> )	$\theta_{max}$ (")
W51C .....	1	19 20 35.9	+14 09 53.6	2710	+72.0	0.9	0.7
	2	19 20 36.4	+14 09 50.3	4760	+69.1	1.2	0.1
G349.7+0.2 ..	1	17 14 36.0	−37 23 01.9	770	+16.2	1.1	1.6
	2	17 14 36.9	−37 22 52.8	1800	+15.2	0.3	1.0
	3	17 14 37.5	−37 23 14.7	1060	+16.7	0.6	0.9
CTB37A .....	1	17 10 51.8	−38 28 51.7	410	−66.2	0.7	0.6
	2	17 10 56.8	−38 28 56.7	730	−63.7	0.5	0.3
	3	17 10 59.3	−38 31 19.2	470	−63.5	1.5	0.2
	4	17 11 01.4	−38 37 32.9	220	−65.3	1.1	0.7
CTB33 .....	1	16 32 06.2	−47 29 53.2	250	−71.8	1.0	1.7
G357.7−0.1 ..	1	17 36 54.6	−30 56 07.6	400	−12.3	0.6	0.8

<sup>a</sup>Errors in the peak flux range from 4 to 8 mJy.

<sup>b</sup>Errors in  $v_{lsr}$  range from 0.02 to 0.002 km s<sup>-1</sup>.

<sup>c</sup>Errors in  $\Delta v_{FWHM}$  range from 0.05 to 0.003 km s<sup>-1</sup>, and the values shown have been deconvolved from the finite channel width (0.27 km s<sup>-1</sup>).



Table 3. Magnetic Fields

SNR	Feature	$B_\theta$ (mG)
W51C .....	1	$+1.5 \pm 0.05$
	2	$+1.9 \pm 0.10$
G349.7+0.2 ...	1	complex <sup>a</sup>
	2	$< 0.1$
	3	$-0.35 \pm 0.05$
CTB37A .....	1	$-0.5 \pm 0.10$
	2	$+0.22 \pm 0.05$
	3	$-0.60 \pm 0.09$
	4	$+1.5 \pm 0.20$
CTB33 .....	1	$+1.1 \pm 0.30$
G357.7–0.1 ....	1	$+0.7 \pm 0.12$

<sup>a</sup>Stokes V profile is complex, probably indicative of blending.

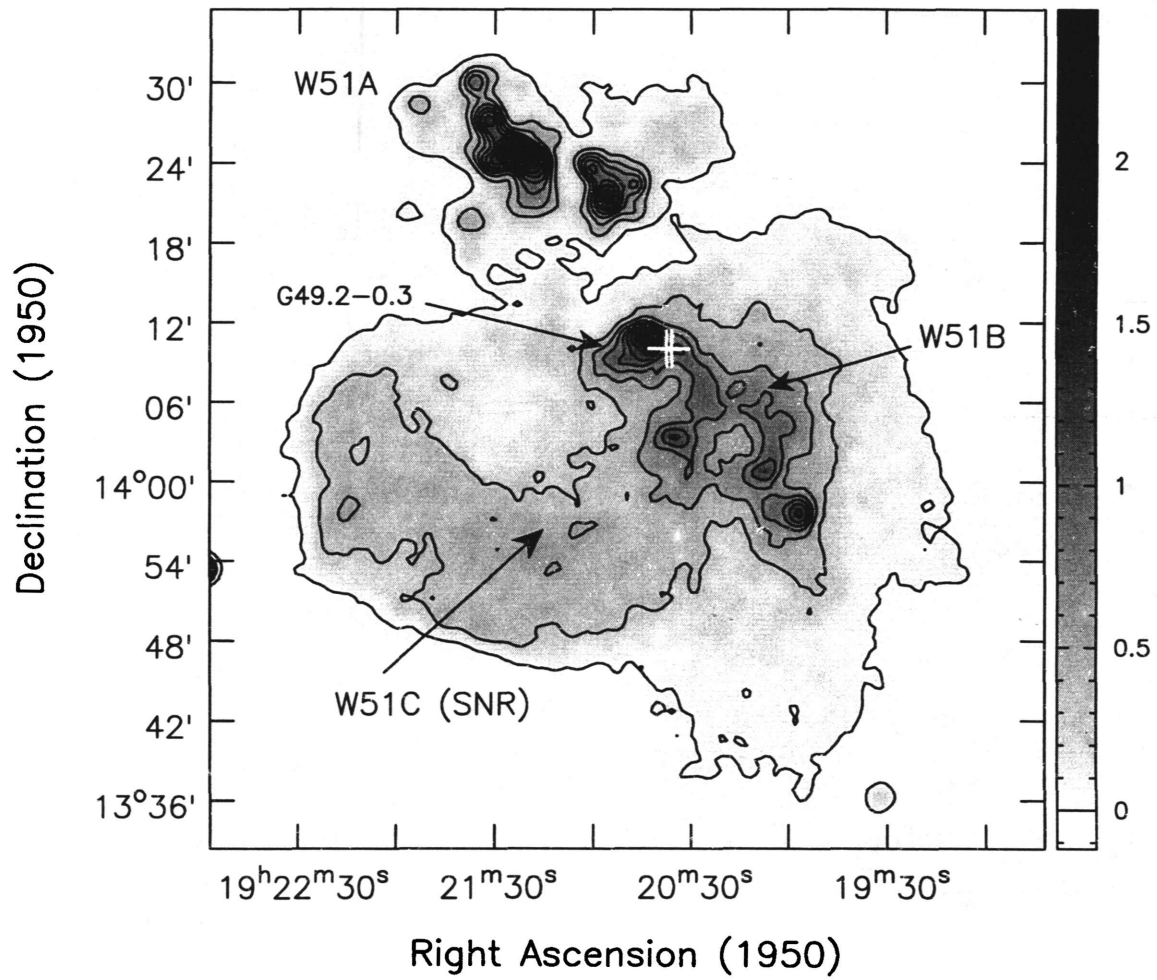


Fig. 1.— W51 330 MHz continuum from Subrahmanyan & Goss (1995) with contours at  $0.05$  to  $2.07 \times 2.46 \text{ Jy beam}^{-1}$  in increments of  $246 \text{ mJy beam}^{-1}$ . The beam is  $\sim 1'$ .

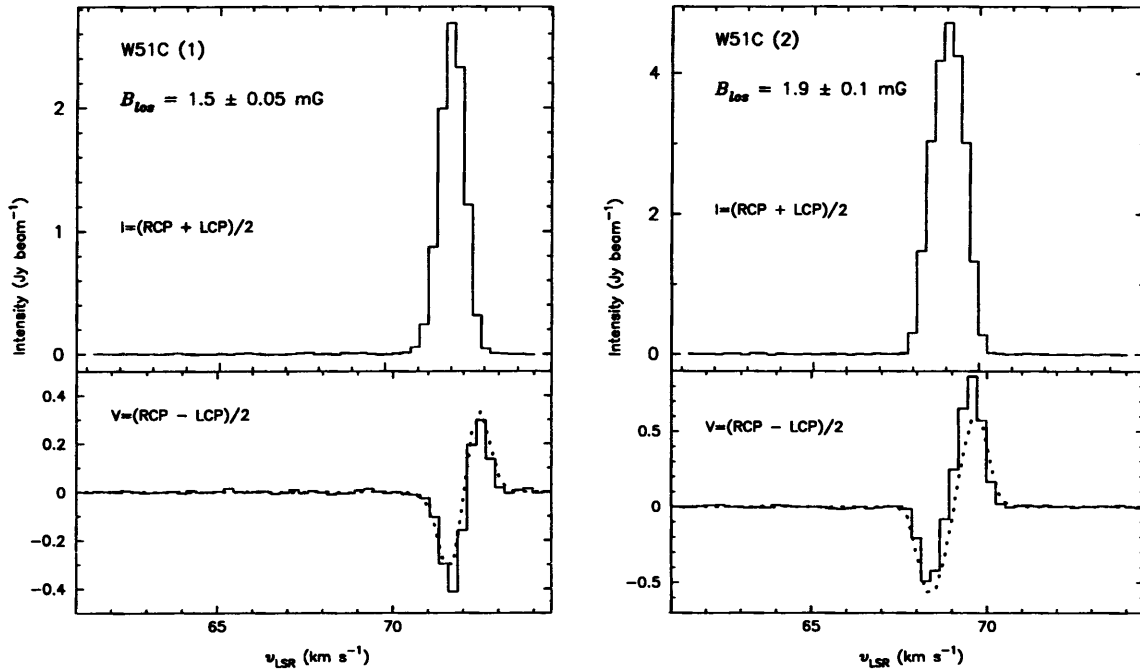


Fig. 2.— Fits of  $B_{\theta}$  for W51 OH (1720 MHz) maser features 1 and 2. The upper panels show the Stokes I profiles (*solid histogram*), and the bottom panels show the Stokes V profiles (*solid histogram*) with the fitted derivative of Stokes I shown as smooth dotted curves. The value of  $B_{\theta}$  fit for each position and its calculated error are given at the top of each plot.

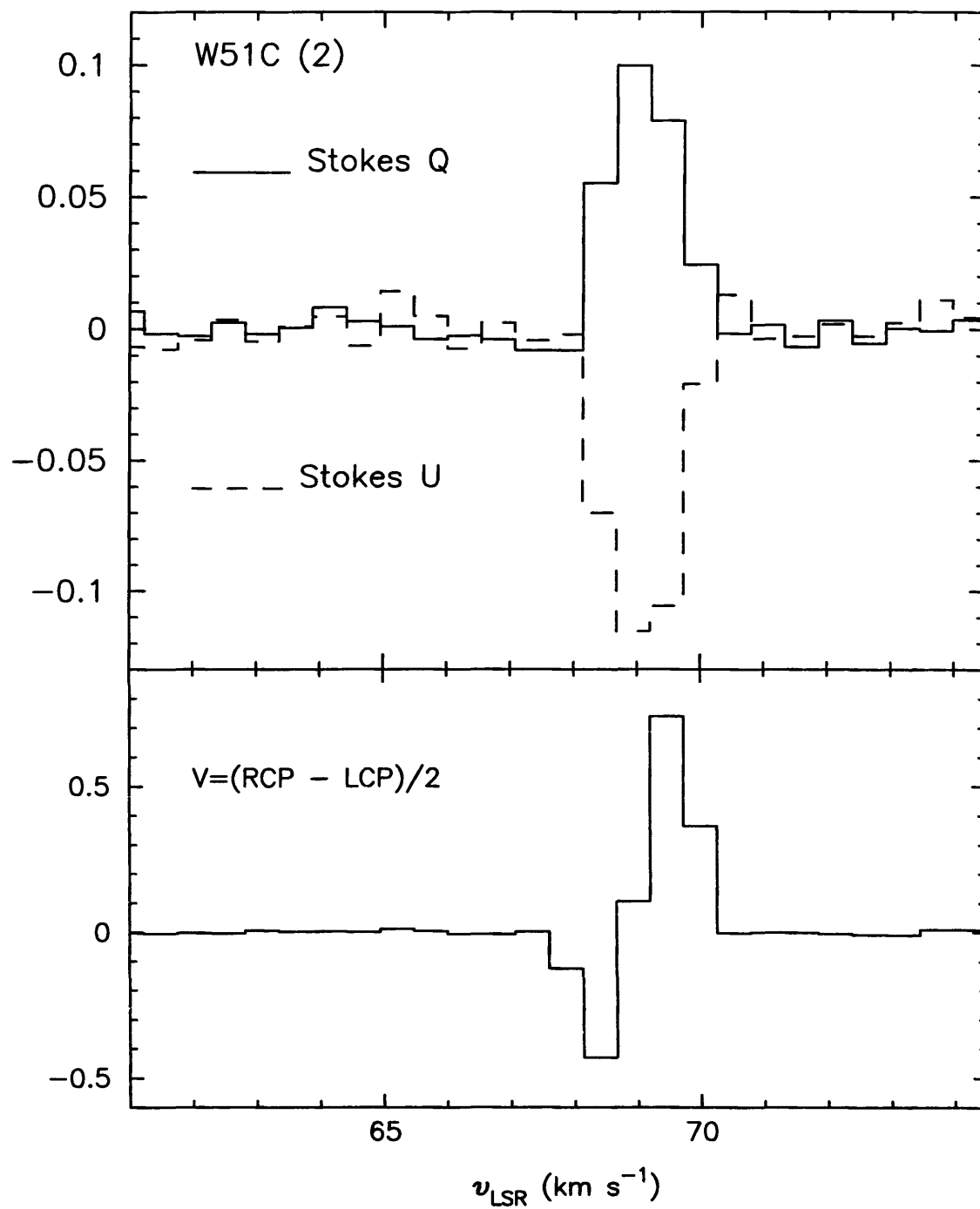


Fig. 3.— W51C maser feature 2 Stokes Q, U, and V profiles.

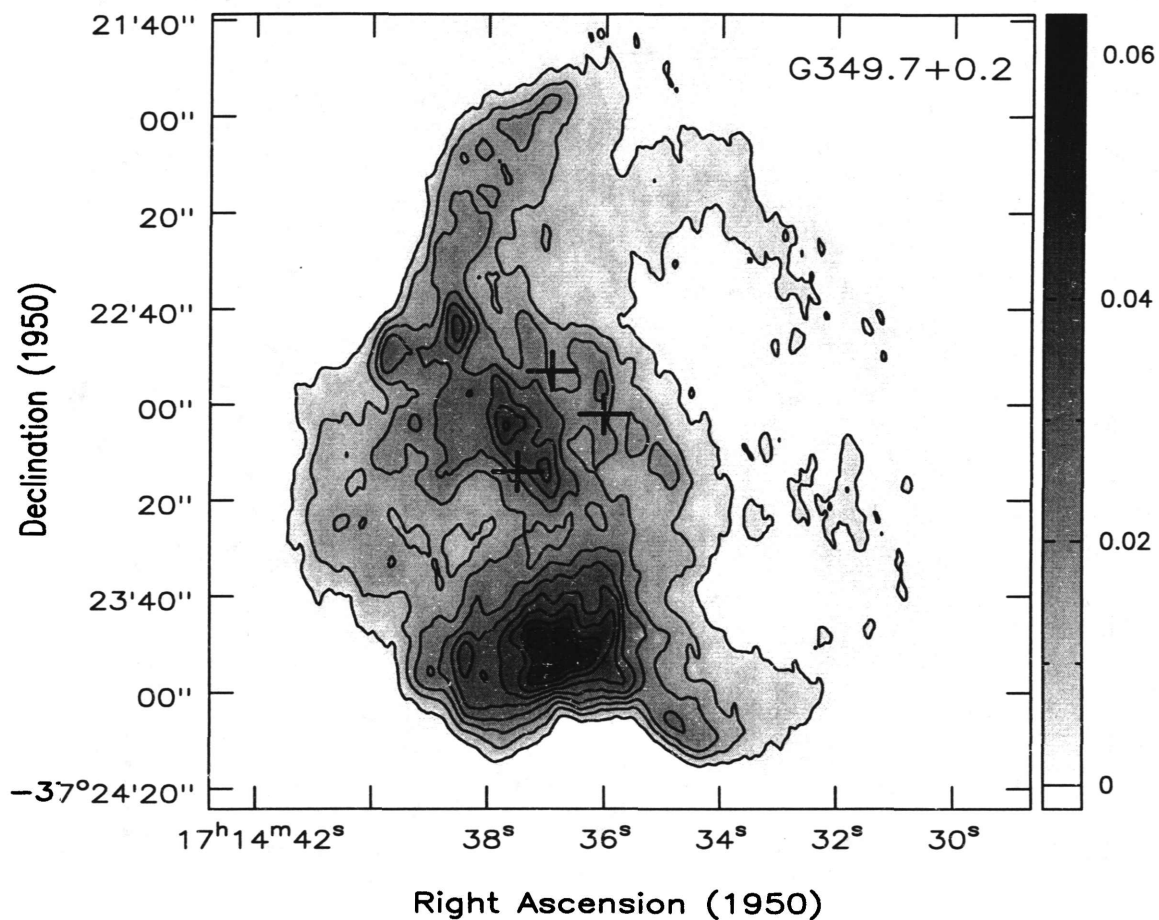


Fig. 4.— G349.7+0.2 L-band continuum contours  $0.05$  to  $0.95 \times 0.0633 \text{ Jy beam}^{-1}$  in increments of  $6.3 \text{ mJy beam}^{-1}$ . This image is composed of archival VLA data from A, B, C, and D configurations. The resolution is  $5'' \times 2''$  (P.A. =  $0.6^\circ$ ) and the peak flux is  $0.063 \text{ Jy beam}^{-1}$  with an rms noise of  $\sim 1 \text{ Jy beam}^{-1}$ .



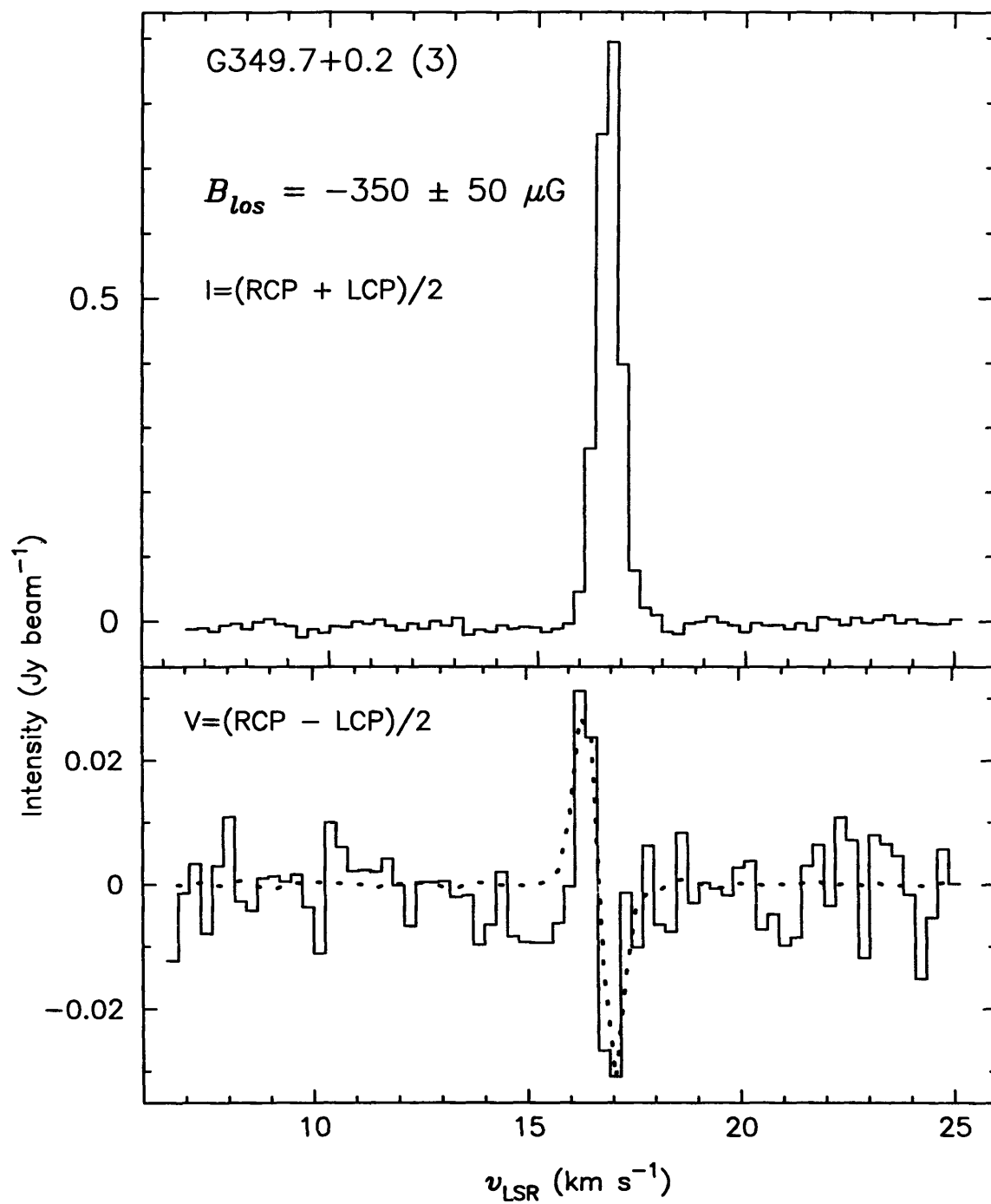


Fig. 5.— Similar to Figure 3 but for G349.7+0.2 OH (1720 MHz) maser feature 3.

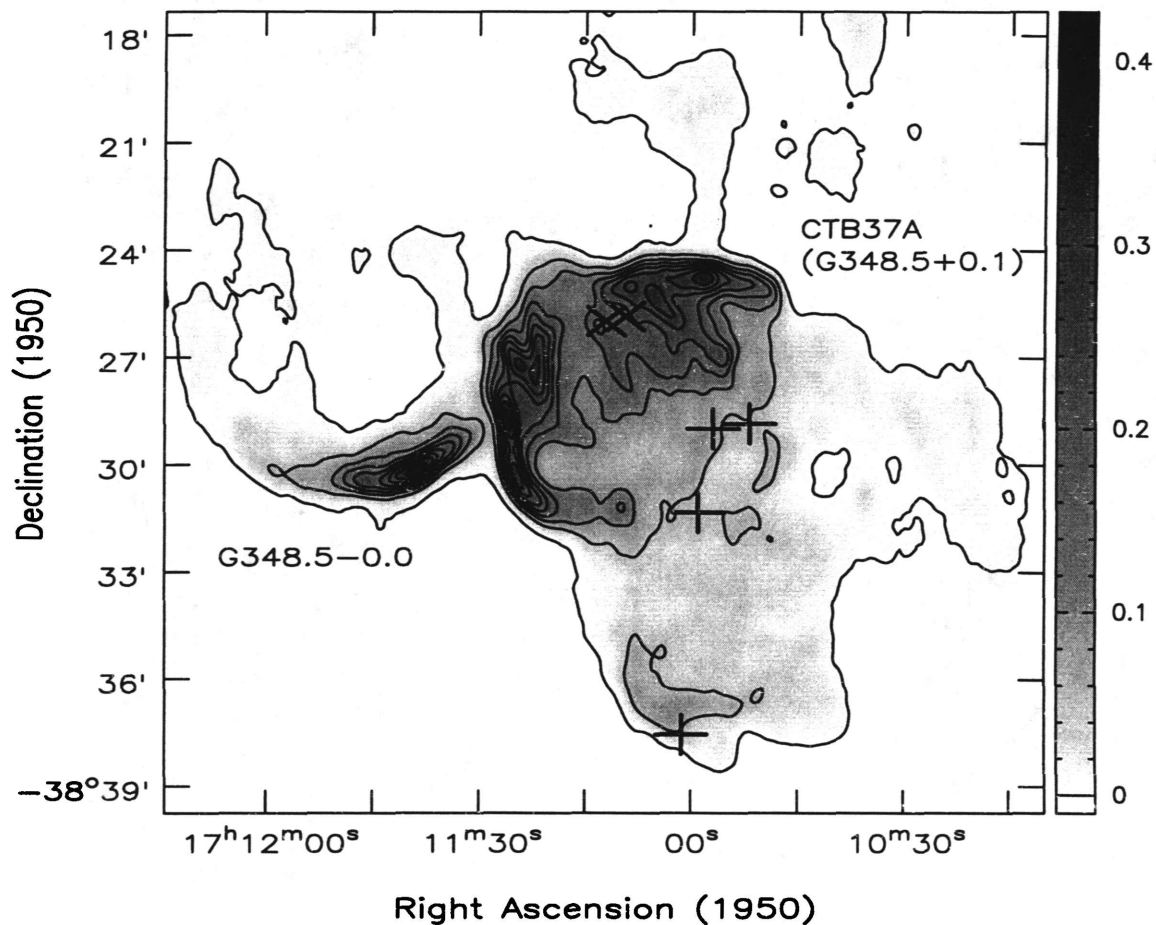


Fig. 6.— CTB37A 20 cm continuum from Kassim et al. (1991) with contours at 0.01 to  $0.88 \times 0.427 \text{ Jy beam}^{-1}$  in increments of  $42.7 \text{ mJy beam}^{-1}$ . The beam is  $33'' \times 18''$  and the rms noise is  $10 \text{ mJy beam}^{-1}$ . The plus symbols mark the locations of the  $\sim -65 \text{ km s}^{-1}$  OH (1720 MHz) maser features. The locations of the  $\sim -22 \text{ km s}^{-1}$  OH (1720 MHz) maser features (not observed, see Frail et al. 1996) are also marked (crosses) for clarity.

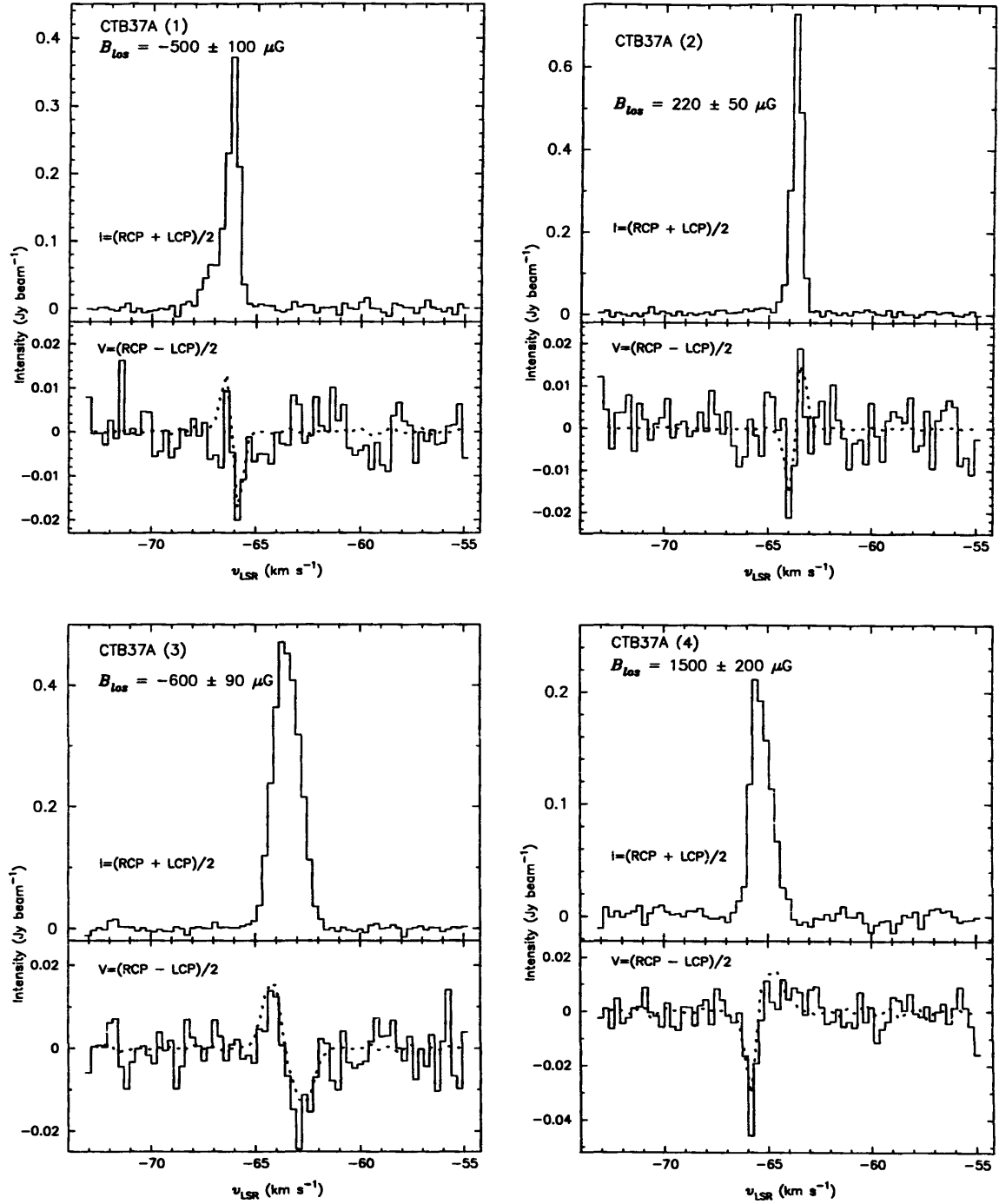


Fig. 7.— Similar to Figure 3 but for CTB37A OH (1720 MHz) maser features 1 - 4.

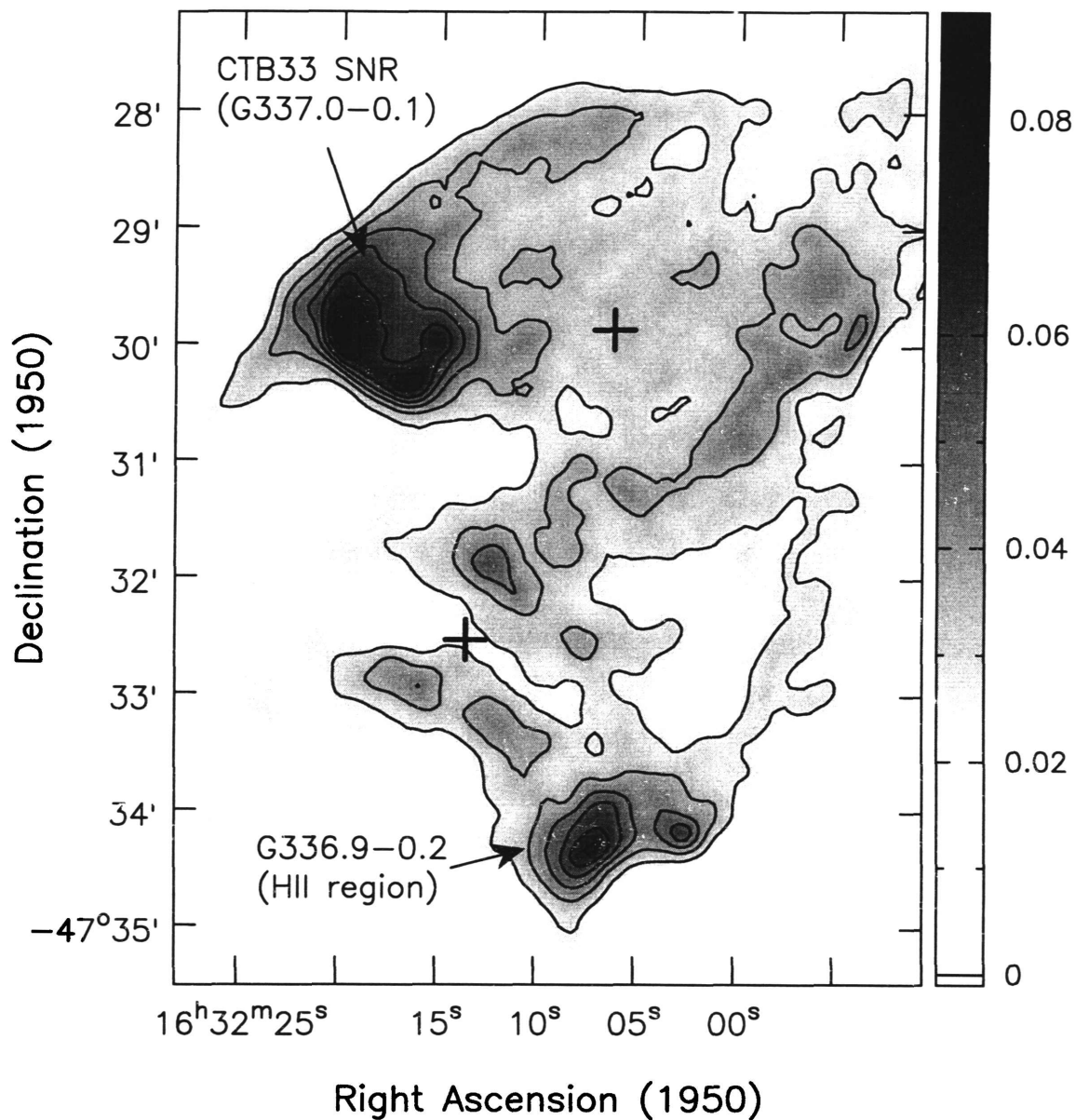


Fig. 8.— CTB33 1375 MHz continuum from Sarma et al. (1997) with contours at  $0.3$  to  $0.9 \times 0.090 \text{ Jy beam}^{-1}$  in increments of  $9 \text{ mJy beam}^{-1}$ . The resolution of this image is  $12.2'' \times 11.5''$ .

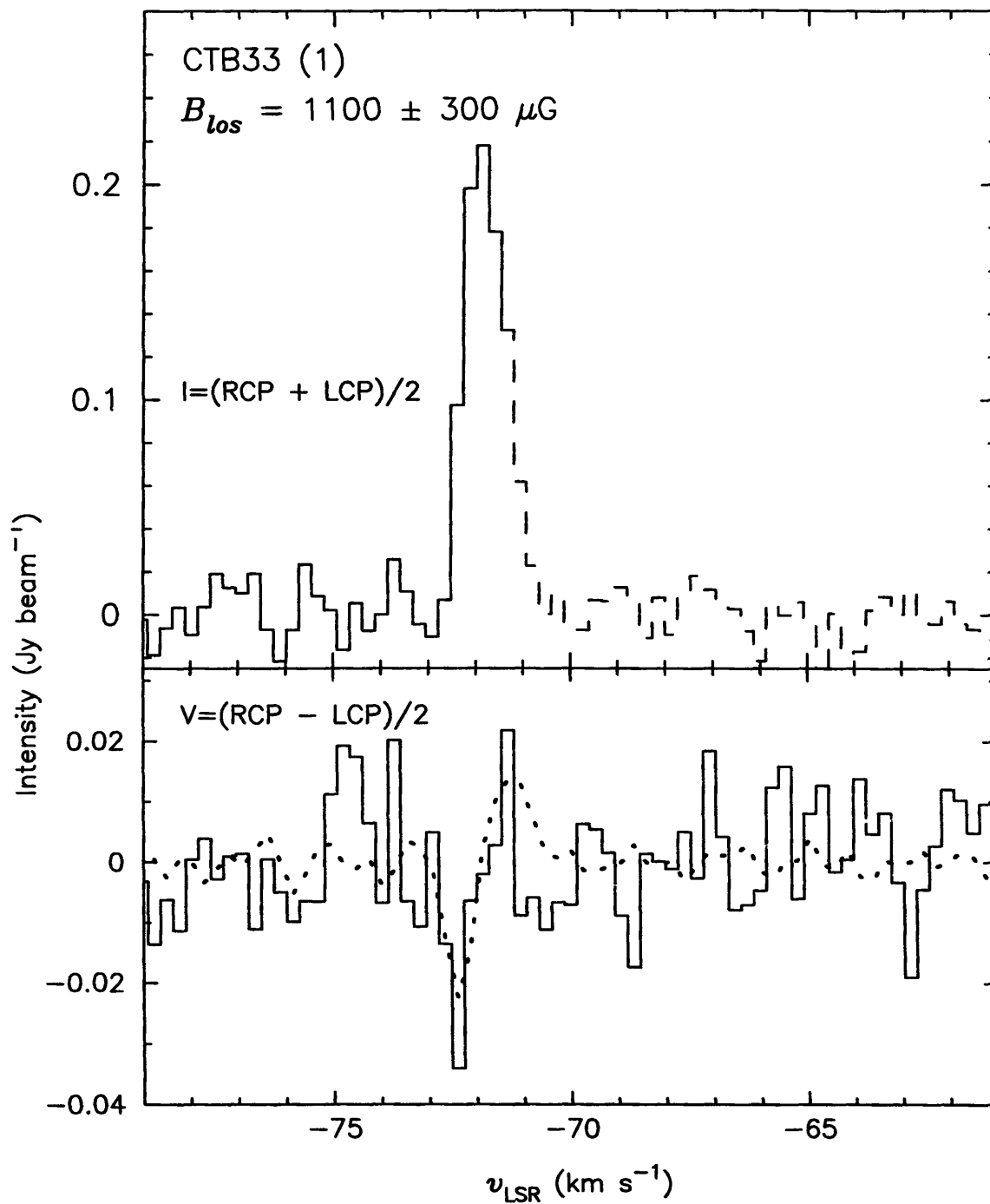


Fig. 9.— Similar to Figure 3 but for CTB33 OH (1720 MHz) maser feature 1. The solid portion of the Stokes I histogram (*upper panel*) shows the velocity range used in the fit.



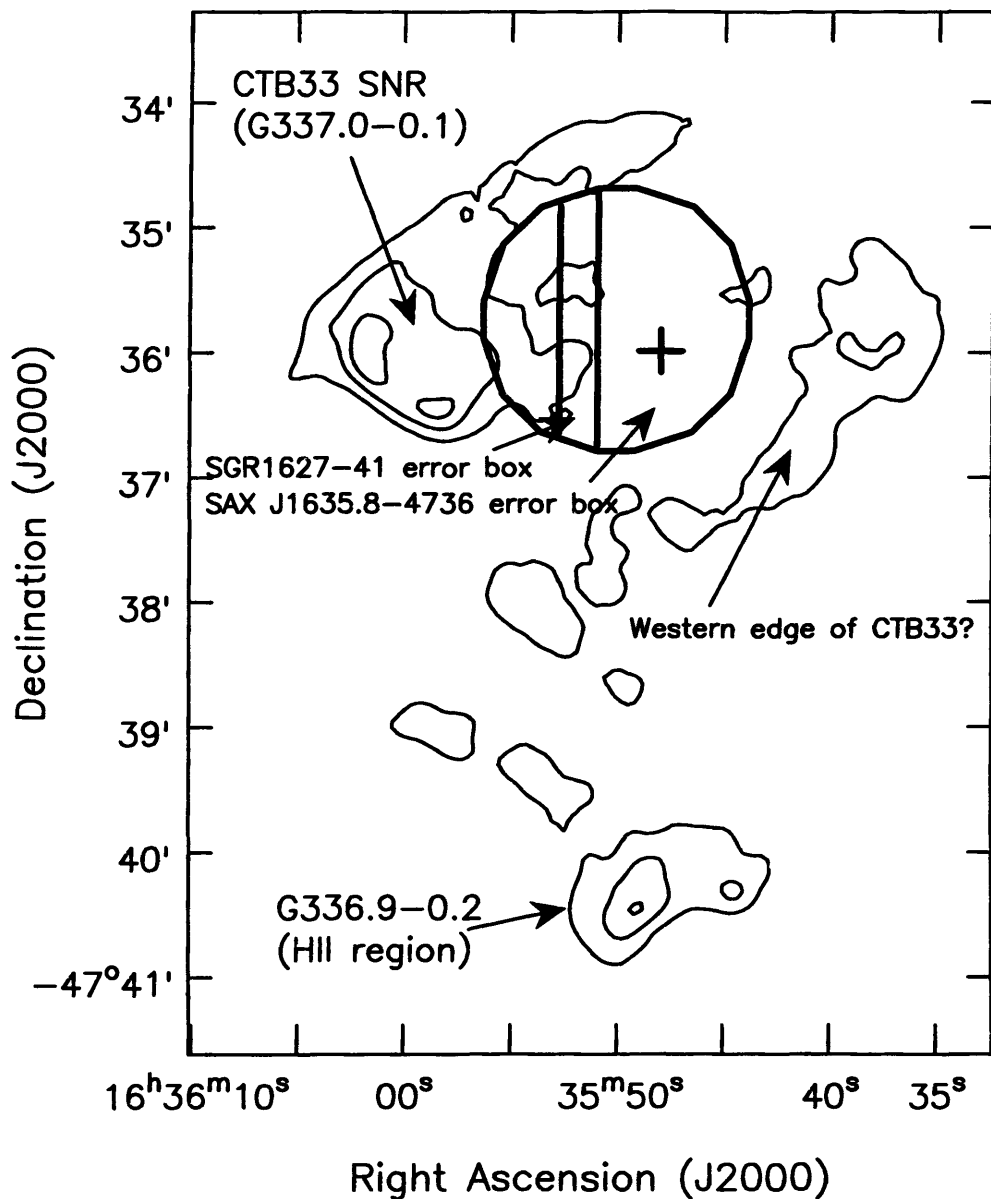


Fig. 10.— Similar to Figure 8, but in J2000 coordinates with contours at 0.4, 0.6, 0.8  $\times 0.090 \text{ Jy beam}^{-1}$ . The IPN and BeppoSAX error boxes are superposed showing the location of SGR1627-41.

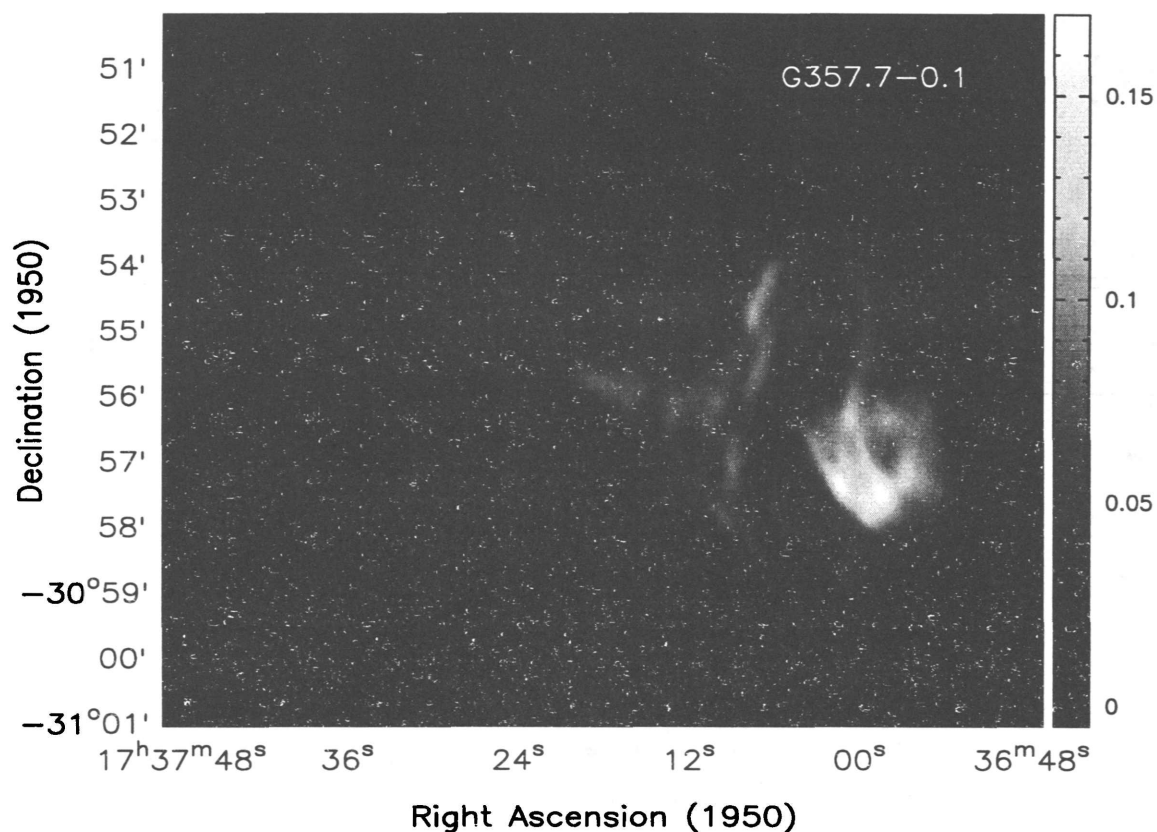


Fig. 11.— Greyscale L-band continuum image of G357.7–0.1 showing its spiral morphology. The resolution of this image is  $11.6'' \times 9.6''$ . This image is composed of archival VLA data from A, B, C, and D configurations. The resolution is  $11.6'' \times 9.6''$  (P.A. =  $13.8^\circ$ ) and the peak flux is  $0.17 \text{ Jy beam}^{-1}$  with an rms noise of  $\sim 5 \text{ Jy beam}^{-1}$ .

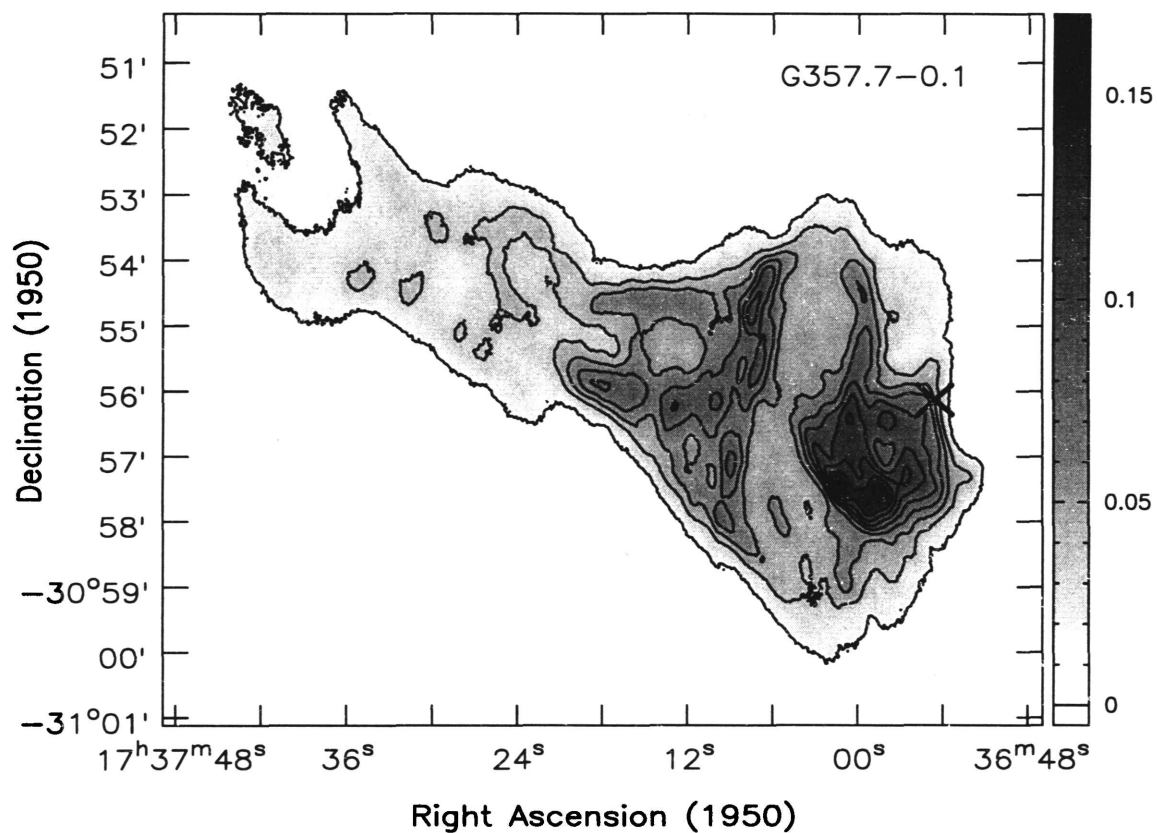


Fig. 12.— Similar to Figure 11, but with contours at  $0.1$  to  $0.9 \times 0.170 \text{ Jy beam}^{-1}$  in increments of  $17 \text{ mJy beam}^{-1}$ .

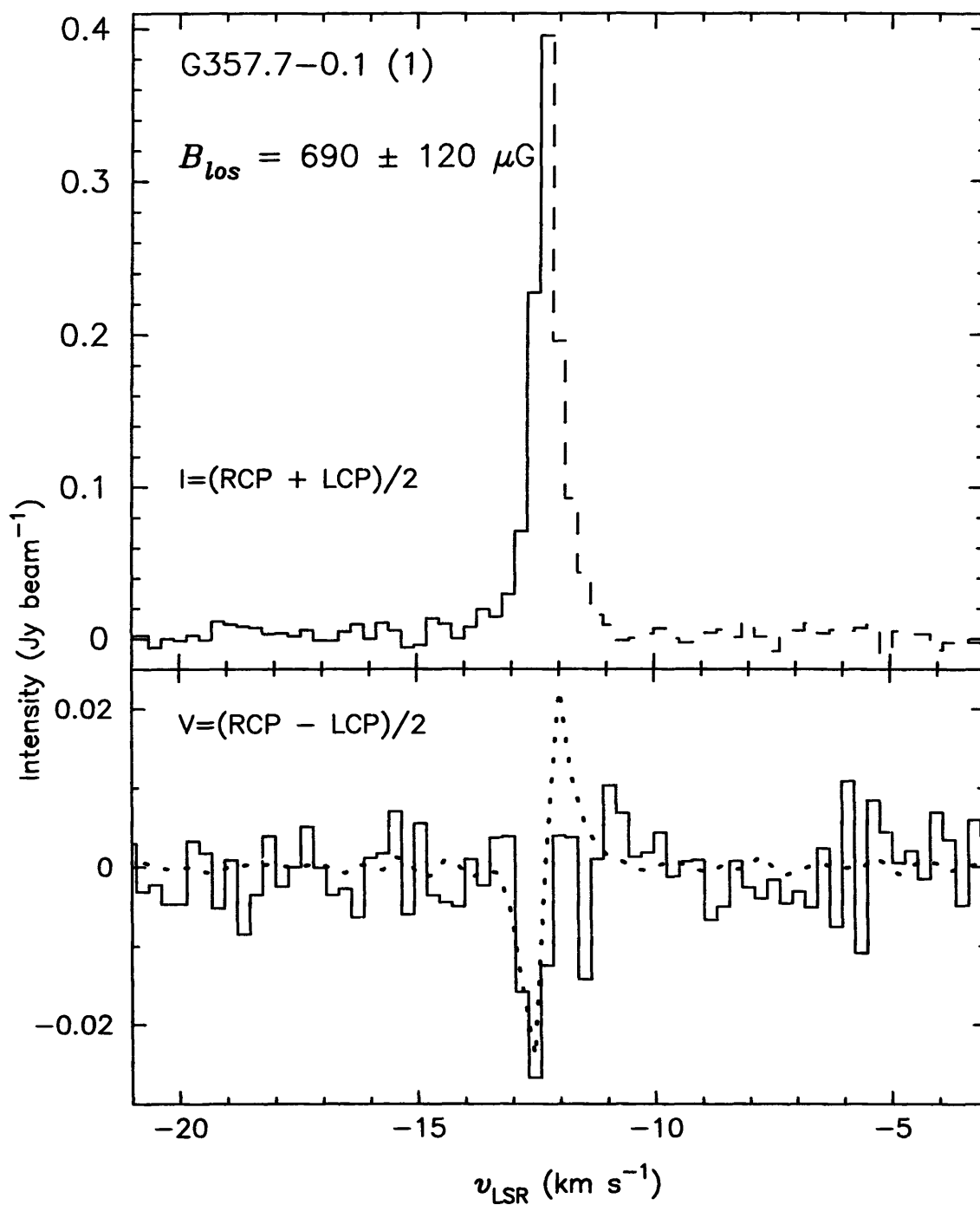


Fig. 13.— Similar to Figure 3 but for G357.7–0.1 OH (1720 MHz) maser feature 1. The solid portion of the Stokes I histogram (*upper panel*) shows the velocity range used in the fit.

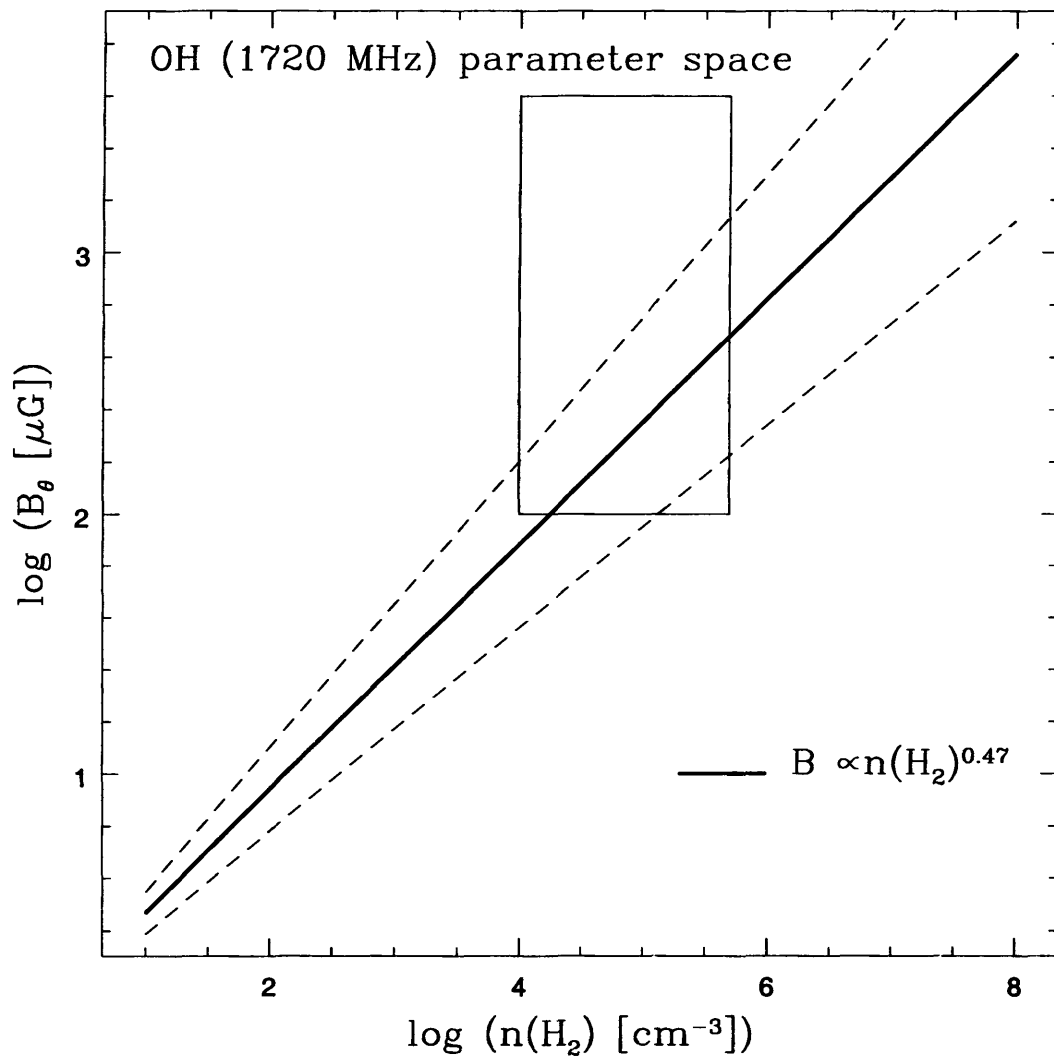


Fig. 14.— Plot of  $B_{\theta} \propto n^{0.47}$  (Crutcher 1999; solid thick line) with the OH (1720 MHz) maser's  $B_{\theta}$  parameter space superposed. The two dashed lines show the  $1\sigma$  errors on the fit obtained by Crutcher.





# Space VLBI Image Simulations

Chi C. T. Cheung<sup>1</sup> & James S. Ulvestad<sup>2</sup>

National Radio Astronomy Observatory, Socorro, NM, 87801

**DRAFT: To be submitted to *Radio Science***

## ABSTRACT

We present image simulations of Space Very Long Baseline Interferometry (SVLBI) data created from an actual observation which utilized the currently orbiting VLBI Space Observatory Programme (VSOP) satellite. By varying the size of the hole in the Fourier UV plane in our simulations, we hope to ascertain a tolerable orbit for upcoming SVLBI missions. Also, the effects of varying the weighting of the data from uniform to natural in the imaging is examined.

## 1. Introduction

Space Very Long Baseline Interferometry (SVLBI; cf. Ulvestad 1998 and references therein) has unique imaging requirements over ground VLBI observations. A single orbiting element with a large apogee height combined with data from ground antennas will create a large hole in the sampling of the Fourier UV plane thus introducing complications in imaging capability. This issue must be addressed in order to maximize the efficiency of any upcoming SVLBI missions like ARISE (Gurvits *et al.* 1996; Ulvestad *et al.* 1997; Ulvestad & Linfield 1998).

---

<sup>1</sup>current address: Department of Physics, Brandeis University, Waltham, MA, 02454; [ccc@quasar.astro.brandeis.edu](mailto:ccc@quasar.astro.brandeis.edu)

<sup>2</sup>[julvesta@nrao.edu](mailto:julvesta@nrao.edu)

We have created image simulations from data obtained by the HALCA (Highly Advanced Laboratory for Communications and Astronomy) satellite of the VLBI Space Observatory Programme (VSOP) currently in orbit in order to determine the image quality obtainable from SVLBI data with various UV hole sizes. HALCA carries an 8 meter radio telescope that works with ground telescopes at 1.6 and 5 GHz to image compact radio sources (see Hirabayashi *et al.*). Table 1 lists the fundamental parameters of the HALCA satellite. We demonstrate that as expected, the image quality (i.e. dynamic range) of the simulated data vary greatly with the size of the UV hole and with different degrees of uniform and natural weighting in the imaging. Simulations like the ones performed here can be applied to data from other current HALCA observations which will help determine plausible apogee heights for upcoming SVLBI missions.

## 2. HALCA Observation

Data for the simulations were taken from a 5 GHz ( $\lambda 6$  cm) HALCA plus the full VLBA and phased VLA observation of the  $\gamma$ -ray blazar 1633+382 (4C 38.41) on 4/5 August 1998. A total of about 8 hours of HALCA data was successfully downlinked through 3 tracking stations (about 4 hours at RZ, more than 3 hours at NZ, and about an hour at TZ) and cross-correlated with 14 hours of ground data at the VLBA correlator in Socorro, NM. The only significant loss or flagging of data on the ground occurred at the end of the observation when the source was setting for the eastern antennas of the VLBA in St. Croix (about 4 hours lost) and in Hancock (about 2 hours lost).

## 2.1. Data Reduction Procedure

The data was calibrated with NRAO’s AIPS reduction package using standard techniques. The absolute flux of the target source, 1633+382 was bootstrapped from the simultaneous VLA observation which utilized scans of 3C 286. The system temperature and gain value of the space antenna at 5 GHz obtained from the HALCA WWW homepage were inputted manually. Estimated corrections to the delay rate for the three tracking stations of HALCA was determined by performing a fringe-fit (using FRING in AIPS) on two minutes of data from each individual station and subsequently applied with the AIPS task CLCOR. The entire data set was then fringe fitted in its entirety with a solution interval of 3.5 minutes.

We used the dirty ground only image as the initial model (figure 2) in our self calibration process. However, we would have preferred a naturally weighted image of the full data set but in this case, returned less believable clean components early in the procedure. The data may have simply been too noisy and the extra resolution proved too confusing as a starting model for the self calibration. After obtaining undesirable results from initial attempts at self-calibration with both AIPS and the Caltech DIFMAP (Shepherd *et al.*) package, the data was put through another round of fringe-fitting. This time, we used a preliminary image of the source obtained through a few rounds of phase self calibration as the model (figure 3) for the fringe fitting.

Previous attempts to self-calibrate the data in DIFMAP showed that a gain correction

of about a factor of 1.4 was needed for the space data and this correction was applied to the data with CLCOR and some modest clipping was done on obviously poor data. The three simulation data sets were created from the full data set with the task UVCOP to isolate data from the selected antennas. The preferred method would have been to isolate the data before fringe fitting but time constraints prevented us from doing so. By removing antennas after fringe fitting, we have tampered with the closure phases of antenna triplets which included antennas removed in the simulations thus the self-calibration process may have been compromised (K. Desai, personal communication). Each individual data set was written out of AIPS and into DIFMAP where it was 30 second averaged and edited vigorously. Since previous self-calibration attempts in AIPS were deemed more successful than in DIFMAP, each data set was returned to AIPS and self calibrated individually.

By trial and error, we determined that inserting a model in each round of self calibration whose clean components were not tightly constrained near the brightest regions of the image gave the best results. By placing really tight clean boxes around the image early on, true flux and structure may be inadvertently lost. Also, symmetric features were rampant in the early stages where only phase self-calibrations were applied which may indicate amplitude errors. As suggested by Walker 1995, we windowed snugly on the eastern edge of the core where a spurious counterjet was present in order to remove it effectively.

## 2.2. Simulations

Three simulation UV data sets were created from the full calibrated data set. The simulations each contain data from HALCA, the phased VLA, and only six of the ten antennas of the VLBA (see table 4 for the list of antennas used for each simulation). The two antennas which constituted the longest ground baselines (St. Croix and Mauna Kea) were removed from all three of the simulations. We switched between removing data from Hancock and Brewster to increase the size of the UV hole, and some redundant antennas in the southwestern region of the U.S. which are close to our reference antenna (the phased VLA) in order to normalize the amount of data between the simulations. We imaged the 3 simulations and the full data set with the 11 available robustness factors (Briggs 1995) available in AIPS to see the effect of different degrees of uniform and natural weighting on the data. Figure 6 shows the UV coverage in the Fourier plane of the complete data set and those from the simulated data. Figure 7 zooms in on the UV coverage of ground baselines. Figure 8 shows the UV plots of the respective data sets. Finally, figure 9 and figure 10 show the final self-calibrated maps imaged with robustness factors of -1 and -2 respectively, corresponding to higher degrees of uniform weighting.

## 3. Results

We discuss our results in terms of the size of the UV hole (distance ratio) related to the degradation of the image quality (dynamic range). The dynamic range is defined in two ways:

- The peak flux to average RMS ratio.
- The ratio of the peak signal of the simulation to the peak signal in the resultant image from subtracting the simulation from the full image.

In both methods, the peak flux is obtained from the verb MAXFIT in AIPS. The distance ratio is defined as the ratio of the maximum space baseline to the maximum ground baseline.

### **3.1. Distance Ratio vs. Dynamic Range I**

Figure 11 shows the dependence of dynamic range (Peak to RMS) on the distance ratio for all the robustness factors available in AIPS. The RMS values quoted are obtained from averaging the RMS values obtained from the verb IMSTAT over three blank corner regions surrounding the source in the map. The fourth corner (northwest region) was specifically excluded from the statistics since the shorter baselines show a weak extension in the jet of 1633+382 towards that direction. This would lead to an unfair bias toward favorable RMS values in the uniformly weighted images when that extension is not seen. In general, the dynamic range improves when switching from degrees of uniform to natural weighting. However, this behavior experiences some fluctuations in the natural weighting regime for the 3 simulations but the full data set is consistently superior to the simulations as also shown in figure 12.

The behavior from Robust 0 to -2 (uniform weightings) is most expected. There is



an approximately linear dependence on the dynamic range with increasing distance ratio (larger UV hole) until the precipitous drop at a distance ratio of about 12 which can be taken to be either anomalous or attributed uniquely to this data set as this degradation is seen at all robustnesses and also in method 2 (see section 3.2). From robustness -3 and less, the dynamic range of the images remain about constant for the various UV hole sizes (except again for the anomalous region at distance ratio above 12). For natural weighting ( $\text{Robust} \geq 1$ ), drastic changes in the dynamic range are seen. There is no refuting that the dynamic range does in general decrease with increasing distance ratio but there may not be a simple linear dependence. However, if the simulation corresponding to simulation C were to be removed, we can draw a fairly strict linear law in the dependence on distance ratio in the dynamic range for the naturally weighted images.

### **3.2. Distance Ratio vs. Dynamic Range II**

In figures 13, 14, and 15, the dynamic range is defined as the ratio of the peak flux to the maximum residual in the map subtracted from the true image of the source. The true image of the source is taken as the map synthesized from including all of the antennas in the experiment. The images were subtracted with the task COMB in AIPS immediately after the self calibration (figure 14). Due to the effects of self calibration which displaces reference positions, the images were also subtracted after being aligned (figure 15) by their peaks as determined by MAXFIT in AIPS. Images were aligned with the task LGEOM where it was deemed reasonable to do so (robust -5 to 1). In the more naturally weighted

images for the simulations (robust 2 to 5) the peaks of the images drifted toward the peak in the jet about 1.5 mas west of the assumed stationary core. In these cases, the shift amount used in the robust 1 image was applied as the best estimate. Only the images produced from robustness factors of -2, -1, and -1 with a substantially larger beam are plotted in figure 13. The definition of dynamic range by difference mapping experiences also the effects seen in section 3.1 where the dependence of dynamic range on distance ratio in the vicinity of distance ratio near 12 is unclear.

The dependence of dynamic range on robust factors in method 2 is quite unexpected. Two of the three simulations which have been aligned (figure 15) experience dynamic range jumps from robust -1 to 0 which corresponds to a degradation of image quality with more natural weighting, which we certainly do not expect and contradicts our results from section 3.1. This may be attributed to uncertainties in the alignment of the images except that in the unshifted images (figure 14), we see the same peak in dynamic range at robust -1 but a spike there rather than a step function. It is interesting to point out that the two higher dynamic range simulations experience the same cross over between robust -1 to 0 in dynamic range in both the aligned and unaligned images, and in method 1 (figure 12) thus substantiating our choice of robust -1 and -2 as being optimal for this data set. The last simulation with the "largest" hole in the UV plane seems minimally affected by the robust factors and shows modest steady improvement toward the more naturally weighted images.

#### 4. Discussion

The HALCA image of 1633+382 (Figure 9A and 10A) shows the familiar core-jet structure extending from east to west and reveals far superior detail than the ground only image (Figure 16). See Ulvestad *et al.* 1999 for the astrophysical discussion of this source. As expected, the components in the jet of 1633+382 seems more defined with correspondingly larger UV holes. There are fewer intermediate baselines (long ground baselines) in the simulations that give the apparent increase in resolution indicated by the tendency of the imaging programs to put the flux into more compact components in this already complex source. The peaks in the outer jet components seem displaced between the simulations and the full data set which is evidence for transfer of flux for position in the images.

#### 5. Conclusion

In method 1, it seems that in general, the image quality (dynamic range) does degrade with bigger UV holes and increasing the degree of uniform weighting. We can draw no direct conclusions about the results shown for the dynamic range from difference mapping. These results have contradictory points to what we expected. The image quality does degrade with larger UV holes only when imaging with uniform weighting. The natural weighting seems to yield more random results in the dependence of dynamic range on UV hole size. This may be due to the fact that the simulations have more than fifty percent less ground baselines than the full data set and weighing the sparse ground data heavily

results in inconsistencies.

However, by this method of sampling image quality from varying the size of the hole in the UV sampling, we can determine a tolerable apogee height for future SVLBI missions from the corresponding distance ratios of the longest space to ground baselines. Since the longest ground baseline is constrained solely by the size of the earth to be 8,600 km? then it can be a simple exercise to determine the apogee height of an orbiting interferometer element by this method. For instance, if we take distance ratio to be approximately 12 (the beginning of the confused regions) and the least distance ratio of HALCA is currently about 4, then we yield an apogee height three times larger than that of HALCA – 60,000 km! In addition to other considerations such as the precession rate of the satellite and eccentricity of the orbit, more careful simulations similar to those performed here are essential to determining the orbit of future SVLBI missions .

## **6. Acknowledgements**

The National Radio Astronomy Observatory is operated by Associated Universities, Inc., under cooperative agreement with the National Science Foundation. Space VLBI at NRAO is funded by NASA. The VSOP project is led by the Japanese Institute of Space and Astronautical Science in cooperation with many organizations and radio telescopes around the world. C.C.T.C. thanks the 1999 NRAO summer student program and its coordinators, and Dan Homan for tips on self calibration.

## REFERENCES

- Briggs, D. 1995, *Ph.D. Thesis*, New Mexico Institute of Mining and Technology
- Gurvits, L.I., Ulvestad, J.S., & Linfield, R.P. 1996, in *Large Antennas in Radio Astronomy*, ed. C.G.M. van't Klooster (Noordwijk: ESTEC), 81-88
- Hirabayashi, H., *et al.* 1998, *Science*, **281**, 1825-1828
- Shepherd, M.C., Pearson, T.J., & Taylor, G.B. 1994, *BAAS*, **26**, 987
- Ulvestad, J.S., Gurvits, L.I., & Linfield, R.P. 1997, in *High Sensitivity Radio Astronomy*, eds. N. Jackson & R. Davis (Cambridge: Cambridge UP), 252-255
- Ulvestad, J.S. & Linfield, R.P. 1998, in *IAU Colloquium 164: Radio Emission from Galactic and Extragalactic Compact Sources*, ASP Conf Series 144, eds. J.A. Zensus, G.B. Taylor, & J.M. Wrobel (San Francisco: ASP), 397-398
- Ulvestad, J.S. 1998, in *Synthesis Imaging in Radio Astronomy II*, ASP Conf Series 180, eds. G.B. Taylor, C.L. Carilli, & R.A. Perley (San Francisco: ASP), 1-23
- Ulvestad, J.S. *et al.* 1999, in preparation
- Walker, R.C. 1995, in *Very Long Baseline Interferometry and the VLBA*, ASP Conf Series 82, eds. J.A. Zensus, P.J. Diamond, & P.J. Napier (San Francisco: ASP), 247-266

Apogee height	21,400 km
Perigee height	560 km
Orbital period	6.3 hr
Eccentricity	0.601
Inclination	31.6 degrees

Fig. 1.— Fundamental parameters of the HALCA orbit

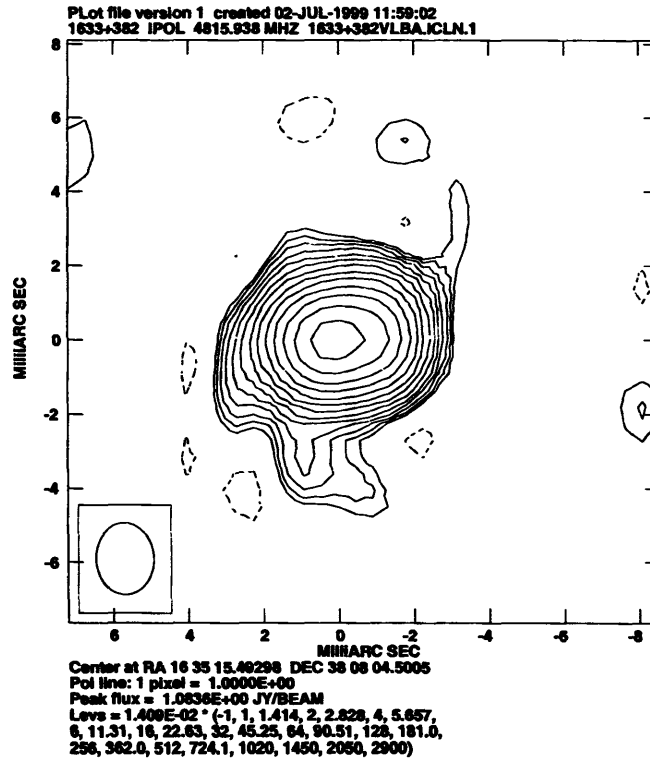


Fig. 2.— Initial model in the self calibration process



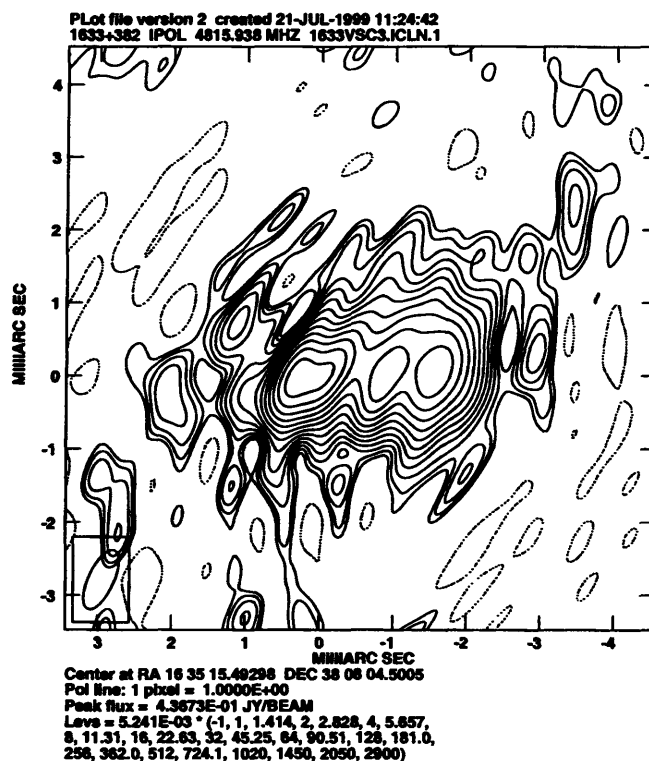


Fig. 3.— Model used in the second fringe fitting

Simulation	Antennas Used*	Antennas Not Used*
A	BR FD HN KP LA NL OV PT SC Y MK HALCA	—
B	BR FD HN KP LA NL Y HALCA	OV PT SC MK
C	BR FD KP LA NL OV Y HALCA	HN PT SC MK
D	FD KP LA NL OV PT Y HALCA	BR HN SC MK

Fig. 4.— Antennas Information for Simulations. \*See table 5 for abbreviations

Antennas	Abbreviation
Brewster, WA	BR
Fort Davis, TX	FD
Hancock, NH	HN
Kitt Peak, AZ	KP
Los Alamos, NM	LA
North Liberty, IA	NL
Owens Valley, CA	OV
Pie Town, NM	PT
St. Croix, Virgin Islands	SC
VLA - Socorro, NM	Y
Mauna Kea, HI	MK

Fig. 5.— Antennas Abbreviations

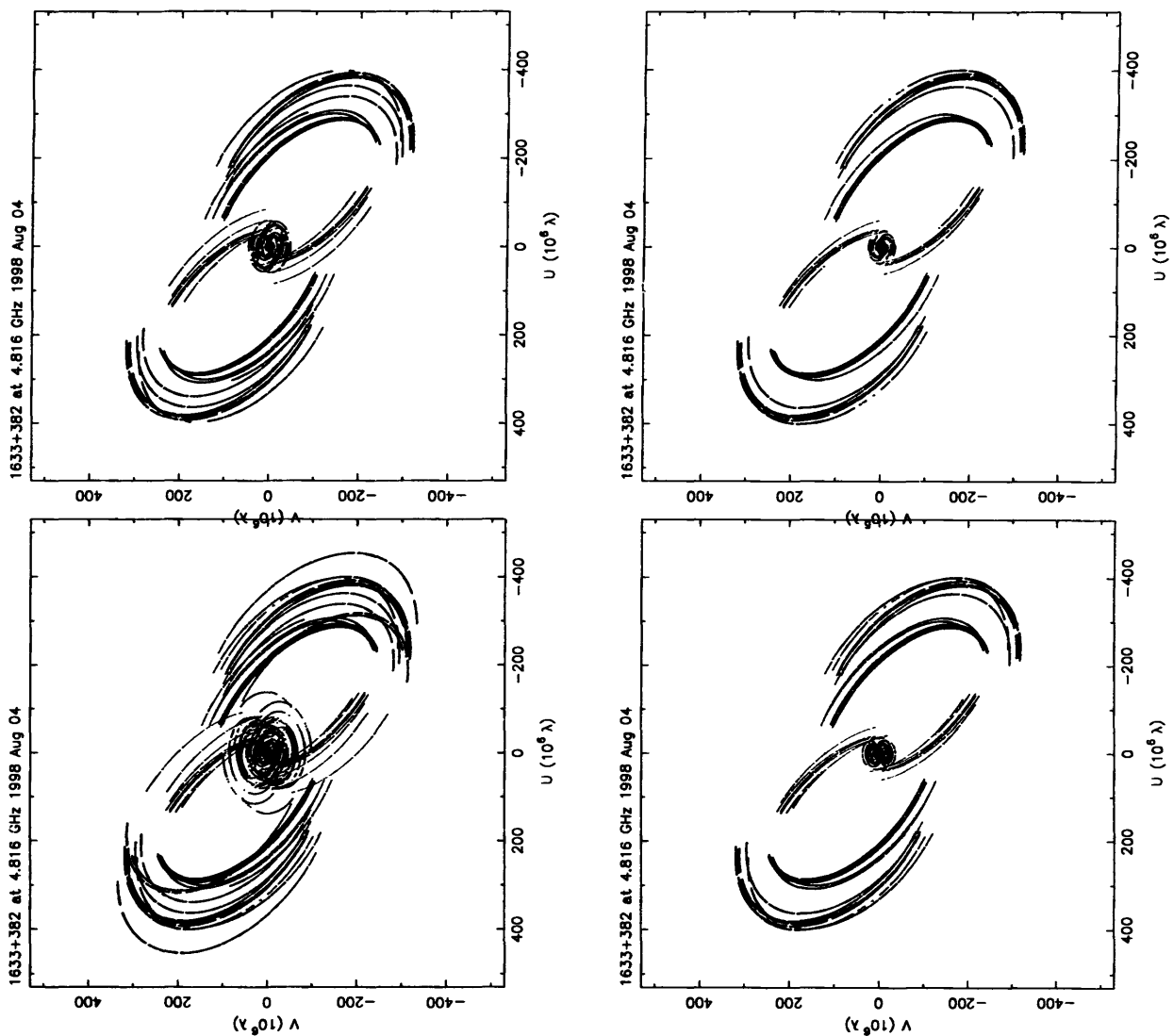


Fig. 6.— Plots of the UV Coverage of the original data and in the simulations. See figure 4 for labels.

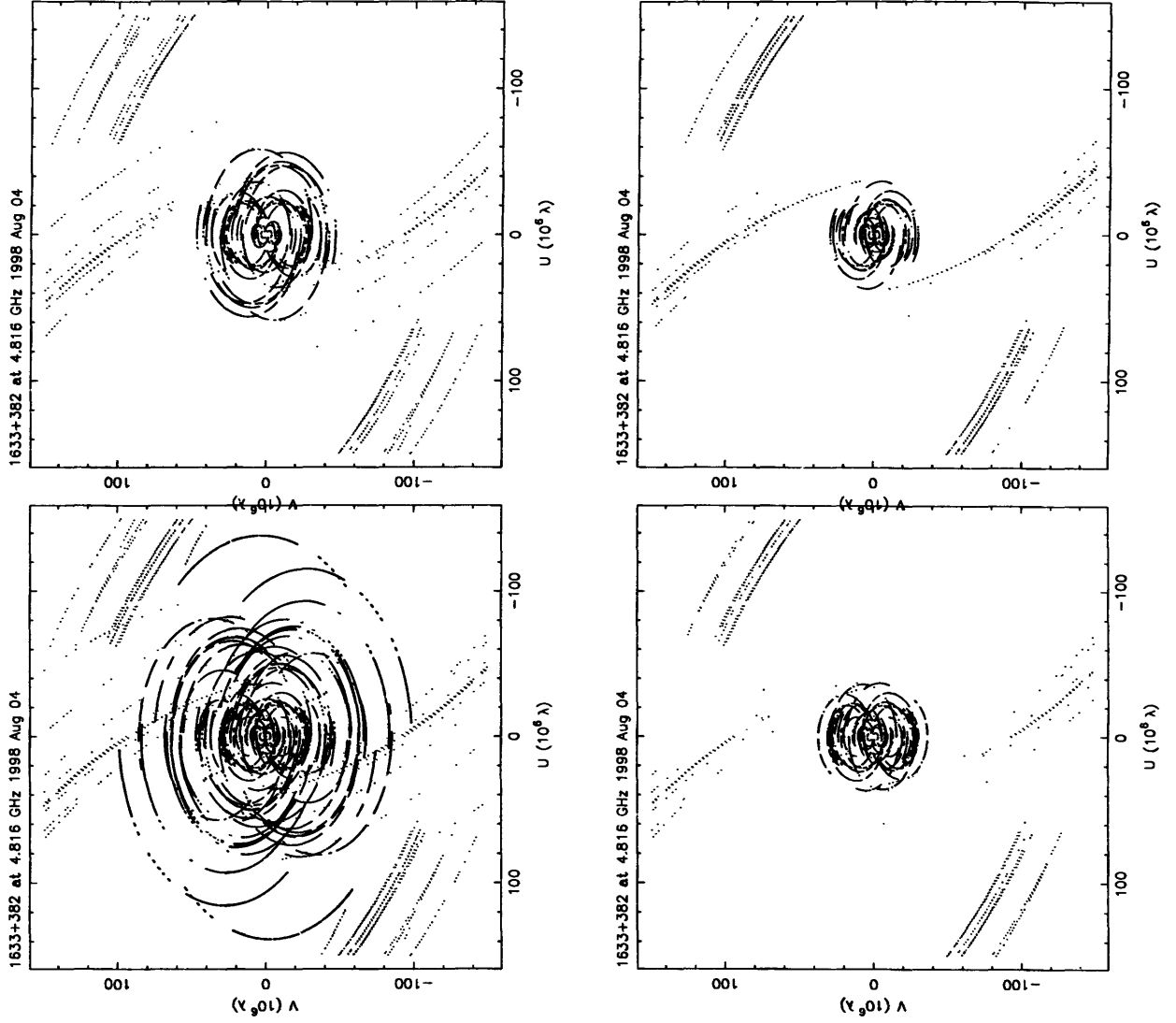


Fig. 7.— Plots of the UV Coverage of the Inner Baselines of the original data and in the simulations. See figure 4 for labels.

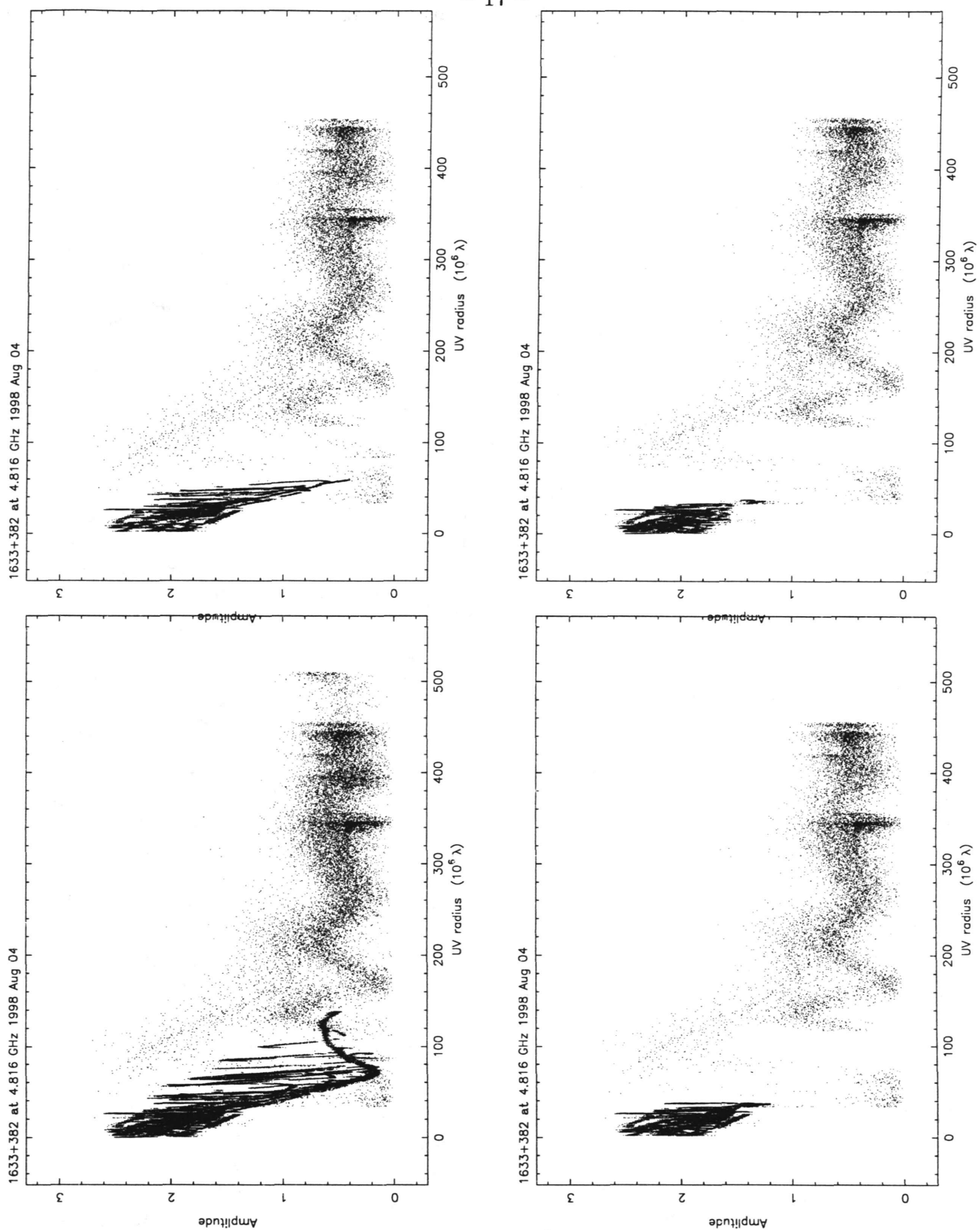


Fig. 8.— Amplitude vs. UV Distance Plots of the original data and in the simulations. See figure 4 for labels.

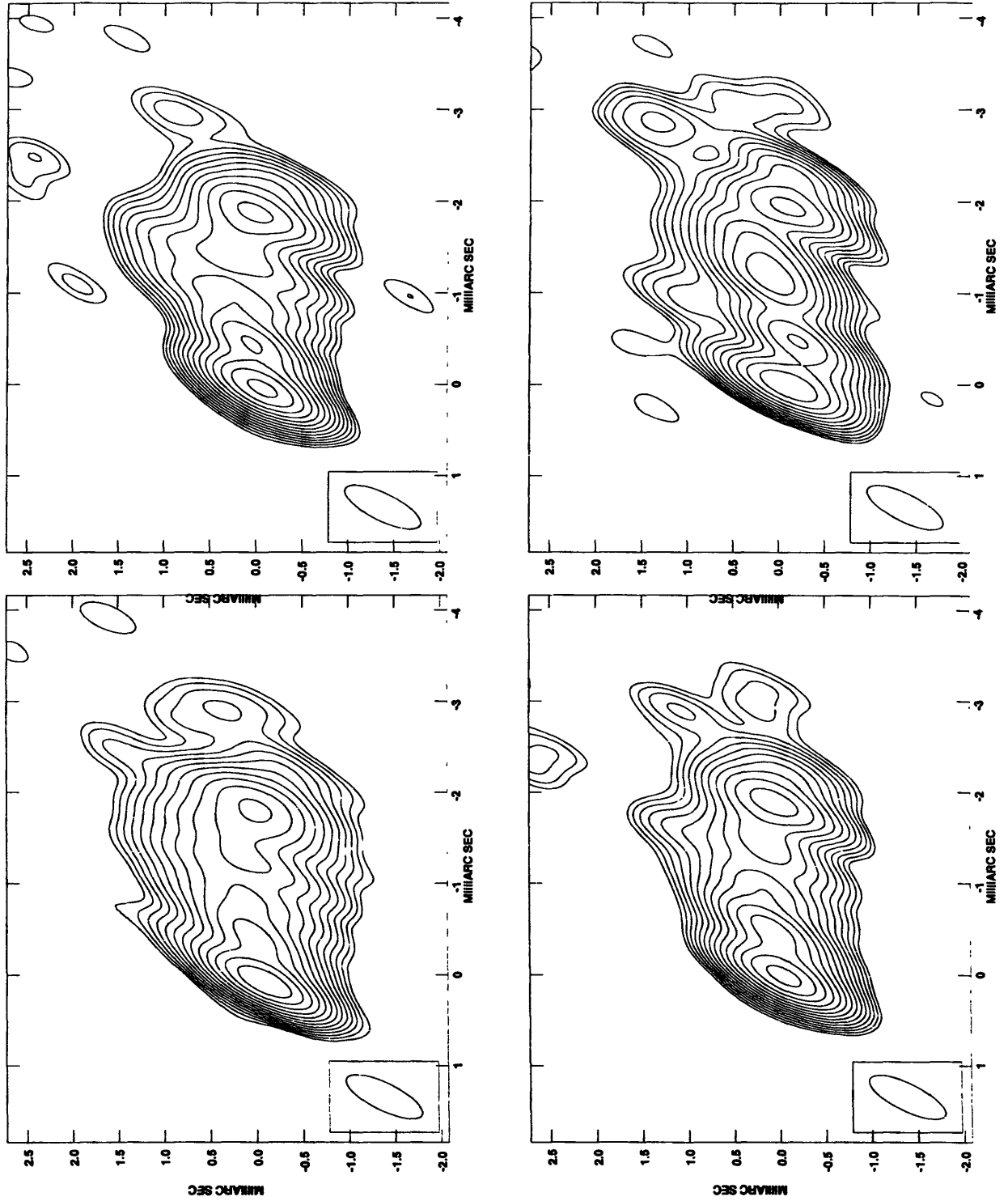


Fig. 9.— Full image and simulations imaged with Robust -1 in AIPS. Beams are  $0.91 \times 0.3$  mas at bpa -26.29 degrees. Lowest contour is 6.5 mJy and increase by factor  $\sqrt{2}$ . The peak fluxes from A to D are 563, 635, 661, and 381 mJy respectively.

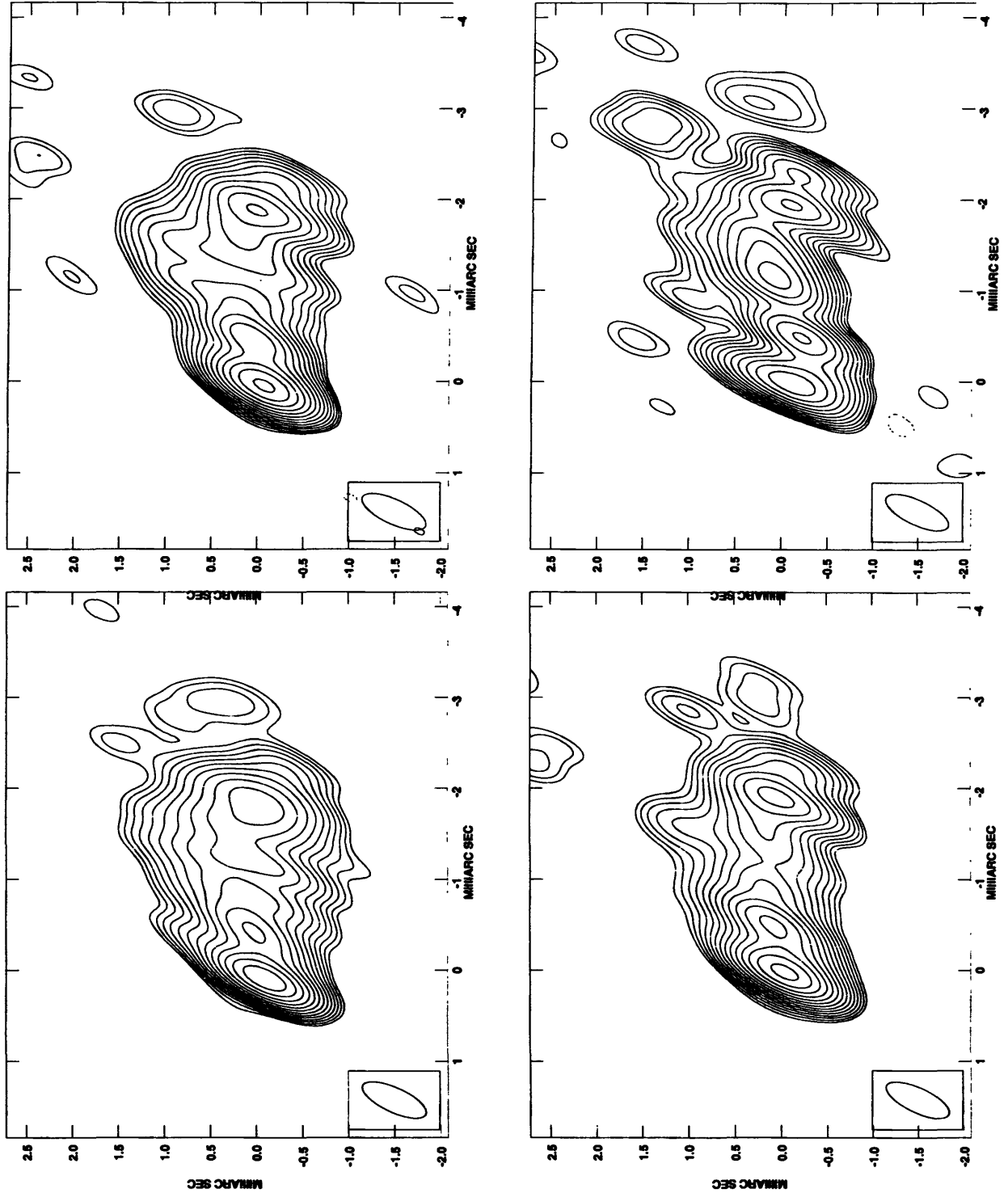


Fig. 10.— Full image and simulations imaged with Robust -2 in AIPS. Beams are  $0.76 \times 0.27$  mas at bpa -24.81 degrees. Lowest contour is 6.5 mJy and increase by factor  $\sqrt{2}$ . The peak fluxes from A to D are 577, 655, 679, and 404 mJy respectively.



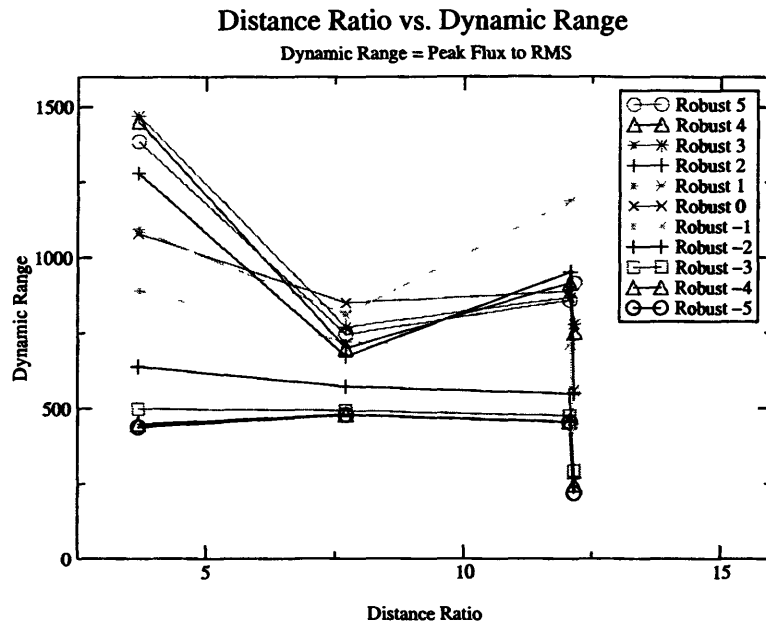


Fig. 11.—

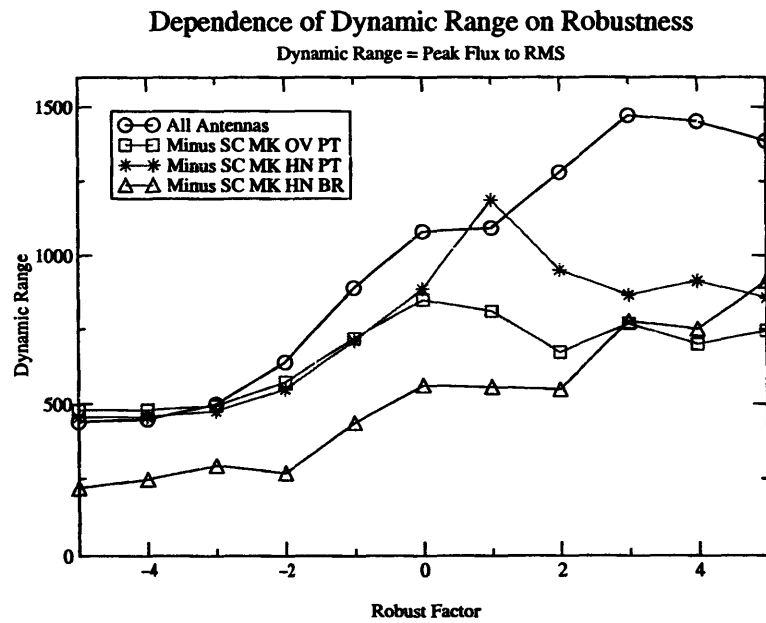


Fig. 12.—

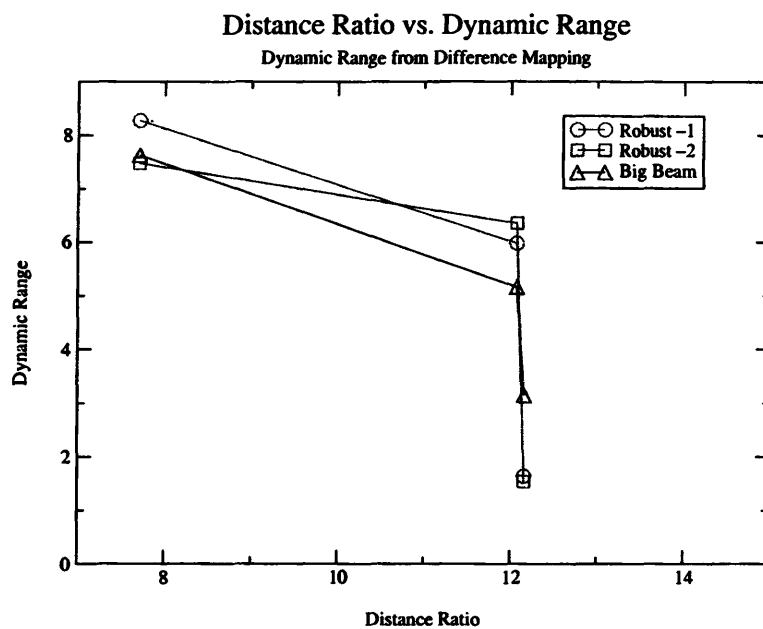


Fig. 13.—

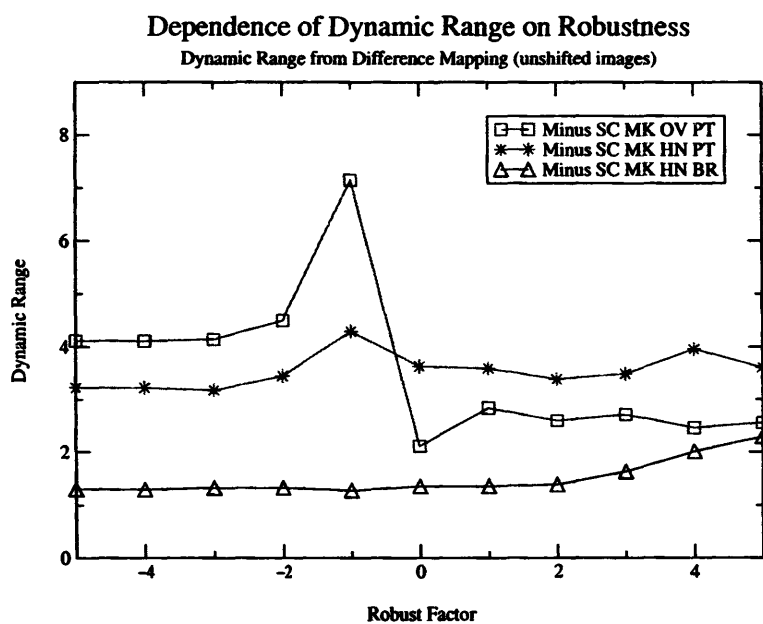


Fig. 14.—

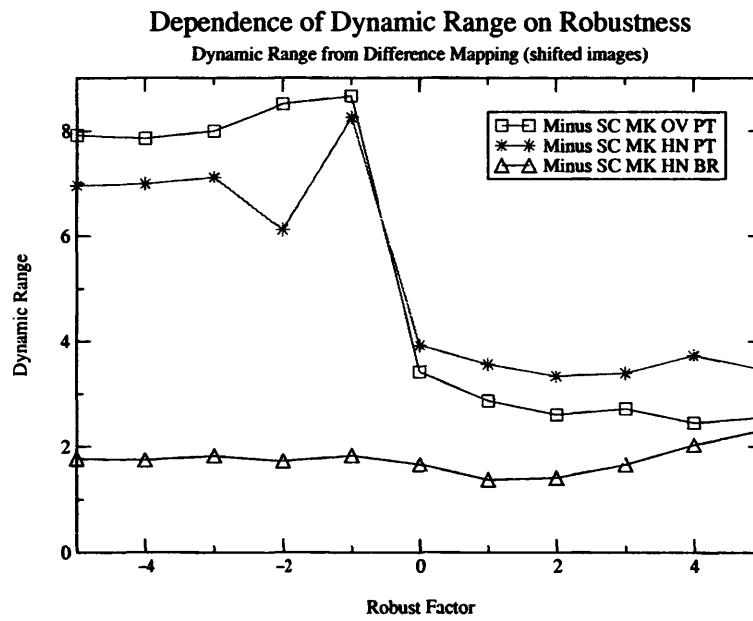


Fig. 15.—

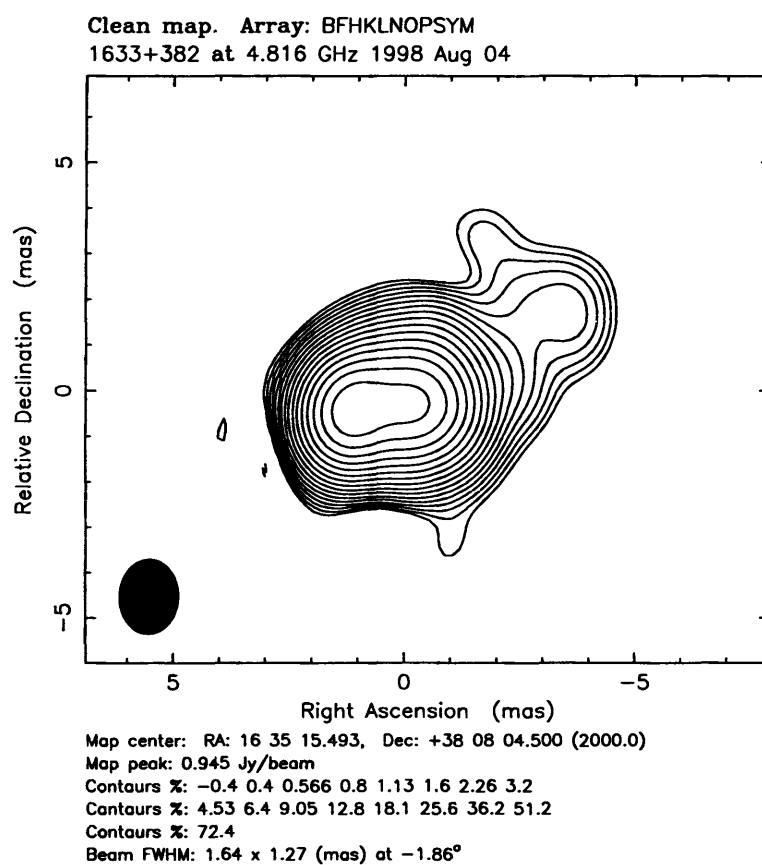


Fig. 16.— Ground Only Image of 1633+382.



# Two Epoch VSOP Imaging of the $\gamma$ -ray Blazar 1633+382 at $\lambda 6$ cm

Chi C. T. Cheung<sup>1</sup> & James S. Ulvestad<sup>2</sup>

National Radio Astronomy Observatory, Socorro, NM

**DRAFT: To be submitted to *Astronomical Journal***

## ABSTRACT

We present two epochs of high resolution space VLBI observations of the  $\gamma$ -ray blazar 1633+382 (4C 38.41) at  $\lambda 6$  cm. The resolution achieved in the images is comparable to that of other higher frequency ground observations of the source but show much more detail of the steep spectrum jet that is less prominent in the ground images. We combine our results with results from an 8 GHz VLBA observation in our proper motion study of the source.

## 1. Introduction

Space Very Long Baseline Interferometry (SVLBI; cf. Ulvestad 1998 and references therein) is a technique used to achieve the highest resolution in imaging possible at any given radio frequency. The currently orbiting HALCA (Highly Advanced Laboratory for Communications and Astronomy) satellite (see Hirabayashi *et al.*) of the VLBI Space Observatory Programme (VSOP) achieves an increase in resolution of a factor of more than three over that of ground only arrays by increasing the maximum baselines to greater than the size of the earth. We used HALCA to observe the  $\gamma$ -ray blazar 1633+382 (4C 38.41) at

---

<sup>1</sup>current address: Department of Physics, Brandeis University, Waltham, MA, 02454; [ccc@quasar.astro.brandeis.edu](mailto:ccc@quasar.astro.brandeis.edu)

<sup>2</sup>[julvesta@nrao.edu](mailto:julvesta@nrao.edu)

$\lambda 6$  cm at the epochs 29/30 July 1997 and 4/5 August 1998 to image the steep spectrum jet that is mostly resolved out by higher frequency ground observations.

The quasar 1633+382 is a flat spectrum radio source and shows rapid variability across the entire electromagnetic spectrum (e.g. Peng & de Bruyn; Raiteri *et al.*; Hartman *et al.*, 1997). Its radio polarization in the cm range is fairly low – 1.3 % at  $\lambda 20$  cm and 1.4 % at  $\lambda 6$  cm from VLA measurements (Perley 1982), and the VLBI core is 1.5 % polarized at 5 GHz (Cawthorne *et al.*). It is however,  $7.9 \pm 2.7$  % polarized at  $\lambda 1.1$  mm (Nartallo *et al.*) during epoch 1993.15. Despite the fact that it is only a marginal highly polarized quasar showing highly variable optical polarization with a maximum of  $2.6 \pm 1.0$  % (Moore & Stockman), its behavior places it securely in the blazar class (Angel & Stockman 1980; Antonucci 1993). All blazars are probably superluminal but not all have confirmed detections. This asserts that blazar jets are relativistic and highly beamed, oriented close to our line of sight thus explaining the high brightness temperatures observed in some sources that exceed the inverse Compton limit. Peng & de Bruyn calculate a value of  $T_B \sim 7.5 \times 10^{18}$  K derived from variability observations which is indeed in excess of the inverse Compton limit. Here also, we report the detection of superluminal motion in 1633+382 seen in a different component than that traced by Barthel *et al.*

Throughout this work we assume a standard Friedmann cosmology with  $H_0 = 100$  h km s<sup>-1</sup> Mpc<sup>-1</sup>. At a redshift of 1.814 (Wills & Wills), a proper motion of  $\mu = 1$  mas/yr translates to an apparent linear velocity of  $\beta_{app}h = 54.73c$  ( $q_0 = 0.05$ ) or  $\beta_{app}h = 39.07c$  ( $q_0 = 0.5$ ).



## 2. Background

### 2.1. VLBI Observations of 1633+382

The blazar 1633+382 has had a long association with VLBI studies. Its mas structure is characterized by a core-jet morphology which initially extends west and then bends southwest at about 50 mas from the core (Polatidis *et al.* at 1.7 GHz; epoch 1990 Sept 20) hinting at a connection towards the north-south lobes detected in an overall core-dominated kpc scale structure seen by the VLA (Murphy *et al.*; Rusk 1988).

The earliest VLBI image comes from the Pearson & Readhead (1988) survey at 5 GHz from epoch 1979.25. Barthel *et al.* have combined this and 5 GHz maps at epochs 1984.40 and 1986.89 in the only other detection of superluminal motion in this source. Cawthorne *et al.* have available, the first VLB polarimetry results of 1633+382 at the same frequency (epoch 1984.77) and more recent VLBA 5 GHz polarimetry has been done by Attridge 1999. We also have 8 GHz VLBA polarization observations which will be presented elsewhere.

On nearly sub-milliarsecond scales, recent monitoring has been done with the VLBA by Kellermann *et al.* (15 GHz) at intervals from 3 months to a year between six epochs from April 1995 to March 1998, and Xu *et al.* 1998 (22 GHz) at intervals from 2 to 6 months of seven epochs from March 1994 to May 1996. Xu *et al.* 1997 observe the jet edge moving constantly about  $0.56 \pm 0.4$  mas over 2.17 years. A number of the 15 and 22 GHz observations are contemporaneous and by inspection of the images, they show a consistent component that is steep spectrum fading away at the higher frequency. Consistency

between their observations with our 2 epochs of VSOP observations and single 8 GHz VLBA observation (1995.39) during this period will help determine if strobing effects are present which is of crucial importance to our proper motions studies. 2 and 8 GHz maps are also available from the USNO archive (Fey & Charlot 1997). Bower (1999) modeled the 86 GHz VLBI structure from the CMVA with a single gaussian of flux density  $2.07 \pm 0.34$  Jy, consistent with a radio spectral index close to zero in the cm to mm range as seen in data from NED and Bloom *et al.* although its spectrum seems to be variable (cf. Landau *et al.*).

## 2.2. Multiwavelength Observations of 1633+382

1633+382 has been detected by the EGRET instrument aboard the Compton Gamma Ray Observatory (CGRO) between September 12-19, 1991 (Kanbach *et al.*, Mattox *et al.*). Valtaoja & Terasranta claim that 1633+382 is one of 21 blazars in their Metsahovi sample that showed a heightened mm state (the 22 and 37 GHz fluxes were either increasing or close to maximum) during an EGRET detection but their flux density curves presented in Terasranta *et al.* (1998) for the period 1981 - 1995.5 show only a very slight increase in the flux at that time. Curiously, Peng & de Bruyn show the 92 cm flux to be at a steady decline from late 1991 to early 1992. Terasranta *et al.* (1992) includes also some 87 GHz monitoring results in addition to the 22 and 37 GHz fluxes. Upon comparison of the mm observations with cm observations from UMRAO, the two mm flares at about epochs 1982.5 and 1986 seem to precede the cm outbursts at about 1983 and 1987 respectively, indicating a lag of about 6 months to a year between the cm and mm bursts. Perhaps examination of

UMRAO data obtained since the beginning of this decade will yield similar connections in the cm/mm flux densities.

The core of 1633+382 went through an outburst in 1995 – a factor of about two increase in flux over the adjacent years (Xu *et al.* 1997). This is coincident with the historical optical maximum on June 27, 1995 (Bosio *et al.*) with an R band magnitude of  $14.96 \pm 0.03$ . Also, the mm flux experiences a significant rise beginning in about 1994 and almost doubling to about 3.5 Jy at 37 GHz by 1995.5 (Terasranta *et al.*, 1998), coincident with the optical flare and core outburst.

The source is in general highly variable, experiencing low frequency variability at 92 cm (Peng & de Bruyn), intraday variability in the optical (Raiteri *et al.*), and  $\gamma$ -ray flux variations over a few days (Hartman *et al.*, 1997). Lahteenmaki & Valtaoja exploit the mm variability and have calculated the variability doppler boosting factor (8.83) and have determined the Lorentz factor (5.78) and viewing angle (5.48 degrees) of the jet. The variability doppler boosting factor is consistent with the minimum value derived by Mattox *et al.* of 7.6, extracted from invoking other arguments.

Its mm to IR spectrum is consistent with a single power law ( $\alpha_{mm} = 0.66$  and  $\alpha_{IR} = 1.26$  with  $S \propto \nu^{-\alpha}$ ; Bloom *et al.* 1994). Nartallo *et al.* however, measure a spectral index of  $\alpha_{mm} = 1.23 \pm 0.19$  from measurements at 2.0, 1.1, and 0.8 mm at epoch 1993.15 which indicates that its spectrum is variable. Other references that may be useful are:

- Kubo *et al.* have compiled the multiband spectrum of 1633+382 and a number of

blazars from work done previously and their own ASCA observations. Their sample show that the spectra of these sources are double peaked.

- Xie *et al.* include 1633+382 in their study of correlations between the near-IR and  $\gamma$ -ray flux densities in  $\gamma$ -ray loud blazars.
- Stevens *et al.* have multifrequency monitoring results of 17 blazars at 375, 270, 230, and 150 GHz from JCMT, 230, 150, and 90 GHz data from IRAM, and 90 GHz data from SEST. Although 1633+382 is not included in this work, Stevens may have unpublished data that is "Available in digital form from jas@star.uclan.ac.uk".
- Hartman *et al.* (1999) have published the third EGRET catalog which includes data up to 1995 October 3. It lists the flux of 1633+382 during its flare in 1991 as well as the non significant  $\gamma$ -ray detections.

### 3. Observations

1633+382 was observed first on 29/30 July 1997 with HALCA together with the VLBA at a central observing frequency of 4.978 GHz. Data from the spacecraft was successfully acquired through two tracking stations for a total of about 5.0 hours (4.3 hours from the NRAO Green Bank and 0.7 hr from the NASA Goldstone station). The ground telescopes spent ten hours on source. Observations from the Los Alamos telescope was eliminated completely due to computer problems there. About three hours of data was flagged from Kitt Peak when they were experiencing severe thunderstorms and about 1-2 hours of data

from Owens Valley and Pie Town were flagged where the source was beginning to rise.

The second epoch was taken on 4/5 August 1998 with HALCA, the full VLBA and the phased VLA at a central observing frequency of 4.816 GHz. A total of about 8.0 hours of spacecraft data was taken from 3 tracking stations (about 4 hours at RZ, more than 3 hours at NZ, and about hour at TZ). This data was combined with 14 hours of data from each ground element (except about 4 hours lost from St. Croix and 2 hours from Hancock when the source was setting at the end of the observation). Data from both epochs were correlated at the VLBA correlator in Socorro, NM. The UV coverage and amplitude vs. UV distance plots are shown in figure 1.

### **3.1. Data Reduction Procedure**

Data from both epochs was calibrated with NRAO's AIPS reduction package using standard techniques. The data was edited and self calibrated in AIPS. The absolute flux in the second epoch was bootstrapped from the simultaneous VLA observation which utilized scans of 3C 286. System temperature and gain value of the space antenna at 5 GHz estimated from the HALCA WWW homepage were inputted manually. Refinements of the delay rate for the three tracking stations were obtained by performing preliminary fringe-fits on two minute pieces of data from each station and applied before the final fringe-fit performed. We performed a second round of fringe-fitting which included a model obtained from some phase self-calibration of the data from the initial fringe-fitting. A gain correction of 1.4 was applied to the data after initial attempts to self-calibrate the data in

Caltech’s DIFMAP (Shepherd *et al.*) package showed this to be necessary. The final phase and amplitude self calibration was done in AIPS after averaging and editing the data in DIFMAP.

## 4. Model Fitting

The model-fitting of components for both epochs of HALCA observations and the 8 GHz VLBA observation were done in DIFMAP’s modelfit program.

### 4.1. Epoch 0: 22/23 May 1995

In DIFMAP, we brought in the UV data, used a mapsize 1024,0.15, and select i. We then did a uvaverage 30. An initial attempt to input the model obtained for the 1997 epoch yielded a  $\chi^2 = 42.257841$ . Curiously enough, not UV-averaging yielded a  $\chi^2 = 3.2889868$  immediately but doing a modelfit or selfcal would hurt the model –  $\chi^2 = 0.1$  to 0.5. This may be a point of concern in the future, whether to average the data before modelfitting and which model to trust over the other. After making some changes to the model (making it look more like J. Ulvestad’s initial fit and Fey & Charlot’s model, i.e. a flat spectrum core and steeper spectrum outer components), we obtained a  $\chi^2 = 20.334309$ . Taking out the component at 17 mas from the core gave a  $\chi^2 = 20.363283$ . We then made the model look as closely to Fey & Charlot’s model and yielded a  $\chi^2 = 5.5776263$ . Performing a modelfit 5 yielded a  $\chi^2 = 0.15341296$  so we inputted back the Fey & Charlot model and performed a selfcal immediately which gave a  $\chi^2 = 1.0323940$ . The model is:

! Flux (Jy)	Radius (mas)	Theta (deg)	Major (mas)	Axial ratio	Phi (deg)	T
1.03000v	0.139262v	122.920v	0.340000v	0.540000v	-65.0000v	1
0.190000v	1.60000v	-76.4683v	1.48000v	1.00000v	0.00000v	1
0.0200000v	4.50500v	-63.1971v	0.0100000v	1.00000v	0.00000v	1
0.730000v	0.870000v	-92.3317v	0.650000v	1.00000v	0.00000v	1

We tried a model fit 5 to change the circular gaussian components into ellipticals but the  $\chi^2$  dropped to 0.20479408. We then tried two things. We took the combination of the Fey & Charlot fluxes and radii but put in the theta, major, axial ratio and phi of the last model which returned the  $\chi^2 = 0.20479408$  and this model gave:

Iteration 00: Reduced Chi-squared=0.96396383

! Flux (Jy)	Radius (mas)	Theta (deg)	Major (mas)	Axial ratio	Phi (deg)	T
1.03000v	0.139262v	124.068v	0.247756v	0.00000v	-83.9416v	1
0.190000v	1.60000v	-71.1947v	1.81399v	0.710313v	51.2878v	1
0.0200000v	4.50500v	-66.2767v	2.02540v	0.630231v	-31.9646v	1
0.730000v	0.870000v	-90.8599v	0.782157v	0.744046v	88.1081v	1

Then, we took the combination of the Fey & Charlot fluxes and position but used the size and shape of the components from the  $\chi^2 = 0.20479408$  model:

Iteration 00: Reduced Chi-squared=0.97400300

! Flux (Jy)	Radius (mas)	Theta (deg)	Major (mas)	Axial ratio	Phi (deg)	T
-------------	--------------	-------------	-------------	-------------	-----------	---



1.03000v	0.139262v	122.920v	0.247756v	0.00000v	-83.9416v 1
0.190000v	1.60000v	-76.4683v	1.81399v	0.710313v	51.2878v 1
0.0200000v	4.50500v	-63.1971v	2.02540v	0.630231v	-31.9646v 1
0.730000v	0.870000v	-92.3317v	0.782157v	0.744046v	88.1081v 1

With the fact in mind that these two last models resulted from performing a self-calibration with a different model as the template, we started DIFMAP over and brought in the last two models separately and performed a self-calibration immediately.

The first model began with a  $\chi^2 = 4.7608747$  and after self-calibration:

Iteration 00: Reduced Chi-squared=0.81503476

! Flux (Jy)	Radius (mas)	Theta (deg)	Major (mas)	Axial ratio	Phi (deg) T
1.03000v	0.139262v	124.068v	0.247756v	0.00000v	-83.9416v 1
0.190000v	1.60000v	-71.1947v	1.81399v	0.710313v	51.2878v 1
0.0200000v	4.50500v	-66.2767v	2.02540v	0.630231v	-31.9646v 1
0.730000v	0.870000v	-90.8599v	0.782157v	0.744046v	88.1081v 1

The second model began with a  $\chi^2 = 5.4704275$  and after self-calibration:

Iteration 00: Reduced Chi-squared=0.89599888

! Flux (Jy)	Radius (mas)	Theta (deg)	Major (mas)	Axial ratio	Phi (deg) T
1.03000v	0.139262v	122.920v	0.247756v	0.00000v	-83.9416v 1
0.190000v	1.60000v	-76.4683v	1.81399v	0.710313v	51.2878v 1

0.0200000v	4.50500v	-63.1971v	2.02540v	0.630231v	-31.9646v	1
0.730000v	0.870000v	-92.3317v	0.782157v	0.744046v	88.1081v	1

These are the best preliminary models fitted to epoch 0: 22/23 May 1995.

#### 4.2. Epoch 1: 29/30 July 1997

The total intensity map is shown in figure 2 beside the 1998 map which is convolved with the same beam as the 1997 epoch. We first attempted to modelfit the ground only data with a 4 component model which shows a good  $\chi^2$  value:

Iteration 05: Reduced Chi-squared=1.5244042

! Flux (Jy)	Radius (mas)	Theta (deg)	Major (mas)	Axial ratio	Phi (deg)	T
0.776410v	0.0586828v	159.092v	0.494207v	0.700710v	-77.1187v	1
0.999026v	1.27928v	-87.9586v	0.984965v	0.789515v	64.2077v	1
0.181380v	1.85519v	-67.6675v	2.29880v	0.559149v	79.0433v	1
0.0284513v	4.58904v	-62.1922v	1.74780v	0.696986v	46.1798v	1

We inputed the ground only model into the data which included HALCA and yielded similar results:

Iteration 00: Reduced Chi-squared=2.5878323

! Flux (Jy)	Radius (mas)	Theta (deg)	Major (mas)	Axial ratio	Phi (deg)	T
0.809711v	0.0494574v	170.398v	0.568291v	0.690602v	-77.6680v	1

0.985038v	1.29408v	-88.0636v	0.966345v	0.792251v	59.4782v 1
0.164375v	1.96957v	-67.3802v	2.26176v	0.502322v	71.3218v 1
0.0307439v	4.56533v	-61.6360v	1.85728v	0.646595v	47.8098v 1
0.0625428v	16.8252v	-75.3552v	18.3136v	0.735037v	13.5039v 1

The component at  $\sim 17$  mas from the core is seen at the second epoch when using a larger cellsize and natural weighting in the imaging so is added for good measure. This extra component hardly disrupted the  $\chi^2$  value which even showed a marginal improvement and does not seem to affect the fit of the model.

Disregarding this model, we started over and slowly converged on an acceptable model that yielded both a low  $\chi^2$  value and a good fit in the UV plane. The data from epoch 1 was best fit with six elliptical gaussian components which yielded the best  $\chi^2$  value (= 2.24).

! Flux (Jy)	Radius (mas)	Theta (deg)	Major (mas)	Axial ratio	Phi (deg)	T
0.542548v	0.139262v	122.920v	0.341528v	0.00000v	-67.5269v	1
0.475302v	0.520529v	-92.3317v	0.787564v	0.894391v	-34.8218v	1
0.585410v	1.42491v	-90.9125v	0.754169v	0.572266v	21.0389v	1
0.348090v	1.65607v	-76.4683v	1.77670v	0.716093v	69.1699v	1
0.0403995v	4.40500v	-63.1971v	1.99429v	0.857836v	26.4681v	1
0.0867147v	16.7506v	-73.1925v	17.9091v	0.864263v	-0.543817v	1

These component positions are best shown relative to the core:

Component	Flux (Jy)	$\Delta x$ (mas)	$\Delta y$ (mas)	Radius (mas)	$\theta$ (deg)
Core	0.542548	0	0	0	0
1	0.475302	0.637	0.0545	0.6393	-85.109
2	0.585410	1.5416	0.0530	1.5425	-88.03
3	0.348090	1.7270	0.4632	1.788	-74.987
4	0.0403995	4.0486	2.0620	4.5435	-63.01
5	0.0867147	16.152	4.9192	16.884	-73.06

### 4.3. Epoch 2: 4/5 August 1998

The total intensity map is shown in figure 3. Compare this to figure 4 which is the best image obtainable with only the ground antennas.

Many decent models were fit to the UV data. We also tried to fit a model to UV data that excluded data from the TZ tracking station whose data overlapped with the ground data and made the inner baselines noisier. One of the decent models obtained is:

! Flux (Jy)	Radius (mas)	Theta (deg)	Major (mas)	Axial ratio	Phi (deg)	T
0.513801v	0.135660v	132.779v	0.0845956v	0.00000v	-0.0873412v	1
0.210143v	1.82891v	-91.9888v	0.363398v	0.701582v	-8.59606v	1
0.0961523v	3.86661v	-67.1370v	3.45305v	0.567551v	-43.0175v	1
0.307409v	0.362020v	-94.3695v	0.601808v	0.00000v	-72.0276v	1
1.00831v	1.29745v	-82.7861v	1.45503v	0.639424v	-83.0281v	1
0.0758986v	17.4839v	-71.6207v	17.6899v	0.794091v	-48.8030v	1

## 5. Results

We have mapped the total intensity structure of the  $\gamma$ -ray blazar 1633+382 at  $\lambda 6$  cm with space VLBI at two epochs. The additional east-west UV coverage in the first epoch does indeed help to resolve the close inner components to the core when compared to the best ground only image of the source (figure 4 – from data at the second epoch which had four additional hours of data and included one more VLBA antenna and the phased VLA). The second epoch (figure 3) shows significant improvement in resolution even when convolved with a larger beam (figure 2).

## 6. Conclusion

## 7. Acknowledgements

The National Radio Astronomy Observatory is operated by Associated Universities, Inc., under cooperative agreement with the National Science Foundation. Space VLBI at NRAO is funded by NASA. The VSOP project is led by the Japanese Institute of Space and Astronautical Science in cooperation with many organizations and radio telescopes around the world. C.C.T.C. thanks the 1999 NRAO summer student program and its coordinators.

## REFERENCES

- Angel, J.R.P. & Stockman, H.S. 1980, *ARA&A*, **18**, 321-361
- Antonucci, R. 1993, *ARA&A*, **31**, 473-521
- Attridge, J.M. 1999, *Ph.D. Thesis*, Brandeis University
- Barthel, P.D., Conway, J.E., Myers, S.T., Pearson, T.J., & Readhead, A.C.S. 1995, *ApJL*, **444**, 21-24
- Bloom, S., *et al.* 1994, *AJ*, **108**, 398-404
- Bosio, S., *et al.* 1995, *IAUC*, **6183C**, 1
- Bower, G.C. 1999, in *Proc. MM VLBI Workshop, Granada*, in press
- Cawthorne, T.V., Wardle, J.F.C., Roberts, D.H., Gabuzda, D.C., & Brown, L.F. 1993, *ApJ*, **416**, 496-518
- Fey, A.L. & Charlot, P. 1997, *ApJS*, **111**, 95-142
- Hartman, R.C., Collmar, W., von Montigny, C., & Dermer, C.D. 1997, in *Proc. of the Fourth Compton Symposium*, eds. C.D. Dermer, M.S. Strickman, & J.D. Kurfess (AIP), 307-327
- Hartman, R.C., *et al.* 1999, *ApJS*, **123**, 79-202
- Hirabayashi, H., *et al.* 1998, *Science*, **281**, 1825-1828

Kanbach, G., *et al.* 1997, *IAUC*, **5431**, 1

Kellermann, K.I., Vermeulen, R.C., Zensus, J.A. & Cohen, M.H. 1998. *AJ*, **115**: 1295-1318

Kubo, H., *et al.* 1998, *ApJ*, **504**, 693-701

Lahteenmaki, A. & Valtaoja, E. 1999, *ApJ*, **521**, 493-501

Landau, R., *et al.* 1986, *ApJ*, **308**, 78-92

Mattox, J.R., *et al.* 1993, *ApJ*, **410**, 609-614

Moore R.L. & Stockman H.S. 1984, *ApJ*, **279**, 465-484

Murphy, D.W., Browne, I.W.A., & Perley, R.A. 1993, *MNRAS*, **264**, 298-318

Nartallo, R., Gear, W.K., Murray, A.G., Robson, E.I., & Hough, J.H. 1998, *MNRAS*, **297**,  
667-686

Pearson, T.J. & Readhead, A.C.S. 1988, *ApJ*, **328**, 114

Peng, B. & de Bruyn, A.G. 1995, *A&A*, **301**, 25-32

Polatidis, A.G., Wilkinson, P.N., Xu, W., Readhead, A.C.S., Pearson, T.J., Taylor, G.B.,  
& Vermeulen, R.C. 1995, *ApJS*, **98**, 1-32

Raiteri, C.M., *et al.* 1996, in *Extragalactic Radio Sources: Proc of the 175th IAUS*, eds.  
R.D. Ekers, C. Fanti, & L. Padrielli (Netherlands: Kluwer), 287-288

Rusk R. 1988, *Ph.D. Thesis*, University of Toronto

Shepherd, M.C., Pearson, T.J., & Taylor, G.B. 1994, *BAAS*, **26**, 987

Stevens, J.A., *et al.* 1994, *ApJ*, **437**, 91-107

Terasranta, H., *et al.* 1992, *A&AS*, **94**, 121-173

Terasranta, H., *et al.* 1998, *A&AS*, **132**, 305-331

Ulvestad, J.S. 1998, in *Synthesis Imaging in Radio Astronomy II*, ASP Conf Series 180, eds.

G.B. Taylor, C.L. Carilli, & R.A. Perley (San Francisco: ASP), 1-23

Valtaoja, E. & Terasranta, H. 1995, *A&A*, **297**, L13-L16

Wills, D., & Wills, B.J. 1976, *ApJS*, **31**, 143

Xie, G.Z., *et al.* 1998, *ApJ*, **508**, 180-185

Xu, W., Wehrle, A.E. & Marscher, A.P. 1997, in *Proceedings of the Fourth Compton*

*Symposium*, eds. C.D. Dermer, M.S. Strickman, & J.D. Kurfess, 1437-1439

Xu, W., Wehrle, A.E. & Marscher, A.P. 1998, in *IAU Colloquium 164: Radio Emission*

*from Galactic and Extragalactic Compact Sources*, ASP Conf Series 144, eds. J.A.

Zensus, G.B. Taylor, & J.M. Wrobel (San Francisco: ASP), 175-176



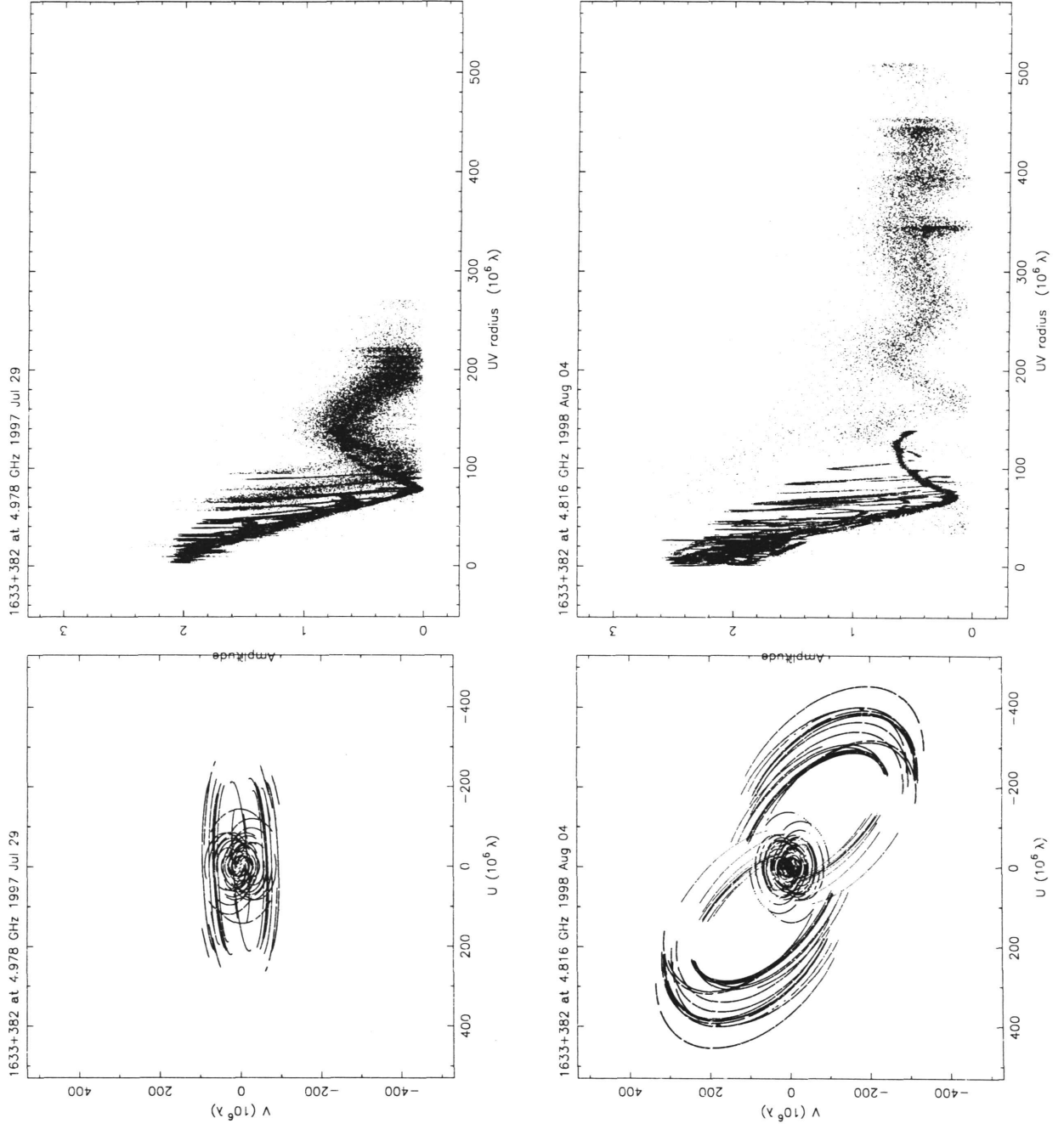


**Fig. 1.—** Top: plots of the UV Coverage and Amplitude vs. UV distance of the epoch 29/30 July 1997 observation. Bottom: corresponding plots of epoch 4/5 August 1998 observation

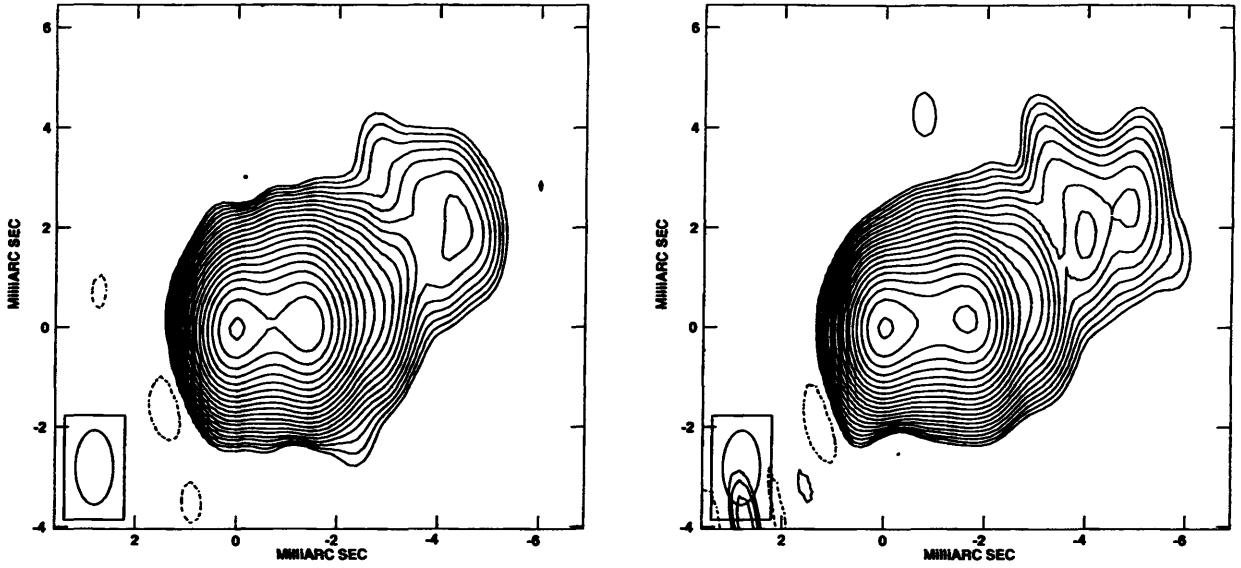


Fig. 2.— Left: epoch 29/30 July 1997 image and at Right: epoch 4/5 August 1998 with a beam of  $1.49 \times .75$  mas at bpa  $-2.42$

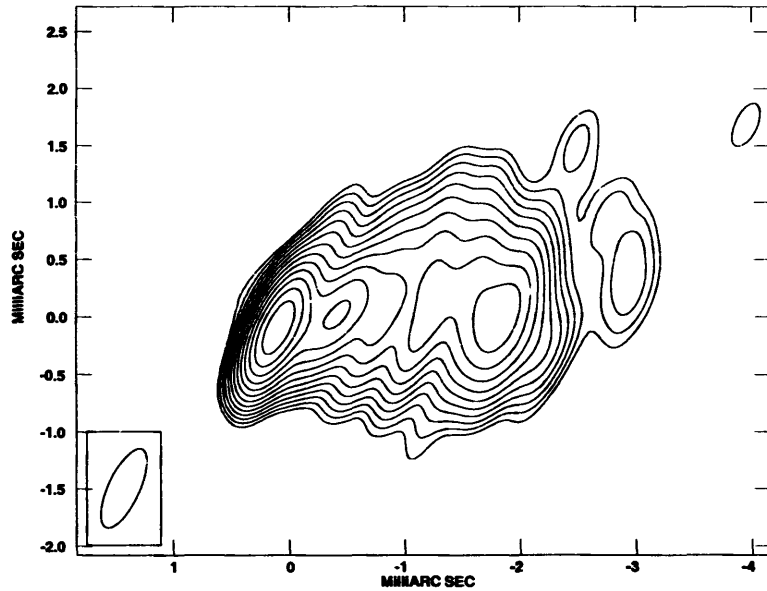


Fig. 3.— Epoch 4/5 August 1998 imaged with Robust -2 in AIPS. Beam is  $0.76 \times 0.27$  mas at bpa  $-24.81$  degrees. Lowest contour is 6.5 mJy and increase by factor root 2 with a peak of 577 mJy

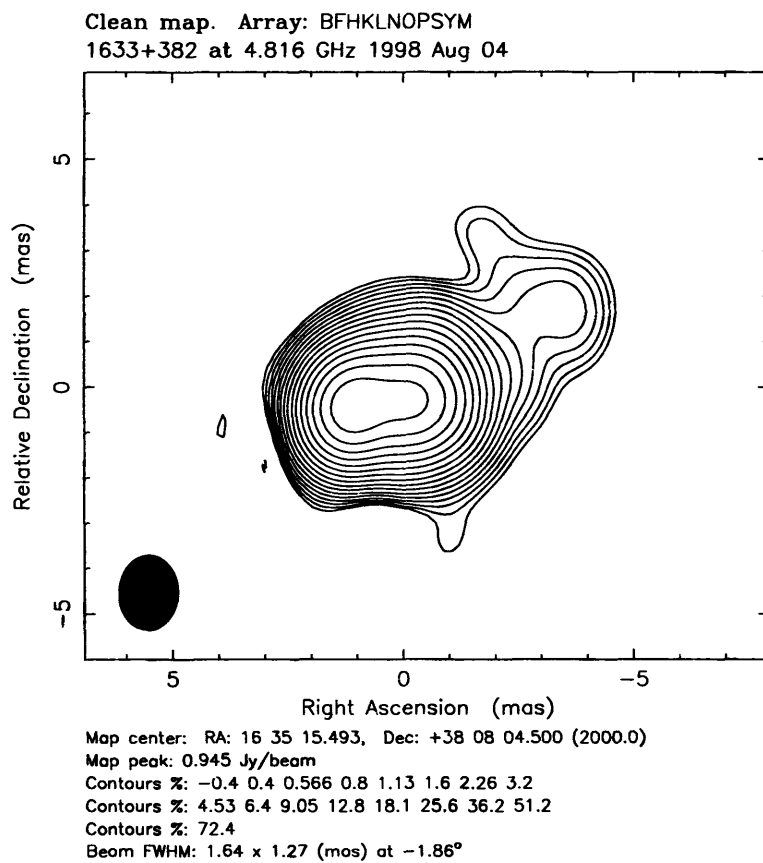


Fig. 4.— Ground Only Image of 1633+382 from epoch 4/5 August 1998

# The EGRET blazar PKS 2255-282

C. C. T. Cheung<sup>1</sup> & J. S. Ulvestad<sup>2</sup>

National Radio Astronomy Observatory, Socorro, NM, 87801

## DRAFT

### 1. Background

The blazar PKS 2255-282 (Wright & Otrupcek) at  $z = 0.926$  (Browne *et al.* 1975, Peterson *et al.*) was detected serendipitously by the EGRET instrument aboard the Compton Gamma Ray Observatory (CGRO) to have flared at the beginning of January 1998 (Bertsch 1998). Tornikoski *et al.* 1999 observed a massive burst in the mm flux in June 1997 and observed the source with the VLBA as a target of opportunity proposal on 13 August 1997 at 5, 22, and 43 GHz. The 22 and 43 GHz observations resolved completely the jet, leaving only the compact core. Very few references turned up during a NED search but recent VLBA maps are available at 15 GHz (Kellermann *et al.* 2 cm survey WWW site; epoch 18/08/97) and 8 GHz (USNO WWW data base at the 1997 epochs Jul 25, Sep 09, and Dec 17; see Fey *et al.* 1996) which show a bright core and an extension towards the southwest about 4 mas away.

### 2. VLBA Observations

We have obtained 2 epochs of VLBA observations at 15, 22, and 43 GHz early this year at January and May.

---

<sup>1</sup>current address: Department of Physics, Brandeis University, Waltham, MA, 02454; [ccc@quasar.astro.brandeis.edu](mailto:ccc@quasar.astro.brandeis.edu)

<sup>2</sup>[julvesta@nrao.edu](mailto:julvesta@nrao.edu)

## 2.1. epoch 5/6 January 1999

### 2.1.1. VLA calibration

About three hours of VLA C-array data at 43, 22, and 15 GHz was obtained during the VLBA observation to help determine absolute flux densities and position angles of the polarization data. Antenna 25 was used as the reference antenna because of its proximity to the center of the array and it has one of the 13 Q band receivers (antennas 3, 4, 6, 8, 11, 12, 13, 14, 16, 20, 22, and 27 are the others). Absolute flux density measurements were taken from the VLA calibrator manual (see figure 2.1.1).

Source (J2000)	2 cm Flux (Jy)	7 mm Flux (Jy)	UV limit?
0137+331	1.78 (S)	0.64 (X)	Max 45 k $\lambda$ at 2 cm
0521+166	1.56 (X)	0.4 (?)	Max of 40 and 100 k $\lambda$ at 2 and .7 cm
2148+069	3.00 (P)	7.6 (S)	none
2258-279	2.60 (P)	1.7 (S)	none

- 15 GHz calibration - No editing seemed necessary from examining the LISTR output. The task SETJY was used to input preliminary fluxes (figure 2.1.1). Setting 0137+331 initially as the primary flux calibrator with the suggested UV limit yielded disagreements in the fluxes of 2148+069 and 2258-279 by almost a factor of 3 greater than expected. We subsequently tried the source 2148+069 to bootstrap the other fluxes which yielded values close to those from figure 2.1.1. The results are in figure 2.1.1.

Source (J2000)	IF 1 Flux (Jy)	IF 2 Flux (Jy)	Errors (Jy)
0137+331	1.78074	1.78092	$\pm 0.006$
0521+166	1.55981	1.55975	$\pm 0.006$
2148+069	3.00	3.00	$\pm 0.006$
2258-279	2.59957	2.59945	$\pm 0.006$

## REFERENCES

- Bertsch, D. 1998, *IAUC*, **6807B**, 1
- Browne, I., *et al.* 1975, *MNRAS*, **173**, 87
- Fey, A.L., Clegg, A.W., & Fomalont, E.B. 1996 *ApJS*, **105**, 299
- Peterson, B.A. *et al.* 1976, *ApJ*, **207**, L5
- Tornikoski, M., *et al.* 1999, in *BL Lac Phenomenon*, ASP Conf Series 159, eds. L.O. Takalo, & A. Sillanpaa (San Francisco: ASP), 305-306
- Wright, A.E. & Otrupcek, R.E. 1990. *PKSCAT90 - The Southern Radio Source Database v1.01*



# **Ionosphere Corrections in Radio Astronomy using GPS Data**

**Bryan Jones  
Rick Perley  
Richard Moeser  
Chris Flatters  
Bill Erickson**

**NRAO  
August 1999**





# Table of Contents

Introduction.....	2
The System.....	3
System Diagram.....	4
GBSS.....	5
GtfFileConverter.....	7
UML for GtfFileConverter.....	8
GtfFileConverter code.....	9
The Daemon.....	26
Daemon code.....	27
Ionosphere Monitor.....	37
Ionosphere Monitor screenshot.....	38
UML for Ionosphere Monitor.....	39
Ionosphere Monitor code.....	40
Sample Ionosphere Data.....	63



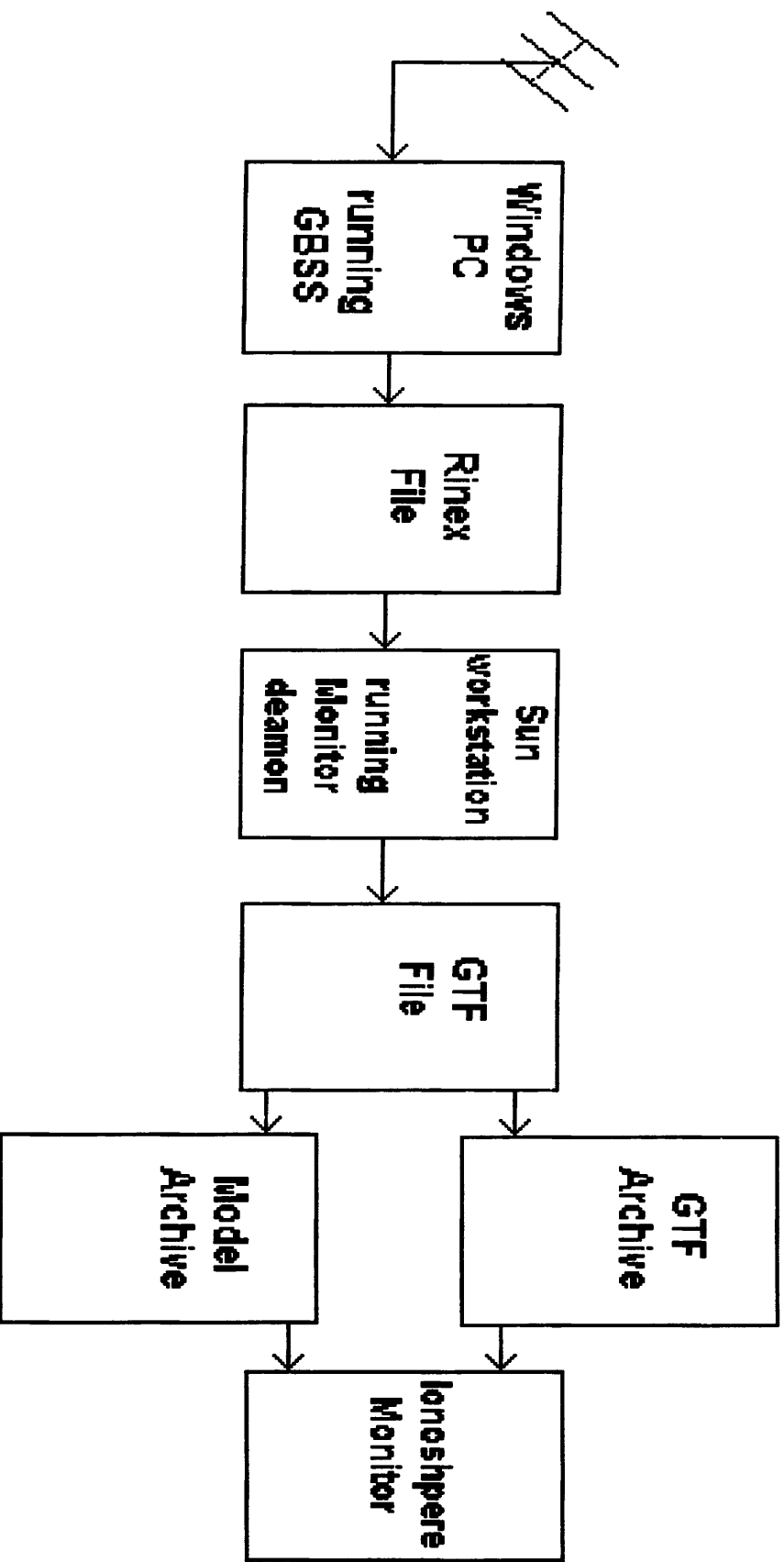
## **Introduction**

When observing at low frequencies one must consider the affects of the ionosphere on astronomical data. We have set up a system using Global Positioning System(GPS) ionosphere data for making Faraday rotation and interferometer phase corrections. Since the GPS data only pertains to the directions in which the satellites are visible, a simple model of the ionosphere was developed. The model consists of three parameters. The zenith Total Electron Content(TEC), the direction of the gradient, and the magnitude of the gradient. With these three parameters it is possible to predict the TEC for any arbitrary direction. With the system that we have developed observers are allowed to conveniently and continuously obtain ionosphere data with a relatively simple and inexpensive GPS receiver.

## **The System**

The system consists of two computers. The first one is a windows PC running Geodetic Base Station Software(GBSS). GBSS is a commercial program designed to monitor GPS satellites by being connected to a GPS receiver. After every nine minutes, GBSS compiles the data it has collected and outputs it as RINEX navigation and a RINEX observation file. GBSS also has the capability to execute a system call on the DOS prompt after compiling the data. In our case we use this feature to FTP the RINEX files to our second computer. The second computer is a SUN workstation running a daemon. The job of the daemon is to lie dormant until the RINEX files appear. The RINEX files have more information than is useful to our project so the first job of the daemon is to convert the RINEX files into the GTF file format. The GTF format is very useful because it is directly usable by AIPS. The conversion is accomplished by calling the program GtfFileConverter. After the GTF file has been created the daemon uses a recursive gradient search method to derive the parameters of the ionosphere model. Once the data is processed, the daemon archives all the data into a database and then waits for the next incoming file. To access the database an observer uses the program IonosphereMonitor. IonosphereMonitor uses a graphical user interface to allow ease of use to enter in specific dates for data retrieval. IonosphereMonitor has the capability to either output the model parameters or the original GTF files.

# System Diagram



## GBSS

In order for GBSS to perform as we would like, certain steps had to be taken to configure GBSS. All of the following configurations can be made from configuration menu in GBSS with the exception of the files that need to be created. Note that these configurations are for the GPS receiver located at the Array Operations Center. If the antenna is moved these figures must be adjusted accordingly.

Port	com1
Speed	115200
Recording Interval	30.00
Elevation Mask	10
Receiver Type	UZ-12
Channel	OA13
Navigation	UE00
Site Name	AOC1
Antenna Height	0.0
North Latitude	34 4
11.865982	
East Longitude	253 5 33.277496
West Longitude	106 54 26.722504
ECEF X	-1538495.2770
ECEF Y	-5061426.6380
ECEF Z	+3553669.5460
Primary Output Path	c:\Outputs
Output Ashtech Formatted B-,E-, and S-Files	√
Convert B-,E- and S-Files to Rinex	√
Trap Communication Data to File	√
File Duration	0.15
File Re-open Rate	60
Epoch Filtering	-1
File deletion Age	-1

## **GBSS (continued)**

The most complicated part of the GBSS setup is the post-session commands. Post-session commands allow GBSS to perform any function that can be executed on the DOS prompt after a data set is accumulated. In our case we will be using this feature to automatically ftp the RINEX files to the SUN workstation. Here is the list of commands that must be entered in the configurations menu. Note that all commands must have the wait option enabled. This makes GBSS wait for a command to finish before going on to the next command.

Cmd1	c:\Outputs\setup.bat \$ROFP\$
Cmd2	c:\WINNT\system32\ftp -s:c:\Outputs\commands.txt
Cmd3	c:\Outputs\setup.bat \$RNFP\$
Cmd4	c:\WINNT\system32\ftp -s:c:\Outputs\commands.txt
Cmd5	c:\Outputs\clean.bat \$ROFP\$ \$RNFP\$ \$SFP\$ \$BFP\$ \$EFP\$ \$TFP\$

In addition to entering these commands in GBSS, we needed to create the following two files in the c:\Outputs directory. Note that user name and password need to be replaced by their values for the specific machine that the files will be sent to.

### **setup.bat**

```
echo (user name)>c:\outputs\commands.txt
echo (password)>>c:\outputs\commands.txt
echo put %1>>c:\outputs\commands.txt
```

### **clean.bat**

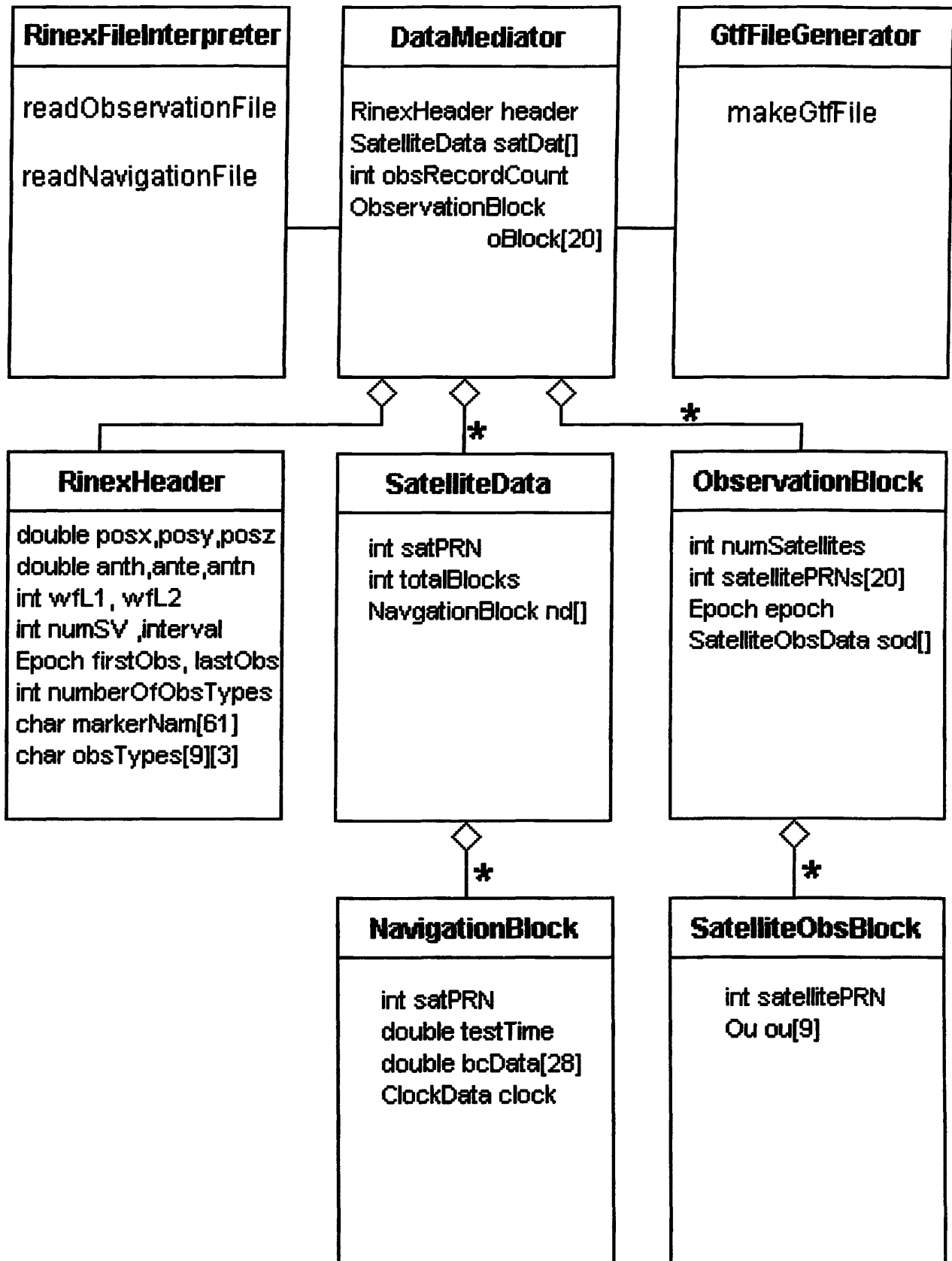
```
del %1
del %2
del %3
del %4
del %5
del %6
```



## **GtfFileConverter**

GtfFileConverter is a standalone program that converts RINEX files to the GTF file format. GtfFileConverter is called through a system call by the monitor daemon and is thus not directly linked to the daemon. The specified file to be converted is passed to GtfFileConverter through its first command line argument. The file name is passed without either the N or the O appended. The results of the conversion are stored in data.gtf where they will be picked up later by the daemon. Note that GtfFileConverter deletes the RINEX files to save space.

# UML Diagram



```

#include<stdio.h>
#include<math.h>
#include<unistd.h>
#include<stdlib.h>
#include "rinex.h"
#include "GpsUtility.cc"
#include "Initializer.cc"
#include "DataMediator.cc"
#include "GtfFileGenerator.cc"
#include "RinexFileInterpreter.cc"

int main(int argc, char* argv[])
{
    Initializer init(argc, argv);
    init.createFiles();           //make the files
    if(!init.initializedCorrectly()) //check to see if program was executed correctly
        exit(1);

    FILE *rinexObsFile, *rinexNavFile, *gtfFile;    //get the files from the Initializer
    rinexObsFile = init.getObsFile();
    rinexNavFile = init.getNavFile();
    gtfFile = init.getGtfFile();

    DataMediator data;           //data storage class

    RinexFileInterpreter interpreter(&data, rinexObsFile, rinexNavFile); //read the files
    interpreter.readObservationFile();
    interpreter.readNavigationFile();

    GtfFileGenerator generator(gtfFile, data); //make the Gtf file
    generator.makeDataFile();

    fclose(rinexObsFile);        //close all the files
    fclose(rinexNavFile);
    fclose(gtfFile);
}
//Class Initializer
//
//This class is used to do all the start up tasks of the program.
//These include checking to see if the program was called correctly
//and opening and creating the files that the program will use

class Initializer
{
public:
    //Constructor
    Initializer(int numArguments, char* argv[])
    {
        if(numArguments == 2)
        {
            strcpy(fileName,argv[1]);
        }
        else
        {
            printf("usage: %s filename, where filename is of the form SSSSDDMO.YY\n",argv[0]);

```

```

        exit(1);
    }
}

//Open all files
void createFiles()
{
    strcpy(obsFileName, fileName);
    strcpy(navFileName, fileName);
    strcpy(gtfFileName, fileName);
    strcat(obsFileName, "O",1);
    strcat(navFileName, "N",1);
    sprintf(gtfFileName,"data.gtf");

    obsFile = fopen(obsFileName,"r");
    navFile = fopen(navFileName,"r");
    gtfFile = fopen(gtfFileName,"w");
}

//function to test if everything when ok
int initalizedCorrectly()
{
    int check = 1;
    if(obsFile == NULL)
    {
        printf("failed to open %s\n",obsFileName);
        check = 0;
    }

    if(navFile == NULL)
    {
        printf("failed to open %s\n",navFileName);
        check =0;
    }

    return check;
}

//Functions for retrieving opened file
FILE* getObsFile()
{
    return obsFile;
}

FILE* getNavFile()
{
    return navFile;
}

FILE* getGtfFile()
{
    return gtfFile;
}

private:
    FILE *obsFile;

```

```

FILE *navFile;
FILE *gtfFile;
char fileName[40];
char obsFileName[40];
char navFileName[40];
char gtfFileName[40];
};

//class DataMediator
//
//This class is used as a storage device to transfer data from
//the RinexFileInterpreter to the GtfFileGenerator

class DataMediator
{
public:
    RinexHeader header;           //header for observation file
    SatelliteData satDat[MAX_SATELLITES]; //data for observation file

    int obsRecordCount;           //number of records in navigation file
    ObservationBlock oBlock[20];  //data for navigation file
};

//class RinexFileInterpreter
//
//This class reads the observation and navigation files and
//stores the data into a DataMediator

class RinexFileInterpreter
{
public:
    //Constructor
    RinexFileInterpreter(DataMediator *d, FILE *obs, FILE *nav)
    {
        data = d;
        obsFile = obs;
        navFile = nav;
    }

    //function to call subfunctions to read the observation file
    void readObservationFile()
    {
        readObservationHeader();
        readObservationBody();
    }

    //function to call sub functions for reading the navigation file
    void readNavigationFile()
    {
        readNavigationHeader();
        readNavigationBody();
    }

private:

```

```

//reads the observation header
void readObservationHeader()
{
    char descriptor[21];
    char lineBuffer[82];
    rewind(obsFile);
    while(!feof(obsFile))
    {
        for(int i=0; i<21; i++)//clear descriptor
            descriptor[i] = '\0';
        fscanf(obsFile,"%81c",lineBuffer);
        sscanf(lineBuffer,"%*60c%21c",descriptor);    //read a line of the file
        clean(descriptor);

        //Now check the string against all possible types of data
        //and process accordingly

        if(strcmp(descriptor, END_OF_HEADER) == 0)
            break;
        else if(strcmp(descriptor, POSITION_XYZ) == 0)
        {
            sscanf(lineBuffer, "%14lf%14lf%14lf",&data->header.posx,
                                                            &data->header.posy,
                                                            &data->header.posz);
        }
        else if(strcmp(descriptor, MARKER_NAME) == 0)
        {
            sscanf(lineBuffer, "%60c", data->header.markerName);
        }
        else if(strcmp(descriptor, ANTENNA_DELTA) == 0)
        {
            sscanf(lineBuffer, "%14lf%14lf%14lf",&data->header.anth,
                                                            &data->header.ante,
                                                            &data->header.antn);
        }
        else if(strcmp(descriptor, WAVELENGTH_FACT) == 0)
        {
            /* TODO: read in more info - not sure what is needed */
            sscanf(lineBuffer, "%6d%6d%6d",&data->header.wfL1,
                                                            &data->header.wfL2,
                                                            &data->header.numSV);
        }
        else if(strcmp(descriptor, OBSERVATION_TYPE) == 0)
        {
            char *pc;
            sscanf(lineBuffer, "%6d", &data->header.numberOfObsTypes);
            pc = lineBuffer + 10; /* align pointer to first observation types */
            for (int i = 0; i < data->header.numberOfObsTypes; i++)
            {
                sscanf(pc, "%s", data->header.obsTypes[i]);
                pc += 6;
            }
        }
        else if(strcmp(descriptor, INTERVAL) == 0)
        {
            sscanf(lineBuffer, "%6d", &data->header.interval);
        }
    }
}

```

```

    }
    else if(strcmp(descriptor, TIME_OF_1ST_OBS) == 0)
    {
        sscanf(lineBuffer, "%6d%6d%6d%6d%6d%12lf",&data->header.firstObs.year,
                &data->header.firstObs.month,
                &data->header.firstObs.day,
                &data->header.firstObs.hour,
                &data->header.firstObs.minute,
                &data->header.firstObs.seconds);
    }
    else if(strcmp(descriptor, TIME_OF_LST_OBS) == 0)
    {
        sscanf(lineBuffer, "%6d%6d%6d%6d%6d%12lf",&data->header.lastObs.year,
                &data->header.lastObs.month,
                &data->header.lastObs.day,
                &data->header.lastObs.hour,
                &data->header.lastObs.minute,
                &data->header.lastObs.seconds);
    }

    /*
    Ignore the following descriptors:
        "RINEX VERSION TYPE"
        "PGM / RUN BY / DATE"
        "COMMENT"
        "OBSERVER / AGENCY"
        "REC # / TYPE / VERS"
        "ANT # / TYPE"
        "LEAP SECONDS"
        "# OF SATELLITES"
        "PRN / # OF OBS"

    */
}
}

//reads the body of the observation file
void readObservationBody()
{
    double dummy;
    int epochFlag;
    char temp[20];

    while(!feof(obsFile))    //while not at end of the file
    {
        //read in date information
        fscanf(obsFile,"%d",&data->oBlock[data->obsRecordCount].epoch.year);
        fscanf(obsFile,"%d",&data->oBlock[data->obsRecordCount].epoch.month);
        fscanf(obsFile,"%d",&data->oBlock[data->obsRecordCount].epoch.day);
        fscanf(obsFile,"%d",&data->oBlock[data->obsRecordCount].epoch.hour);
        fscanf(obsFile,"%d",&data->oBlock[data->obsRecordCount].epoch.minute);
        fscanf(obsFile,"%11c",temp);
        data->oBlock[data->obsRecordCount].epoch.seconds = atof(temp);
        fscanf(obsFile,"%d",&epochFlag);
        fscanf(obsFile,"%d",&data->oBlock[data->obsRecordCount].numSatellites);

        for(int i=0; i<data->oBlock[data->obsRecordCount].numSatellites; i++)
        {

```

```

    fscanf(obsFile,"%d",&data->oBlock[data->obsRecordCount].satellitePRNs[i]);
}

fscanf(obsFile,"%f",&dummy);          //don't know what this number is

if(epochFlag == 0)
{
    fseek(obsFile,1,SEEK_CUR);          //move forward one space to get over \n
    for(int a=0; a<data->oBlock[data->obsRecordCount].numSatellites; a++)//loop through the block
    {
        data->oBlock[data->obsRecordCount].sod[a].satellitePRN = //write the PRN# on th oBlock
        data->oBlock[data->obsRecordCount].satellitePRNs[a];
        for(int i=0; i<data->header.numberOfObsTypes; i++) //loop through the line
        {
            fscanf(obsFile,"%14c",temp);
            data->oBlock[data->obsRecordCount].sod[a].ou[i].data = atof(temp);
            fscanf(obsFile,"%c",&data->oBlock[data->obsRecordCount].sod[a].ou[i].los);
            fscanf(obsFile,"%c",&data->oBlock[data->obsRecordCount].sod[a].ou[i].sigStr);
        }
        if(!feof(obsFile))              //This is becuae fseek will ruin EOF
            fseek(obsFile,-1,SEEK_CUR);
    }
}
data->obsRecordCount++; //increment counter
}
}

//read the navigation header
//it doesn't do anything with the data it just gets the file
//pointer to the right spot
void readNavigationHeader()
{
    char lineBuffer[82];
    char descriptor[21];

    for(int i=0; i<MAX_SATELLITES; i++)
        data->satDat[i].totalBlocks = 0;

    rewind(navFile); //make sure at the beginnig

    for(int i=0; i<21; i++)
        descriptor[i] = '\0';

    fscanf(navFile,"%81c", lineBuffer);
    sscanf(lineBuffer, "%*60c%21c", descriptor);
    clean(descriptor);

    if(strcmp(descriptor, RINEX_VERSION_TYPE) != 0)
    {
        fprintf(navFile,"food");
        fclose(navFile);
        printf("Not a RINEX navigation file. %x\n",navFile);
        printf("%s\n%s\n",lineBuffer,RINEX_VERSION_TYPE);
        exit(1);
    }
}

```



```

sscanf(lineBuffer,"%6d",&versionNum); //get version number

while(!feof(navFile))                //read until the end of the header
{
    for(int i=0; i<20; i++)
        descriptor[i] = '\0';

    fscanf(navFile,"%81c",lineBuffer);
    sscanf(lineBuffer, "%*60c%21c", descriptor);
    clean(descriptor);
    if(strcmp(descriptor, END_OF_HEADER) == 0)
        break;
}
}

//read the body of the navigation file
void readNavigationBody()
{
    int increment = 4;
    NavigationBlock navBlock;
    char temp[20];

    while(!feof(navFile))    //while not at end of file
    {
        fscanf(navFile,"%d",&navBlock.satPRN);
        fscanf(navFile,"%d",&navBlock.epoch.year);    //read in date
        fscanf(navFile,"%d",&navBlock.epoch.month);
        fscanf(navFile,"%d",&navBlock.epoch.day);
        fscanf(navFile,"%d",&navBlock.epoch.hour);
        fscanf(navFile,"%d",&navBlock.epoch.minute);
        fscanf(navFile,"%5c",temp);
        navBlock.epoch.seconds = atof(temp);

        if(feof(navFile))                //make sure not at end of file
            return;

        //read in clock information
        temp[19]='\0';
        fscanf(navFile,"%19c",temp);
        fixExponent(temp);
        navBlock.clock.bias = atof(temp);
        fscanf(navFile,"%19c",temp);
        fixExponent(temp);
        navBlock.clock.drift = atof(temp);
        fscanf(navFile,"%19c",temp);
        fixExponent(temp);
        navBlock.clock.driftRate = atof(temp);

        int linesToRead = (versionNum > 1) ? 7:6;    //6 if version 1; 7 if version > 1

        for(int i=0; i<linesToRead; i++)    //loop through block
        {
            fscanf(navFile,"%*4c%19c",temp);
            fixExponent(temp);
            navBlock.bcData[i*increment] = atof(temp);
        }
    }
}

```

```

    fscanf(navFile,"%19c",temp);
    fixExponent(temp);
    navBlock.bcData[i*increment + 1] = atof(temp);

    fscanf(navFile,"%19c",temp);
    fixExponent(temp);
    navBlock.bcData[i*increment + 2] = atof(temp);

    fscanf(navFile,"%19c",temp);
    fixExponent(temp);
    navBlock.bcData[i*increment + 3] = atof(temp);
}

GpsUtility utility;
GpsTime gps;
utility.gpsWeek(navBlock.epoch, &gps);
navBlock.testTime = gps.numDays + navBlock.epoch.hour/24.0
                    + navBlock.epoch.minute/1440.0
                    + navBlock.epoch.seconds/86400.0;

int i = navBlock.satPRN - 1;
//store dat into the DataMediator
data->satDat[i].nd[data->satDat[i].totalBlocks] = navBlock;
data->satDat[i].totalBlocks++;
data->satDat[i].satPRN = navBlock.satPRN;
}
}

//changes all \n into \0 in a string
void clean(char *s)
{
    for(int i=0; i<21; i++)
        if(s[i] == '\n')
            s[i]='\0';
}

//changes all D to E
void fixExponent(char *s)
{
    for(int i=0; i<81; i++)
    {
        if(s[i] == 'D')
            s[i] = 'E';
        if(s[i] == '\0' || s[i] == '\n')
            break;
    }
}

DataMediator *data;
FILE *obsFile;
FILE *navFile;
int versionNum;
};

//class GpsUtility
//

```

```

//This class serves as a tool box of functions for the program
//
//methods:
// void gpsWeek(Epoch ,GpsTime *)
// int dayOfYear(Epoch )
// int getObsTypeIndex(char *, RinexHeaderh )
// int getClosestTime(SatelliteData ,long )
// void gpsEphemerisToXYZ(NavigationBlock *,SV_struct *,XYZ *,long )
// void kepler(double *, double *, double *)
// void azel(SV_struct *, XYZ *, AltAz *)
// void tau(double ,double ,double *)
// void pha(double ,double ,double *)

class GpsUtility
{
public:
//This function takes data from an Epoch and converts it to usable
//data by a GpsTime
void gpsWeek(Epoch epoch, GpsTime *gps)
{
    int monthEnd[12] = {0,31,59,90,120,151,181,212,243,273,304,334};
    int ndyyr;
    int nleapyr;
    int doy = dayOfYear(epoch);

    if (epoch.year > 1900)
        epoch.year -= 1900;

    ndyyr = (epoch.year - 80) * 365 + 2 - 7;
    nleapyr = 0;

    if (epoch.year > 80)
        nleapyr = (epoch.year - 1 - 80) / 4 + 1;

    gps->numDays = ndyyr + nleapyr + doy - 1;
    gps->week = gps->numDays / 7;
    gps->dayOfWeek = gps->numDays - gps->week * 7;
    gps->seconds =(long)(gps->dayOfWeek * 86400 + epoch.hour * 3600 + epoch.minute * 60
                        + (int)epoch.seconds);
}

//Computes the day of the year based on an Epoch
int dayOfYear(Epoch epoch)
{
    int monthEnd[12] = {0,31,59,90,120,151,181,212,243,273,304,334};
    int doy;

    /* compute the day of year */
    doy = monthEnd[epoch.month - 1] + epoch.day;

    /* if after Feb and leap year, add a day */
    if (epoch.month >= 3 && epoch.year%4 == 0)
        doy += 1;

    return doy;
}

```

```
//returns the index of the location of the type specified
int getObsTypeIndex(char *type, RinexHeader rh)
```

```
{
    int index = -1;
    for(int i=0; i<rh.numberOfObsTypes; i++)
    {
        if(strcmp(rh.obsTypes[i], type) == 0)
        {
            index = i;
            break;
        }
    }
    return index;
}
```

```
//returns the index of the navigation block with the closest seconds value
int getClosestTime(SatelliteData psd, long seconds)
```

```
{
    int minIndex = -1;
    long minDiff = 0;
    long diff = 0;
    GpsTime gps;
    for(int i=0; i<psd.totalBlocks; i++)
    {
        gpsWeek(psd.nd[i].epoch, &gps);
        diff = (long)fabs(seconds - gps.seconds);
        if(i==0)
        {
            minIndex = i;
            minDiff = diff;
            continue;
        }
        if(diff<minDiff)
        {
            minIndex = i;
            minDiff = diff;
        }
    }
    return minIndex;
}
```

```
//Converts an Ephemeris to a XYZ position
```

```
//written by Richard Moser
```

```
void gpsEphemerisToXYZ(NavigationBlock *pnb, SV_struct *svs, XYZ *vel,
    long secondsOfGpsWeek)
```

```
{
    double n0, n, tk, mk, ek, vk, pk, sin2pk, cos2pk, uk, duk, drk, dik;
    double rk, ik, xkp, ykp, ok, sinok, cosok;
    double ykpcosik, sinvk, cosvk, sinek, cosek;
    double en, a, roote, omegakd, dlatd;
    double sin2pd, cos2pd, corlatd, corrd, corid;
    double rkd, xikd, xkd, ykd, vx, vy, vz, ekdot;
```

```
n0 = sqrt(MU / pow(pnb->bcData[INDEX_SQRT_A], 6.0));
tk = secondsOfGpsWeek - pnb->bcData[INDEX_TOE];
```

```

if (tk > HALFWEEK) tk -= WEEK;
if (tk < -HALFWEEK) tk += WEEK;
n = n0 + pnb->bcData[INDEX_DELTA_N];
mk = pnb->bcData[INDEX_M0] + n * tk;

/* test kepler - begin */
/* the following is the way the fortran code handles KEA */
ek = mk;
en = n0 + pnb->bcData[INDEX_DELTA_N];
ekdot = en;
for (int i = 0; i < 4; i++) {
    cosek = cos(ek);
    sinek = sin(ek);
    ek = mk + pnb->bcData[INDEX_ECC] * sinek;
    ekdot = en + pnb->bcData[INDEX_ECC] * cosek * ekdot;
}
/* test kepler end */

cosvk = cosek - pnb->bcData[INDEX_ECC];
sinvk = sqrt(1.0 - pnb->bcData[INDEX_ECC] * pnb->bcData[INDEX_ECC]) * sinek;

vk = atan2(sinvk, cosvk);
if (vk < 0.0) vk += 2 * PI;

pk = vk + pnb->bcData[INDEX_AOP];
sin2pk = sin(2.0 * pk);
cos2pk = cos(2.0 * pk);
duk = pnb->bcData[INDEX_CUC] * cos2pk + pnb->bcData[INDEX_CUS] * sin2pk;
drk = pnb->bcData[INDEX_CRC] * cos2pk + pnb->bcData[INDEX_CRS] * sin2pk;
dik = pnb->bcData[INDEX_CIC] * cos2pk + pnb->bcData[INDEX_CIS] * sin2pk;

uk = pk + duk;
rk = pnb->bcData[INDEX_SQRT_A] * pnb->bcData[INDEX_SQRT_A]
    * (1.0 - pnb->bcData[INDEX_ECC] * cosek) + drk;
ik = pnb->bcData[INDEX_I0] + dik /* + pnb->bcData[INDEX_I_DOT] * tk */;

xkp = rk * cos(uk);
ykp = rk * sin(uk);

ok = pnb->bcData[INDEX_OMEGA0] + (pnb->bcData[INDEX_OMEGA_DOT] - OMEGA_DOT_E)
    * tk - OMEGA_DOT_E * pnb->bcData[INDEX_TOE];

ykpcosik = ykp * cos(ik);
sinok = sin(ok);
cosok = cos(ok);

svs->pos.x = xkp * cosok - ykpcosik * sinok;
svs->pos.y = xkp * sinok + ykpcosik * cosok;
svs->pos.z = ykp * sin(ik);

roote = sqrt(1.0 - pnb->bcData[INDEX_ECC] * pnb->bcData[INDEX_ECC]);
a = pnb->bcData[INDEX_SQRT_A] * pnb->bcData[INDEX_SQRT_A];
omegakd = pnb->bcData[INDEX_OMEGA_DOT] - OMEGA_DOT_E;
dlatd = en * roote * (a * a) / (rk * rk);

sin2pd = 2.0 * cos2pk * dlatd;

```

```

cos2pd = -2.0 * sin2pk * dlatd;

corlatd = pnb->bcData[INDEX_CUC] * cos2pd + pnb->bcData[INDEX_CUS] * sin2pd;
corrd = pnb->bcData[INDEX_CRC] * cos2pd + pnb->bcData[INDEX_CRS] * sin2pd;
corid = pnb->bcData[INDEX_CIC] * cos2pd + pnb->bcData[INDEX_CIS] * sin2pd;

dlatd += corlatd;
rkd = a * pnb->bcData[INDEX_ECC] * sinek * ekdot + corrd;
xikd = corid;

xkd = rkd * cos(uk) - rk * sin(uk) * dlatd;
ykd = rkd * sin(uk) + rk * cos(uk) * dlatd;

vel->x = (xkd * cosok) - (ykd * cos(ik) * sinok) - (xkp * sinok * omegakd)
        - (ykp * cos(ik) * cosok * omegakd) + (ykp * sin(ik) * xikd * sinok);
vel->y = (xkd * sinok) + (ykd * cos(ik) * cosok) + (xkp * cosok * omegakd)
        - (ykp * cos(ik) * sinok * omegakd) - (ykp * sin(ik) * xikd * cosok);
vel->z = ykd * sin(ik) + ykp * cos(ik) * xikd;
}

//Written by Richard Moser
void kepler(double *mk, double *ecc, double *ek) {
    double x, y, x1, y1, x2;
    int i;
    x = *mk;
    y = *mk - (x - *ecc * sin(x));
    x1 = x;
    x = y;
    for (i = 0; i < 16; i++) {
        x2 = x1;
        x1 = x;
        y1 = y;
        y = *mk - (x - *ecc * sin(x));
        if (fabs(y - y1) < 1.0E-15) break;
        x = (x2 * y - x * y1) / (y - y1);
    }
    *ek = x;
}

//Converts a XYZ into an azimuth and elevation
//Written by Richard Moser
void azel(SV_struct *svs, XYZ *vel, AltAz *ae) {
    const double dtr = 57.29577951;
    double dx, dy, dz, distance;
    double sdx, sdy, sdz;
    double cosx, cosy, cosz;
    double azimuth, elevation, range;
    int i;
    /* Pietown coordinates */
    //double pt_x = -1640882.5849;
    //double pt_y = -5014790.3071;
    //double pt_z = +3575445.3681;
    double pt_x = -1538495.2770;
    double pt_y = -5061426.6380;
    double pt_z = 3553669.5460;
    //double stn_lat = 34.3015033;

```

```

//double stn_lon = 251.8814578;
double stn_lat = 34.06996333;
double stn_lon = 253.09257667;
double coscl = cos(((double)90.0 - stn_lat) / dtr);
double sincl = sin(((double)90.0 - stn_lat) / dtr);
double cosln = cos(stn_lon / dtr);
double sinln = sin(stn_lon / dtr);

dx = sv->pos.x - pt_x;
dy = sv->pos.y - pt_y;
dz = sv->pos.z - pt_z;
distance = sqrt(dx*dx + dy*dy + dz*dz);

for (i = 0; i < 2; i++) {
    double dt, dtom, usx, usy, svpx, svpy, svpz;
    dt = -(distance / C);
    dtom = dt * OMEGA_DOT_E;
    usx = sv->pos.x + vel->x * dt;
    usy = sv->pos.y + vel->y * dt;

    svpx = usx * cos(dtom) - usy * sin(dtom);
    svpy = usy * cos(dtom) + usx * sin(dtom);
    svpz = sv->pos.z + vel->z * dt;

    dx = svpx - pt_x;
    dy = svpy - pt_y;
    dz = svpz - pt_z;

    distance = sqrt(dx*dx + dy*dy + dz*dz);
}

sdx = coscl * cosln * dx + coscl * sinln * dy - sincl * dz;
sdy = -sinln * dx + cosln * dy;
sdz = sincl * cosln * dx + sincl * sinln * dy + coscl * dz;

cosx = sdx / distance;
cosy = sdy / distance;
cosz = sdz / distance;

ae->azimuth = dtr * atan2(cosy, -cosx);
if (cosz < -1.0) cosz = -1.0;
if (cosz > 1.0) cosz = 1.0;
ae->elevation = 90.0 - dtr * acos(cosz);
ae->range = distance / 1000.0;
}

//calculates the tau-tec
//Written by Richard Moser
void tau(double pseudoRangeL1, double pseudoRangeL2, double *tauTec) {
    double delta_t = (pseudoRangeL2 - pseudoRangeL1); /* meters */
    /* convert to nanoseconds */
    delta_t /= (C / NANOSECS_PER_SEC);
    *tauTec = 2.853 * delta_t;
}

//calculates the pha-tec

```

```

//Written by Richard Moser
void pha(double phaseL1, double phaseL2, double *phaTec) {
    /* there is another calc for this in the fortran code */
    /* may want to verify which calc to use and find out */
    /* what the numbers below represent */
    *phaTec = 2.853 * (phaseL1 / 1.57542 - phaseL2 / 1.2276);
}
};
/* Header labels */

#include<math.h>
#include<unistd.h>

#define RINEX_VERSION_TYPE "RINEX VERSION / TYPE"
#define ANTENNA_DELTA      "ANTENNA: DELTA H/E/N"
#define END_OF_HEADER      "END OF HEADER   "
#define INTERVAL           "INTERVAL   "
#define POSITION_XYZ        "APPROX POSITION XYZ "
#define TIME_OF_1ST_OBS    "TIME OF FIRST OBS  "
#define TIME_OF_LST_OBS    "TIME OF LAST OBS   "
#define OBSERVATION_TYPE   "# / TYPES OF OBSERV "
#define MARKER_NAME        "MARKER NAME "
#define WAVELENGTH_FACT    "WAVELENGTH FACT L1/2"

#define MAX_NAV_BLOCKS     20 /* maximum number of navigation data blocks */
                                /* per satellite */
#define MAX_SATELLITES     35

#define BROADCAST_ORBIT_FORMAT "%*3c%19lg%19lf%19lg%19lf"

#define WEEK               604800      /* total seconds in a week */
#define HALFWEEK           302400      /* total seconds in 1/2 week */

#define OMEGA_DOT_E        7.2921151467E-5
#define C                  2.99792458e+8 /* speed of light (m/s) */
#define F                  4.442807633E-10
#define MU                 3.986008E+14
#define PI                 3.141592653589793
#define NANOSECS_PER_SEC  1.0e+9

#define INDEX_IODE         0
#define INDEX_CRS          1
#define INDEX_DELTA_N      2
#define INDEX_M0           3
#define INDEX_CUC          4
#define INDEX_ECC          5
#define INDEX_CUS          6
#define INDEX_SQRT_A       7
#define INDEX_TOE          8
#define INDEX_CIC          9
#define INDEX_OMEGA0       10
#define INDEX_CIS          11
#define INDEX_I0           12
#define INDEX_CRC          13
#define INDEX_AOP          14
#define INDEX_OMEGA_DOT    15

```



#define INDEX\_I\_DOT 16

//The classes that follow are only used as data storage devices

```
class Epoch
{
public:
    int year;                /* 4-digit year format I6 */
    int month;               /* month format I6 */
    int day;                 /* day format I6 */
    int hour;                /* hour format I6 */
    int minute;              /* minute format I6 */
    double seconds;          /* seconds format F12.6 */
};

class RinexHeader
{
public:
    double posx;              /* format F14.4 */
    double posy;              /* format F14.4 */
    double posz;              /* format F14.4 */
    char markerName[61];      /* Name of antenna marker format A60 */

    double anth;              /* Antenna height: Height of bottom surface */
                                /* of antenna above marker format (m) F14.4 */
    double ante;              /* Eccentricities of antenna center relative*/
                                /* to marker to the east (m) format F14.4 */
    double antn;              /* Eccentricities of antenna center relative*/
                                /* to marker to the north (m) format F14.4 */

    int interval;             /* Observational interval (seconds) format I6 */
    int wfl1;                 /* Wavelength factor L1 format I6 */
    int wfl2;                 /* Wavelength factor L2 format I6 */
    int numSV;                /* Number of satellites format I6 */
    Epoch firstObs;
    Epoch lastObs;

    int numberOfObsTypes;     /* Number of different observation types */
    char obsTypes[9][3];      /* types of observations */
};

class ClockData
{
public:
    double bias;              /*sv clock bias (seconds) format I19.12*/
    double drift;              /*sv clock drift (sec/sec) format I19.12*/
    double driftRate;         /*sv clock drift rate (sec/sec2)*/
};

class NavigationBlock
{
public:
    int satPRN;                /*satellite id*/
    double bcData[28];         /*broadcast orbit data*/
    double testTime;           /*derived time*/
    Epoch epoch;               /*time of data*/
};
```

```

    ClockData clock;           /*clock info*/
};

class SatelliteData
{
public:
    int satPRN;                //PRN number
    int totalBlocks;
    NavigationBlock nd[MAX_NAV_BLOCKS];
};

class Ou
{
public:
    double data;
    char los;                  //loss of signal
    char sigStr;               //signal strength
};

class SatelliteObsData
{
public:
    int satellitePRN;
    Ou ou[9];
};

class ObservationBlock
{
public:
    Epoch epoch;
    int numSatellites;
    int satellitePRNs[20];
    SatelliteObsData sod[20];
};

class GpsTime
{
public:
    int numDays;               /*number of days since Jan. 5-6 1980*/
    int week;                  /*gps week number*/
    int dayOfWeek;             /*gps day number*/
    int numLeapYrs;            /*number of leap years since 1980*/
    long seconds;              /*seconds into the gps week*/
};

class AltAz
{
public:
    double azimuth;
    double elevation;
    double range;
};

class XYZ
{
public:

```

```
double x;  
double y;  
double z;  
};  
  
class SV_struct  
{  
public:  
double rel;  
double iode;  
XYZ pos;  
};
```

## **The daemon**

The job of the daemon is to handle any incoming files from GBSS running on the PC. Between files the daemon goes into a sleeping idle loop in order to relieve the CPU. Approximately every second the daemon checks the contents of a specified directory looking for files that begin with the receivers prefix and end with either a “N” or a “O”. Upon finding such a file the daemon calls gtfFileconverter which stores the data into data.gtf. The ionosphere model is then applied to the data on five-minute boundaries. However the data is moved from the PC to the workstation on nine-minute boundaries. Thus the daemon is responsible for holding on to excess data for later use. After the model has been calculated the model parameters and the GTF file is stored into the gpsData directory.

```

#include<stdio.h>
#include<unistd.h>
#include<string.h>
#include "Modeler.cc"

main()
{
    char command[80];
    char dataFile[50];
    char navigationFileName[50];
    char observationFileName[50];
    char observationCommand[50];
    char navigationCommand[50];
    int day, year;
    FILE *fp;

    Modeler model;

    /*loop forever*/
    while(1)
    {
        while(1)      /*wait for file to appear*/
        {
            for(int i=0; i<50; i++)
            {
                dataFile[i] = '\0';
                navigationFileName[i] = '\0';
                observationFileName[i] = '\0';
                navigationCommand[i] = '\0';
                observationCommand[i] = '\0';
            }
            for(int i=0; i<80; i++)
                command[i] = '\0';

            //list all files that match AOC*N and put them into tempFile
            //note that this needs to be changed if changing the file name
            system("rm tempFile 2> /dev/null");
            system("ls /home/filehost/bjones/AOC*N > tempFile 2> /dev/null");
            fp = fopen("tempFile", "r+");
            fscanf(fp, "%s", navigationFileName); //get information out of tempFile
            fclose(fp);

            //same for AOC*O
            system("rm tempFile");
            system("ls /home/filehost/bjones/AOC*O > tempFile 2> /dev/null");
            fp = fopen("tempFile", "r+");
            fscanf(fp, "%s", observationFileName);
            fclose(fp);

            if(strlen(navigationFileName) != 0) //check if it found any files
            {
                navigationFileName[33] = '\0';
                sprintf(command, "gtfFileConverter %s", navigationFileName);
                printf("%s\n", command);
                navigationFileName[33] = 'N';
                sleep(5);           //wait for ftp to finish
            }
        }
    }
}

```

```

        system(command);                //call gtfFileConverter

        fp = fopen("data.gtf","r+"); //results stored in data.gtf
        if(fp == 0)
        {
            printf("could not open data.gtf\n");
            break;
        }

        fscanf(fp,"%d",&year);
        fscanf(fp,"%d",&day);
        fclose(fp);

        //make sure file exists
        sprintf(dataFile,"gpsData/gpsData_%d_%d.dat",day,year);
        fp=fopen(dataFile,"r+");
        if(fp == 0)
        {
            fp=fopen(dataFile,"w");
        }
        fclose(fp);

        //archive gtf data
        sprintf(command,"cat %s data.gtf > tempFile\0",dataFile);
        system(command);
        sprintf(command,"mv tempFile %s\0",dataFile);
        system(command);

        //apply Ionosphere model
        model.readFile("data.gtf");
        model.applyModel();

        system("rm data.gtf");
        break;
    }

    usleep(250000);    /*pause to relieve CPU*/
}

//erase RINEX files
sprintf(observationCommand,"rm %s",observationFileName);
sprintf(navigationCommand,"rm %s",navigationFileName);
system(observationCommand);
system(navigationCommand);
}
}

//-----

#include<stdio.h>
#include<math.h>
#include<stdlib.h>
#include "rinex.h"
#include "GtfFileInterpreter.cc"
#include "AltAzInterpreter.cc"

```

```

#include "IonosphereModel.cc"

class Modeler
{
public:
Modeler() //constructor
{
    numPoints = 0;
    numData = 0;
    cutOff = 0;
    start = 0;
    deltaT = 0.00347;      //5 minutes

    for(int i=0; i<30; i++) //insure everything zero
    {
        data[0][i] = 0.0;
        data[1][i] = 0.0;
        data[2][i] = 0.0;
        data[3][i] = 0.0;
        data[4][i] = 0.0;
    }

    for(int i=0; i<500; i++)
    {
        data_list[0][i] = 0.0;
        data_list[1][i] = 0.0;
        data_list[2][i] = 0.0;
        data_list[3][i] = 0.0;
        data_list[4][i] = 0.0;
    }

    //these are the satellite offsets
    offset[0] = 0.0;
    offset[1] = 0.738 * 2.853;
    offset[2] = 1.678 * 2.853;
    offset[3] = -0.714 * 2.853;
    offset[4] = -0.813 * 2.853;
    offset[5] = 0.148 * 2.853;
    offset[6] = -1.077 * 2.853;
    offset[7] = 1.89 * 2.853;
    offset[8] = -0.274 * 2.853;
    offset[9] = -0.582 * 2.853;
    offset[10] = 1.693 * 2.853;
    offset[11] = 0.0;
    offset[12] = 0.0;
    offset[13] = -5.137 * 2.853;
    offset[14] = 1.389 * 2.853;
    offset[15] = 1.1 * 2.853;
    offset[16] = 2.413 * 2.853;
    offset[17] = 1.1 * 2.853;
    offset[18] = -0.937 * 2.853;
    offset[19] = 0.321 * 2.853;
    offset[20] = 0.0;
    offset[21] = 1.506 * 2.853;
    offset[22] = 0.269 * 2.853;
    offset[23] = 1.554 * 2.853;

```

```

offset[24] = 2.056 * 2.853;
offset[25] = -1.646 * 2.853;
offset[26] = -1.434 * 2.853;
offset[27] = -0.055 * 2.853;
offset[28] = 0.0;
offset[29] = -1.494 * 2.853;
offset[30] = -2.238 * 2.853;
offset[31] = -1.449 * 2.853;
offset[32] = 0.0;
}

void readFile(char *fileName)
{
    int prn, i;
    double alt, azi, dLat, dLong, tau_tec;
    Epoch epoch;

    GtfFileInterpreter gtfInterpreter(fileName);
    //gtfInterpreter.readHeader(); no header in archives
    i=0;

    for(int a=start; a<500; a++)
    {
        data_list[0][a] = 0.0;
        data_list[1][a] = 0.0;
        data_list[2][a] = 0.0;
        data_list[3][a] = 0.0;
        data_list[4][a] = 0.0;
    }

    //read the whole file into memory
    while(gtfInterpreter.readObservation(&tau_tec, &azi, &alt, &epoch,&prn) == 1)
    {
        if(alt == -1 || azi == -1 || tau_tec == -1) //check to see if bad data
            continue;

        AltAzInterpreter interpreter(alt, azi);
        interpreter.getOffsets(&dLat, &dLong); //convert to lat and long offsets

        data_list[0][start+i] += dLat;
        data_list[1][start+i] += dLong;
        data_list[2][start+i] += (tau_tec-13.3-offset[(int)prn])*secant((PI/180)*alt);//13.3 is reciever offset
        data_list[3][start+i] = (double)prn;

        double time = (double)epoch.day +
            (double)epoch.hour/24 +
            (double)epoch.minute/(24*60) +
            epoch.seconds/(24*60*60);

        data_list[4][start+i] = time; //store the time

        i++;
    }

    year = epoch.year;

```



```

numData = start+i;

gtfInterpreter.closeFile(); //close file
}

void applyModel()
{
    int flag=0;
    double time = data_list[4][0];
    cutOff = 0;

    for(int i=0; i<numData; i++) //figure out where time cutoff is
    {
        if(data_list[4][i] > time + deltaT)
        {
            cutOff = i;
            flag=1;
            break;
        }
    }

    start = numData-cutOff;           //set start for next time around

    if(flag==0)                       //for recursion
        return;

    numPoints = 0;

    for(int i=0; i<30; i++)
    {
        data[0][i] = 0.0;
        data[1][i] = 0.0;
        data[2][i] = 0.0;
        data[3][i] = 0.0;
        data[4][i] = 0.0;
    }

    for(int i=0; i<cutOff; i++) //put data into data[]
    {
        for(int a=0; a<30; a++)
        {
            if(data[3][a] != 0.0 && data[3][a] != data_list[3][i])
                continue;

            data[0][a] += data_list[0][i];    //dlat
            data[1][a] += data_list[1][i];    //dlong
            data[2][a] += data_list[2][i];    //tec
            data[3][a] = data_list[3][i];     //prn
            data[4][a] += 1;                  //count;
            a=30;                             //stop looping
        }
    }

    for(int i=0; i<30; i++) //figure out how many data points
    {
        if(data[0][i] == 0.0)

```

```

    {
        numPoints = i;
        break;
    }
}

for(int i=0; i<numPoints; i++)    //average data
{
    data[0][i] /= data[4][i];
    data[1][i] /= data[4][i];
    data[2][i] /= data[4][i];
}

for(int i=0; i<numPoints; i++)    //calculate standard deviation
{
    int count=0;
    for(int a=0; a<cutOff; a++)
    {
        if(data[3][i] == data_list[3][a])
        {
            data[4][i] += fabs(data[2][i]-data_list[2][a]);
            count++;
        }
    }
    data[4][i] /= count;
}

ionModel.calculateGradient(data,numPoints); //calculate gradient

FILE *fp1,*fp2,*fp3,*fp4;
char name[60];

//open model pararameter archive files
sprintf(name,"gpsData/zenith%d.dat",year);
fp1=fopen(name,"r+");
sprintf(name,"gpsData/direction%d.dat",year);
fp2=fopen(name,"r+");
sprintf(name,"gpsData/accuracy%d.dat",year);
fp3=fopen(name,"r+");
sprintf(name,"gpsData/magnitude%d.dat",year);
fp4=fopen(name,"r+");

//ensure they exist
if(fp1==NULL)
{
    sprintf(name,"gpsData/zenith%d.dat",year);
    fp1=fopen(name,"w");
}

if(fp2 == NULL)
{
    sprintf(name,"gpsData/direction%d.dat",year);
    fp2=fopen(name,"w");
}

if(fp3 == NULL)

```

```

{
    sprintf(name,"gpsData/accuracy%d.dat",year);
    fp3=fopen(name,"w");
}

if(fp4 == NULL)
{
    sprintf(name,"gpsData/magnitude%d.dat",year);
    fp4=fopen(name,"w");
}

fseek(fp1,0,SEEK_END);
fseek(fp2,0,SEEK_END);
fseek(fp3,0,SEEK_END);
fseek(fp4,0,SEEK_END);

fprintf(fp1,"%f %f\n",data_list[4][0],ionModel.getZenithTEC());
fprintf(fp2,"%f %f\n",data_list[4][0],ionModel.getDirection());
fprintf(fp3,"%f %f\n",data_list[4][0],ionModel.getAccuracy());
fprintf(fp4,"%f %f\n",data_list[4][0],ionModel.getMagnitude());

fclose(fp1);
fclose(fp2);
fclose(fp3);
fclose(fp4);

for(int i=cutOff, index=0; i<numData; i++, index++) //shift everything down
{
    data_list[0][index] = data_list[0][i];
    data_list[1][index] = data_list[1][i];
    data_list[2][index] = data_list[2][i];
    data_list[3][index] = data_list[3][i];
    data_list[4][index] = data_list[4][i];
}

numData -= cutOff;
applyModel(); //call again to process further
}

private:
double secant(double alt) //calculates the effects of looking through the atmosphere
{
    double M = tan(alt);
    double D = 6371; //radius of earth

    double a = M*M + 1;
    double b = 2*D*M;
    double c = D*D - (575+D)*(575+D);

    double x1 = (-b+sqrt(b*b - 4*a*c))/(2*a);
    double y1 = M*x1 + D;

    c = D*D - (400+D)*(400+D);
    double x2 = (-b+sqrt(b*b - 4*a*c))/(2*a);
    double y2 = M*x2 + D;

```

```

double s = 175/sqrt((x2-x1)*(x2-x1) + (y2-y1)*(y2-y1));
return s;
}

```

```

int start, numData, numPoints, cutOff;
int year;
IonosphereModel ionModel;
double data[5][30], data_list[5][500];
double deltaT;
double offset[33];
};

```

```

//-----

```

```

class IonosphereModel
{
public:
    calculateGradient(double tempData[5][30], int points)
    {
        numPoints = points;
        lat_gradient = 0;
        long_gradient = 0;
        zenithTEC = 40;
        minimum = 100000000;

        //move data to class variable
        for(int i=0; i<numPoints; i++)
        {
            data[0][i] = tempData[0][i]; //dlat
            data[1][i] = tempData[1][i]; //dlong
            data[2][i] = tempData[2][i]; //tec
            data[3][i] = tempData[4][i]; //standard deviations
        }

        recursive_search(); //do gradient search
    }

    double getZenithTEC()
    {
        return zenithTEC;
    }

    double getDirection()
    {
        double temp = atan2(long_gradient,lat_gradient);
        if(temp < 0)
            temp += 2*PI;
        temp *= (180/PI);
        return temp;
    }

    double getAccuracy()
    {
        double diff = 0.0;
        for(int i=0; i<numPoints; i++)

```

```

    {
        diff+= pow(data[2][i] - (lat_gradient*data[0][i] + long_gradient*data[1][i] + zenithTEC),2);
    }
    return diff;
}

double getMagnitude()
{
    return sqrt(lat_gradient*lat_gradient + long_gradient*long_gradient);
}

//calculates TEC for random direction. Currently not used.
double calculateTEC(double alt, double azi)
{
    double dLat, dLong;
    AltAzInterpreter interpreter(alt, azi);
    interpreter.getOffsets(&dLat, &dLong);

    return lat_gradient*dLat + long_gradient*dLong + zenithTEC;
}

private:

void recursive_search()
{
    double tempDlat=0, tempDlon=0, tempDzen=0, delta=0.5;
    double tempMin=calculateDifference(lat_gradient, long_gradient, zenithTEC);

    if(getAccuracy() < 500)
        delta = 0.1;

    //check all 27 different directions for search
    for(double dlat=-1*delta; dlat<=delta; dlat+=delta)
    {
        for(double dlon=-1*delta; dlon<=delta; dlon+=delta)
        {
            for(double dzen=-1*delta; dzen<=delta; dzen+=delta)
            {
                double diff;
                if((diff=calculateDifference(lat_gradient+dlat, long_gradient+dlon, zenithTEC+dzen)) < tempMin)
                { //record smallest difference
                    tempDlat = dlat;
                    tempDlon = dlon;
                    tempDzen = dzen;
                    tempMin = diff;
                }
            }
        }
    }
    //add changes
    lat_gradient += tempDlat;
    long_gradient += tempDlon;
    zenithTEC += tempDzen;
    if(tempMin < minimum && tempMin > 0) //loop again if found a better solution
    {
        minimum = tempMin;
    }
}

```

```

    recursive_search();
}
}

//helper function to calculate difference between model and data
double calculateDifference(double lat, double lon, double zen)
{
    double diff = 0.0;
    for(int i=0; i<numPoints; i++)
    {
        double sigma = 1/(data[3][i] * data[3][i]);
        diff+=sigma * pow(data[2][i] - (lat*data[0][i] + lon*data[1][i] + zen),2);
    }
    return diff;
}

double zenithTEC;
double magnitude;
double lat_gradient;
double long_gradient;
double data[4][20];
int numPoints;
double minimum;
};

```

## **Ionosphere Monitor**

Ionosphere Monitor is a JAVA based graphical program that allows an observer easy access to the archived GPS data. When given specified starting and ending times in IAT, Ionosphere Monitor retrieves the appropriate data from the archive and displays the model parameters to the screen. The user is then given the option to write either the model parameters or the raw GTF data to a file. The files are named according to the receiver name and the times specified for retrieval.

Another option given by Ionosphere Monitor is to display the last week's worth of data. With this option Ionosphere Monitor automatically updates itself every ten minutes.

No Name

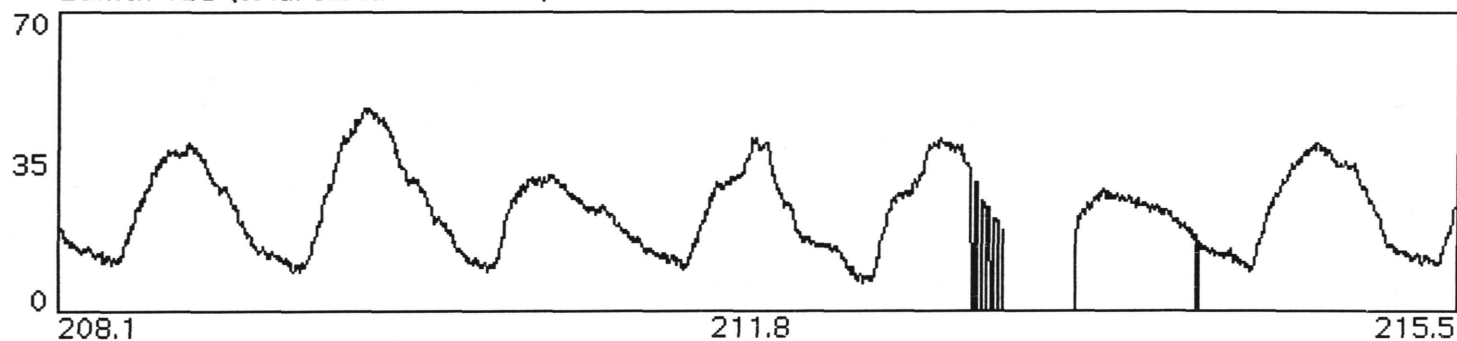
File Mode

from: Year 1999 July Day 28 Hour 3 Minute 56

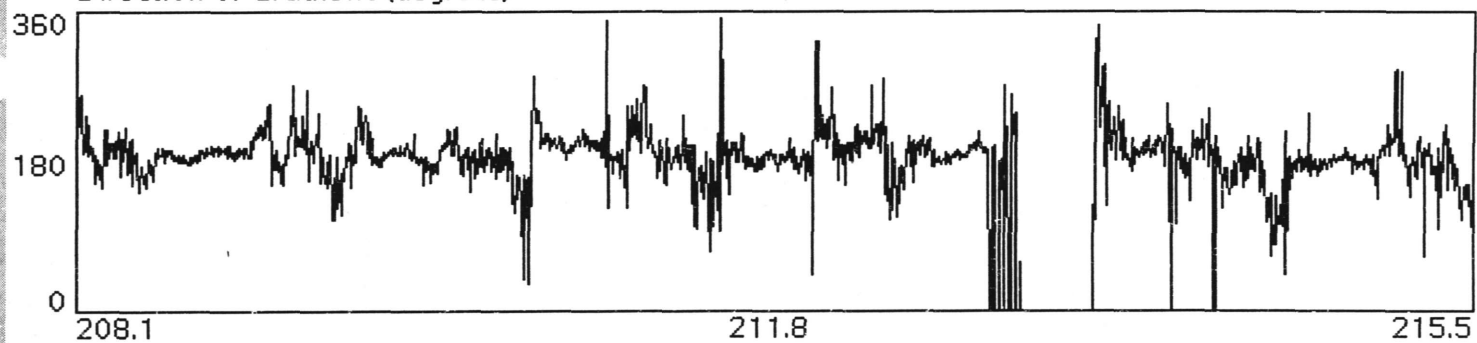
to: Year 1999 August Day 4 Hour 14 Minute 16

Retrieve Info

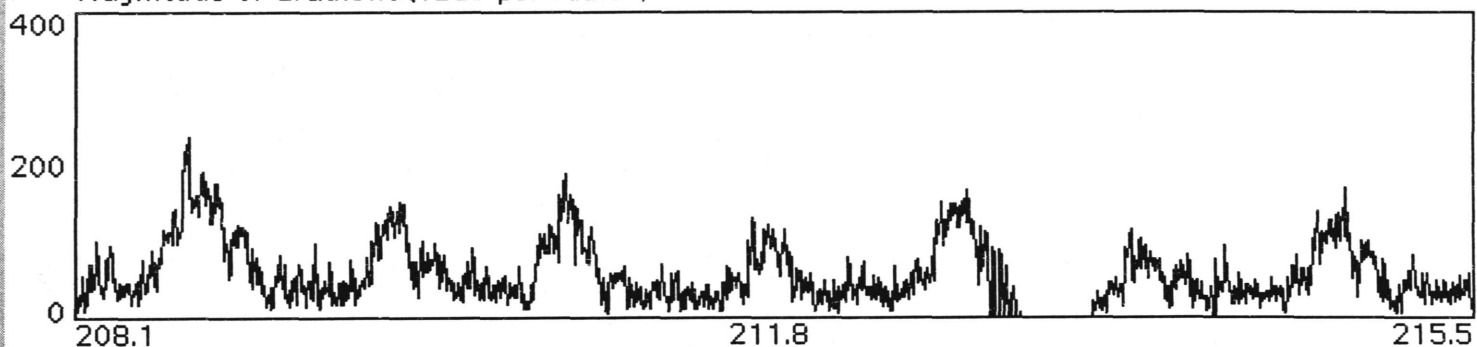
Zenith TEC (total electron content)



Direction of Gradient (degrees)



Magnitude of Gradient (TECs per radian)

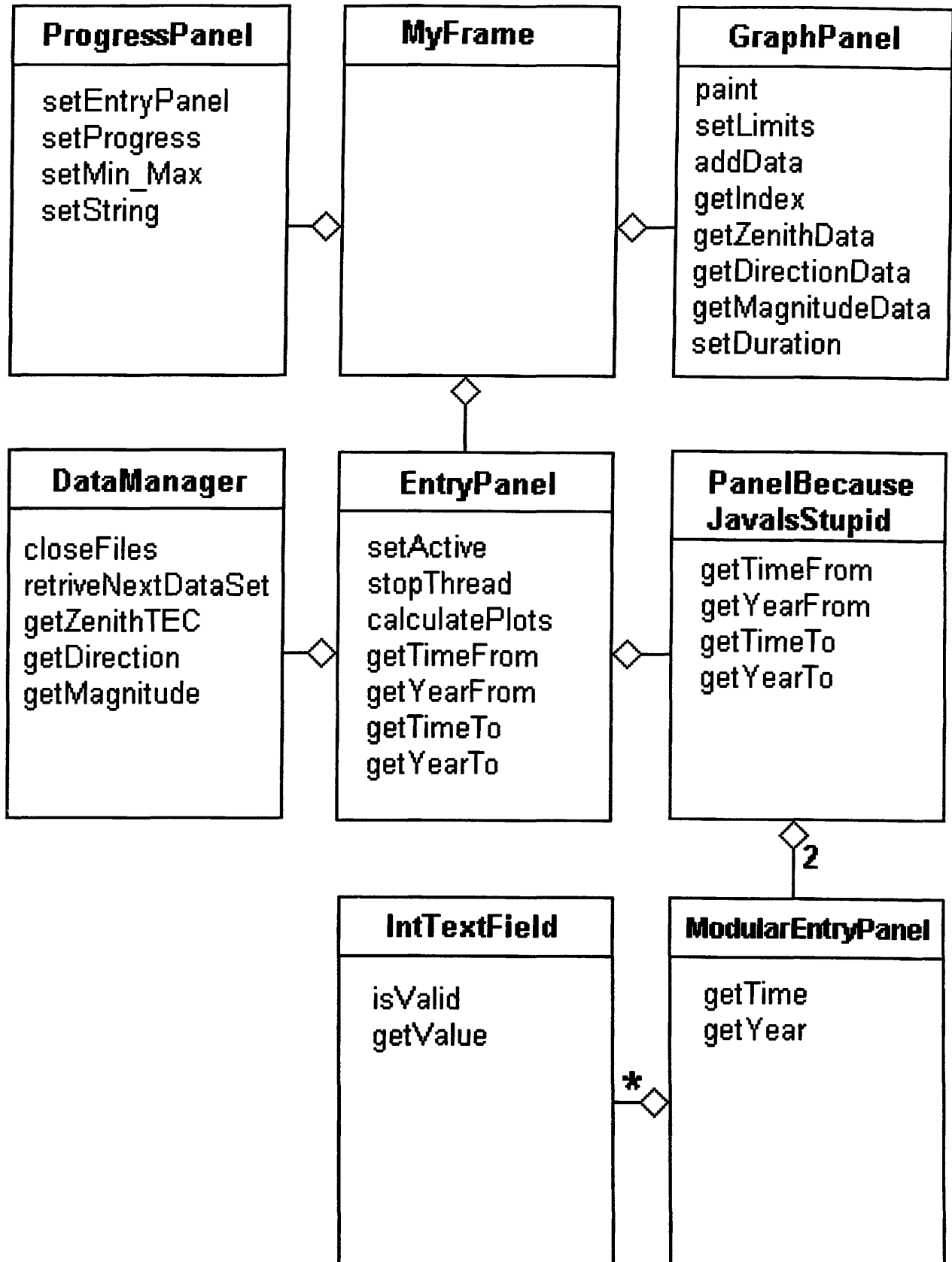


100%

Cancel



# UML Diagram



```

import java.awt.*;
import java.awt.event.*;
import java.util.*;
import javax.swing.*;

//panel for displaying data
class GraphPanel extends JPanel
{
    public GraphPanel() //constructor
    {
        super();
        index = 0;
        duration = 0;
        timeFrom = 0;
        timeTo = 0;
        zenithData = new double[10000]; //10000 max number of data points
        directionData = new double[10000];
        magnitudeData = new double[10000];
    }

    public void paint(Graphics g) //paints the drawing area
    {
        super.paint(g);
        setBackground(Color.white);
        drawBoxes(g);
        plotData(g);
    }

    public void setLimits(double timefrom, double timeto)
    {
        timeFrom = timefrom;
        timeTo = timeto;
    }

    public void addData(double zenith, double direction, double magnitude)
    {
        zenithData[index] = zenith;
        directionData[index] = direction;
        magnitudeData[index] = magnitude;
        index++;
    }

    public int getIndex()
    {
        return index;
    }

    public double[] getZenithData()
    {
        return zenithData;
    }

    public double[] getDirectionData()
    {
        return directionData;
    }
}

```

```

public double[] getMagnitudeData()
{
    return magnitudeData;
}

public void setDuration(double d)
{
    duration = Math.floor(d/0.0034722)-1;
}

public void resetIndex()
{
    index = 0;
}

private void drawBoxes(Graphics g)    //draws the boxes for the graphs
{
    int width = getWidth();
    int height = getHeight();
    String string;

    g.drawString("Zenith TEC (total electron content)",30, 15);
    g.drawString("Direction of Gradient (degrees)",30, 35+(int)((height-70)/3));
    g.drawString("Magnitude of Gradient (TECs per radian)",30, 55+2*(int)((height-70)/3));

    g.drawLine(30,20,
               width-10,20);
    g.drawLine(30,20+(int)((height-70)/3)-12,
               width-10,20+(int)((height-70)/3)-12);
    g.drawLine(30,20,
               30,20+(int)((height-70)/3)-12);
    g.drawLine(width-10,20,
               width-10,20+(int)((height-70)/3)-12);

    g.drawString("70",10,30);
    g.drawString("35",10,20+(int)((height-70)/6));
    g.drawString("0",18,20+(int)((height-70)/3)-12);

    if(timeFrom != 0 && timeTo != 0)
    {
        string = ""+timeFrom;
        g.drawString(string.substring(0,5),30,20+(int)((height-70)/3));
        if(timeFrom > timeTo)
        {
            string = ""+(timeTo+timeFrom+360)/2;
            g.drawString(string.substring(0,5),(int)(width/2)-10,20+(int)((height-70)/3));
        }
        else
        {
            string = ""+(timeTo+timeFrom)/2;
            g.drawString(string.substring(0,5),(int)(width/2)-10,20+(int)((height-70)/3));
        }
        string = ""+timeTo;
        g.drawString(string.substring(0,5),width-45,20+(int)((height-70)/3));
    }
}

```

```

g.drawLine(30,40+(int)((height-70)/3),
           width-10,40+(int)((height-70)/3));
g.drawLine(30,40+2*(int)((height-70)/3)-12,
           width-10,40+2*(int)((height-70)/3)-12);
g.drawLine(30,40+(int)((height-70)/3),
           30,40+2*(int)((height-70)/3)-12);
g.drawLine(width-10,40+(int)((height-70)/3),
           width-10,40+2*(int)((height-70)/3)-12);

g.drawString("360",2,40+10+(int)((height-70)/3));
g.drawString("180",2,40+(int)((height-70)/3)+(int)((height-70)/6));
g.drawString("0",18,40+2*(int)((height-70)/3)-12);

if(timeFrom != 0 && timeTo != 0)
{
    string = ""+timeFrom;
    g.drawString(string.substring(0,5),30,40+2*(int)((height-70)/3));
    if(timeFrom > timeTo)
    {
        string = ""+(timeTo+timeFrom+360)/2;
        g.drawString(string.substring(0,5),(int)(width/2)-10,40+2*(int)((height-70)/3));
    }
    else
    {
        string = ""+(timeTo+timeFrom)/2;
        g.drawString(string.substring(0,5),(int)(width/2)-10,40+2*(int)((height-70)/3));
    }
    string = ""+timeTo;
    g.drawString(string.substring(0,5),width-45,40+2*(int)((height-70)/3));
}

g.drawLine(30,60+2*(int)((height-70)/3),
           width-10,60+2*(int)((height-70)/3));
g.drawLine(30,height-10-12,
           width-10,height-10-12);
g.drawLine(30,60+2*(int)((height-70)/3),
           30,height-10-12);
g.drawLine(width-10,60+2*(int)((height-70)/3),
           width-10,height-10-12);

g.drawString("400",2,60+10+2*(int)((height-70)/3));
g.drawString("200",2,60+2*(int)((height-70)/3)+(int)((height-70)/6));
g.drawString("0",18,height-10-10);

if(timeFrom != 0 && timeTo != 0)
{
    string = ""+timeFrom;
    g.drawString(string.substring(0,5),30,height-10);
    if(timeFrom > timeTo)
    {
        string = ""+(timeTo+timeFrom+360)/2;
        g.drawString(string.substring(0,5),(int)(width/2)-10,height-10);
    }
    else
    {

```

```

        string = ""+(timeTo+timeFrom)/2;
        g.drawString(string.substring(0,5),(int)(width/2)-10,height-10);
    }
    string = ""+timeTo;
    g.drawString(string.substring(0,5),width-45,height-10);
}

private void plotData(Graphics g) //graphs the points on the graphs
{
    int width = getWidth();
    int height = getHeight();
    int boxHeight = (int)((height-70)/3);
    int boxWidth = width-40;
    //draw zenith data
    for(int i=0; i<index-1; i++)
        g.drawLine((int)((i/duration)*(boxWidth)+30), (int)(20+boxHeight-12 - (zenithData[i]/70)*(boxHeight-12)),
            (int)((i+1)/duration)*(boxWidth)+30,(int)(20+boxHeight-12 - (zenithData[i+1]/70)*(boxHeight-12)));

    //draw direction
    for(int i=0; i<index-1; i++)
        g.drawLine((int)((i/duration)*(boxWidth)+30), (int)(40+2*boxHeight-12 - (directionData[i]/360)*(boxHeight-12)),
            (int)((i+1)/duration)*(boxWidth)+30,(int)(40+2*boxHeight-12 - (directionData[i+1]/360)*(boxHeight-12)));

    //draw magnitude data
    for(int i=0; i<index-1; i++)
    {
        if(magnitudeData[i+1] > 400)
            magnitudeData[i+1] = 400;

        g.drawLine((int)((i/duration)*(boxWidth)+30), (int)(height-10-12 - (magnitudeData[i]/400)*(boxHeight-12)),
            (int)((i+1)/duration)*(boxWidth)+30,(int)(height-10-12 - (magnitudeData[i+1]/400)*(boxHeight-12)));
    }
}

private int index;
private double duration;
private double timeFrom, timeTo;
private double[] zenithData;
private double[] directionData;
private double[] magnitudeData;
}

//panel for data entry
class EntryPanel extends JPanel implements ActionListener
{
    public EntryPanel(GraphPanel g, ProgressPanel p)
    {
        graph = g;
        progress = p;
        active = true;

        stupidPanel = new PanelBecauseJavaIsStupid();
        retrieve = new JButton("Retrieve Info");
        retrieve.addActionListener(this);
    }
}

```

```

setLayout(new BorderLayout());

add(BorderLayout.CENTER,stupidPanel);
add(BorderLayout.EAST,retrieve);
}

public void setActive(boolean value)    //disabled for monitor mode
{
    active = value;
}

class myThread extends Thread
{
    public void run()
    {
        calculatePlots();
    }
}

public void stopThread() //stops the thread
{
    stop = true;
}

public void actionPerformed(ActionEvent evt)
{
    if(!active)
        return;
    stop = false;
    (thread = new myThread()).start();
}

public void calculatePlots()    //gets the data from the files
{
    double yearFrom, yearTo, timeFrom, timeTo;
    int count = 0, COUNT = 0;
    int check=0;

    timeFrom = stupidPanel.getTimeFrom();
    timeTo = stupidPanel.getTimeTo();

    yearFrom = stupidPanel.getYearFrom();
    yearTo = stupidPanel.getYearTo();

    if((timeFrom < 194 && yearFrom == 1999) || yearFrom < 1999)
    {
        JOptionPane.showConfirmDialog(this,"The time specified is before the birth of this system",
                                      "error",JOptionPane.CANCEL_OPTION,JOptionPane.ERROR_MESSAGE);
        return;
    }

    if(yearFrom > yearTo)
        return;

    if(timeFrom > timeTo && yearTo <= yearFrom)
        return;
}

```

```

count = (int)((timeTo-timeFrom)/0.0034722);
COUNT = (int)((timeTo-timeFrom)/0.0034722);

graph.setDuration(timeTo - timeFrom);
graph.resetIndex();

DataManager manager = new DataManager(timeFrom,timeTo,yearFrom,yearTo);

progress.setMin_Max(0,count);

graph.setLimits(timeFrom,timeTo);

while(true)
{
    count--;
    check = manager.retrieveNextDataSet();

    if(check == -1)
    {
        //data missing. fill with zeros
        graph.addData(0,0,0);
    }
    else
    {
        graph.addData(manager.getZenithTEC(), manager.getDirection(), manager.getMagnitude());
    }

    progress.setProgress(COUNT - count);

    graph.repaint();

    if(check == 0 || count <= 0 || stop)
    {
        manager.closeFiles();
        break;
    }
}

public double getTimeFrom()
{
    return stupidPanel.getTimeFrom();
}

public double getTimeTo()
{
    return stupidPanel.getTimeTo();
}

public int getYearFrom()
{
    return (int)(stupidPanel.getYearFrom());
}

public int getYearTo()
{

```

```

    return (int)(stupidPanel.getYearTo());
}

private boolean stop;
private boolean active;
private Thread thread;
private ProgressPanel progress;
private GraphPanel graph;
private PanelBecauseJavaIsStupid stupidPanel;
private JButton retrieve;
}

class ProgressPanel extends JPanel implements ActionListener
{
    public ProgressPanel()
    {
        monitor = new JProgressBar();
        monitor.setStringPainted(true);
        cancel = new JButton("Cancel");
        cancel.addActionListener(this);

        setLayout(new BorderLayout());

        add(BorderLayout.CENTER,monitor);
        add(BorderLayout.EAST,cancel);
    }

    public void actionPerformed(ActionEvent evt)
    {
        entryPanel.stopThread();
    }

    public void setEntryPanel(EntryPanel e)
    {
        entryPanel = e;
    }

    public void setProgress(int value)
    {
        monitor.setValue(value);
    }

    public void setMin_Max(int min, int max)
    {
        monitor.setMinimum(min);
        monitor.setMaximum(max);
    }

    public void setString(String s)
    {
        monitor.setString(s);
    }

    private EntryPanel entryPanel;
    private JProgressBar monitor;
    private JButton cancel;

```



```

}

class PanelBecauseJavaIsStupid extends JPanel
{
    public PanelBecauseJavaIsStupid()
    {
        top = new ModularEntryPanel("from: ");
        bottom = new ModularEntryPanel(" to: ");

        setLayout(new BorderLayout());

        add(BorderLayout.NORTH,top);
        add(BorderLayout.SOUTH,bottom);
    }

    public double getTimeFrom()
    {
        return top.getTime();
    }

    public double getTimeTo()
    {
        return bottom.getTime();
    }

    public double getYearFrom()
    {
        return top.getYear();
    }

    public double getYearTo()
    {
        return bottom.getYear();
    }

    private ModularEntryPanel top;
    private ModularEntryPanel bottom;
}

class ModularEntryPanel extends JPanel    //contains the entry objects
{
    public ModularEntryPanel(String l)
    {
        label = l;
        adjustment = 0;
        year = new IntTextField(1999,4);
        month = new JComboBox();
        month.addItem("January");
        month.addItem("Febuary");
        month.addItem("March");
        month.addItem("April");
        month.addItem("May");
        month.addItem("June");
        month.addItem("July");
        month.addItem("August");
        month.addItem("September");
    }

```

```

month.addItem("October");
month.addItem("November");
month.addItem("December");
day = new IntTextField(10,2);
hour = new IntTextField(0,2);
minute = new IntTextField(0,2);
front_label = new JLabel(label,JLabel.LEFT);
year_label = new JLabel(" Year",JLabel.LEFT);
day_label = new JLabel(" Day",JLabel.LEFT);
hour_label = new JLabel(" Hour",JLabel.LEFT);
minute_label = new JLabel(" Minute",JLabel.LEFT);

add(front_label);
add(year_label);
add(year);
add(month);
add(day_label);
add(day);
add(hour_label);
add(hour);
add(minute_label);
add(minute);
}

public double getTime() //returns the time in decimal days
{
    if(day.isValid() && hour.isValid() && minute.isValid() &&
        day.getValue() < 31 && hour.getValue() < 24 && minute.getValue() < 60
        && day.getValue() > 0)
    {
        double currentDay = 0;
        String choice = (String)month.getSelectedItem();

        if(choice == "January")
            currentDay=0;
        else if(choice == "Febuary")
            currentDay=31;
        else if(choice == "March")
            currentDay=59;
        else if(choice == "April")
            currentDay=90;
        else if(choice == "May")
            currentDay=120;
        else if(choice == "June")
            currentDay=151;
        else if(choice == "July")
            currentDay=181;
        else if(choice == "August")
            currentDay=212;
        else if(choice == "September")
            currentDay=243;
        else if(choice == "October")
            currentDay=273;
        else if(choice == "November")
            currentDay=304;
        else if(choice == "December")

```

```

        currentDay=334;

        if(year.getValue()%4 == 0 && year.getValue() != 2000 && currentDay > 31)
        {
            currentDay++;
        }

        //currentDay+=0.74;
        if(currentDay > 366)
        {
            currentDay%=366;
            adjustment = 1;
        }
        else
            adjustment = 0;
        return currentDay + day.getValue()-1 + (double)hour.getValue()/24 + (double)minute.getValue()/1440;
    }
    else
        return -1;
}

public double getYear()
{
    if(year.isValid())
        return adjustment + year.getValue();
    else
        return -1;
}

private int adjustment;
private IntTextField year;
private JComboBox month;
private IntTextField day;
private IntTextField hour;
private IntTextField minute;
private String label;
private JLabel front_label;
private JLabel year_label;
private JLabel day_label;
private JLabel hour_label;
private JLabel minute_label;
}

class MyFrame extends JFrame implements ActionListener
{
    public MyFrame()
    {
        stop = true;
        setTitle("Ionosphere Monitor");
        setSize(650,650);
        setBackground(Color.white);
        addWindowListener(new WindowAdapter()
        {
            public void windowClosing(WindowEvent e)
            {
                System.exit(0);
            }
        });
    }
}

```

```

    }
});
graph = new GraphPanel();
ProgressPanel progress = new ProgressPanel();
entry = new EntryPanel(graph,progress);
progress.setEntryPanel(entry);
getContentPane().add(BorderLayout.CENTER,graph);
getContentPane().add(BorderLayout.SOUTH,progress);
getContentPane().add(BorderLayout.NORTH,entry);

JMenuBar menuBar = new JMenuBar();
JMenu fileMenu = new JMenu("File");
JMenu modeMenu = new JMenu("Mode");

quitItem = new JMenuItem("quit");
makePlotsItem = new JMenuItem("make plots");
gtfItem = new JMenuItem("make gtf file");

monitorItem = new JCheckBoxMenuItem("monitor");
retrieveItem = new JCheckBoxMenuItem("retrieve");
retrieveItem.setState(true);

quitItem.addActionListener(this);
makePlotsItem.addActionListener(this);
gtfItem.addActionListener(this);

monitorItem.addActionListener(this);
retrieveItem.addActionListener(this);

fileMenu.add(quitItem);
fileMenu.addSeparator();
fileMenu.add(makePlotsItem);
fileMenu.add(gtfItem);

modeMenu.add(monitorItem);
modeMenu.add(retrieveItem);

menuBar.add(fileMenu);
menuBar.add(modeMenu);
setJMenuBar(menuBar);
}

class myThread extends Thread //inner class
{
    public void run()
    {
        waitForData(this);
    }
}

public void waitForData(Thread thread)
{
    while(true)
    {
        if(stop)
            return;
    }
}

```

```

long time = System.currentTimeMillis();
Calendar calendarBecauseJavaIsStupid = new GregorianCalendar();
calendarBecauseJavaIsStupid.setTime(new Date(time));

double timeTo = calendarBecauseJavaIsStupid.get(Calendar.DAY_OF_YEAR) +
                (double)calendarBecauseJavaIsStupid.get(Calendar.HOUR)/24 +
                (double)calendarBecauseJavaIsStupid.get(Calendar.MINUTE)/1440;

timeTo+=0.74;
timeTo%=365;

double timeFrom = timeTo - 7;

double yearTo = calendarBecauseJavaIsStupid.get(Calendar.YEAR);
double yearFrom;
if(timeTo < 7)
    yearFrom = yearTo - 1;
else
    yearFrom = yearTo;

DataManager manager = new DataManager(timeFrom,timeTo,yearFrom,yearTo);

graph.setLimits(timeFrom,timeTo);
if(timeTo > timeFrom)
    graph.setDuration(timeTo - timeFrom);
else
    graph.setDuration(timeTo - timeFrom + 365);
graph.resetIndex();

while(true)
{
    int check = manager.retrieveNextDataSet();

    if(check == -1)
    {
        graph.addData(0,0,0);
    }
    else
    {
        graph.addData(manager.getZenithTEC(), manager.getDirection(), manager.getMagnitude());
    }

    graph.repaint();

    if(check == 0 || stop)
    {
        manager.closeFiles();
        break;
    }
}

for(long i=0; i<600; i++)
{
    try
    {

```

```

        thread.sleep(1000);
    }
    catch(InterruptedException e)
    {}
    if(stop)
        return;
}
}
}

public void actionPerformed(ActionEvent evt) //handles all events
{
    if(evt.getSource() == quitItem)
        System.exit(0);
    else if(evt.getSource() == makePlotsItem && graph.getIndex() > 0)
    {
        PlotFileWriter writer = new PlotFileWriter();
        writer.setDateAndTime(entry.getYearFrom(),entry.getTimeFrom());

        writer.setData(graph.getZenithData(), graph.getIndex());
        writer.setName("zenith");
        writer.makeFile();

        writer.setData(graph.getDirectionData(), graph.getIndex());
        writer.setName("direction");
        writer.makeFile();

        writer.setData(graph.getMagnitudeData(), graph.getIndex());
        writer.setName("magnitude");
        writer.makeFile();
    }
    else if(evt.getSource() == gtfItem)
    {
        GtfFileGenerator writer = new GtfFileGenerator(entry.getTimeFrom(),entry.getTimeTo(),
                                                         entry.getYearFrom(),entry.getYearTo());

        writer.makeGtfFile();
    }
    else if(evt.getSource() == retrieveItem)
    {
        entry.setActive(true);
        retrieveItem.setState(true);
        monitorItem.setState(false);
        stop = true;
    }
    else if(evt.getSource() == monitorItem)
    {
        if(monitorItem.getState() == false)
        {
            monitorItem.setState(true);
            return;
        }
        entry.setActive(false);
        monitorItem.setState(true);
        retrieveItem.setState(false);
        stop = false;
    }
}

```

```

        (thread = new myThread()).start();
    }
}

private boolean stop;
private Thread thread;
private EntryPanel entry;
private GraphPanel graph;
private JMenuItem quitItem;
private JMenuItem makePlotsItem;
private JMenuItem gtfItem;
private JCheckBoxMenuItem monitorItem;
private JCheckBoxMenuItem retrieveItem;
}

//class that usses JTextField to only use integers
class IntTextField extends JTextField
{
    public IntTextField(int defval, int size)
    {
        super("" + defval, size);
    }

    public boolean isValid()
    {
        try
        {
            Integer.parseInt(getText());
            return true;
        }
        catch(NumberFormatException e)
        {
            return false;
        }
    }

    public int getValue()
    {
        try
        {
            return Integer.parseInt(getText());
        }
        catch(NumberFormatException e)
        {
            return 0;
        }
    }
}

public class IonosphereMonitor
{
    public static void main(String args[])
    {
        JFrame f = new MyFrame();
        //f.pack();
        f.setVisible(true);
    }
}

```

```

    }
}
import java.io.*;

//class that deals with retrieving data out of the files
public class DataManager
{
    public DataManager(double timefrom, double timeto, double yearfrom, double yearto)
    {
        timeFrom = timefrom;
        timeTo = timeto;
        yearFrom = yearfrom;
        yearTo = yearto;
        day = (int)timeFrom;
        currentTime = 1000000000;
        wait = 0;

        //initialize the files
        try
        {
            FileReader f = new FileReader("/home/filehost/bjones/gpsData/zenith"+(int)yearFrom+".dat");
            zenithFile = new BufferedReader(f);

            f = new FileReader("/home/filehost/bjones/gpsData/direction"+(int)yearFrom+".dat");
            directionFile = new BufferedReader(f);

            f = new FileReader("/home/filehost/bjones/gpsData/magnitude"+(int)yearFrom+".dat");
            magnitudeFile = new BufferedReader(f);
        }
        catch(FileNotFoundException e)
        {
            System.out.println("Unable to open dat files");
        }
    }

    public void closeFiles()
    {
        try
        {
            zenithFile.close();
            directionFile.close();
            magnitudeFile.close();
        }
        catch(IOException e)
        {}
    }

    public int retrieveNextDataSet()
    {
        if(wait>0)
        {
            wait--;
            return -1;
        }

        String zenithBuffer="0.0 0.0";

```



```

String directionBuffer="0.0 0.0";
String magnitudeBuffer="0.0 0.0";
double time;

do
{
    try
    {
        zenithBuffer = zenithFile.readLine();
        directionBuffer = directionFile.readLine();
        magnitudeBuffer = magnitudeFile.readLine();
    }
    catch(IOException e) //if failed it means at end of file
    {
        if(yearFrom == yearTo)
            return 0;

        yearFrom++;
        try
        {
            FileReader f = new FileReader("/home/filehost/bjones/gpsData/zenith"+(int)yearFrom+".dat");
            zenithFile = new BufferedReader(f);

            f = new FileReader("/home/filehost/bjones/gpsData/direction"+(int)yearFrom+".dat");
            directionFile = new BufferedReader(f);

            f = new FileReader("/home/filehost/bjones/gpsData/magnitude"+(int)yearFrom+".dat");
            magnitudeFile = new BufferedReader(f);
        }
        catch(FileNotFoundException E)
        {
            System.out.println("Unable to open dat files");
            return 0;
        }
    }

    int index = zenithBuffer.indexOf(" ",0)+1;

    time = Double.parseDouble(zenithBuffer.substring(0,index-1));
    zenith = Double.parseDouble(zenithBuffer.substring(index,zenithBuffer.length()));
    direction = Double.parseDouble(directionBuffer.substring(index,directionBuffer.length()));
    magnitude = Double.parseDouble(magnitudeBuffer.substring(index,magnitudeBuffer.length()));
} while(time<timeFrom);

if(time > currentTime + 0.004) //check to see holes in the data
{
    wait = (int)((time-currentTime)/0.0034722);
    currentTime = time;
    return -1;
}
currentTime = time;

if(time > timeTo)
{
    return 0;
}

```

```

        return 1;
    }

    public double getZenithTEC()
    {
        return zenith;
    }

    public double getDirection()
    {
        return direction;
    }

    public double getMagnitude()
    {
        return magnitude;
    }

    private BufferedReader zenithFile;
    private BufferedReader directionFile;
    private BufferedReader magnitudeFile;
    private double zenith;
    private double direction;
    private double magnitude;
    private int day;
    private int wait;
    private double currentTime;
    private double yearFrom, yearTo, timeFrom, timeTo;
}
import java.io.*;

//class to read Gtf files
public class GtfFileInterpreter
{
    public GtfFileInterpreter(String fileName)
    {
        try
        {
            FileReader f = new FileReader(fileName);
            file = new BufferedReader(f);
        }
        catch(FileNotFoundException e)
        {
            System.out.println("Unable to open " + fileName);
        }
    }

    //get the next line
    public boolean readObservation()
    {
        String temp;
        try
        {
            temp = file.readLine();
        }
    }

```

```

    catch(IOException e)
    {
        return false;
    }

    if(temp == null)
        return false;

    StringBuffer buf = new StringBuffer(temp);

    year = Integer.parseInt(buf.substring(0,4));
    day  = Integer.parseInt(buf.substring(5,8));
    hour = Integer.parseInt(buf.substring(9,11));
    minute = Integer.parseInt(buf.substring(12,14));
    seconds = Double.parseDouble(buf.substring(15,20));

    prn = Integer.parseInt(buf.substring(25,27).trim());

    az  = Double.parseDouble(buf.substring(30,36).trim());

    el  = Double.parseDouble(buf.substring(40,45).trim());
    if(el<15)
        el = -1;

    double pha = Double.parseDouble(buf.substring(46,60).trim());

    tec = Double.parseDouble(buf.substring(66,75).trim());
    if(tec > 200)
        tec = -1;

    return true;
}

public boolean fastRead()
{
    try
    {
        line = file.readLine();
    }
    catch(IOException e)
    {
        return false;
    }
    if(line == null)
        return false;
    return true;
}

public String getLine() //used for fast reads
{
    return line;
}

public void closeFile()
{
    try

```

```

    {
        file.close();
    }
    catch(IOException e)
    {
    }
}

//rest are access functions
public double getAzi()
{
    return az;
}

public double getAlt()
{
    return el;
}

public double getTec()
{
    return tec;
}

public int getPRN()
{
    return prn;
}

public double getTime()
{
    return (double)day + (double)hour/24 + (double)minute/1440;
}

private BufferedReader file;
private int year;
private int day;
private int hour;
private int minute;
private double seconds;
private int prn;
private double az;
private double el;
private double tec;
private String line;
}
//Class GtfFileGenerator
import java.io.*;

//class to make gtf files
public class GtfFileGenerator
{
    public GtfFileGenerator(double timefrom, double timeto, double yearfrom, double yearto)
    {
        timeFrom = timefrom;
        timeTo = timeto;
    }

```

```

yearFrom = yearfrom;
yearTo = yearto;
recieverOffset = 13.3;
day = (int)timeFrom;

interpreter = new GtfFileInterpreter(
    "/home/filehost/bjones/gpsData/gpsData_" + day + "_" + (int)yearFrom + ".dat");
}

//Function to call all sub functions
public void makeGtfFile()
{
    try
    {
        file = new FileWriter("AOC_" + day + "_" + (int)yearFrom + ".gtf");
    }
    catch(IOException e)
    {
        return;
    }

    writeBias();
    writeReceiverData();
    writeData();
    printSlash();

    try
    {
        file.close();
    }
    catch(IOException e)
    {}
}

//Writes GPS bias info
private void writeBias()
{
    try
    {
        file.write("GPS BIAS = 2.106, 4.787, -2.037, -2.319,\n");
        file.write("    0.422, -3.073, 5.392, -0.782,\n");
        file.write("    -1.660, 4.830, 0.0, 0.0,\n");
        file.write("    -14.656, 3.963, 3.138, 6.884,\n");
        file.write("    3.138, -2.673, 0.916, 0.0,\n");
        file.write("    4.300, 0.767, 4.434, 5.866,\n");
        file.write("    -4.696, -4.091, -0.157, 0.0,\n");
        file.write("    -4.262, -6.385, -4.134, 0.0 TECU \n");
        file.write("\n! Biases from JPL global model\n!\n");
    }
    catch(IOException e)
    {}
}

//Write reciever data to gtf file
private void writeReceiverData()

```

```

{
    try
    {
        file.write("GPSDATA Receiver='AOC' BIAS = "+recieverOffset+" TECU\n");
        file.write("      X = -1538495.277000 Y = -5061426.638000 Z = 3553669.546000 ^n!\n");
        file.write("!Year\tDay\tTime\tPRN\tAz\tEl\tTEC-pha\t\tTEC-tau\n");
    }
    catch(IOException e)
    {}
}

//Writes body of data to gtf file
private void writeData()
{
    String buf;

    while(true)
    {
        if(!interpreter.fastRead())
        {
            day++;
            if(day > 364)
            {
                day = 0;
                yearFrom++;
            }
            interpreter.closeFile();
            interpreter = new GtfFileInterpreter(
                "/home/filehost/bjones/gpsData/gpsData_" + day + "_" + (int)yearFrom + ".dat");
            interpreter.fastRead();
        }

        buf = interpreter.getLine();

        int day = Integer.parseInt(buf.substring(5,8));
        int hour = Integer.parseInt(buf.substring(9,11));
        int minute = Integer.parseInt(buf.substring(12,14));

        if(((double)day+(double)hour/24 + (double)minute/1440 > timeTo)
            break;

        if(((double)day + (double)hour/24 + (double)minute/1440 + 1 > timeFrom)
        {
            try
            {
                file.write(buf+"\n");
            }
            catch(IOException e)
            {}
        }
    }
}

private void printSlash()
{
    try

```

```

    {
        file.write("\n");
    }
    catch(IOException e)
    {}
}

private double timeFrom;
private double timeTo;
private double yearFrom;
private double yearTo;
private double recieverOffset;
private int day;
private FileWriter file;           //GTF file
private GtfFileInterpreter interpreter;
}
import java.io.*;

//class that writes the plots to a file
public class PlotFileWriter
{
    public PlotFileWriter()
    {
        year = 0;
        day = 0;
        hour = 0;
        index = 0;
        timeFrom = 0;
        data = null;
        name = null;
    }

    public void setDateAndTime(int y, double timefrom)
    {
        timeFrom = timefrom;
        year = y;
        day = (int)timeFrom;
        hour = (int)((timeFrom%1)*24);
    }

    public void setName(String n)
    {
        name = n;
    }

    public void setData(double[] d, int i)
    {
        data = d;
        index = i;
    }

    public void makeFile()
    {
        if(year == 0)
            return;

```

```

    FileWriter file;
    double time = timeFrom;

    try //open the file
    {
        file = new FileWriter(""+name+day+"."+hour+"."+year+".dat");
    }
    catch(IOException e)
    {
        return;
    }

    for(int i=0; i<index; i++)
    {
        String s1 = ""+time;
        if(s1.length() > 8)
            s1=s1.substring(0,8);
        String s2 = ""+data[i];
        if(s2.length() > 5)
            s2=s2.substring(0,5);
        try
        {
            file.write(s1+" "+s2+"\n");
        }
        catch(IOException e)
        {
        }
        time+=0.00347222;
    }

    try
    {
        file.close();
    }
    catch(IOException e)
    {
    }
}

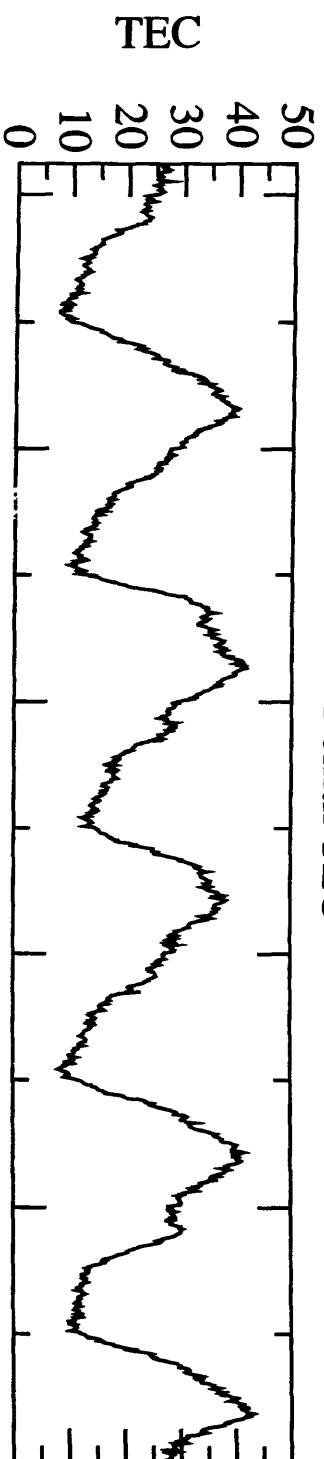
private int year;
private int day;
private int hour;
private int index;
private double timeFrom;
private String name;
private double[] data;
}

```

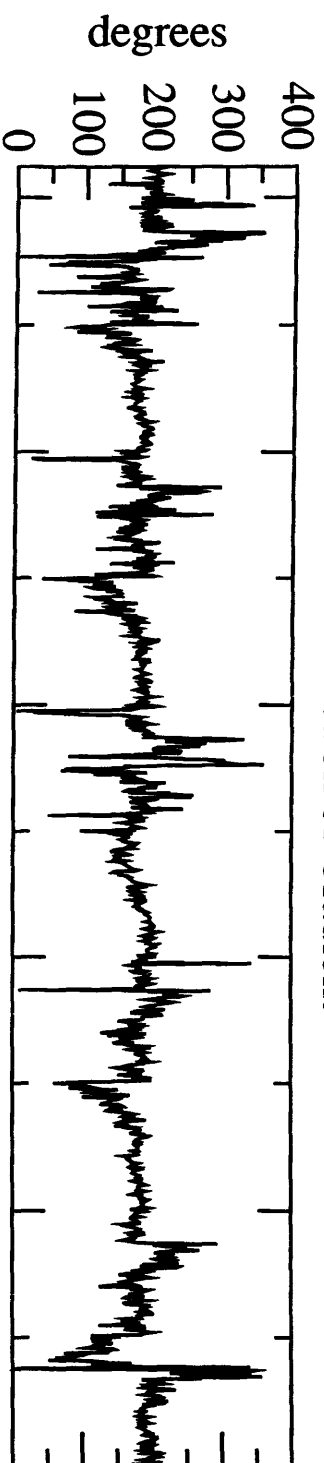


# Model Parameters

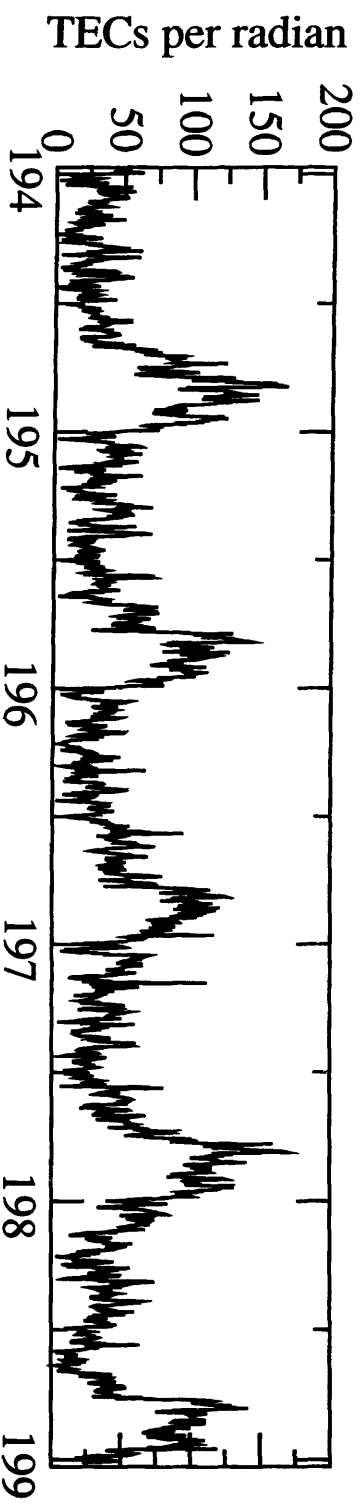
Zenith TEC



Direction of Gradient

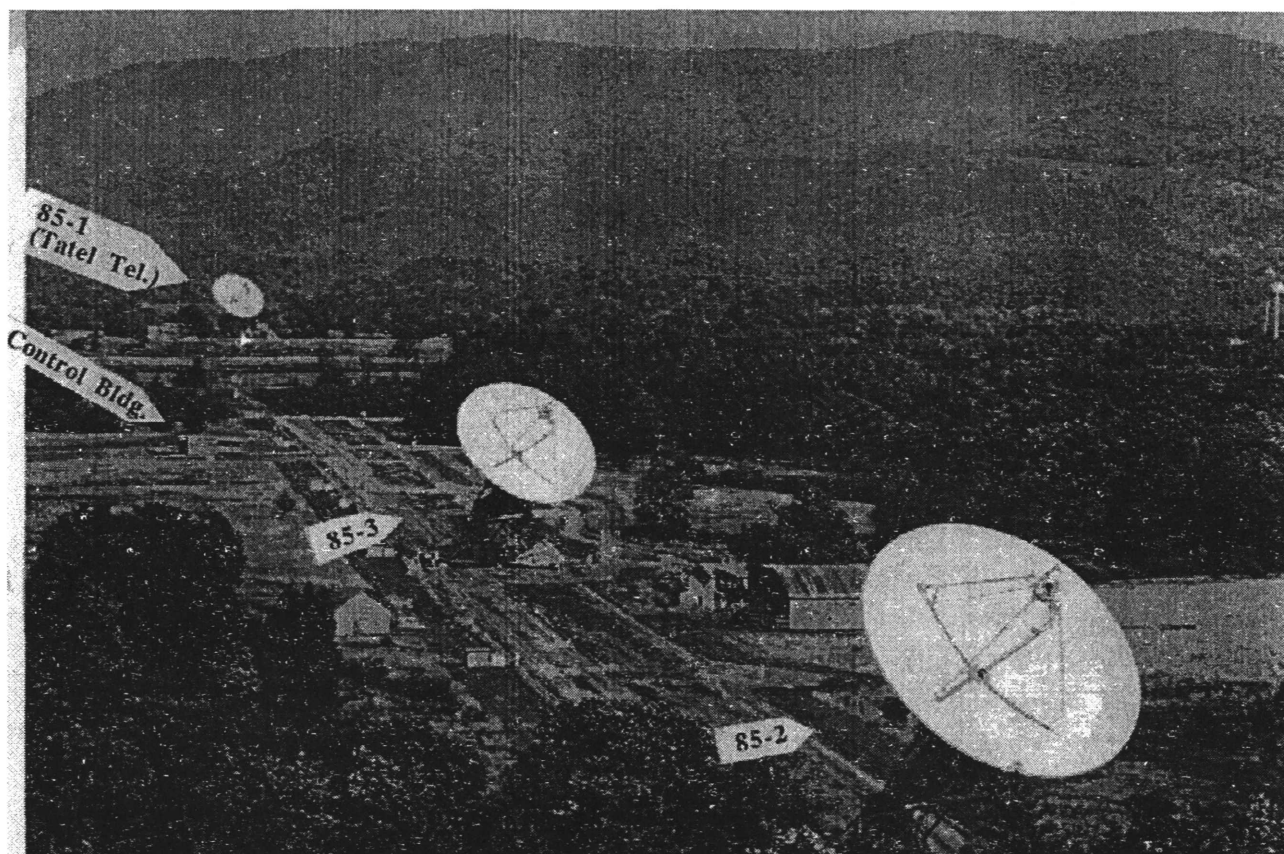


Magnitude of Gradient



# Green Bank Interferometer Summer Project Report

Jill Kamienski





# Contents

- 1 Control 2**
- 2 Calibration 3**
  - 2.1 Flagging Bad Data . . . . . 3
    - 2.1.1 Documentation . . . . . 3
    - 2.1.2 What Still Needs to be Done . . . . . 5
  - 2.2 Creating Flag File from Existing Counts . . . . . 6
    - 2.2.1 Documentation . . . . . 6
- 3 Learning Curses 7**
- 4 The Rest of the Summer 8**



# Chapter 1

## Control

An attempt was made to work with the monctrl system to create control software for the interferometer.

This would have been getting the single board computer to monitor certain points on the telescope and to change some values.

The documentation was on a fairly basic level and somewhat difficult to follow in a logical order making it difficult to get started and slow moving. Also there was a lot of source code involved in the monctrl system making it difficult to follow through all the required parts, causing it to be a project that would have taken someone of my experience much longer than a summer to complete.

It was exciting when I was first able to actually read in some data from the single board computer and know that it was correct. This had meant that I had correctly added samplers, but it had just taken a bit too long to get to that point.

## Chapter 2

# Calibration

### 2.1 Flagging Bad Data

When bad data is written to the counts file it needs to be somehow marked so that it can be eliminated from the computations when converting the counts into Janskys.

The FlagData program allows a user to mark data as bad, creating a flags file.

This is improved from the old method which involved editing many files and changing the counts to 0. This had the consequence of losing the original value of the counts unless the files were regenerated. It also took too much time to edit all the files.

With the FlagData program the user can quickly switch between sources to flag the data they need.

The program was also written using the curses interface, allowing the program to run on an xterm so that it could be brought up on any system and would be fast over a remote connection.

#### 2.1.1 Documentation

The program is started by typing `fd` (short for FlagData). It may be given a few options if desired. The most important option is the `-c` flag. This allows a user to continue even if their xterm is too small. In order for the data to be displayed accurately on the screen it must be at least 100 characters wide. If it is less than that the program will quit with an error. The `-c` flag gets around the error and runs the program anyway, but it will contain characters wrapping around the screen.

The other options allow you to set menu selections from the command line. `-arith` or `-vector`, `-source` or `-cal`, and `-counts` or `-fluxes` set these.

A screen shot of the program is included on the back of the report. Beginning with the top left is the arithmetic/vector menu. This allows the user to choose between arithmetic mode, which is the average of amplitudes, or the vector mode, which takes the cosine and sine components. Next comes the source/calibrator menu which allows the user to choose just that. Third is the counts/fluxes

menu. Counts shows each piece of data as an arbitrary number that represents some portion of the total power, which fluxes shows the same data converted into units of Janskys. Next comes the source menu which allows a user to choose the source to be displayed on the screen. Below these menus is the data list. This shows the data beginning with the date, the time, the hour angle, and the gain. Then the actual data appears, SLL first, then SRR, XLL, and XRR. If data is flagged it appears in bold. Below the data is the calibrate button to run the calibrate script, the save button to write the flags to disk, and the exit button.

Once in the program you can tab forward through the menus with the TAB key or backwards with the "" key (this can be changed by editing line 49 of the file fd.h, which means redefining the value of BACK\_MENU\_SELECT).

When a menu is selected the list of choices can be brought down with the down arrow key. If the ENTER key is pressed the menu will toggle through its options.

When the data field is selected it will have a box around it and be labelled on the top. When in this mode the cursor can be moved around over any data with the arrow keys. If the cursor is over a piece of data (SLL, SRR, XLL, or XRR) it can be flagged by pressing "f" or unflagged by pressing "u". If the cursor is in another column (date, time, hour angle, or gain) then "f" and "u" will flag or unflag the entire row of data. If it is ever desired to have more options than just flagged or unflagged this can be accomplished by adding the key press to the switch statement under main. When this key is pressed it should just call flag\_data(int) with int being whatever number is desired. Currently flagged data is "0" and unflagged data is "1."

No information is permanently written until the user has asked to save it. This can be accomplished in any of three ways. The first is to run the calibrate script. This will bring up a prompt asking to save the data. The second is to click on the save menu, and the last is to choose the exit menu and select exit with save.

When a flag file is saved for a source which already has a flag file the old file will be moved to the same location but with a ".bak" extension and the new one will take its place.

The resulting file contains a set of rows each including the date, time, and a column for each piece of data (SLL, SRR, XLL, XRR) appearing as a "1" or "0". A "0" means the data is flagged, while a "1" means it is not. Later, if it is desired, weights may be added to the program by changing this number (see above concerning how to flag the data).

The calibrate button is designed to run the calibrate script which currently does not exist. This can be added into the program at the bottom of fd.c in the function cal\_script(). See the notes in the code for accessible variables.

Help can be brought up at any time by typing "h". This gives a list of the basic characters the program will recognize, shown below:

```
-----  
|                               |  
|          FLAGDATA HELP      |  
|                               |  
| Use TAB to move to the next field  
| Use '' to move to the previous field  
| Use ENTER to tab through menu  
| Use ESCAPE to leave a menu without selecting  
| Use the arrow keys to select menu item  
| To flag a field highlight it and then press 'f'  
| To unflag a field highlight it and then press 'u'  
| To reset all values press 'r'  
|                               |
```



```
| To redraw the current screen press 'l'
| Quit without saving at any time with 'q'
| For help press 'h' (this screen)
|
|     Press any key to return to main screen
|
-----
```

On Osiris the program is located in `/o/gbi/gbical/src/flagdata/` and is set up to run correctly from there. It can be compiled by simply typing "make" on the command line.

### 2.1.2 What Still Needs to be Done

As time ran out there were still some things left that could improve the program. Following is a list of what probably should be done and a brief explanation as to how to do each.

The program should read in all the pieces of data from a file, not just the last part. This can be done by using dynamically allocated arrays instead of the current static arrays. This should be added to the `readin_data()` function where it is bringing `NUM_LINES` worth of data. First the number of lines in the file should be gotten, then a dynamic array of `struct Data` (see `fd.h`) should be allocated with `malloc()` for that number of lines.

The most important thing that needs to be done is to compile the program under SunOS. It has been running under Linux all summer. An attempt to compile it under SunOS failed because it could not find the curses library. It either was not in my current path or it is not installed on the machine. Either is easy to fix.

In some xterms the bold shrinks the text, causing the screen to format strangely. This could be fixed by putting an asterisk or something similar next to the number instead of changing it to bold. The most important place to change this is in the `draw_source_data()` function. The lines that include `A_BOLD` need to instead add the desired notation.

The last thing that really needs to be fixed in the code is that when the screen is taller than the number of rows being shown some strange characters get printed. This can be fixed in the `draw_source_data()` function by adding a condition to the while loop that checks for screen size and compares it with the number of lines being printed.

## 2.2 Creating Flag File from Existing Counts

After the FlagData program was written it was desired that the old files be recreated so that they contained all the counts instead of having some set to 0. Before this could be done flag files needed to be generated for the existing files.

### 2.2.1 Documentation

The program CreateFlags is started by running `cf`. A couple arguments can be specified on the command line. It needs to know if it is looking at an arithmetic file or a vector file. This is done by either a `-a` or `-v`.

The other options are `-i input_file` and `-o output_file`. This allows a user to specify input and output, but is not required. If these are not specified then standard input and standard output are used.

The result of running this program will be a flag file in the same format as created by FlagData. This is done by comparing each piece of data with the integer 0. This allows combinations of 0s (such as 00) to also be flagged as bad data.

The program is located in `/o/gbi/gbical/src/createflags/`.

## Chapter 3

# Learning Curses

It was decided that a fast interface was needed so that the program could be run remotely without bogging down the network.

The curses library runs under Unix and makes a convenient, quick user interface. I had to figure out how to keep the screen updated and how to catch user typed characters without allowing the character to be seen on the screen. I also had to figure out how to get keys other than letters, such as the arrow keys (turns out curses has them pre-defined as `KEY_UP`, `KEY_DOWN`, etc), and `ENTER` (which needs to be accessed by its ascii value of 13).

Until I figured out what was going on, I would sometimes get a strange error when I ran the program which I hadn't gotten when running it immediately before. It turns out that with curses, if the curses screen did not get shut down properly, it would effect the program the next time it was run, so I had to make sure that any possible error that could occur would properly close curses.

## Chapter 4

# The Rest of the Summer

Many activities contributed to making this summer a great experience. The people were great. Everyone was friendly and helpful. The area is beautiful for walking around or just looking out the window.

I really enjoyed the presentations designed for the students. It made for a good chance to get an introduction to different areas on a level we could comprehend. The science lunches and colloquia were also interesting, though sometimes a bit over our heads.

The Elkins trips were always an excitement when we needed to do some real food shopping. We would talk about the trip for a week ahead of time and figure out what to do when we went to the "big city."

The caving trip was great. It was fun crawling around in the mud, and was a nice way to spend time together as a group.

One of our favorite trips was one we made a couple times a week. We would take one of the old blue diesel vans and take a drive down past all the dishes, many times stopping to see what was going on in the 40 foot or 140 foot. It made a nice way to get out of the "summer student dungeon" for a bit, as well as to get to see some other science that was going on and to meet some neat people.

I got the chance to make a few trips to the Shenandoah airport to get some flying in during the summer. Shenandoah Flight Services was great, very friendly and nice planes.



27 August 1999

Dear Alwyn Wooten,

During the summer of 1999 (12 June through 27 August) I worked at the National Radio Astronomy Observatory (NRAO) in Socorro, New Mexico. This position was sponsored by the National Science Foundation's (NSF) Research Experience for Undergraduates (REU) program. Under the supervision of Dr. R.C. Walker I studied the radio galaxy 3C 120 using observations taken with Very Long Baseline Interferometry (VLBI). The results of this study will be submitted for publication in an appropriate scientific journal.

The following document is a very early draft of the paper we are preparing. It is not yet complete and I will help to see the project to completion from my home university. We expect the paper to be submitted before the new year.

My work involved using the 1.67 GHz VLBI data presented and included image processing (see figures 5, 6 and 7). I also worked on writing some of the paper. Concurrently Dr. Walker, my advisor, was studying the reported 5 GHz monitoring data.

I would like to thank the NSF for providing this opportunity for undergraduates and NRAO for encouraging a positive and productive experience.

Respectfully,

A handwritten signature in black ink, appearing to read 'Makenzie Lystrup', with a stylized flourish at the end.

Makenzie Lystrup  
Department of Physics  
Portland State University  
PO Box 751  
Portland, OR 97207  
lystrum@psu4.pdx.edu



# STRUCTURE AND MOTION OF THE 3C 120 RADIO JET ON SCALES OF 0.5 TO 250 PARSECS

R. C. Walker, J. M. Benson

National Radio Astronomy Observatory, Socorro, NM 87801

M. B. Lystrup

Portland State University, Portland, OR, 97207

S. C. Unwin

Jet Propulsion Laboratory, Pasadena, CA, 91109

T. R. Hunter

Harvard-Smithsonian Center for Astrophysics, Cambridge, MA, 02138

G. Pilbratt

ESA Astrophysics Division/Space Science Department, Noordwijk, The Netherlands

Received \_\_\_\_\_; accepted \_\_\_\_\_

D R A F T

August 27, 1999

D R A F T





## ABSTRACT

**NOTE TO READERS:** This copy of this paper is far from ready for publication. It is being used to document the nature of the REU project of Makenzie Lystrup under the supervision of R. Craig Walker. It is not meant for general distribution. In fact some of the authors whose participation was in the form of producing images many years ago are not yet aware that the paper is in preparation.

Results of long term VBLI monitoring the parsec-scale radio jet in 3C 120 at 5 and 1.7 GHz are presented. Superluminal features are seen leaving the core at intervals of less than a year, about as often as we could distinguish new features with the about 0.6 parsec resolution of the observations. In fact, the situation is probably more accurately described as a continuous, relativistic jet pointed near the line-of-sight with fluctuations in brightness along its length. The fluctuations, be they density changes or slight direction changes with different relativistic beaming, move with the jet material and are seen as the superluminal “features”. The velocities of different features varies, but not by more than a factor of 2. Individual features have constant velocities as far as we can tell, although there are hints of acceleration near the core. Some features that we observe leaving the core in the 5 GHz observations with 0.6 pc resolution are followed at 1.7 GHz with 2.4 pc resolution to distances in excess of 25 pc from the core. Older moving features are seen in the 1.7 GHz images at distances of well over 100 pc from the core, so we have not found the region where the jet slows. There are suggestions of stationary features, or brightening and dimming regions through which the moving features pass. This reinforces the idea that the knot at 4” (2 kpc) that has been found to be stationary might not actually imply that the jet has slowed by that position.

*Subject headings:* galaxies: individual(3C 120) — galaxies:jets — galaxies:  
active — radio continuum: galaxies

## 1. Introduction

The radio source 3C 120 has observed structure on all scales from under a parsec to hundreds of kiloparsecs. It is dominated by a variable core that is resolved with Very Long Baseline Interferometry (VLBI). A prominent one-sided jet is seen extending from the core on subparsec scales to about a hundred kiloparsecs. On the largest scales there is a complex, two-sided lobe structure extending to about half a megaparsec ( $14''$ ) (Walker, Benson, and Unwin 1987). The close proximity of 3C 120 ( $z=0.033$ , Baldwin et al. (1980)) allows its jet structure to be studied with exceptionally fine linear resolution, compared with other superluminal sources, using VLBI. Not only does its close proximity make it a convenient source for quality VLBI observations, it is also an interesting source that exhibits complex jet structure and variability on a wide range of scales and wavelengths. Superluminal motion is present in the jet and due to its rapid angular motions many components can be followed to larger angular scales where lower resolution must be used. For these reasons the morphology and motion of 3C 120 have been studied extensively with VLBI for nearly three decades (Benson et al. 1988; Walker 1997; Gómez et al. 1998; Cohen et al. 1977, and references therein).

Because 3C 120 is a strong and variable emitter of radiation at all observed frequencies information is available concerning wavelengths other than those in the radio regime (Maraschi et al. 1991). The galaxy associated with 3C 120 is usually referred to as a Seyfert 1 galaxy (Burbidge 1967), although its properties are also consistent with that of a broad line radio galaxy (BLRG) and to a finite extent, a quasar or QSO. Its classification is thus not completely certain. An optical counterpart to the radio jet, extending out to  $15''$ , has

been detected, one of only several such optical jets observed thus far (Hjorth et al. 1995). In the optical wavelengths variability is observed in both the continuum (Lyutyi 1979; Wlerick, Westerlund, and Garnier 1979; Pollock et al. 1979) and the spectral lines (Oke, Readhead, and Sargent 1980). Also it is a powerful X-ray source. Studies have shown an x-ray emission knot that is coincident with the 20" radio knot and is most likely explained by synchrotron emission (Harris et al. 1999). In the X-ray the spectral index varies with the intensity (Halpern 1984), a property not seen in Seyfert galaxies.

Radio frequency studies of 3C 120 have been carried out in many frequencies and on a variety of scales. Recent high frequency VLBI observations at 86, 43 and 22 GHz (Gómez, Marscher, and Alberdi 1999) have produced high resolution data of the innermost features of the jet. Gómez, Marscher, and Alberdi (1999) have, with the 86 GHz Coordinated Millimeter VLBI Array (CMVA) put an upper limit on the core of  $.025h^{-1}\text{pc}$  (core size lies below the resolution of the 86 GHz map, i.e.  $\leq 54 \mu\text{as}$ ) and the 43 and 22 GHz observations show the inner jet structure to be quite complex. A radio knot in the jet 4" from the core has been shown to exhibit sub luminal motion and is perhaps a stationary feature (Walker 1997). Previous linear polarization studies carried out with the National Radio Astronomy Observatory's (NRAO) Very Large Array (VLA) indicate that the magnetic field is mostly parallel to the jet with some rotation (Walker, Benson, and Unwin 1987). However, the most recent linear polarization from 86, 43 and 22 GHz VLBI observations show variability in the polarized flux density accompanied by the rotation of the magnetic field from orthogonal to parallel the jet axis (Gómez, Marscher, and Alberdi 1999). It is interesting to note that measurements taken in 1996 showed an insignificant amount of circular polarization (Homan and Wardle 1999).

The standard model for superluminal motion in jets such as the one associated with 3C 120 involves relativistic plasma flows moving from the center of the active galactic

nucleus (AGN) viewed at small angles to the line of sight (Blandford and Königl 1979). 3C 120 is a quintessential example of a source exhibiting such motion. One of the first extragalactic superluminal sources detected in the early 1970s, 3C 120 is also one of the closest of such objects. Superluminal motion has been observed on scales of subparsecs (Gómez et al. 1998) to tens of parsecs (Benson et al. 1988; Walker 1997; Cohen et al. 1977, and references therein).

According to the standard model, the observation of superluminal motions is good evidence that a jet is relativistic. The fact that a large proportion of bright, compact radio sources show superluminal motions suggests that many jets are relativistic on parsec scales, although there are selection effects due to relativistic beaming. It is not clear how far from the core the jet remains relativistic. At larger core distances, the jet becomes broader and features larger, so measurement of small angular changes is more difficult. Because of its close proximity 3C 120 has high angular rates of motion compared to other superluminal sources making it a prime candidate for attempts to find motions at large core distances. So far superluminal motion has been seen to distances of tens of parsecs in 3C 120 (Benson et al. 1988). Attempts to measure the motions of a knot at about 2 kpc produced a negative result (Maraschi et al. 1991; Walker 1997). While detected superluminal motion is a good indication of relativistic motion, observed sub luminal or no motion does not have a clear interpretation; it could indicate that the jet has slowed or that there is a standing shock or interaction region in a relativistic jet.

Recent studies (Gómez et al. 1998) have begun to apply observations of 3C 120 to physical models of jets. Hydrodynamical jet theories incorporating shocks have been used to model superluminal sources (Gómez et al. 1997), and it has been suggested that the motion of the inner jet structure 3C 120 may be described in this way (Gómez et al. 1998). Also there are suggestions of helical patterns in the 3C 120 jet. The superluminal motion

along a curved trajectory seen in the radio source 3C 345 can be explained by helical jet models (Hardee 1987; Owen et al. 1989; Steffan et al. 1995) (get some details).

In this paper we present the results obtained from five epochs of 1.7 GHz ( $\lambda 18$  cm) VLBI observations spanning from 1982 to 1997. We also present 5 GHz ( $\lambda 6$  cm) VLBI monitoring data which was taken approximately three times per year from 1977 through 1988. With our observations we can attempt to discern how frequently components are ejected from the core. Also we are interested to learn if the velocities of components are constant and if velocities vary for different components. Finally we are interested in how the trajectories relate to each other. By addressing these questions we hope to obtain a better understanding of 3C 120.


## **2. The Observations**

### **2.1. Monitoring at 5 GHz**

Between 1977 and 1988, 3C 120 was observed approximately 3 times per year with VLBI. Until 1981, the observations alternated between 10.7 GHz and 5.0 GHz. After 1981, it was realized that the motions in the source were sufficiently fast that the interval between same-frequency observations was too long to follow features unambiguously. After that date, nearly all observations were made at 5.0 GHz. The early observations used the main antennas of the U.S. VLBI Network. As the years progressed, so did the size of the arrays as more U.S. antennas and, especially, as European antennas were added. The first observations involved only 3 antennas. By the time the series was terminated, a typical observation involved 11 antennas. All of these observations used the Mark II VLBI recording system, with a 2 MHz bandwidth and 1 bit sampling. Correlation was done on one of the Caltech 5 station correlator, the NRAO 3 station correlator, or the Caltech

Block II (16 Mark II stations) correlator, depending on epoch. Results up to 1980.27 were reported by Walker et al. (1982). This paper will not consider the first few observations, but will include observations after 1978.91 in the analysis, even though the first few of those were previously reported. The antennas involved in both these observations and in the 1.7 GHz observations described below are listed in Table 1. The dates, frequencies, and antennas for each of the observations at 5.0 or 10.7 GHz are listed in Table 2.

EDITOR: PLACE TABLE 2 HERE.

The 5.0 and 10.7 GHz observations were calibrated and imaged using standard procedures using either the Caltech VLBI package or AIPS at near the time of the observations. The flux scales are usually based on antenna temperatures measured at one or more of Effelsberg, Green Bank, and Owens Valley. They are probably good to about 10%  in most cases. However at least one image (1983.25) seems to have an inconsistent flux density scale relative to the others — the measured fluxes are low. Perhaps this is because that epoch did not include any short baselines. No attempt at correction has been made, partly for lack of an obvious way to determine a correction.

The images, consisting of CLEAN components convolved with a common restoring beam of  $7.0 \times 1.0$  mas in position angle  $-10^\circ$ , are shown in Figures 1 to 3. For most epochs, the residuals are not included, but this does not make a significant difference at the contour levels used. Some of the more recent images do include the residuals. The quality of the images improved over the years, as is reflected in the differing lowest contour level displayed in each of the figures.

EDITOR: PLACE FIGURE 1 HERE.

EDITOR: PLACE FIGURE 2 HERE.

EDITOR: PLACE FIGURE 3 HERE.

Figure 4 shows the component motions. A slice was made along the ridge line of the jet in each of the images. The parts of that slice that appear to be reliable for identification of features were fit using between 2 and 6 gaussian components. In Figure 4, the amplitudes along each slice are displayed as the width of the shaded structure centered at the date of observation. The slice has been shifted so that the position of the easternmost gaussian, which is presumed to represent the core, is set at zero offset. Therefore the positions of other components are relative to the core. Some such alignment scheme is required because, without use of phase calibration using a reference source, there is no absolute position information available. The fitted gaussians were used to produce a model for the amplitudes along the slice. This model is shown as the thin lines that appear to outline each of the shaded regions. The fact that the lines appear to outline the shading, rather than either having shading extend outside the lines, or having white space inside the lines, indicates that the gaussian fits produce a good discription of the slice data. Note that the lines only extend over the region where structures are thought to be reasonably reliable — the region over which the fits were made. Especially in some of the earliest, and least reliable epochs, the fits were not extended over all regions that seem to show emission. Each component also is marked with an error bar that is the geometric sum of the formal fit errors for that component and for the presumed core. Thus the error bars should reflect the formal errors in the measurement of the relative offset of the core and the component.

EDITOR: PLACE FIGURE 4 HERE.



Most of the components whose positions are shown in Figure 4 were marked as belonging to a specific feature seen at multiple epochs and labeled with a letter. Such components are marked with closed circles. Components marked with open circles in Figure 4 are not included in any motion analysis. The positions of all components belonging to each moving feature were fit, in a least squares sense, for a feature angular speed and a start date. Straight lines indicating the fitted motion are drawn on the figure. The rates for each feature, along with the formal fit errors, are displayed on the figure.

## 2.2. Observations at 1.7 GHz

EDITOR: PLACE TABLE 3 HERE.

There have been 5 VLBI observations of 3C 120 at 1.7 GHz as summarized in Table /refobs18. Images from the first two have been published in Benson et al. (1988). All of these observations involved a large number of antennas. However the low declination of the source, combined with the wide longitude range of the antennas, makes the coverage of the (u,v) plane, especially for the longer baselines, rather poor. See the plots in Benson et al. (1988) for examples. The first 3 observations used the Mark II VLBI system with 2 MHz bandwidth and 1 bit sampling. The 1982.78 data were correlated on the Caltech 5 station correlator. The 1984.26 data were correlated on the NRAO 3 station correlator as part of what has since become known as the “World Radio Array” set of observations of 4 sources. The 1989.85 data were correlated on the Caltech Block II correlator. The final two epochs were recorded on the wider bandwidth VLBA and Mark IV recording systems. The 1994.44 observation was made with just the 10 antennas of the VLBA (Napier et al. 1994) using a total of 32 MHz bandwidth and 1 bit sampling. The 1997.71 data used a global array and both VLBA and Mark IV recording systems. The total bandwidth was again 32

MHz, but this time 2 bit samples were used. Both the 1994.44 and 1997.71 observations were correlated on the VLBA correlator. The improvement of data quality with the wider bandwidth systems and the better (u,v) coverage of the VLBA is readily apparent in the images.

EDITOR: PLACE FIGURE 5 HERE.

EDITOR: PLACE FIGURE 6 HERE.

EDITOR: PLACE FIGURE 7 HERE.


The 1.7 GHz images are displayed on 3 different scales in Figures 5, 6, and 7. Figure 5 shows the two wide bandwidth observations over the full region in which emission was detected. That region extends to about 0.5 arcseconds. These images were made with a taper of .... and have the resolutions noted in the figure caption. These images show that the jet is a continuous structure from the core region to at least a 0.5 arcsecond. In fact, it is known to be a continuous structure from milliarcseconds to about 14 arcminutes (Walker, Benson, and Unwin 1987). The current images show much more clearly than before that the jet has a smooth envelope - the edges follow smooth curves. However, there is considerable structure in the emission internal to the jet, with significant side-to-side variations and pronounced knots along the jet. this is mainly what was seen before.

Figure 6 shows all 5 epochs with a window that includes everything out to the big bulge at a bit over 200 mas. All images have been made using a gaussian restoring beam that with a 10 by 4 mas FWHM at a position angle of  $-10^\circ$ . Note that the larger scale regions are much smoother in the recent images than in the ones based on the older Mark II

data. This is not a real effect in the source, but a reflection of the behavior of the CLEAN deconvolution algorithm when dealing with a combination of lower signal-to-noise ratio data, poorer (u,v) coverage, and probably higher closure errors in the older data. The closure errors are violations of the assumption made in self-calibration that all calibration errors are station dependent - affecting all baselines to a station equally. Closure errors can be caused by problems, such as mismatched bandpasses, that tend to be worse in the older data (one station even used a 1 MHz filter in one of the observations!).

Figure 7 shows the central regions for all 5 epochs of the same images shown in Figure 6. For this figure, the vertical spacing between the images is proportional to the time separation between the observations. This explains why the 1982.77 image has been cropped to allow it to be placed close to the 1984.26 image. With this vertical placement, any feature moving at constant velocity will move along a straight line. The alignment of the images along the jet direction has been done by aligning the image peaks, except for 1984.26. For the other epochs, the image peak appears to be on the core at the extreme eastern end of the source. For 1984.26, the image peak appears to be to the west of the end of the jet — there is probably a bright knot that has recently left the core. In fact, this may well be Knot B, or a combination of Knots B, C, D, and E seen in the 5.0 GHz data. In Figure 7, dashed vertical lines have been drawn through the presumed core position and at positions of some apparently stationary features, both dimmings and brightenings, that will be discussed below. Solid lines have been drawn to highlight what we believe to be moving features. Some of these features appear to pass through the stationary features noted above, dimming or brightening in the process.

The image from 1989.84 shows a double jet structure between about 10 and 80 mas that is not seen at the other epochs. We do not believe that this is real, but rather some artifact of the processing and imaging. But we have not managed to isolate the cause. It

is possible to force the source into a single ridged structure by not allowing the CLEAN deconvolution algorithm to place components in the regions that we believe show spurious structure. Images made this way are not much worse in dynamic range than ones where we have not tried to force the structure. But, when we use those images as starting models for further calibration, and allow CLEAN to put the “spurious” components back it it wants to, it does. This is usually an indication that the components are real, or at least weren’t created by the deconvolution. What we believe here is that the components are indicative with something wrong in the actual data rather than the deconvolution. But, since we don’t understand the problem, we have shown the image with the double structure.  - try to fix the image.

### 3. Discussion

The impression gained from examination of our 5 GHz monitoring data, along with the high resolution images of Gómez et al. (1998) and Gómez, Marscher, and Alberdi (1999) made at higher frequency, is one of a continuous superluminal jet with fluctuations in brightness. The jet is always there, but there is considerable structure in the distribution of brightness, and hence probably in distribution of material in the jet. This seems likely to be due to fluctuations in the feeding rate of the presumed central black hole from an accretion disk, although we have no direct evidence for this. At any given frequency, imaging observations show “features” spaced about as closely as can be distinguished given the resolution available. The “features” seen at 5 GHz all travel at similar, but not identical speeds ranging from 3.0 c (4.5 c if you ignore features only followed for about 2 mas from the core) to about 7 c. There is some weak evidence for acceleration near the core, but that is a region where the position measurements are complicated by blending with the core feature. Otherwise the features appear to have roughly constant speeds in the 5 GHz data.

Two of the features (B and I (■■■■■ - this will be H), or perhaps blends of those features and others nearby) are followed out to about 50 and 30 mas, respectively from the core in our 1.7 GHz images with no obvious change in speed.

Features first appear as brightenings of the core, and then decay in brightness as they move outward through the region observed with the 5 GHz data. However on the larger scales of the 1.7 GHz images, the features appear to undergo fluctuations in brightness, perhaps with brightenings and dimmings at systematic locations. Any material moving fast enough to exhibit superluminal motions also has its brightness strongly affected by relativistic beaming and this beaming is a strong function of angle of motion relative to the line-of-sight. Small changes in that angle can have dramatic effects on observed flux density. Therefore any brightness changes are at least as likely to reflect changes in flow direction as actual changes in the amount of radiation emitted in a comoving frame.

The high resolution images of Gómez, Marscher, and Alberdi (1999) and Gómez, Marscher, and Alberdi (1999) show that the 3C 120 jet is first seen at submilliarcsecond scales to have a position angle of about  $-125^\circ$ . Our 1.7 GHz images show an angle of roughly  $-100^\circ$  out to about half an arcsecond. The high resolution images suggest that most of the curvature between these values occurs between about 2 and 3 mas. However our 5 and 1.7 GHz observations suggest that a position angle of near  $-115^\circ$  is maintained as far as about 30 mas, at least in the more recent data. It would be very interesting to know how constant the position angle has been, especially on the small scales near the core. But unfortunately, the very poor north-south resolution of the 5 GHz images makes it difficult to obtain accurate position angle measurements. The images of Figures 1, 2, and 3 do show that the position angle did not change a lot between 1979 and 1988. All images show position angles between the main features of between about  $-112$  and  $-118^\circ$ . There are indications from a 1999 5 GHz image currently being processed that the position angle

is more like -122 deg (Benson, private communication). Perhaps there has been a rotation over the last 20 years, but the data are not yet convincing.

One of the more interesting results of this study is the apparent observation of both moving and roughly stationary features in the same region of the jet, with moving features passing through stationary features, brightening and dimming according to the nature of the stationary features. There are at least a couple of possible ways to have such a situation. One involves a curved trajectory, perhaps a helix of some form. The apparent flux changes occur as a result of the motion getting closer to, or farther from, the line-of-sight. Another would involve interactions with the medium about the jet. The brightenings could occur at places where the jet is constricted. The dimmings could be regions of freer expansion than average. (■■■■ - how do we tell them apart? Polarization structure? Appearance?)

If the stationary features are related to changes in jet direction, the details of what happens depends on the actual angle. Figure (■■■■) shows the brightness and apparent speed of a feature as a function of angle to the line of sight for a jet with  $\gamma = 5$ . The well known characteristic that the apparent speed peaks at about an angle of about  $1/\gamma$  radians at a speed of about  $\gamma c$  is apparent. The apparent velocity does not change drastically over a rather wide range of angles, although it drops very fast at very low angles. The brightness is a strong function of angle with the brightest sources very close to the line-of-sight. From this plot, it is clear that most sources in flux limited samples will be inside the speed peak at  $1/\gamma$  and will have velocities significantly lower than  $\gamma c$ . But it is not clear what angle to the line-of-sight 3C 120 has. It might be possible to tell if one could determine both the change in flux density and in speed as a feature changes flow angle. For example, if  $\gamma = 5$ , the flux should increase and the speed decrease as the jet gets closer to the line of sight for angles less than  $1/\gamma$ . For larger angles, the speed will increase and the intensity increase for a turn toward the line-of-sight.

Below are notes concerning work left to do.

Try modeling. The features look like helix parts. I (RCW) am writing a program to help compare helical models with the data.

Looks like there are periods of enhanced emission. We see it at 6cm. The bulges in the 18 cm jet give sort of an archaeological history. Can we use that? Can we compare with historical data on the flux density.

Can we say anything about the features seen in the 70's and how they relate to the 18cm features.

Try improving the images in AIPS++. Especially see if anything can be done to remove the double structure of the 89 image or to improve the 82 image.

Generally polish and check what has been written. This includes getting the actual stations used for some epochs where I have only see the schedules.

#### 4. Conclusions

The main conclusions of this study are:

- New superluminal components are emitted from the core of 3C 120 at intervals of under a year. In fact, it is likely that there is a continuous relativistic jet, with brightness structure which is seen as “components”. With the approximately 1 mas resolution available to this study at 5 GHz, only structures spaced by around 2 mas could be distinguished. With angular velocities of between about 2 and 3 mas yr<sup>-1</sup>, this naturally leads to the observation of new components at somewhat under a year intervals. The higher resolution studies at high frequencies by Gomez (get references ) show clearly that the actual structures in the jet are considerably smaller

than our resolution, at least within the first few mas of the core.

- The speeds of the components are not all the same. There is some tendency for the first component from a new burst of activity to be faster than others that follow it.
- Roughly the same velocity is seen on scales from sub-mas (Gomez??) to around 250 mas. This suggests that the underlying jet is not significantly accelerating or decelerating over this range of scales. Any evidence for changes of speed of individual components is weak at best. There is no evidence yet for a region where the jet slows.
- The 1.7 GHz data show evidence that there are both moving and stationary features in the same regions. In fact, it appears that moving components can pass through the stationary features, dimming or brightening as they do so. The stationary features could either be places of interaction with the external medium or could reflect changes in jet direction with corresponding changes in the intensity of the relativistic beaming.
- The stationary brightening regions have structure reminiscent of the feature at 4 arcseconds for which no, or at least subluminal, motion has been found (Walker 1997). This enhances the suspicion that the 4 arcsecond knot's lack of motion does not imply that the underlying jet is not relativistic. The knot may, like the stationary brightening regions in the 1.7 GHz images here, be regions of interaction with the external medium or a result of jet bending.
- The 1.7 GHz images show fossil evidence for occasional significant increases in ejected material. The bulge on the south side of the jet at about 200 mas, along with the distinct drop in flux density by about 250 mas suggests that there was a significant outburst whose effects are just now reaching this region. If the jet speed is typically  $2.5 \text{ mas yr}^{-1}$ , this would suggest that the outburst occurred about 100 years ago. The structure is somewhat similar to the structures at about 15 mas in 3C 84, which are



thought to be the result of the big outburst that started in about 1959 (e.g. (Walker, Romney, and Benson 1994)).

The picture that emerges is one of a continuous, relativistic jet with lots of internal structure. The velocity is maintained from sub parsec to hundreds of parsecs scales. The structure includes both features that move with the jet, perhaps density enhancements or shocks, and also features that do not move with the flow. The moving features can pass through the stationary features, suggesting that the stationary features do not significantly disrupt the flow. The stationary features can be either locations where the jet is either especially dim or especially bright. These could be places where there is interaction with the external medium. The dimmings could be regions of free expansion while the brightenings could be regions of compression or shocks. On the other hand, the dimmings and brightenings may be regions where the jet either goes further from or closer to the line-of-sight.

## REFERENCES

- Baldwin, J.A., Carswell, R.F., Wampler, E.J., Burbidge, E.M., and Boksenberg, A. 1980, ApJ, 236, 388
- Benson, J.M., Walker, R.C., Unwin, S.C., Muxlow, T.W.B, Wilkinson, P.N., Booth, R.S., Pilbratt, G., and Simon, R.S. 1988, ApJ, 334, 560
- Biretta, J.A., Zhou, F., and Owen, F.N. 1995, ApJ, 447, 582
- Blandford, R.D. and Königl, A. 1979, ApJ, 232, 34
- Burbidge, E.M. 1967, ApJ, 149, L51
- Cohen, M.H., Kellermann, K.I., Shaffer, D.B., Linfield, R.P., Moffet, A.T., Romney, J.D., Seielstad, G.A., Pauliny-Toth, I.I.K., Preuss, E., Witzel, A., Schilizzi, R.T., and Geldzhaler, B.J. 1977, Nature, 268, 405
- Conway, J.E. and Murphy, D.W. 1993, ApJ, 411, 89
- Gómez, J.L., Martí, J.M., Marscher, A.P., Ibañez, J.M., and Alberdi, A. 1997, ApJ, 482, L33
- Gómez, J., Marscher, A. P., Alberdi, A., Martí, J. M., and Ibáñez, J. M. 1998, ApJ, 499, 221.
- Gómez, J.L., Marscher, A.P., and Alberdi, A. 1999, ApJ, 521, L29
- Halpern, J.P. 1984, ApJ290, 130
- Hardee, P.E. 1987, ApJ, 318, 78
- Harris, D.E., Hjorth, J., Sadun, A.C., Silverman, J.D., and Vestergaard, M. 1999, ApJ, 518, 213

Hjorth, J., Vestergaard, M., Sørensen, A.N., and Grundahl, F. 1995, ApJ, 452, L17

Homan, D.C. and Wardle, J.F.C. 1999, ApJ, in press

██████

Lyutiy, V.M. 1979, Soviet Astr., 23, 518

Maraschi, L., Chiapetti, L., Falomo, R., Garilli, B., Malkan, M., Tagliaferri, G., Tanzi, E.G., and Treves, A. 1991, ApJ368, 138

Napier, P. J., Bagri, D. S., Clark, B. G., Rogers, A. E. E., Romney, J. D., Thompson, A. R., & Walker, R. C. 1994, Proc. IEEE, 82, 658

Oke, J.B. and Zimmermann, B. 1979, ApJ, 231, L13

Oke, J.B., Readhead, A.C.S., and Sargent, W.L.W. 1980, PASP, 92, 758

Owen, F.N., Hardee, P.E., and Cornwell, T.J. 1989, ApJ, 340, 698

Pollock, J.T., Pica, A.J., Smith, A.G, Leacock, R.J., Edwards, P.L., and Scott, R.L. 1979, ApJ, 290, 130

Steffan, W., Zensus, J.A., Krichbaum, T.P., Witzel, A., and Qian, S.J. 1995, A&A, 302, 335

Walker, R.C., Seielstad, G.A., Simon, R.S., Unwin, S.C., Cohen, M.H., Pearson, T.J., & Linfield, R.P. 1982, ApJ, 257, 56

Walker, R.C., Benson, J.B., and Unwin, S.C. 1987, ApJ, 316, 546

Walker, R. C., Romney, J. D., and Benson, J. M. 1994, ApJ, 430, L45

Walker, R.C. 1997, ApJ, 488, 675

Wlerick, G., Westerlund, B., and Garnier, R. 1979, A&A, 72, 277



Fig. 1.— The images from the 3C 120 Network VLBI monitoring program between 1978.91 and 1981.10. The images were made at either 5.0 or 10.7 GHz — see Table 2 for details. All are CLEAN images convolved with a elliptical gaussian beam 7.0 by 1.0 mas, elongated along position angle  $-10^\circ$ . The contour levels are 0.1, 0.2, 0.28, 0.4, 0.57, 0.8, 1.13, and 1.60 Jy beam $^{-1}$ .

Fig. 2.— The images from the 3C 120 Network VLBI monitoring program between 1981.63 and 1983.91. The images were made at 5.0 GHz. All are CLEAN images convolved with a elliptical gaussian beam 7.0 by 1.0 mas, elongated along position angle  $-10^\circ$ . The contour levels are 20, 40, 57, 80, 113, 160, 226, 320, 453, and 640 mJy beam $^{-1}$ .

Fig. 3.— The images from the 3C 120 Network VLBI monitoring program between 1984.25 and 1988.87. The images were made at 5.0 GHz. All are CLEAN images convolved with a elliptical gaussian beam 7.0 by 1.0 mas, elongated along position angle  $-10^\circ$ . The contour levels are -10, 10, 20, 28, 40, 57, 80, 113, 160, 226, 320, 453, 640, 905, 1280, and 1810 mJy beam $^{-1}$ .

Fig. 4.— This figure shows the motions of components in 3C120 between 1978 and 1988. For each image, there is a shaded profile whose width represents the amplitude along a slice that runs along the ridge line of the jet. The region of significant emission at each epoch has been fitted with between 2 and 6 gaussians. The profile predicted by these gaussians is shown as the thin solid line that outlines each shaded region. That the fits are good is demonstrated by the fact that the shading just reaches the line. The line only extends to the limits of the regions of the fit. Some of the early images were based on very few antennas by modern standards, so only the brightest features were considered believable and were fit. All profiles have been shifted in position so that the eastern-most feature, presumed to be the core, is at zero offset. The fitted positions, relative to the core, of other features are shown by circles with error bars that reflect the combined formal position errors for that feature

and for the core. Features with filled circles are ones that are identifiable at multiple epochs and for which speeds are measured with a least squares fit. The components are labeled and a straight line with the slope corresponding to the fitted velocity is drawn through the points. The velocity, with formal errors, for each feature is written on the figure.

Fig. 5.— Low resolution versions of the 1.7 GHz images from 1994.44 and 1997.70. These were the epochs that used wide band recording systems and had the sensitivity to see the structures between 270 and 540 mas from the core. Both of these images have been made with a taper that uses mainly the continental and shorter baselines. Then they were convolved with a common beam of 18 by 13 mas at position angle  $3^\circ$ . The contour levels are ....

Fig. 6.— The inner 300 mas of the 5 images available at 1.7 GHz. All have been convolved to a common beam of 10 by 4 mas elongated in position angle  $-10^\circ$ . The contour levels are ..... The bar at the top of each panel gives the relationship between shade of grey and flux density in  $\text{mJy beam}^{-1}$ .

Fig. 7.— The inner 190 mas of the 5 images available at 1.7 GHz. These are the same images with the same contour levels as those in Figure 6. The images have been spaced vertically on the page so that the separations between the cores is proportional to the time intervals between the observations. This allows features moving with constant apparent speed to be marked with straight lines. The source appears to contain both moving and stationary features. Stationary features have been marked with dashed lines. These include the core, two dimming regions and two brightening regions. The solid lines connect identifiable moving features whose motion we believe can be tracked.

Table 1. VLBI Antennas

Name	Code	Location	Diameter (m)
US VLBI Network:			
Arecibo	A	Puerto Rico	300
Haystack	K	Massachusetts	37
Green Bank 140'	G	West Virginia	43
North Liberty	I	Iowa	18
Fort Davis (GRAS)	F	Texas	26
VLA (single antenna)	Y1	New Mexico	25
VLA (phased array)	Yp	New Mexico	25x27
Owens Valley	O	California	40
Hat Creek	H	California	25
Maryland Point (NRL)	N	Maryland	25
European VLBI Network:			
Jodrell Mark I	J	United Kingdom	76
Jodrell Mark II	J2	United Kingdom	76
Onsala	S	Sweden	26
Westerbork	W	The Netherlands	25 (x12)
Effelsberg	B	Effelsberg	100
Medicina	M	Italy	32
Torun 18	T	Poland	18

Table 1—Continued

Name	Code	Location	Diameter (m)
Torun 32	Tr	Poland	32
Crimea	R	Russia	22
Noto	Nt	Italy	32
VLBA:			
Saint Croix	Sc	Virgin Islands	25
Hancock	Hn	New Hampshire	25
North Liberty	Nl	Iowa	25
Fort Davis	Fd	Texas	25
Los Alamos	La	New Mexico	25
Pie Town	Pt	New Mexico	25
Kitt Peak	Kp	Arizona	25
Owens Valley	Ov	California	25
Brewster	Br	Washington	25
Mauna Kea	Mk	Hawaii	25
Other:			
Defford	U	United Kingdom	25
Cambridge	E	United Kingdom	18
Dwingeloo	D	The Netherlands	25
Penticton	P	British Columbia	25



Table 1—Continued

Name	Code	Location	Diameter (m)
Pushchino (sp)	Pu	Russia	25
Hartebeesthoek	X	South Africa	25

Table 2. The 3C 120 VLBI Observations at 5.0 and 10.7 GHz

Epoch	Frequency (GHz)	Antennas <sup>a</sup>
1978.91	10.7	KGFO
1979.25	5.0	BGFOH
1979.44	10.7	BKGFO
1979.92	5.0	BKGFO
1980.27	10.7	BKGO
1980.52	10.7	BKGFO
1980.72	5.0	BKFO
1981.10	10.7	KGFO
1981.63	5.0	BKGYOH
1981.93	5.0	BSKGFYOH
1982.25	5.0	BSAGFYOH
1982.58	5.0	BKGFYO
1982.94	5.0	BSWJAKNGFYO
1983.25	5.0	BAKGO
1983.57	5.0	BSKNGFYO
1983.91	5.0	BSKGIFYO
1984.25	5.0	scheduled BSAKGIFYOH
1984.40	5.0	scheduled BSAKGIFYOH
1984.78	5.0	BSKGFYOK

Table 2—Continued

Epoch	Frequency (GHz)	Antennas <sup>a</sup>
1985.12	5.0	scheduled BSAKGIFYOH
1985.41	5.0	scheduled BSAKNGIFYOH
1986.42	5.0	BSAKGFYOH
1986.90	5.0	BSKGYO
1987.41	5.0	BSWJMTXKGYOH
1987.73	5.0	scheduled BSAKNGIFYOH
1988.19	5.0	BSWJAKGIFYO
1988.45	5.0	BSWJMKNPtYO
1988.87	5.0	BSJMKGIFPtO

<sup>a</sup>See Table 1 for station codes.

Table 3. The 3C 120 VLBI Observations at 1.7 GHz

Epoch	Antennas <sup>a</sup>
1982.78	S B D J K N G A I F YpO P H
1984.26	S B W J2T E U R K N G A I F YpO P H
1989.85	S B W R PuM X J A K G I PtKpLaY1
1994.44	VLBA <sup>b</sup>
1997.71	B J M NtTrW G Y1 VLBA <sup>b</sup>

<sup>a</sup>See Table 1 for station codes.

<sup>b</sup>“VLBA” means all 10 VLBA antennas.

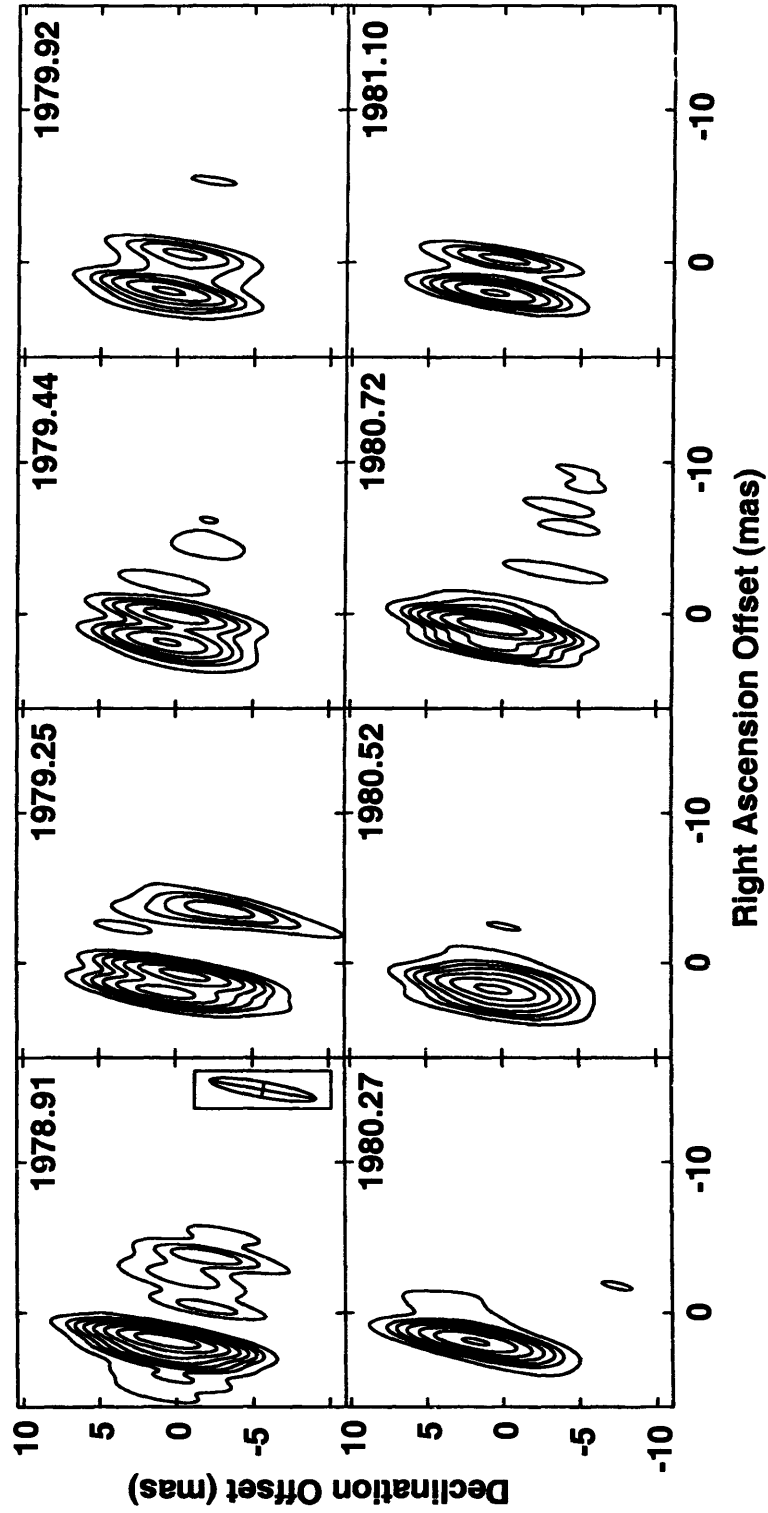


Figure 1

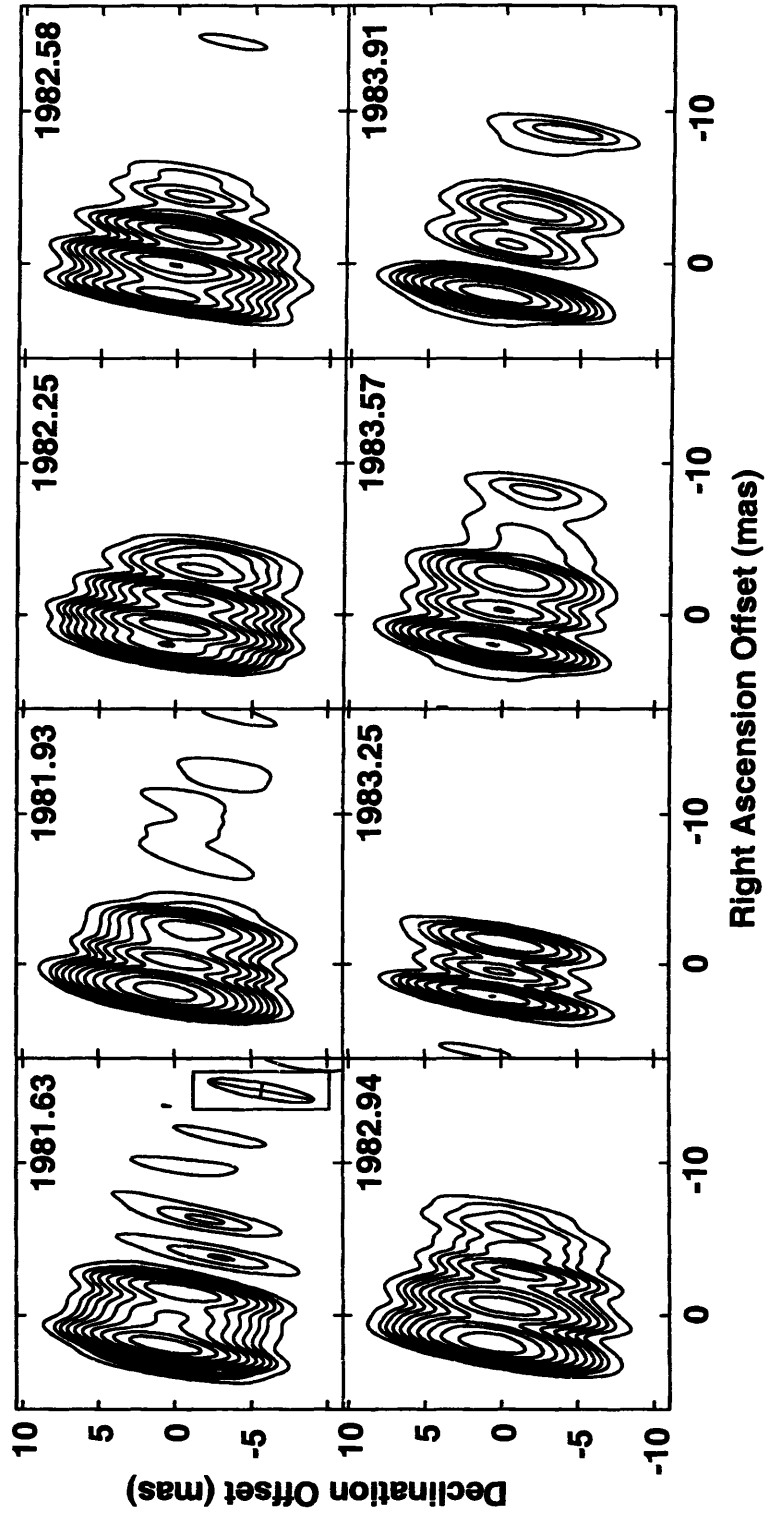


Figure 2

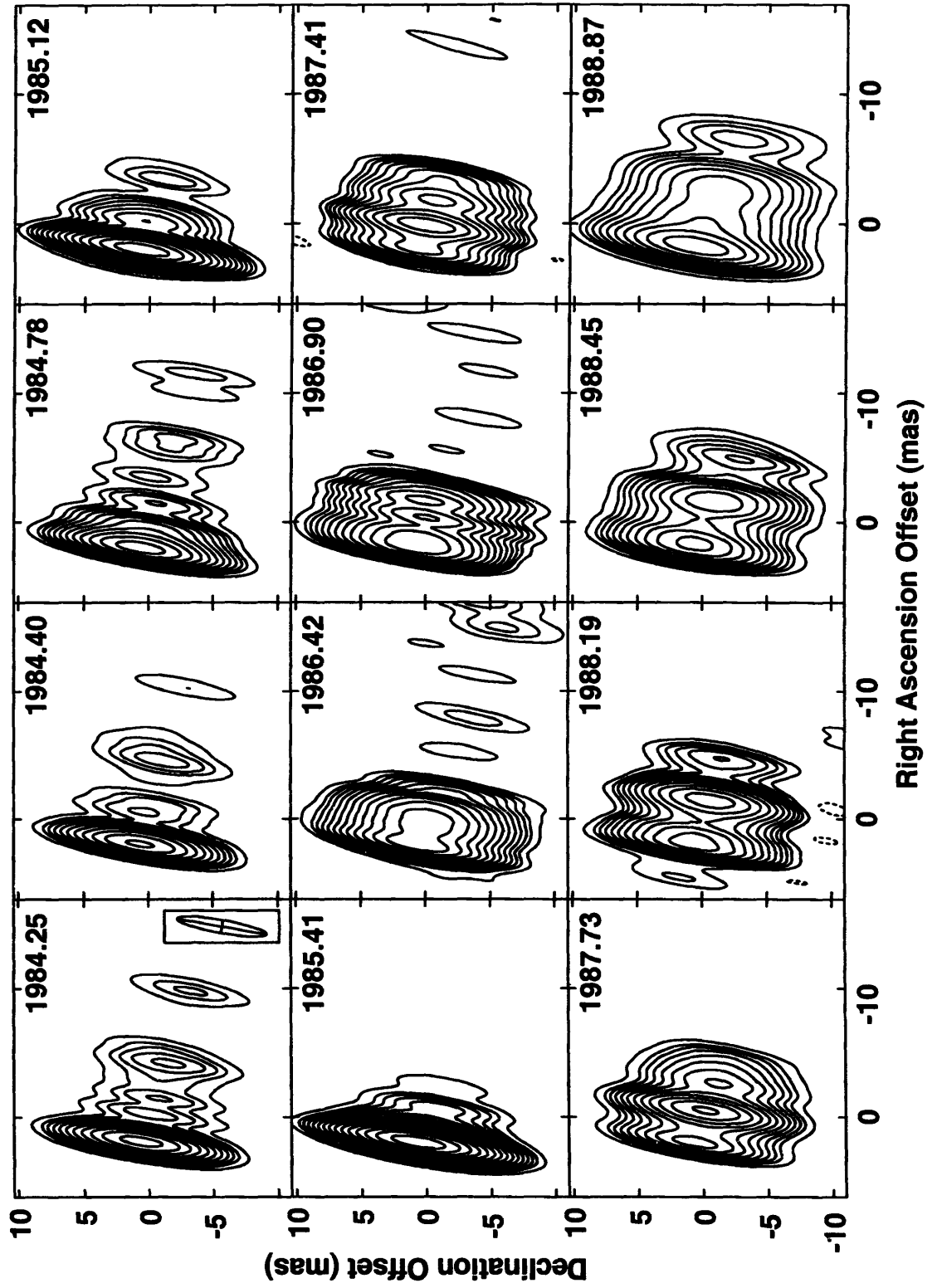


Figure 3

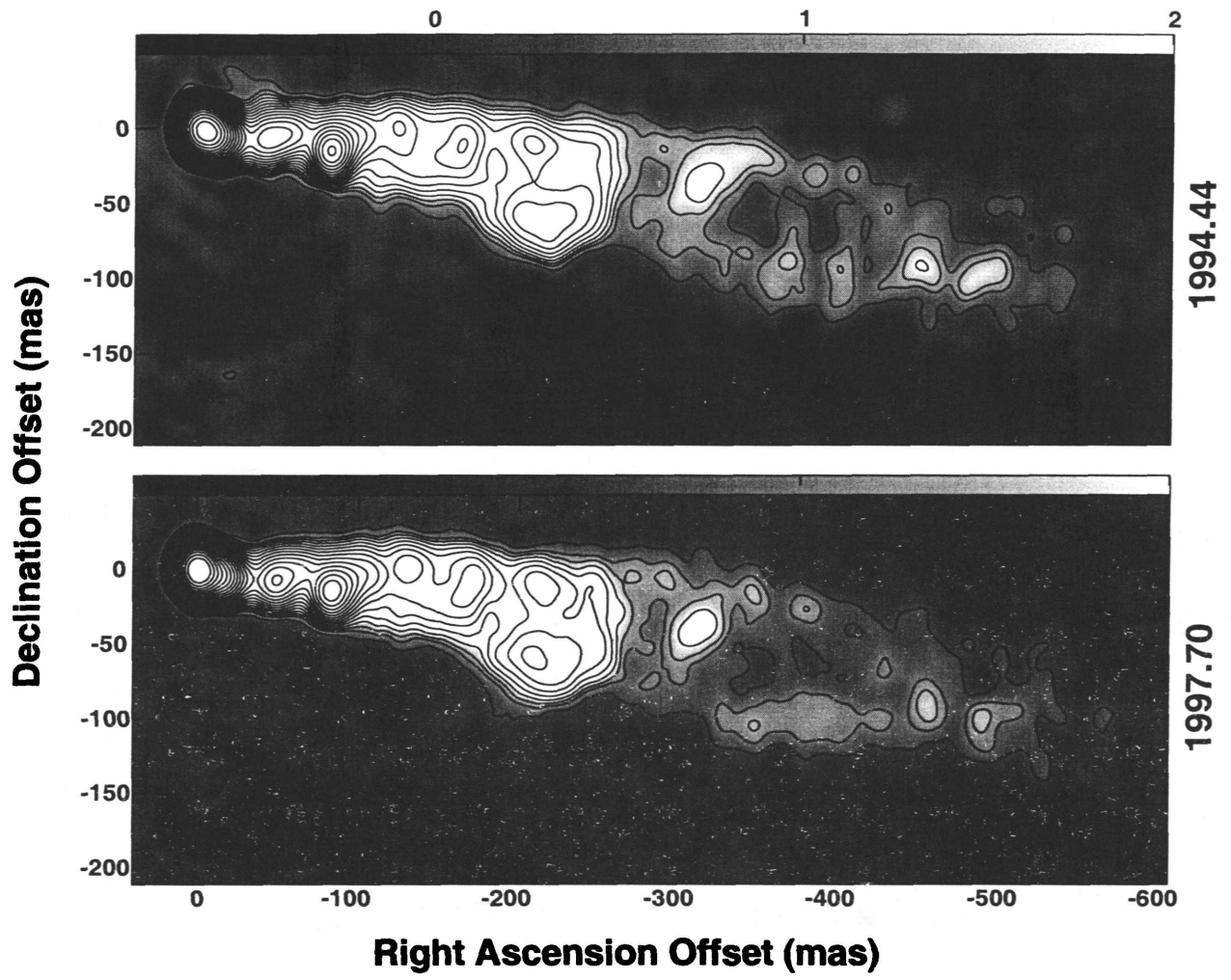
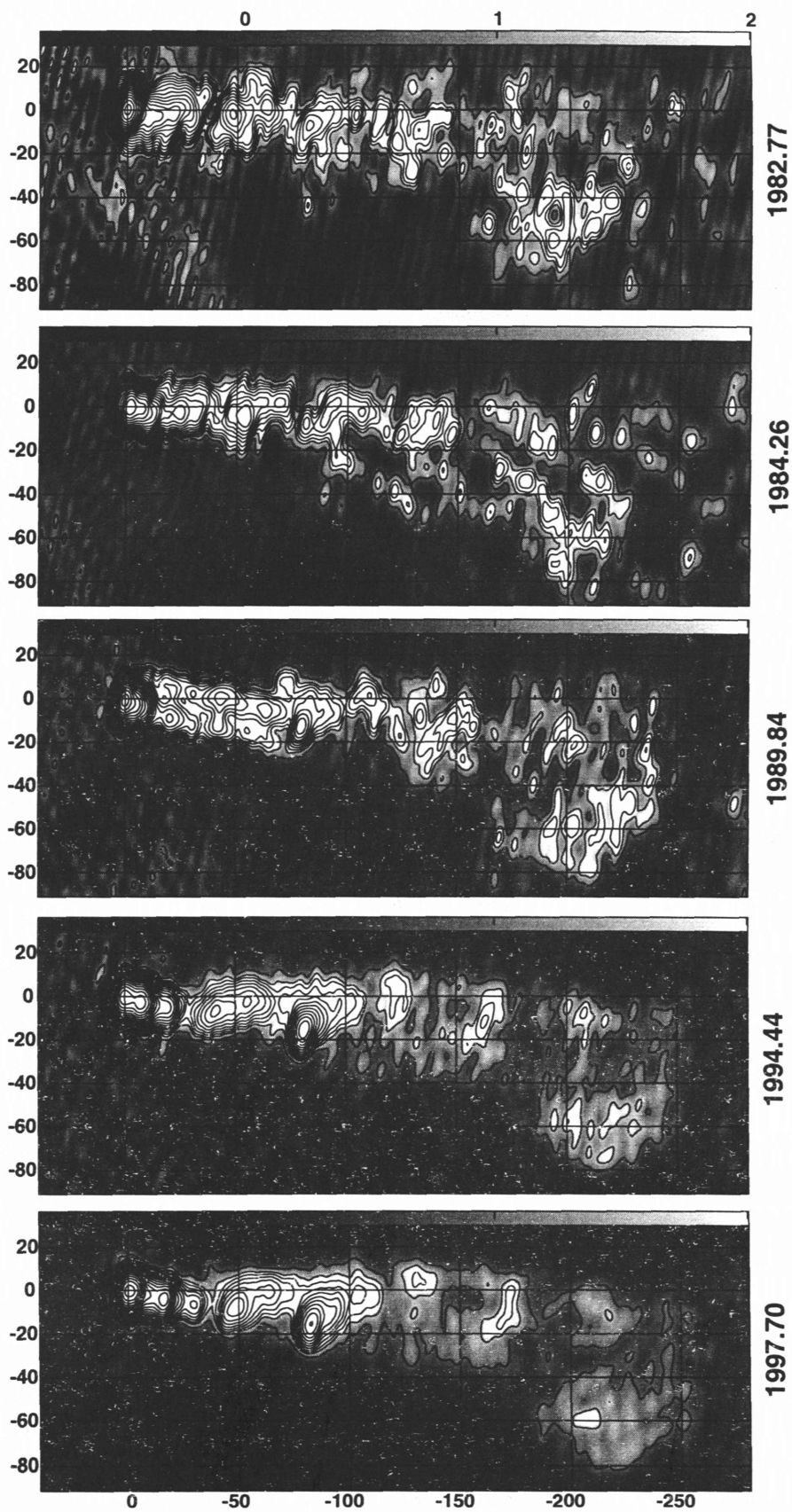


Figure 5

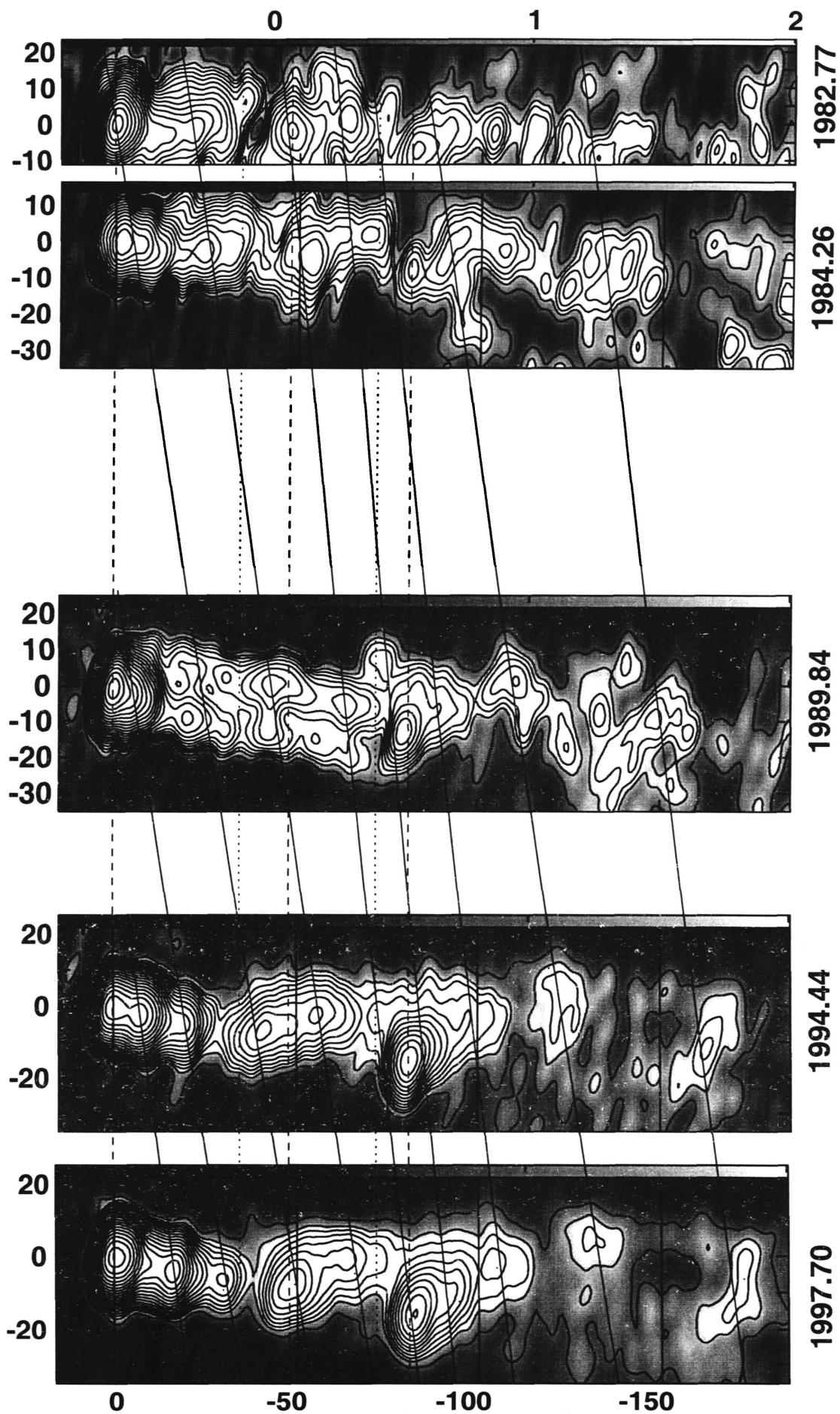


Declination Offset (mas)



Right Ascension Offset (mas)

**Declination Offset (mas)**



**Right Ascension Offset (mas)**



## **H<sub>2</sub>O Maser Emission in W49N**

Elizabeth J. McGrath '01, Vassar College (elmgrath@vassar.edu)

*Advisor: W. Miller Goss, NRAO–Socorro*

**Abstract:** W49A, one of the most energetic star forming regions in our galaxy, is located in the constellation Aquila in the galactic plane. This region is optically thick for wavelengths shorter than  $\sim 1$  cm. We have observed the northern part of this region (W49N) with the Very Large Array (VLA) at 43 GHz and 22 GHz in A and B configuration, with resolutions between  $0.045''$  and  $0.30''$  ( $0.0025$  pc to  $0.017$  pc at a distance of  $11.4$  kpc). Maser features in this source extend out to a few hundred km/s. We present here a map of 312 H<sub>2</sub>O masers overlaid on the continuum with a velocity range between  $-260$  km/s and  $+270$  km/s, whose relative positions we estimate are accurate to  $\sim 0.01''$ . The center of outflow of these maser features appears to be located between two ultra-compact (UC) HII regions, within  $0.2''$  of the bright source G2.

### **I. Introduction**

W49 is a well known HII region, first catalogued by Westerhout in 1958. It consists of two main regions—to the east, W49B, and to the west, W49A, separated by  $\sim 12'$ . W49B is a supernova remnant, while W49A is an intense star-forming region, divided into a northern and a southern component. In addition, there are many ultracompact (UC) HII regions within the northern component, W49N. Our observations center on W49N, where all the maser activity is taking place. In particular, we were interested in determining which UC HII region was associated with the maser activity.

H<sub>2</sub>O masers are important to study for many reasons. They are both signposts of star formation, and tracers of extremely dense ( $\sim 10^9$  cm<sup>-3</sup>) gas. H<sub>2</sub>O masers are also extremely intense—more so than any other masers—which makes them easy to observe. W49N, in particular, has maser sources ranging from 1 to 4000 Jy. If the Orion Nebula, at a distance of  $\sim 0.5$  kpc, was at the distance of W49 ( $\sim 11.4$  kpc as determined through HI absorption measurements by Gwinn, Moran & Reid 1992), then it would be an extremely faint continuum source—60 times fainter than W49.

Masers are the result of shocks from high density star-forming regions. Young stars have high velocity outflows that push into the dense surrounding gas region and form the shocks, which propagate through the material. The winds become entrapped behind the dense shells that they carve out, and we observe the masers that form on the edge of these shocked shells. The more massive the star, the more intense the maser emission. Masers have a population inversion which means that there are more electrons in the excited state than in the ground state. They release this energy through a rotational transition, much the same as a laser here on Earth.

Elitzur first demonstrated his theory of a jet-driven cocoon in 1995, where H<sub>2</sub>O masers form on the edge of the expanding shell. The shell expands quickly along the axis of the jet, and slower perpendicular to it. His model gives a dynamical timescale of only 300 years which accounts for why we don't see masers in the other UC HII regions in W49N—they've already passed their maser lifetime. Thus we are seeing W49N at a crucial stage in its star-forming history.

## II. Observations and Reductions

Maser observations of W49N were done using the VLA in line mode using 2 intermediate frequencies (IF's), at 22 GHz at four different time periods—24 July 1998, 6 September 1998, 26 June 1999, 18 July 1999. The 1998 data was in B configuration, with a resolution of 0.30", and the 1999 data was in A configuration, with a resolution of 0.045". The first IF was centered on velocity multiples of  $\pm 30$  km/s from the local standard of rest. IF 2 was centered on a velocity of +170 km/s. Phase referencing with our phase calibrator, 1923+210, was done in order to keep the phases coherent.

All data reduction was done with standard techniques using the NRAO package, AIPS (Astronomical Image Processing System). We found a strong maser feature in IF 2 in channel 31, at a velocity of 170.7 km/s which we used to self calibrate our data. Self calibration destroys all absolute positioning, so all maser positions are relative to this feature. We then used the position of this maser feature in our August 1998 continuum data as a reference to all other dates, and shifted the IF 1 cubes by the appropriate amount to ensure that ch 31 in IF 2 was at the correct reference coordinates. This uses the assumption that the ch 31 feature is moving by negligible amounts between observations. This allowed us to align the masers to our August continuum data. We also had continuum data from A configuration in April 1998 at 43 GHz, and continuum from the BIMA array (A and C configuration) at 90 GHz. These continuums were aligned to each other using the basic assumption that the continuum shows similar features at all frequencies. We estimate that our absolute astrometry is good to  $\sim 0.1''$  and our relative astrometry is good to  $\sim 0.01''$ . This is a factor of ten better than previous observations.

## III. Results and Conclusions

We catalogued a list 312 H<sub>2</sub>O maser positions between velocities  $-260$  and  $+270$  km/s. These show strikingly similar structure as the ones previously observed by Gwinn et al. 1992, Walker et al. 1982, and Moran et al. 1973. In particular, the three main clumps that are nearly vertical north-south remain apparent in all observations. And the pattern of an outflow from a central source is apparent, as well. Masers to the east show redshifted velocities, and masers to the west show blueshifted velocities. Note that this could not be due to rotation, as the velocities are too high. Thus, Elitzur's model of a jet-driven cocoon from a young star, or cluster of young stars, is the best model for the observations. We calculate the center of outflow of the masers to be within  $0.2''$  of the bright UC HII continuum source, G2.

### Acknowledgements

I would like to thank my advisor, Miller Goss, for his constant patience and wisdom throughout the project. In addition, I would like to thank my advisors at Vassar, Debra Elmegreen and Fred Chromey, for their support. Thanks to Niruj Mohan for his expertise in AIPS, and to Teddy Cheung for his help with DIFMAP.

I would also like to thank the NSF sponsored REU program for its generous grant that made this research possible.

### References

- Elitzur 1995, *Revista Mexicana de Astronomia y Astrofisica Serie de Conferencias*, 1, 85
- Gwinn, Moran & Reid 1992, *ApJ*, 393, 149
- Moran et al. 1973, *ApJ*, 185, 535
- Walker et al. 1982, *ApJ*, 255, 128
- Westerhout, G. 1958, *Bull. Ast. Inst. Netherlands*, 14, 215

TABLE 1. Maser Positions

RA (1950)	Dec (1950)	Velocity (km s <sup>-1</sup> )	RA error	DEC error	Flux (Jy)
19 07 49.8976	09 01 15.920	271.3	0.0001	0.001	6.3 ± 0.1
19 07 49.8918	09 01 16.009	259.1	0.0001	0.001	1.066 ± 0.027
19 07 49.8932	09 01 15.841	256.5	0.0000	0.000	17.094 ± 0.044
19 07 49.8938	09 01 15.866	253.2	0.0000	0.000	17.394 ± 0.042
19 07 49.8933	09 01 15.841	250.5	0.0000	0.000	3.203 ± 0.024
19 07 49.8971	09 01 15.901	247.9	0.0000	0.000	5.047 ± 0.024
19 07 49.8893	09 01 15.807	238.0	0.0001	0.001	1.335 ± 0.023
19 07 49.8968	09 01 15.903	236.7	0.0001	0.001	1.588 ± 0.021
19 07 49.8973	09 01 15.910	234.1	0.0001	0.001	1.120 ± 0.022
19 07 49.8818	09 01 15.858	232.7	0.0001	0.002	0.640 ± 0.022
19 07 49.8998	09 01 15.940	229.1	0.0002	0.004	0.437 ± 0.028
19 07 49.8900	09 01 15.816	227.1	0.0001	0.001	2.300 ± 0.028
19 07 49.8818	09 01 15.858	226.8	0.0000	0.001	2.177 ± 0.023
19 07 49.8688	09 01 15.594	225.8	0.0000	0.001	2.324 ± 0.025
19 07 49.8493	09 01 16.103	223.8	0.0000	0.000	3.160 ± 0.025
19 07 49.8499	09 01 16.104	218.6	0.0000	0.000	4.560 ± 0.025
19 07 49.8500	09 01 16.104	212.6	0.0000	0.000	7.143 ± 0.028
19 07 49.8478	09 01 15.715	211.3	0.0002	0.003	0.538 ± 0.024
19 07 49.8867	09 01 15.804	209.3	0.0000	0.000	3.608 ± 0.025
19 07 49.8867	09 01 15.900	207.4	0.0001	0.001	1.293 ± 0.025
19 07 49.8440	09 01 15.746	204.7	0.0001	0.001	1.118 ± 0.025
19 07 49.8865	09 01 15.822	204.1	0.0001	0.002	0.712 ± 0.028
19 07 49.8519	09 01 16.143	202.7	0.0000	0.000	9.120 ± 0.029
19 07 49.8673	09 01 15.773	201.4	0.0001	0.001	1.247 ± 0.029
19 07 49.8439	09 01 15.753	200.8	0.0001	0.002	0.910 ± 0.028
19 07 49.8464	09 01 16.097	199.1	0.0000	0.000	9.560 ± 0.035
19 07 49.8871	09 01 15.821	198.1	0.0001	0.001	1.040 ± 0.025
19 07 49.8672	09 01 15.774	197.8	0.0001	0.001	1.553 ± 0.032
19 07 49.8871	09 01 15.821	196.2	0.0001	0.001	1.726 ± 0.025
19 07 49.8684	09 01 15.788	194.5	0.0000	0.000	6.276 ± 0.028
19 07 49.8441	09 01 15.751	193.2	0.0000	0.000	4.126 ± 0.026
19 07 49.8529	09 01 16.131	191.2	0.0001	0.001	1.345 ± 0.025
19 07 49.8684	09 01 15.790	189.9	0.0000	0.001	2.235 ± 0.024
19 07 49.8672	09 01 15.776	187.3	0.0001	0.001	1.201 ± 0.026
19 07 49.8444	09 01 15.745	186.6	0.0000	0.000	11.011 ± 0.031
19 07 49.8517	09 01 15.789	183.3	0.0000	0.000	22.984 ± 0.053
19 07 49.8880	09 01 15.823	183.3	0.0000	0.001	5.869 ± 0.053
19 07 49.8442	09 01 15.749	181.3	0.0000	0.000	3.682 ± 0.027
19 07 49.8413	09 01 15.985	180.7	0.0001	0.001	2.161 ± 0.027
19 07 49.8521	09 01 16.128	179.3	0.0000	0.000	16.456 ± 0.042
19 07 49.8655	09 01 15.760	178.0	0.0000	0.000	22.122 ± 0.078
19 07 49.8490	09 01 16.087	178.0	0.0000	0.000	21.811 ± 0.078
19 07 49.8447	09 01 15.754	178.0	0.0001	0.001	5.582 ± 0.078
19 07 49.8412	09 01 15.985	178.0	0.0001	0.001	2.450 ± 0.078
19 07 49.8514	09 01 15.795	177.4	0.0000	0.000	10.169 ± 0.053
19 07 49.8836	09 01 15.803	175.4	0.0000	0.001	2.793 ± 0.028
19 07 49.8790	09 01 15.973	174.7	0.0001	0.001	1.553 ± 0.028
19 07 49.8519	09 01 16.114	172.8	0.0000	0.000	5.786 ± 0.042

TABLE 1. (continued)

RA (1950)	Dec (1950)	Velocity (km s <sup>-1</sup> )	RA error	DEC error	Flux (Jy)
19 07 49.8400	09 01 15.962	172.8	0.0000	0.000	13.214 ± 0.042
19 07 49.8788	09 01 15.973	172.1	0.0000	0.000	5.579 ± 0.036
19 07 49.8521	09 01 16.117	172.1	0.0000	0.000	5.850 ± 0.036
19 07 49.8843	09 01 15.789	172.1	0.0001	0.002	1.175 ± 0.036
19 07 49.8411	09 01 15.983	170.8	0.0000	0.001	9.812 ± 0.107
19 07 49.8443	09 01 15.748	170.1	0.0000	0.000	84.154 ± 0.154
19 07 49.8547	09 01 16.126	170.1	0.0001	0.002	3.982 ± 0.154
19 07 49.8521	09 01 15.792	168.8	0.0000	0.000	4.570 ± 0.037
19 07 49.8414	09 01 15.984	166.8	0.0000	0.000	94.67 ± 0.21
19 07 49.8541	09 01 16.108	165.8	0.0000	0.001	47.128 ± 0.169
19 07 49.8443	09 01 15.760	165.2	0.0000	0.001	85.52 ± 0.26
19 07 49.8443	09 01 15.747	164.8	0.0000	0.000	127.10 ± 0.24
19 07 49.8546	09 01 16.131	162.9	0.0000	0.000	7.420 ± 0.042
19 07 49.8649	09 01 15.824	159.9	0.0001	0.001	18.989 ± 0.122
19 07 49.8493	09 01 16.064	156.6	0.0000	0.001	25.060 ± 0.105
19 07 49.8728	09 01 15.809	154.6	0.0000	0.001	7.372 ± 0.023
19 07 49.8447	09 01 15.763	152.6	0.0000	0.001	29.697 ± 0.079
19 07 49.8551	09 01 16.125	152.0	0.0000	0.001	14.975 ± 0.045
19 07 49.8347	09 01 13.799	150.0	0.0000	0.001	21.236 ± 0.061
19 07 49.8455	09 01 15.760	146.7	0.0000	0.001	17.504 ± 0.049
19 07 49.8458	09 01 15.759	145.4	0.0000	0.001	19.919 ± 0.061
19 07 49.8705	09 01 15.784	144.1	0.0002	0.003	8.214 ± 0.120
19 07 49.8346	09 01 13.799	144.1	0.0000	0.001	38.095 ± 0.120
19 07 49.8495	09 01 16.068	138.8	0.0000	0.001	13.294 ± 0.036
19 07 49.8339	09 01 13.802	138.4	0.0007	0.011	2.271 ± 0.129
19 07 49.8810	09 01 15.856	136.2	0.0001	0.001	6.615 ± 0.035
19 07 49.9002	09 01 15.911	133.8	0.0001	0.001	7.447 ± 0.034
19 07 49.8347	09 01 13.798	131.2	0.0000	0.001	9.820 ± 0.036
19 07 49.8813	09 01 15.815	129.2	0.0000	0.001	14.159 ± 0.044
19 07 49.8438	09 01 14.198	127.2	0.0001	0.001	4.536 ± 0.022
19 07 49.8335	09 01 13.808	125.3	0.0002	0.004	9.927 ± 0.196
19 07 49.8828	09 01 15.801	124.0	0.0000	0.000	198.04 ± 0.50
19 07 50.5377	09 01 27.850	121.3	0.0004	0.006	1.415 ± 0.046
19 07 49.8435	09 01 15.786	121.3	0.0000	0.001	12.626 ± 0.046
19 07 49.8347	09 01 13.807	116.7	0.0001	0.001	4.086 ± 0.022
19 07 49.8433	09 01 14.137	116.7	0.0002	0.003	1.525 ± 0.022
19 07 49.8446	09 01 15.783	113.4	0.0000	0.001	42.609 ± 0.117
19 07 49.5333	09 01 16.008	113.4	0.0009	0.014	1.585 ± 0.117
19 07 49.8458	09 01 15.776	110.1	0.0000	0.001	13.668 ± 0.037
19 07 50.5369	09 01 27.846	108.8	0.0007	0.012	0.431 ± 0.026
19 07 49.5361	09 01 16.023	107.5	0.0000	0.001	20.422 ± 0.065
19 07 49.7829	09 01 14.872	105.2	0.0001	0.001	4.935 ± 0.035
19 07 49.8369	09 01 15.808	102.5	0.0001	0.001	22.445 ± 0.170
19 07 49.5366	09 01 16.022	101.9	0.0001	0.001	35.013 ± 0.154
19 07 49.8830	09 01 15.737	100.5	0.0000	0.001	154.82 ± 0.45
19 07 49.8357	09 01 15.811	99.2	0.0001	0.001	27.562 ± 0.138
19 07 49.5360	09 01 16.033	97.2	0.0000	0.000	101.98 ± 0.22
19 07 49.8399	09 01 15.006	94.6	0.0004	0.007	2.594 ± 0.094

TABLE 1. (continued)

RA (1950)	Dec (1950)	Velocity (km s <sup>-1</sup> )	RA error	DEC error	Flux (Jy)
19 07 49.6660	09 01 15.702	93.3	0.0005	0.008	2.140 ± 0.084
19 07 49.8826	09 01 15.735	92.0	0.0000	0.000	565.12 ± 1.47
19 07 49.6665	09 01 15.705	89.3	0.0002	0.003	1.676 ± 0.029
19 07 49.8436	09 01 14.312	87.4	0.0003	0.006	1.174 ± 0.034
19 07 49.8427	09 01 16.517	85.4	0.0002	0.003	2.869 ± 0.042
19 07 49.5366	09 01 16.034	84.7	0.0001	0.001	9.921 ± 0.045
19 07 49.8031	09 01 15.444	83.4	0.0001	0.001	5.382 ± 0.038
19 07 49.8396	09 01 14.011	81.4	0.0003	0.005	2.205 ± 0.059
19 07 49.8422	09 01 14.272	80.1	0.0003	0.004	1.880 ± 0.044
19 07 49.8143	09 01 15.685	78.8	0.0000	0.001	42.346 ± 0.111
19 07 49.8489	09 01 16.611	78.1	0.0001	0.002	6.768 ± 0.077
19 07 49.8204	09 01 15.674	74.8	0.0001	0.001	15.162 ± 0.079
19 07 49.8557	09 01 15.905	72.2	0.0001	0.001	42.339 ± 0.260
19 07 49.8572	09 01 16.594	70.5	0.0002	0.004	5.357 ± 0.120
19 07 49.8296	09 01 16.600	70.5	0.0002	0.004	5.375 ± 0.120
19 07 49.8817	09 01 15.833	67.9	0.0001	0.001	151.19 ± 0.78
19 07 49.8422	09 01 14.021	66.6	0.0001	0.002	17.099 ± 0.220
19 07 49.8579	09 01 16.574	64.6	0.0001	0.002	31.645 ± 0.400
19 07 49.8242	09 01 15.647	64.6	0.0003	0.005	14.402 ± 0.400
19 07 49.8303	09 01 16.592	64.0	0.0002	0.003	20.383 ± 0.356
19 07 49.8828	09 01 15.780	61.3	0.0001	0.001	415.13 ± 1.95
19 07 49.8328	09 01 15.479	61.3	0.0009	0.015	24.41 ± 1.95
19 07 49.8399	09 01 14.138	61.3	0.0007	0.012	29.70 ± 1.95
19 07 49.8518	09 01 15.926	58.7	0.0001	0.001	520.81 ± 3.39
19 07 49.9141	09 01 14.663	58.0	0.0010	0.016	31.88 ± 2.83
19 07 49.8287	09 01 16.653	58.0	0.0011	0.018	28.61 ± 2.83
19 07 49.9355	09 01 14.402	56.7	0.0007	0.012	147.63 ± 9.97
19 07 49.8799	09 01 15.727	56.7	0.0001	0.001	1414.0 ± 10.0
19 07 49.8641	09 01 16.620	56.7	0.0012	0.020	90.88 ± 9.97
19 07 49.8321	09 01 14.056	56.7	0.0011	0.019	96.49 ± 9.97
19 07 49.8514	09 01 15.926	55.4	0.0002	0.004	72.75 ± 1.57
19 07 49.8490	09 01 14.977	55.4	0.0005	0.008	35.25 ± 1.57
19 07 49.8292	09 01 16.572	54.1	0.0002	0.003	48.393 ± 0.818
19 07 49.8344	09 01 16.467	52.8	0.0002	0.003	24.156 ± 0.424
19 07 49.8502	09 01 15.949	52.1	0.0002	0.003	35.375 ± 0.507
19 07 49.8544	09 01 16.560	51.4	0.0003	0.005	34.195 ± 0.858
19 07 49.8360	09 01 15.525	51.4	0.0001	0.002	90.953 ± 0.858
19 07 49.8069	09 01 15.533	50.8	0.0003	0.006	20.667 ± 0.647
19 07 49.8602	09 01 16.600	48.1	0.0005	0.008	17.372 ± 0.747
19 07 49.8366	09 01 16.471	48.1	0.0001	0.002	62.836 ± 0.747
19 07 49.5378	09 01 16.038	45.5	0.0003	0.006	12.675 ± 0.382
19 07 49.8253	09 01 15.639	43.8	0.0002	0.003	36.789 ± 0.644
19 07 49.8818	09 01 15.826	43.5	0.0003	0.005	367.6 ± 10.3
19 07 49.8577	09 01 16.570	42.5	0.0002	0.003	27.897 ± 0.541
19 07 49.8413	09 01 14.018	41.2	0.0001	0.001	47.983 ± 0.360
19 07 49.8830	09 01 15.813	38.6	0.0001	0.001	319.01 ± 1.47
19 07 49.8576	09 01 16.565	37.2	0.0003	0.004	28.512 ± 0.642
19 07 49.8651	09 01 15.631	33.3	0.0002	0.003	164.26 ± 2.89



TABLE 1. (continued)

RA (1950)	Dec (1950)	Velocity (km s <sup>-1</sup> )	RA error	DEC error	Flux (Jy)
19 07 49.8819	09 01 15.831	33.3	0.0000	0.001	767.16 ± 2.89
19 07 49.8061	09 01 15.494	32.6	0.0007	0.011	40.88 ± 2.56
19 07 49.8570	09 01 16.619	32.6	0.0005	0.008	59.95 ± 2.56
19 07 49.5368	09 01 16.035	31.3	0.0007	0.011	11.641 ± 0.691
19 07 49.8229	09 01 16.642	29.3	0.0007	0.012	12.322 ± 0.801
19 07 49.7993	09 01 15.529	29.3	0.0010	0.016	8.868 ± 0.801
19 07 49.5384	09 01 16.035	27.4	0.0004	0.007	31.25 ± 1.13
19 07 49.8830	09 01 15.851	27.4	0.0001	0.001	245.94 ± 1.13
19 07 49.8250	09 01 16.616	26.0	0.0005	0.008	13.353 ± 0.591
19 07 49.5371	09 01 16.027	24.7	0.0003	0.005	26.293 ± 0.796
19 07 49.8470	09 01 13.997	24.1	0.0003	0.005	40.03 ± 1.04
19 07 49.8821	09 01 15.853	24.1	0.0001	0.001	218.79 ± 1.04
19 07 49.7953	09 01 14.993	23.4	0.0002	0.004	45.685 ± 0.940
19 07 50.5362	09 01 27.866	23.4	0.0004	0.007	24.531 ± 0.940
19 07 50.5355	09 01 27.846	21.4	0.0004	0.006	39.44 ± 1.41
19 07 49.7749	09 01 15.594	20.8	0.0010	0.017	18.89 ± 1.81
19 07 49.8065	09 01 15.515	20.8	0.0007	0.012	27.24 ± 1.81
19 07 49.8832	09 01 15.840	20.1	0.0001	0.002	243.11 ± 2.33
19 07 49.8526	09 01 16.532	19.5	0.0001	0.002	239.05 ± 2.77
19 07 49.9123	09 01 15.153	19.5	0.0011	0.018	27.07 ± 2.77
19 07 49.8491	09 01 14.031	18.1	0.0003	0.004	478.1 ± 11.2
19 07 49.8487	09 01 15.923	16.2	0.0002	0.002	285.51 ± 3.82
19 07 49.8102	09 01 15.822	16.2	0.0002	0.002	284.53 ± 3.82
19 07 49.7696	09 01 15.537	15.5	0.0004	0.006	85.06 ± 2.89
19 07 49.3866	09 01 13.958	15.5	0.0004	0.007	73.79 ± 2.89
19 07 49.8254	09 01 15.492	14.9	0.0005	0.008	89.29 ± 4.07
19 07 49.8853	09 01 15.854	14.5	0.0001	0.001	313.95 ± 1.83
19 07 50.5217	09 01 27.636	13.8	0.0001	0.002	237.25 ± 3.00
19 07 49.8556	09 01 16.562	13.2	0.0008	0.014	36.37 ± 2.77
19 07 49.8532	09 01 14.149	13.2	0.0003	0.005	103.56 ± 2.77
19 07 49.8549	09 01 15.924	12.5	0.0004	0.007	102.84 ± 4.20
19 07 49.8373	09 01 13.820	12.5	0.0007	0.011	69.37 ± 4.20
19 07 49.8862	09 01 15.846	11.2	0.0002	0.003	424.00 ± 7.93
19 07 49.7681	09 01 15.598	11.2	0.0003	0.005	290.29 ± 7.93
19 07 49.8026	09 01 15.588	9.2	0.0001	0.001	5039.3 ± 31.2
19 07 49.8376	09 01 14.682	9.2	0.0007	0.012	480.6 ± 31.2
19 07 49.8571	09 01 14.002	7.9	0.0008	0.014	312.6 ± 23.5
19 07 49.8082	09 01 15.253	5.9	0.0001	0.002	1083.9 ± 10.5
19 07 50.5221	09 01 27.469	5.3	0.0006	0.009	98.81 ± 5.03
19 07 49.8532	09 01 15.897	3.9	0.0001	0.001	383.97 ± 3.12
19 07 49.7677	09 01 15.565	3.9	0.0001	0.002	306.79 ± 3.12
19 07 49.8012	09 01 15.827	3.3	0.0001	0.001	362.19 ± 2.09
19 07 49.8530	09 01 15.991	2.0	0.0001	0.001	220.78 ± 1.61
19 07 49.8136	09 01 15.178	0.7	0.0001	0.001	282.02 ± 1.44
19 07 49.8537	09 01 15.995	-0.7	0.0002	0.003	109.61 ± 1.79
19 07 49.8403	09 01 15.442	-0.7	0.0001	0.002	161.05 ± 1.79
19 07 49.7692	09 01 15.627	-0.7	0.0002	0.003	118.04 ± 1.79
19 07 49.8144	09 01 15.149	-1.3	0.0001	0.001	242.45 ± 1.73

TABLE 1. (continued)

RA (1950)	Dec (1950)	Velocity (km s <sup>-1</sup> )	RA error	DEC error	Flux (Jy)
19 07 49.8416	09 01 15.422	-3.3	0.0001	0.002	188.18 ± 2.06
19 07 49.7476	09 01 15.383	-3.9	0.0001	0.001	349.90 ± 2.59
19 07 49.8036	09 01 15.574	-6.6	0.0001	0.001	2065.7 ± 9.5
19 07 49.7711	09 01 15.696	-9.2	0.0001	0.001	510.37 ± 3.07
19 07 49.7714	09 01 15.687	-13.2	0.0001	0.001	544.20 ± 2.83
19 07 49.7705	09 01 15.618	-15.8	0.0003	0.004	909.4 ± 22.2
19 07 49.8040	09 01 15.160	-15.8	0.0006	0.011	373.0 ± 22.2
19 07 49.8033	09 01 15.306	-16.8	0.0001	0.001	506.50 ± 3.32
19 07 49.8085	09 01 15.829	-21.4	0.0001	0.002	133.44 ± 1.22
19 07 49.7718	09 01 15.655	-25.4	0.0001	0.001	126.52 ± 0.99
19 07 49.8111	09 01 15.863	-25.4	0.0001	0.002	77.835 ± 0.988
19 07 49.8040	09 01 15.346	-33.3	0.0001	0.001	2516.6 ± 14.4
19 07 49.7711	09 01 15.639	-36.6	0.0001	0.002	178.38 ± 1.69
19 07 49.8102	09 01 15.807	-37.2	0.0001	0.001	182.38 ± 1.35
19 07 49.7709	09 01 15.688	-41.8	0.0001	0.002	339.34 ± 3.68
19 07 49.8023	09 01 15.676	-43.8	0.0001	0.001	1353.8 ± 7.0
19 07 49.7729	09 01 15.585	-45.8	0.0010	0.016	107.72 ± 9.83
19 07 49.8143	09 01 15.895	-47.5	0.0001	0.001	109.57 ± 0.56
19 07 49.8053	09 01 15.371	-48.8	0.0001	0.001	71.568 ± 0.451
19 07 49.8034	09 01 15.668	-54.1	0.0001	0.001	1644.6 ± 6.8
19 07 49.7710	09 01 15.687	-58.7	0.0000	0.001	1826.6 ± 7.0
19 07 49.8027	09 01 15.679	-60.0	0.0001	0.001	619.31 ± 3.99
19 07 49.7713	09 01 15.691	-60.7	0.0001	0.001	1243.0 ± 6.8
19 07 49.8020	09 01 15.678	-67.2	0.0001	0.002	106.28 ± 1.09
19 07 49.8328	09 01 15.534	-70.9	0.0001	0.002	308.74 ± 3.42
19 07 49.7721	09 01 15.682	-72.5	0.0001	0.001	4791.3 ± 2.4
19 07 49.8333	09 01 15.534	-73.8	0.0001	0.001	716.22 ± 4.54
19 07 49.8015	09 01 15.679	-76.2	0.0001	0.001	570.63 ± 1.70
19 07 49.7714	09 01 15.570	-76.8	0.0000	0.001	523.48 ± 1.72
19 07 49.8316	09 01 15.534	-79.5	0.0001	0.001	233.59 ± 0.90
19 07 49.8124	09 01 15.887	-80.1	0.0001	0.001	178.90 ± 0.92
19 07 49.8048	09 01 15.415	-82.8	0.0001	0.001	177.59 ± 0.83
19 07 49.8322	09 01 15.530	-84.1	0.0000	0.000	325.20 ± 0.70
19 07 49.8322	09 01 15.533	-86.1	0.0000	0.000	868.9 ± 1.8
19 07 49.7665	09 01 15.617	-88.7	0.0000	0.001	88.89 ± 0.25
19 07 49.7989	09 01 15.621	-92.0	0.0001	0.001	45.812 ± 0.182
19 07 49.7696	09 01 15.638	-92.6	0.0000	0.000	98.74 ± 0.21
19 07 49.8312	09 01 15.535	-95.9	0.0001	0.001	32.776 ± 0.207
19 07 49.8053	09 01 15.525	-97.9	0.0001	0.001	48.255 ± 0.191
19 07 49.7718	09 01 15.667	-100.5	0.0000	0.000	349.80 ± 0.78
19 07 49.8325	09 01 15.537	-100.9	0.0001	0.002	99.75 ± 0.82
19 07 49.7752	09 01 15.744	-102.5	0.0000	0.000	461.69 ± 0.93
19 07 49.7731	09 01 15.714	-103.6	0.0001	0.001	197.43 ± 0.76
19 07 49.8317	09 01 15.540	-103.8	0.0001	0.001	40.241 ± 0.269
19 07 49.8072	09 01 15.534	-107.5	0.0002	0.004	28.092 ± 0.540
19 07 49.8045	09 01 15.307	-112.1	0.0004	0.006	44.73 ± 1.33
19 07 49.7711	09 01 15.668	-113.4	0.0000	0.000	1209.7 ± 3.1
19 07 49.8411	09 01 15.559	-120.7	0.0003	0.005	19.014 ± 0.530

TABLE 1. (continued)

RA (1950)	Dec (1950)	Velocity (km s <sup>-1</sup> )	RA error	DEC error	Flux (Jy)
19 07 49.7702	09 01 15.684	-195.5	0.0000	0.000	12.163 ± 0.069
19 07 49.7541	09 01 15.466	-195.8	0.0001	0.001	3.560 ± 0.106
19 07 49.7542	09 01 15.462	-196.2	0.0001	0.001	2.886 ± 0.072
19 07 49.8036	09 01 15.475	-199.5	0.0000	0.000	67.587 ± 0.121
19 07 49.7466	09 01 15.347	-200.1	0.0001	0.001	4.412 ± 0.097
19 07 49.8080	09 01 15.380	-201.5	0.0000	0.000	10.691 ± 0.070
19 07 49.8035	09 01 15.481	-204.7	0.0000	0.000	991.1 ± 1.9
19 07 49.7467	09 01 15.348	-206.7	0.0001	0.001	13.295 ± 0.290
19 07 49.8032	09 01 15.482	-208.0	0.0000	0.000	917.2 ± 1.9
19 07 49.7628	09 01 15.451	-212.6	0.0001	0.001	1.816 ± 0.028
19 07 49.7416	09 01 15.194	-222.3	0.0001	0.002	0.883 ± 0.032
19 07 49.7337	09 01 15.302	-223.6	0.0001	0.001	1.180 ± 0.028
19 07 49.8177	09 01 15.553	-225.5	0.0002	0.003	0.640 ± 0.030
19 07 49.8044	09 01 15.483	-225.5	0.0000	0.000	8.551 ± 0.030
19 07 49.7592	09 01 15.436	-228.8	0.0000	0.000	15.545 ± 0.044
19 07 49.7416	09 01 15.199	-230.1	0.0000	0.000	10.668 ± 0.090
19 07 49.8048	09 01 15.481	-231.5	0.0000	0.000	15.893 ± 0.047
19 07 49.7592	09 01 15.433	-232.8	0.0000	0.000	28.461 ± 0.090
19 07 49.7415	09 01 15.205	-236.7	0.0000	0.000	5.362 ± 0.028
19 07 49.7592	09 01 15.434	-238.0	0.0000	0.000	9.754 ± 0.030
19 07 49.7535	09 01 15.397	-242.6	0.0000	0.000	4.209 ± 0.022
19 07 49.7589	09 01 15.428	-245.3	0.0000	0.000	2.374 ± 0.022
19 07 49.7337	09 01 15.080	-248.5	0.0000	0.000	8.791 ± 0.027
19 07 49.7339	09 01 15.080	-255.8	0.0000	0.000	3.542 ± 0.025

TABLE 1. (continued)

RA (1950)	Dec (1950)	Velocity (km s <sup>-1</sup> )	RA error	DEC error	Flux (Jy)
19 07 49.8052	09 01 15.858	-123.9	0.0001	0.002	67.82 ± 0.61
19 07 49.8054	09 01 15.462	-129.9	0.0000	0.000	182.41 ± 0.46
19 07 49.8072	09 01 15.535	-133.2	0.0001	0.001	59.592 ± 0.320
19 07 49.8052	09 01 15.428	-133.6	0.0001	0.002	77.77 ± 0.72
19 07 49.7720	09 01 15.671	-133.6	0.0000	0.001	218.98 ± 0.72
19 07 49.8026	09 01 15.702	-137.5	0.0001	0.001	159.16 ± 0.90
19 07 49.7719	09 01 15.659	-138.8	0.0000	0.000	289.06 ± 0.67
19 07 49.7711	09 01 15.670	-142.8	0.0000	0.000	299.57 ± 0.66
19 07 49.8013	09 01 15.869	-145.4	0.0002	0.003	22.037 ± 0.288
19 07 49.7714	09 01 15.671	-146.1	0.0000	0.000	152.60 ± 0.36
19 07 49.8188	09 01 15.645	-147.4	0.0001	0.001	31.641 ± 0.147
19 07 49.8387	09 01 15.474	-147.4	0.0002	0.002	11.516 ± 0.147
19 07 49.8169	09 01 15.673	-151.3	0.0001	0.001	22.147 ± 0.129
19 07 49.7712	09 01 15.661	-152.0	0.0000	0.000	90.09 ± 0.20
19 07 49.8021	09 01 15.820	-152.6	0.0001	0.002	19.840 ± 0.161
19 07 49.8185	09 01 15.649	-154.6	0.0001	0.002	6.712 ± 0.070
19 07 49.7718	09 01 15.650	-160.3	0.0000	0.000	103.80 ± 0.23
19 07 49.8046	09 01 15.420	-162.5	0.0001	0.001	13.942 ± 0.053
19 07 49.7719	09 01 15.649	-162.9	0.0000	0.000	130.84 ± 0.24
19 07 49.7668	09 01 15.451	-163.6	0.0001	0.002	9.796 ± 0.260
19 07 49.8039	09 01 15.464	-164.2	0.0000	0.000	33.645 ± 0.134
19 07 49.8047	09 01 15.867	-165.5	0.0002	0.003	1.299 ± 0.072
19 07 49.8098	09 01 15.591	-166.2	0.0002	0.003	1.356 ± 0.076
19 07 49.7561	09 01 15.347	-168.8	0.0001	0.001	2.338 ± 0.043
19 07 49.7668	09 01 15.454	-169.5	0.0000	0.001	3.392 ± 0.039
19 07 49.7721	09 01 15.660	-173.4	0.0000	0.000	84.737 ± 0.166
19 07 49.7666	09 01 15.452	-174.7	0.0001	0.001	2.598 ± 0.039
19 07 49.7439	09 01 15.141	-174.7	0.0001	0.001	1.786 ± 0.039
19 07 49.8153	09 01 15.835	-174.7	0.0001	0.002	1.043 ± 0.039
19 07 49.7471	09 01 15.350	-175.4	0.0001	0.001	1.591 ± 0.030
19 07 49.8150	09 01 15.831	-178.7	0.0000	0.001	4.609 ± 0.045
19 07 49.7642	09 01 15.701	-178.7	0.0001	0.001	2.436 ± 0.045
19 07 49.7842	09 01 15.483	-179.3	0.0000	0.000	4.917 ± 0.052
19 07 49.7620	09 01 15.782	-179.3	0.0001	0.001	2.180 ± 0.052
19 07 49.8048	09 01 15.482	-180.0	0.0000	0.000	12.505 ± 0.053
19 07 49.7467	09 01 15.351	-180.7	0.0001	0.001	2.079 ± 0.046
19 07 49.7651	09 01 15.455	-181.3	0.0001	0.001	2.121 ± 0.036
19 07 49.7468	09 01 15.349	-184.6	0.0000	0.000	5.814 ± 0.036
19 07 49.7606	09 01 15.786	-185.3	0.0002	0.003	0.753 ± 0.035
19 07 49.7469	09 01 15.346	-186.6	0.0000	0.001	7.330 ± 0.069
19 07 49.7633	09 01 15.441	-186.6	0.0001	0.001	4.333 ± 0.069
19 07 49.7560	09 01 15.275	-187.2	0.0000	0.000	27.555 ± 0.076
19 07 49.7709	09 01 15.680	-188.5	0.0000	0.000	11.180 ± 0.059
19 07 49.7634	09 01 15.440	-189.2	0.0000	0.000	8.813 ± 0.058
19 07 49.7542	09 01 15.471	-189.9	0.0001	0.001	4.602 ± 0.058
19 07 49.7469	09 01 15.349	-191.2	0.0000	0.000	22.176 ± 0.061
19 07 49.7467	09 01 15.349	-193.6	0.0000	0.000	21.955 ± 0.063
19 07 49.7637	09 01 15.448	-194.9	0.0000	0.001	5.498 ± 0.060



# VLBA Imaging of the CfA Seyferts

Cristina M. Murray

Advisor: Jack Gallimore

## Introduction

Seyfert Galaxies are low power active galactic nuclei. It is popularly thought that the radio sources of Seyfert galaxies are low-power analogs of the radio jets found in radio galaxies and quasi-stellar objects (QSOs). The support for this notion is that the VLA and MERLIN telescopes have resolved linear radio structures in a handful of relatively bright Seyfert galaxies. In fact, looking at systematic surveys of Seyfert galaxies, only 10 – 20% clearly resolve into linear radio structures that resemble jets; the majority of Seyfert galaxies are faint point sources at centimeter wavelengths.

It is further interesting to examine the main differences between known Seyfert jets and the jets in more powerful active galaxies. Seyfert jets tend not to display the “double lobe” structure that defines radio galaxies, although there are exceptions (e.g., NGC 1068, NGC 2110). Often compact knots along the outflow axis dominate the radio emission, giving the appearance of “beads on a string” on radio images (e.g., Mkn 3, NGC 4151). The radio structure often appears disturbed, with position angle changing from the innermost regions to the outermost extent of the jet. It appears that flat-spectrum cores are uncommon among Seyfert galaxies. Finally, Seyfert jets tend to be much fainter and smaller than the jets of radio galaxies.

The relative paucity of obvious jets and the morphological differences between Seyfert jets and radio galaxy jets raise several questions about the nature of the radio sources in Seyfert galaxies. Firstly, are the unresolved sources jets? The radio sources in Seyfert galaxies are often weak enough and insufficiently resolved that active star-formation near the nucleus might account for the radio emission. Secondly, why are the Seyfert jets so stunted and deformed? In this regard Seyferts might be compared with Compact Symmetric Objects; either the jets are young, and they have not yet expanded to their maximum extent, or they suffer birth defects owing to interaction with a dense interstellar medium. Finally, where are the flat spectrum sources? Eventually, faint flat-spectrum sources in QSOs and radio galaxies turn up with sensitive imaging. Why are there so few flat-spectrum sources in Seyfert galaxies?

To address these questions, we have begun a series of systematic studies of the compact radio structure of Seyfert galaxies. The present work focuses on a radio flux-limited subsample of the CfA Seyfert catalog (Huchra & Burg 1992), in which Seyfert galaxies were identified by optical spectroscopy. The observations employed the Very Long Baseline Array (VLBA) of the National Radio Astronomy Observatory. The VLBA is the first VLBI array with dedicated phase-referencing capabilities. Phase-referencing was vital to this work because the sources are much too faint for self-referencing using standard

VLBI techniques. Our main goals were (1) to resolve compact radio structure and explore the radio morphology; (2) to search for compact, flat-spectrum sources that may have been confused with surrounding steep-spectrum emission; and (3) to look for evidence of free-free absorption that might hide radio structure very near the central engine. This latter goal is motivated by a prediction of the Seyfert unifying schemes, in which it is proposed that the central engine of Seyfert galaxies is surrounded by a parsec-scale ring of molecular gas. The ionized surface of the ring may be highly opaque to centimeter-wave radio emission (Neufeld, Maloney, & Conger 1994).

## **Sample**

We chose to observe those Seyfert galaxies from the CfA survey with unresolved flux sufficient to be detected by the VLBA. In particular, we selected targets from the 8.4 GHz, VLA A-array survey of Kulkarni et al. (1995). The flux cutoff was 3.5 mJy in unresolved flux at 8.4 GHz, so that either flat-spectrum or steep spectrum emission might be detected by the VLBA at 2.2 GHz. Twelve Seyfert galaxies satisfied this cutoff, out of which eight had not yet been observed with the VLBA. We elected to observe those eight Seyferts that had not previously been observed.

## **Observations and Data Reduction**

We observed each target Seyfert with two-hour snapshots as they transited the Pie Town telescope in New Mexico. All ten antennas of the VLBA were used for the observations. Observations also employed the S/X-band dichroic which enables simultaneous scans at 2.2 and 8.4 GHz. Phase-referencing was performed against nearby calibrators with a duty cycle of three minutes on-source and 2.5 minutes on reference. All of the references were within three degrees of their targets, except for the Seyfert galaxy NGC 5252, for which the reference was over five degrees away. The calibrator for NGC 5252 was also resolved at S-band. The undesirable characteristics of the phase reference may have affected the image quality and astrometry of the NGC 5252 data.

Data reduction followed the conventional procedures as outlined in the AIPS cookbook. We developed an automated reduction script, VLBACAL, to process the data in a uniform manner. The only deviation from the conventional reduction procedure was that we aligned the intermediate frequencies (IFs) using scans of a bright fringe reference source rather than using the internal pulse calibrator.

## **Results**

We detected six of the eight sources at 2.2 GHz. NGC 7682 suffered from a well-resolved calibrator, and the data could not be phase referenced at 2.2 GHz. Mrk 766 was not detected at the  $0.1 \text{ mJy beam}^{-1}$  sensitivity of this survey. Four sources were detected at 8.4 GHz: Mrk 533, NGC 4235, NGC 5252, and NGC 7682.

All of the detected VLBI sources resolve into structures that are compatible with jet morphology. The following table summarizes the VLBI structure of the detected sources in comparison with the known VLA morphology.

Source ID	Reference	VLA (8.4 GHz)	S-Band (2.2 GHz)	X-Band (8.4 GHz)	Flat- spectrum?
0152+06	a	Unresolved	10 pc double	—	—
Mrk 231	b	Unresolved	40 pc jet (L-band)	10 pc, extended source	Inverted
Mrk 533	a	1 kpc double	10 pc double + jet	10 pc triple	—
Mrk 766	a	Unresolved	—	—	—
NGC 1068	c	Kpc-scale jet	Multiple, resolved components (L-band)	Multiple, resolved components	Resolved flat-spectrum source
NGC 3079	d	90 pc extended			
NGC 3227	a	40 pc extended	1 pc double	—	—
NGC 4151	e	300 pc, linear jet	Multiple resolved components (L-band)	Two resolved components	—
NGC 4235	a	Compact, flat spectrum	1 pc double	Unresolved	Inverted
NGC 5252	a	Unresolved, steep spectrum	Extended	Unresolved	New flat spectrum source
NGC 7469		Unresolved	?	?	?
NGC 7682	a	Unresolved	—	2 pc triple + jet	—

**Notes:** The VLA properties were taken from Kukula et al. 1995. References for VLBI structure: (a) This work; (b) Ulvestad, Wrobel, & Carilli 1999; (b) Ulvestad et al. 1998; (c) Gallimore, Baum, & O’Dea 1997; (d) Trotter et al. 1999; (e) Ulvestad et al. 1998. We note that Mundell and collaborators have independently detected the flat-spectrum source in NGC 5252 (Mundell et al. 2000).

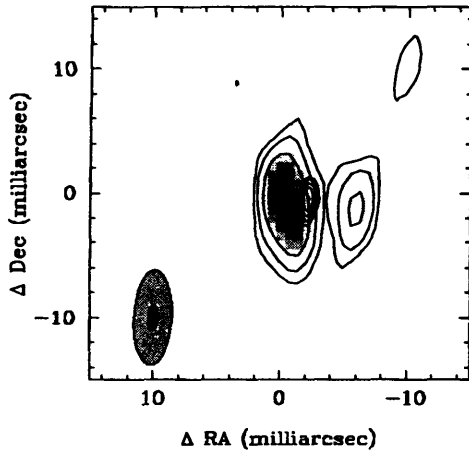
We find evidence that the parsec-scale jet structure tends to misalign with the VLA-scale structure. Typical bending angles are 10 – 20 degrees. It seems likely that the jets are interacting with interstellar clouds as they travel away from the nucleus. Mrk 231, NGC 1068, and NGC 4151 present the most extreme cases, in which the parsec-scale structure is nearly perpendicular to the jet on larger scales. In these cases, the parsec-scale radio



emission probably traces the working surfaces of shock fronts where the jet interacts with the interstellar medium.

### NGC 4235

NGC 4235 presents a special case because it is long known to host a compact, flat-spectrum source. At 2.2 GHz, the VLBA resolves the radio structure into a double source, but at 8.4 GHz there is only a single compact source. The following figure compares the locations of the 2.2 and 8.4 GHz sources.



The 2.2 GHz data are represented by dark contours on grayscale, and the 8.4 GHz data are represented by shaded contours. The shaded (dark) ellipse in the lower left corner indicates the beam size at 2.2 GHz (8.4 GHz). The coordinates are referenced to the position of the peak on the 2.2 GHz image.

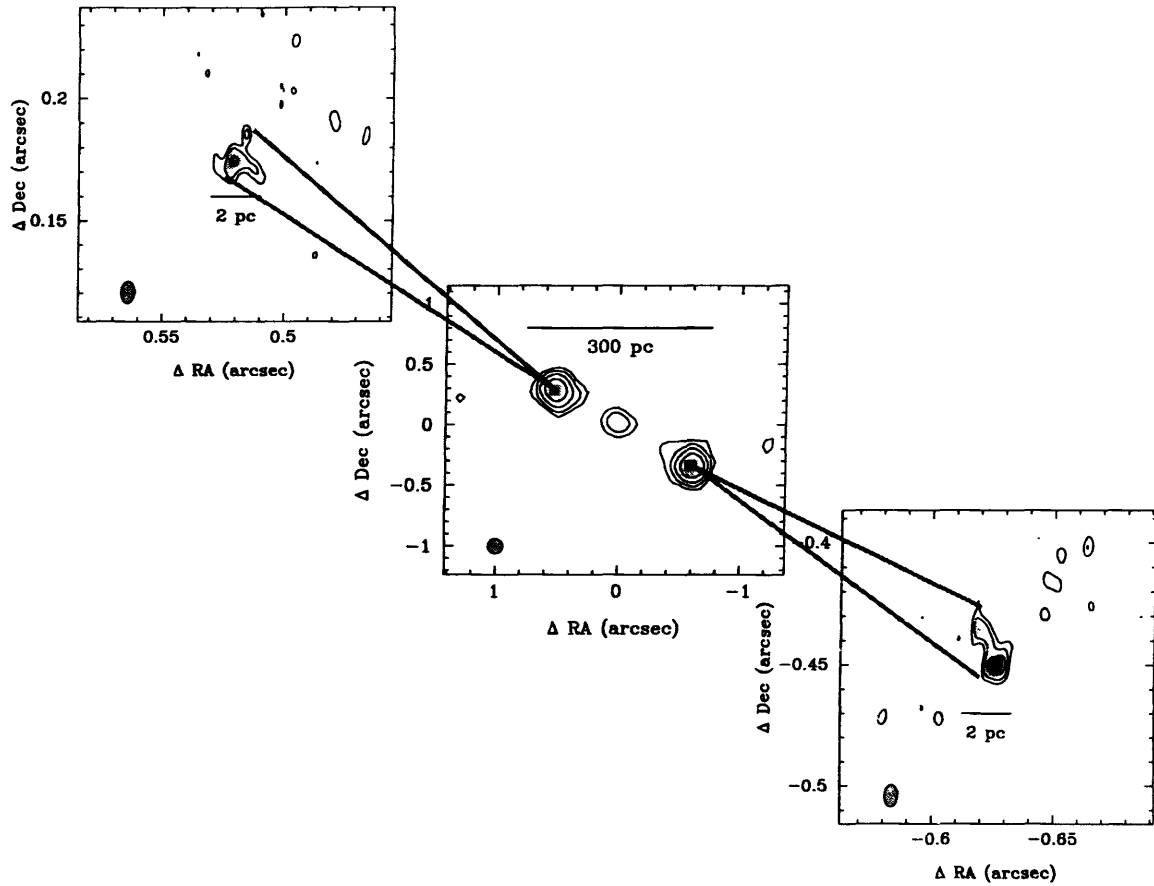
We find that the peak of the 8.4 GHz data is offset towards the center of the two 2.2 GHz features. This result may be an artifact of poor calibration transfer, but we have found

that the phases were well-behaved at both frequencies during the observations, and there are no strong artifacts that would owe to poor phase calibration.

Instead, it appears that the offset may be real, in which case the central source has an inverted spectrum and the neighboring 2.2 GHz sources are steep. The structure is reminiscent of a classical double-lobe radio source, although the scale for NGC 4235 is only 1 parsec in projected extent. Knowing that the high frequency spectrum is flat (Gallimore et al., work in progress), either synchrotron self-absorption or free-free absorption may explain the inverted spectrum at low frequencies. Either way, the central 8.4 GHz source marks the likely location of the central engine.

### NGC 5929

NGC 5929 presents another unusual case because VLA and MERLIN images resolve a core-lobe structure that is similar to the large-scale jets in radio galaxies. Based on VLA observations, Wilson and Keel (1989) report a flat spectrum for the central source between 5 and 15 GHz. The following figure compares MERLIN and our VLBA images of NGC 5929.



We fail to detect the central flat-spectrum source, but we detect compact, steep-spectrum features in the radio lobes. The conventional interpretation for flat-spectrum emission is synchrotron self-absorption, but in this case the brightness temperature is too low. On the other hand, interstellar scattering can diffuse a compact source and reduce its apparent brightness temperature. The scattering would have to be intrinsic to the source and localized around the central engine because we detect compact emission from the lobes. This model does not seem feasible, however, because the apparent size of a scattering-diffused source drops with the distance between the observer and the scattering medium.

We considered another possible explanation for the low-brightness temperature, flat spectrum source. In collecting archival observations of NGC 5929, we noticed that the central source brightened somewhat at low frequencies as observed by MERLIN (Cole et al. 1998). We made a model for the source in which we assumed that the source might be partially resolved below the detection limit by long-baseline observations and at high frequencies. We fit (1) the source spectral index and (2) the source size to data with different baseline lengths (VLA, MERLIN, and VLBA) and over different frequencies. The best-fit spectral index was  $-0.5 \pm 0.1$  (steep-spectrum), and the best-fit source size is  $\sim 60$  milliarcseconds (just resolved by MERLIN at 5 GHz). We conclude that the central source is probably steep-spectrum, and the reported flat-spectrum may have been an artifact of resolution effects.

## Conclusions

We have detected and resolved the radio structures of seven of eight of the CfA Seyfert galaxies. Three of the remaining four have been resolved in independent observations. The remaining source, NGC 7469, has been observed but the data are not yet published. The structures are usually collinear and resemble the larger jets observed in other Seyfert galaxies. We have uncovered only one new flat spectrum source in the sample. This result argues that the flat spectrum sources are not hidden by confusion with neighboring steep spectrum emission. Instead, it appears that the flat-spectrum sources in Seyfert galaxies are usually intrinsically faint or are heavily obscured by ionized gas in the foreground. We also find that Seyfert jets tend to bend by 10 – 20 degrees as they travel from parsec scales to hundred-parsecs scales. Transverse structures are found among the brighter CfA Seyferts; these structures may trace working surfaces where the jet interacts with the interstellar medium of the host galaxy. These results support the picture that Seyfert jets are suppressed by interactions with dense clouds in the circumnuclear environment.

## References

- Cole, G.H.J., Pedlar, A., Mundell, C.G., Gallimore, J.F., & Holloway, A.J. 1998, *MNRAS*, 301, 782  
Gallimore, J.F., Baum, S.A., & O'Dea, C.P. 1997, *Nature*, 388, 852  
Kukula, M.J., Pedlar, A., Baum, S.A., & O'Dea, C.P. 1995, *MNRAS*, 276, 1262  
Mundell, C.G., Wilson, A.S., Ulvestad, J.S., & Roy, A.L. 2000, *ApJ*, in press  
Trotter, A.S., Greenhill, L.J., Moran, J.M., Reid, M.J., Irwin, J.A., & Lo, K.-Y. 1998, *ApJ*, 495, 740  
Ulvestad, J.S., Roy, A.L., Colbert, E.J.M., & Wilson, A.S. 1998, *ApJ*, 496, 196  
Ulvestad, J.S., Wrobel, J.M., & Carilli, C.L. 1999, *ApJ*, 516, 127  
Wilson, A.S., & Keel, W.C. 1989, *AJ*, 98, 1581

# CL0939+47

Andreea Petric (NMIMT) Frazer Owen (NRAO) Michael Rupen (NRAO)

## 1. Introduction

The intriguing discovery (Butcher and Oemler 1984) that the fraction of blue galaxies in clusters increases with redshift was followed by extensive optical spectroscopic work to explore the implications of this effect for the history of star formation and galaxy evolution in cluster environments. These studies found a puzzling population of E+A galaxies, characterized by lack of emission lines (hence little or no ongoing star formation), and very strong Balmer absorption lines (implying a recent starburst). This apparent cessation of star formation in the present E+A galaxies has been blamed on high-speed encounters within clusters, galaxy harassment, and interactions with the intracluster medium. Another piece was added to the puzzle with the discovery that the number of E+A's appears to be an order of magnitude higher in rich cluster environments than it is in the field while there seems to be a general reduction in the star formation rate (Dressler 98). These workers classified the galaxies inside these clusters by the equivalent widths of their OII emission and H $\delta$  absorption lines. In their classification scheme E+A's are called k, k+a, and a+k's, where for all three subclasses  $EW[OII] \leq 5\text{\AA}$ ; for k systems  $EW[H\delta] \leq 3$ , for k+a  $3 \leq EW[H\delta] \leq 8$  and a+k have  $EW[H\delta] \geq 8$ .

Spectral synthesis models (Poggianti et. al. 1999) indicate that strong H $\delta$  equivalent widths ( $EW[H\delta] > 4 - 5$ ) are produced only by galaxies in a quiescent phase soon after the starburst. Thus k+a spectra are identified with post-starburst galaxies. However, the progenitor starbursts with high [OII] equivalent widths are not seen; Poggianti et al propose that dust obscures these emission lines. They suggest that these progenitors are dusty, merging, starburst galaxies (classified as e(a)'s). Local galaxies with e(a) spectra are indeed dusty. However we don't know whether galaxies in clusters at moderate redshifts are similarly extinguished. Both Dressler and Poggianti use a classification system based on the equivalent widths of [OII] and [H $\delta$ ]; where H $\alpha$  is not available [OII] is used to determine star formation rates. This is problematic since [OII] is more affected by dust than H $\alpha$ . Also, not-knowing the amount of dust in the observed objects can lead to systematic errors when comparing samples of galaxies with differential dust properties e.g. clusters and field.

The present work, consisting of multi-object spectroscopy on cluster CL0939+47, is intended to help determine how important dust extinction is in moderate redshift clusters, and clarify what types of galaxies exist in  $z=0.3-0.5$  clusters. Several methods

of analysis are available. The amount of differential reddening through the ratios  $\frac{EW[OII]}{EW[H\alpha]}$  and  $\frac{EW[H\alpha+NII]}{EW[H\beta]}$ . Also, because the radio continuum is a dust-independent measure of star formation, comparing 1.4GHz and optical star formation estimates provides another method of determining dust extinction.

## 2. Observations and data reduction

The spectra were taken with the HYDRA multiobject spectrometer at Kitt Peak. The great advantage of this instrument is its ability to observe the spectra of 100 galaxies simultaneously; stepping motors and fishing wire in the positioner (Fig. 1) move optical fibers to the objects of interest; then light from the fibers passes through a bench spectrograph and thence onto the CCD. The resulting image is shown in Fig. 2.

The IRAF data reduction package was used to process the data. Thus the raw data was corrected from the variations in the electronic pedestal level of the CCD. The spectra were then flat fielded and their dispersion was determined by the DOHYDRA routine in IRAF. This routine fits for the positions of the apertures, fits for the dome flat, divides the other apertures by the domeflat. It also calculates the throughput using a skyflat and measures the dispersion of the spectra using the spectra of standard lamps located in the positioner (labeled calibration lamps in Fig. 1).

## 3. Errors and uncertainties

The sky subtraction was one of the dominant uncertainty in the processing of the spectra. There are several reasons for this: the regions of the sky from which we derive the sky spectrum are different than the regions of “sky” next to the galaxies from which we want to subtract the sky spectrum; imperfect alignment and dispersion determination of spectra make the dispersion of the average sky slightly different than that of an individual sky or a galactic spectrum. Incorrect sky subtraction can even lead to a narrowing of certain lines from which a sky feature was subtracted.

Meaningful fluxes are hard to get. True luminosities as opposed to CCD counts are obtained by looking at the way the CCD responds to a star; that is how many counts per wavelength interval are received at the CCD and how that compares to the known flux of the star in that wavelength range. The response of the CCD and the filter system are thus both taken into account.

The difficulty in this fluxing procedure is twofold. The first problem is instrumental. Second order scattering effects from the blue into the red region makes it difficult to determine the true response of the CCD in the red region. Apertures smaller than the size of the galaxies and insufficiently accurate pointing create another difficulty in fluxing the data. While this uncertainty can be partially removed by scaling the fluxes with absolute R magnitudes, the uncertainty in the CCD response prevents this scaling from determining the true flux at certain wavelengths.

Finally, errors in measuring equivalent widths come from non-uniform noise and difficulty in choosing the true pedestal flux level for a line.

#### 4. Results

The OII emission line is the best star formation tracer in the blue. Among nearby galaxies dominated by stellar photoionization the data follow a mean relation  $EW[OII] = 0.4EW[H\alpha + NII]$  with an rms dispersion of  $\sim 50\%$  (Kennicutt 92). For our cluster some of the low  $z$  galaxies have higher [OII] than predicted by this relation. These galaxies could be Seyfert 1 galaxies which have strong [OII] emission independent of Balmer line strength. However in the medium redshift objects the  $H\alpha$  is systematically higher than the [OII] more than the local relation would suggest (Fig. 3). This could be explained by differential reddening by dust.

Supporting evidence for is presented in Fig. 4. which shows the deviations of our data from the local  $\frac{H\alpha+NII}{I(H\beta)}$  ratio. Our data might also suggest that objects with more  $H\alpha$  appear to be dustier. However the large scatter and an insufficient number of points do not permit a firm conclusion.

The optical data therefore suggest significant dust extinction in these galaxies. Radio continuum observations provide a dust-free measure of star formation rates, if dust is indeed present we expect to derive a higher SFR from the radio than from the optical data with the discrepancy increasing with the amount of dust extinction. Fig. 5 bears this out. For the objects at  $z = 0.4$  in the CL0939+47 cluster, star formation rates derived from 1.4 GHz radio continuum data are higher than those inferred from the  $H\alpha$  recombination line. While it is possible that some of the objects are AGN's, this result, coupled with our  $EW[OII]$  vs  $EW[H\alpha + NII]$  analysis, suggest that dust extinction in medium redshift clusters is not negligible.

## 5. Conclusions and future work

The analysis on CL0939+47's objects suggest that: medium redshift objects are dustier and objects with more  $H\alpha$  are dustier. This is apparent from both differential reddening measurements and higher radio derived star formation than optically derived rates. However an insufficient number of data points and large uncertainties in the data processing and analysis of the spectra does not permit us to assert the significance of these results. Further analysis of clusters A370 and Cl0024+16 as well as better sky subtraction and fluxing should settle the significance of these results.

# *Hydra/WIYN Multi-Fiber Positioner*

*Spacer Assembly*

*Positioner*

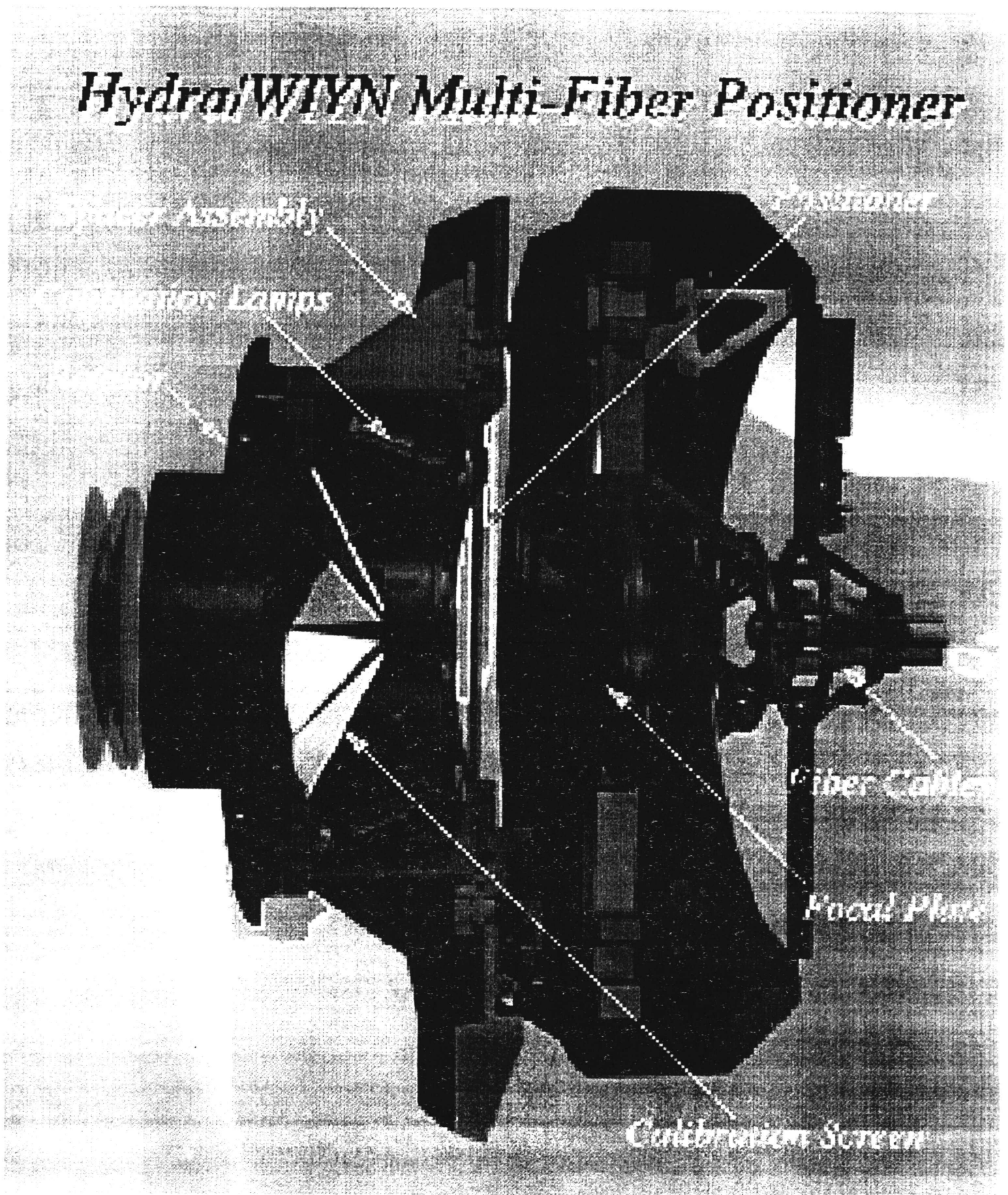
*Calibration Lamps*

*Calibrator*

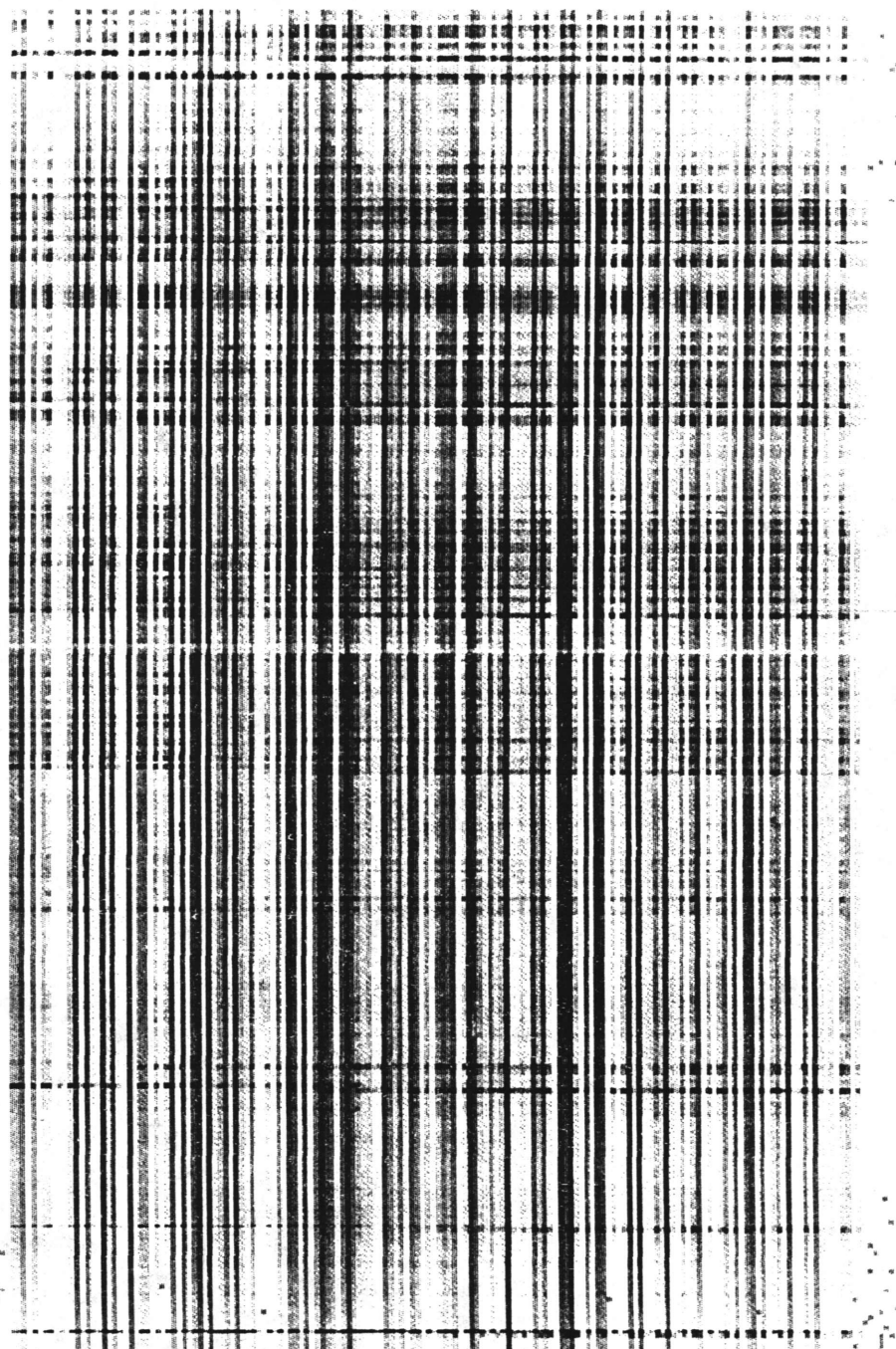
*Fiber Cables*

*Focal Plane*

*Calibration Screen*







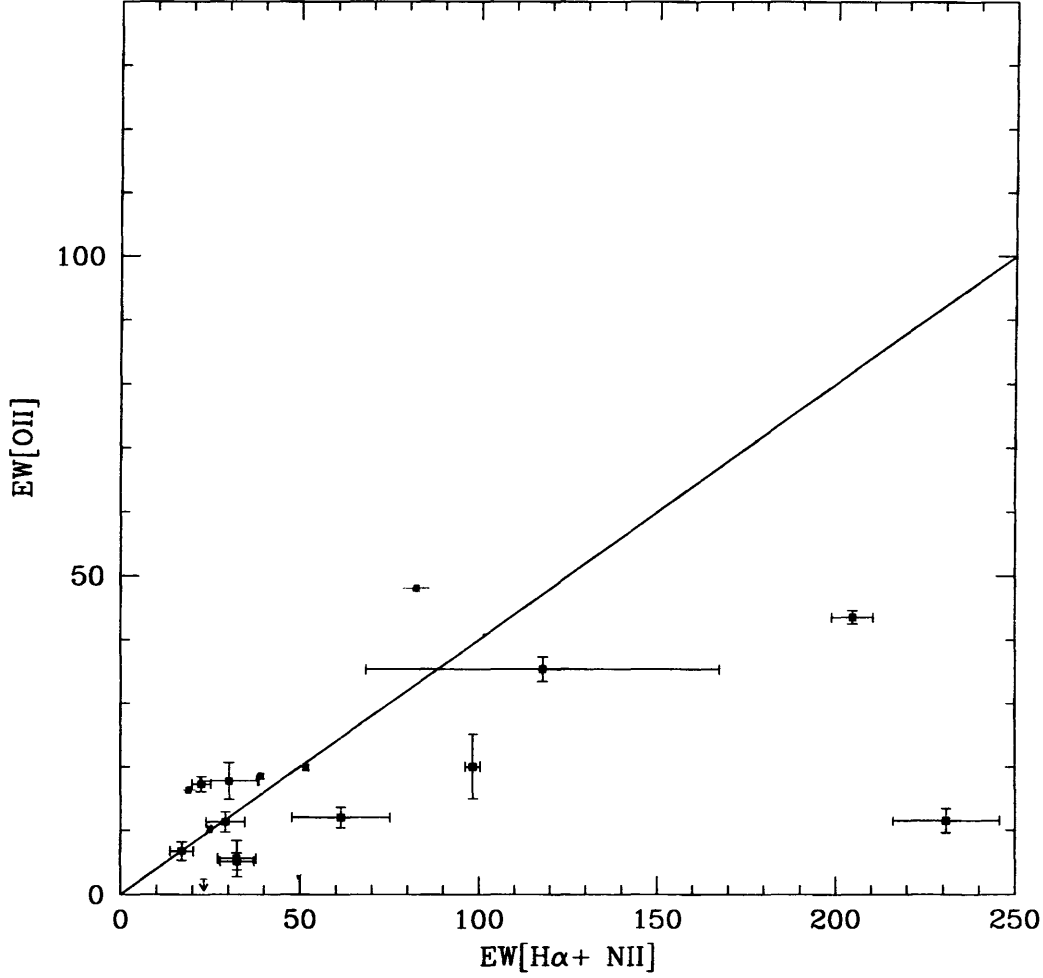


Fig. 1.— Figure 3 shows  $EW[H\alpha + NII]$  vs.  $EW[OII]$  for all objects in this study for which the  $H\alpha$  line was available in our study. The solid black line is the relation between  $EW[OII]$  and the  $EW[H\alpha + NII]$  as derived from nearby galaxy data. The red points - galaxies in the cluster at redshift of 0.4 are generally below this line. This can be explained by differential reddening and it suggests that these galaxies are dustier than local systems. Upper limits of  $EW[OII]$  were derived for objects where we detected  $H\alpha$  but not  $[OII]$ . Three of the low redshift upper limits were also below the solid line, thus more points are necessary to verify if indeed medium redshift cluster galaxies are dustier than nearby systems.

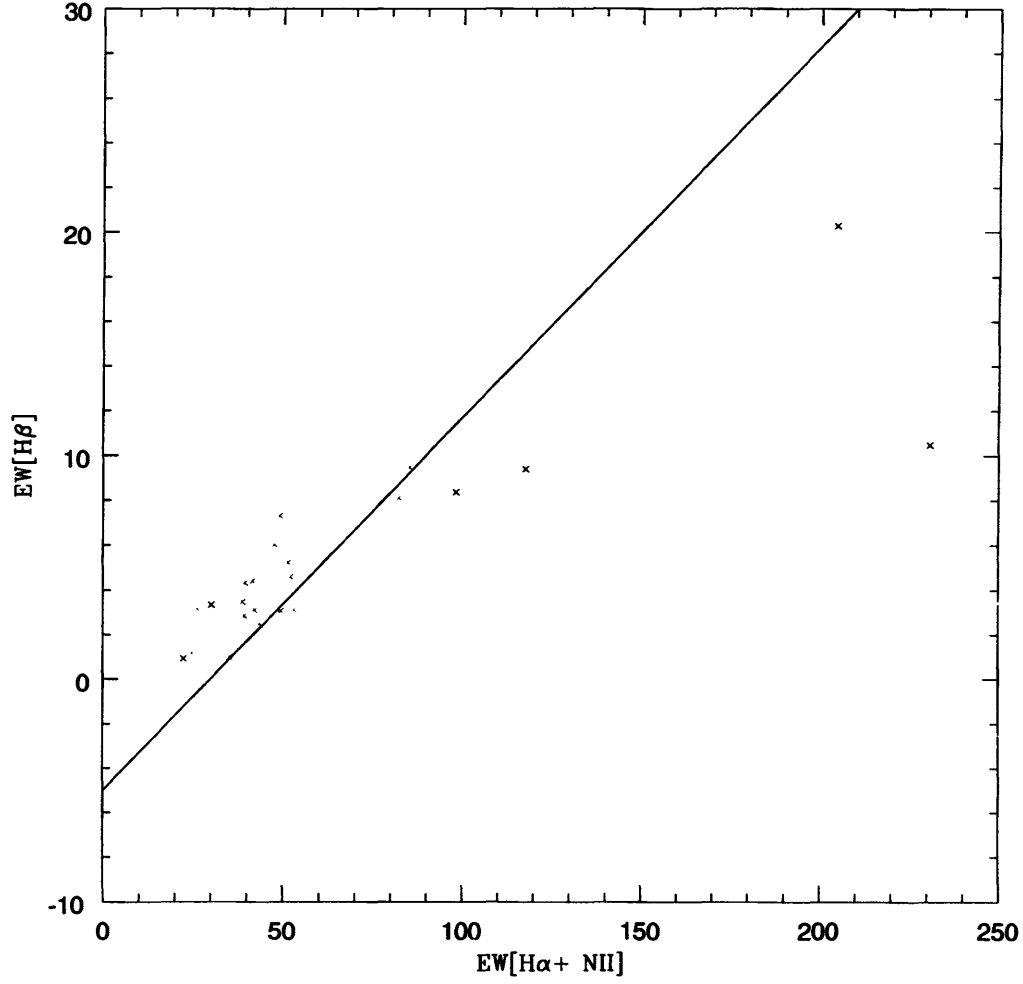
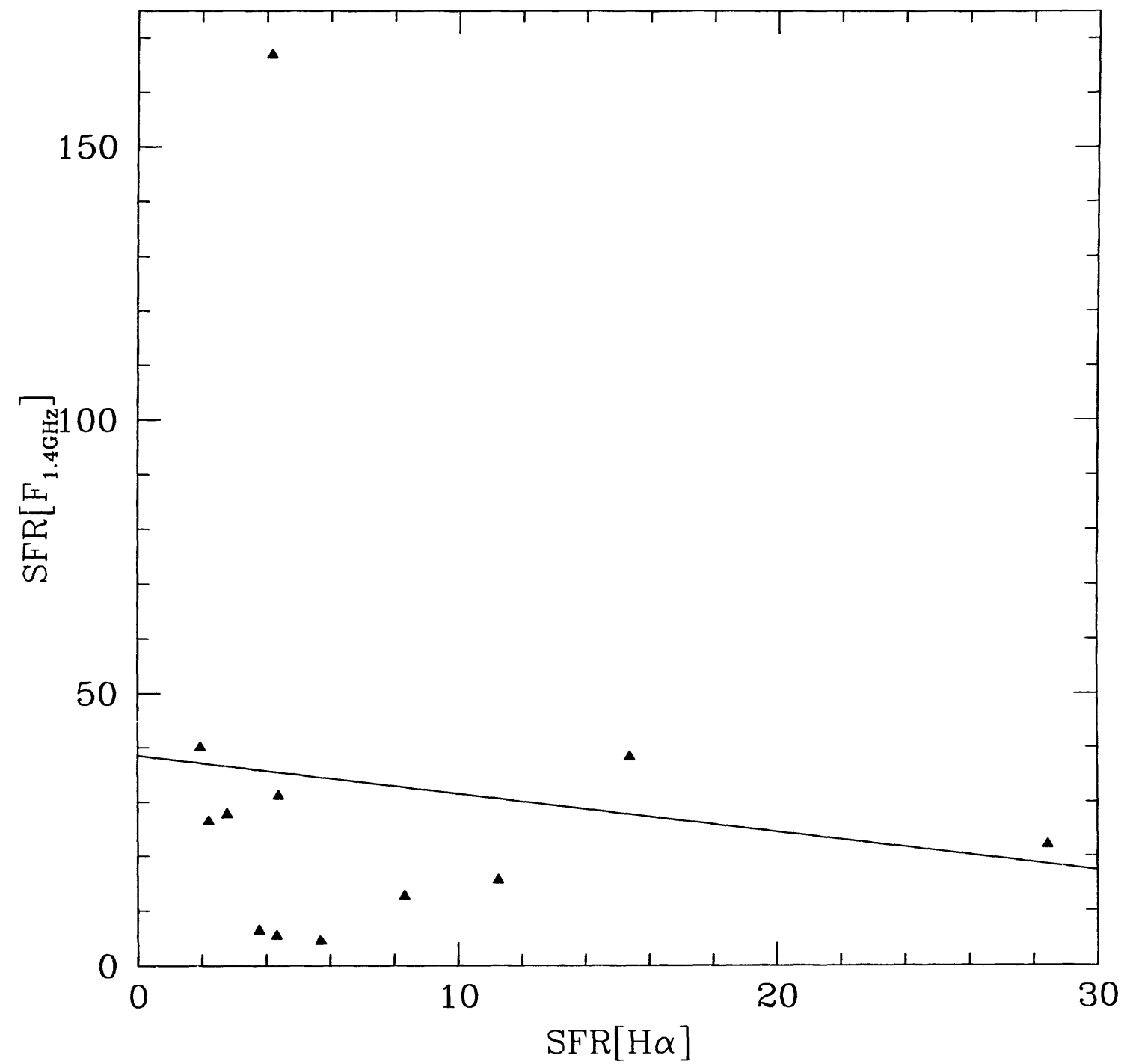


Fig. 1.— The solid line shows the relation expected for a simple model with  $\frac{f(H\alpha+NII)}{(H\beta)} = 6$  and a mean stellar absorption EW of 5 Å. Blue is used for galaxies of redshift lower than 0.3 and red for galaxies of 0.3 - 0.5 redshift.





# Summer student report, 1999

**Darrell Osgood**  
**with Frazer Owen**

Matching radio, IR, and optical coordinates, images, and sources.

We are looking in the vicinity of Abell 2125 to match radio, IR, and optical coordinates, images, and sources. This is a small part of a very large ongoing project. There is no publication in sight.

There are two regions (center and southwest) of HST images, each done in B and R filters and with double exposures (one day apart, slightly different orientations). We have mosaiced VLA A array radio images and K band infrared images from KPNO. Frazer also has J band data that I have not touched. He says he eventually wants to use about nine bands to tie constrain some theories.

The main optical image of A2125 is shown in the first figure. The contours are from earlier x-ray work. The B filter HST images of the cluster center are HSTSI1 and HSTSI2. The COMBined image is called HST1+2.

Frazer already reduced the data on all images, including putting a coordinate system on the radio and IR images. I still needed to put a coordinate system on the Hubble pictures then force those coordinates to match the radio positions. We wanted to know if the USNO's A2.0 catalog of optical stars would be sufficient for our needs.

To this end I divided the rather large A2125\_60 into nine regions and picked a bunch of sources (tens are needed) with  $1000 < \text{peak flux} < 30000$  (to avoid poor S/N and washout). Also, the A2.0 lists stars, so I avoided galaxies as indicated by lower than expected flux.

The bottom right region had problems. The first group of objects I selected in that part had an abnormally high goofball count. Goofballs are stars with XTRAN residuals  $> .5''$ . I found no systematic shifts, rotations, or distortions. So I picked another, larger, random group of objects in the region and they were fine.

I iteratively reduced the objects to go into XTRAN, chose the linear fitting (npoints=3), ran XTRAN one last time, and found that the A2.0 is adequate for our needs. I called the output A2125X.

Next, I loaded HSTSI1, found positions of galaxies with tvmax, then ran XTRAN once again, this time with x-y positions from HSTSI1 and RA-Dec positions from A2125X. It turned out that XTRAN failed to rotate the image correctly (though Eric Griesen has since fixed this) so I put the XTRAN results straight into the image header using PUTHEAD.

I aligned the infrared image to the radio coordinates using OHGEO (the updated version of HGEOM). Since the IR image is smaller than the radio one, I used the IR as the template (in2name). The radio image used was one of the mosaic pieces, A2125A1.

The last step is to identify sources in the radio, IR, and optical that spatially coincide. I ran SAD at three sigma on the region of A2125A1 that maps onto HST1+2. I made a STARS file with the results and applied it to both images (see figure 2). I found 33 radio sources in the HST field. Of those thirty-three, seven coincided with optical galaxies. Three of the seven

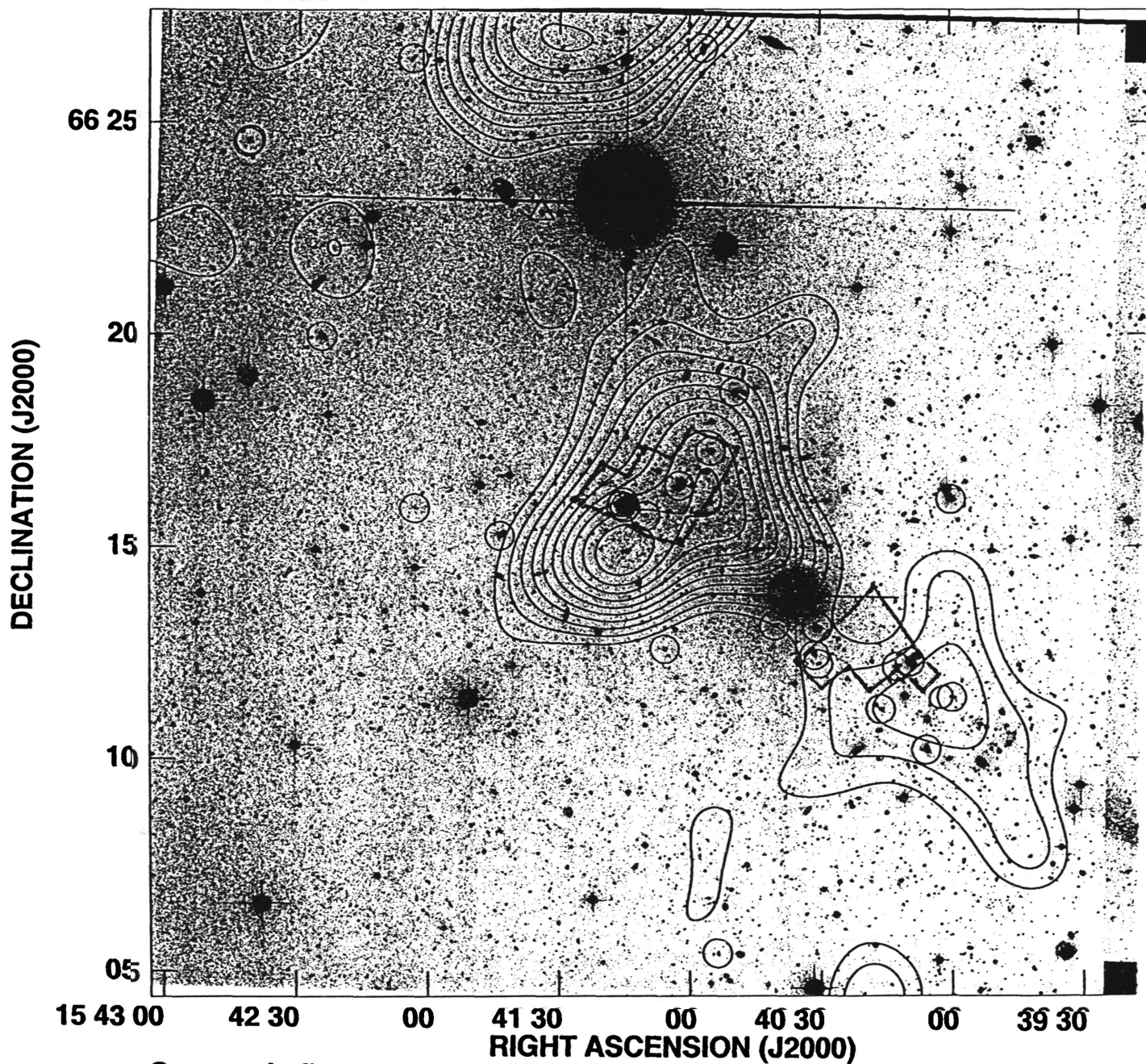
(#22,23, and 47) were obvious; they were part of the reason why this field was chosen. Two others (#26 and 41) were off-centered but contiguous to their optical counterparts. Looking at #37 and 38 we see that they lie on either side of their optical counterpart - clearly they are jet sources. So I count six optical sources with radio counterparts. The other 26 radio sources clearly had no optical counterparts detected.

I used a similar approach for the IR/radio comparison. I ran SAD on both images and now I need to compare the two for coincidences. But with a much more crowded field I must beware of statistical coincidence, like optical binaries.

This work will continue for quite a while. Frazer Owen will continue as my research advisor at New Mexico Tech in the fall and possibly beyond. He has been a very good advisor.

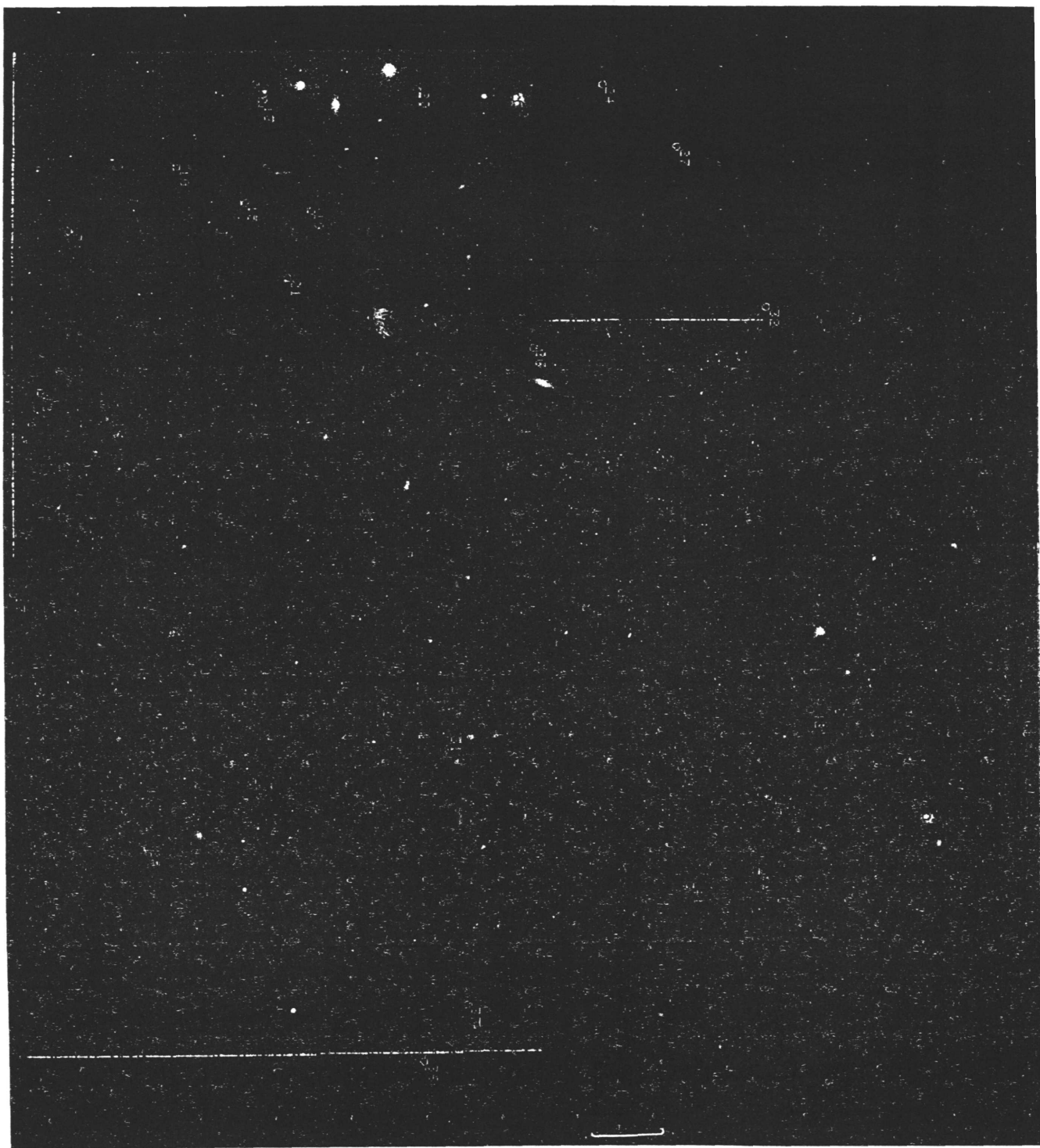
The rest of this report is a nine minute report I gave to the AOC staff in July. The last page's IR results were preliminary. I now believe those results are under sampled.

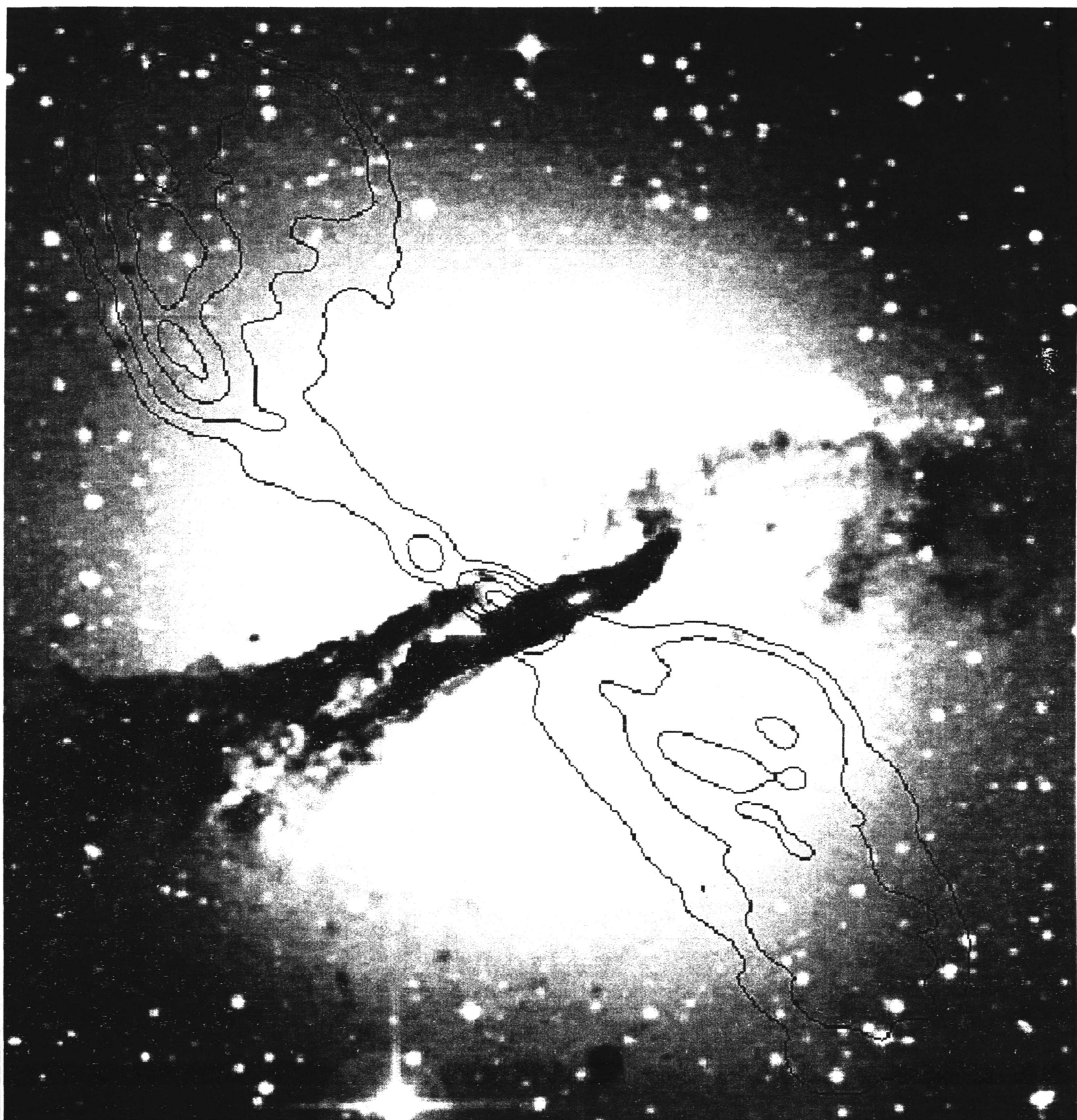
CONT: A2125 A2125XH.HGEOM.1  
GREY: A2125 - A2125R.XTRAN.1



Grey scale flux range= -1.00 30.00  
Cont peak flux =  $1.0149 \times 10^{-2}$  CNTS/SEC  
Levs =  $6.765 \times 10^{-4} \times (5, 6, 7, 8, 9, 10, 11, 12, 13, 14, 15, 16)$







## HOW DO GALAXIES FORM?

This is the fundamental question.

{fig 1: Madau's optical data curve}

"Initial studies of optical galaxies with the Hubble Deep Field suggested a sharp peak in the cosmic star formation density at around  $z=1.5$ . However, studies of faint submm counts argue that the star formation rate may be roughly constant between  $z=1$  to 5... optical studies may be missing a substantial amount of star formation occurring in dust obscured starbursts at high  $z$ ."

{fig 2: Smail's dusty starbursts}

We want to study the dust enshrouded starburst galaxies to fill in the high redshift data. The downside is that we have a very small submm population to work with. The upside is the submm objects are also seen at longer radio wavelengths. Thus we plan to use longer wavelength radio images instead.

Models and observations show luminosity versus rest frequency curves basically like this {M82 curve}. Consider a galaxy moving away at some unknown redshift. Compare the luminosity at two points along the curve, one in radio, the other in IR. A redshift will decrease the ratio of IR to radio luminosity. So we can use this spectral index (350Ghz to 1.4 Ghz) as a rough indication of the redshift.

{fig 4: list of freqs, etc.} What is my part in this?

Right now we are looking at A2125 using radio from the VLA, IR from KP 2.1m, and optical from the HST. Eventually we want to use ~9 bands to constrain the models well. For now, we must align the various images precisely then catalog the sources in each image. We compare positions and decide if, say, an IR source is actually aligned with a radio source.

{fig 5: optical-xray image of A2125 and overlay}

A2125 is in the center of this optical grey-scale image with xray contours. We focus on the off-center portion of the cluster as indicated on the overlay.

{fig 6: USNO A2.0, [www.nofs.navy.mil](http://www.nofs.navy.mil)}

To compare the radio and IR sources to the optical images, we must give HST a coordinate system. Luckily, our friends at the US Naval Observatory in Flagstaff made a wonderful catalog called the A2.0. We convinced ourselves that the A2.0 is adequately correlated to our radio positions. The residuals, or offsets, were under .5". So we use the USNO A2.0 coordinate system on our HST image, then transformed it to align with the radio coordinates.

While transforming all our images to the same coordinates we discovered that xtran had conniptions trying to rotate images more than a few degrees. Our very talented Eric Griesen has pretty well fixed that; look for expanded options in the next exciting episode of AIPS.

In conclusion, here are the fields we have been working with.

{fig 7: HST} This is the HST image. I will have results on this by next week.

{fig 8: radio and overlay} This is the radio image and an IR overlay for size

perspective. Notice how few objects we can see in that region. The obvious ones are within the Abell cluster, so they aren't interesting. We are interested in the point sources only.

{fig 9: IR and overlay} Finally, the IR image with the HST size overlay for comparison. The marked objects are the radio sources. Blue means the IR and radio sources match, red means there is a radio source but no IR source. Ignore the big galaxies.

{fig 10: object counts, Jy limits} The numbers corresponding to the last image.

For the rest of my time here, I will look in the HST image for any objects that coincide with IR and radio objects. Then we will compare the luminosities of the various objects as a rough estimate of redshift, as explained earlier.

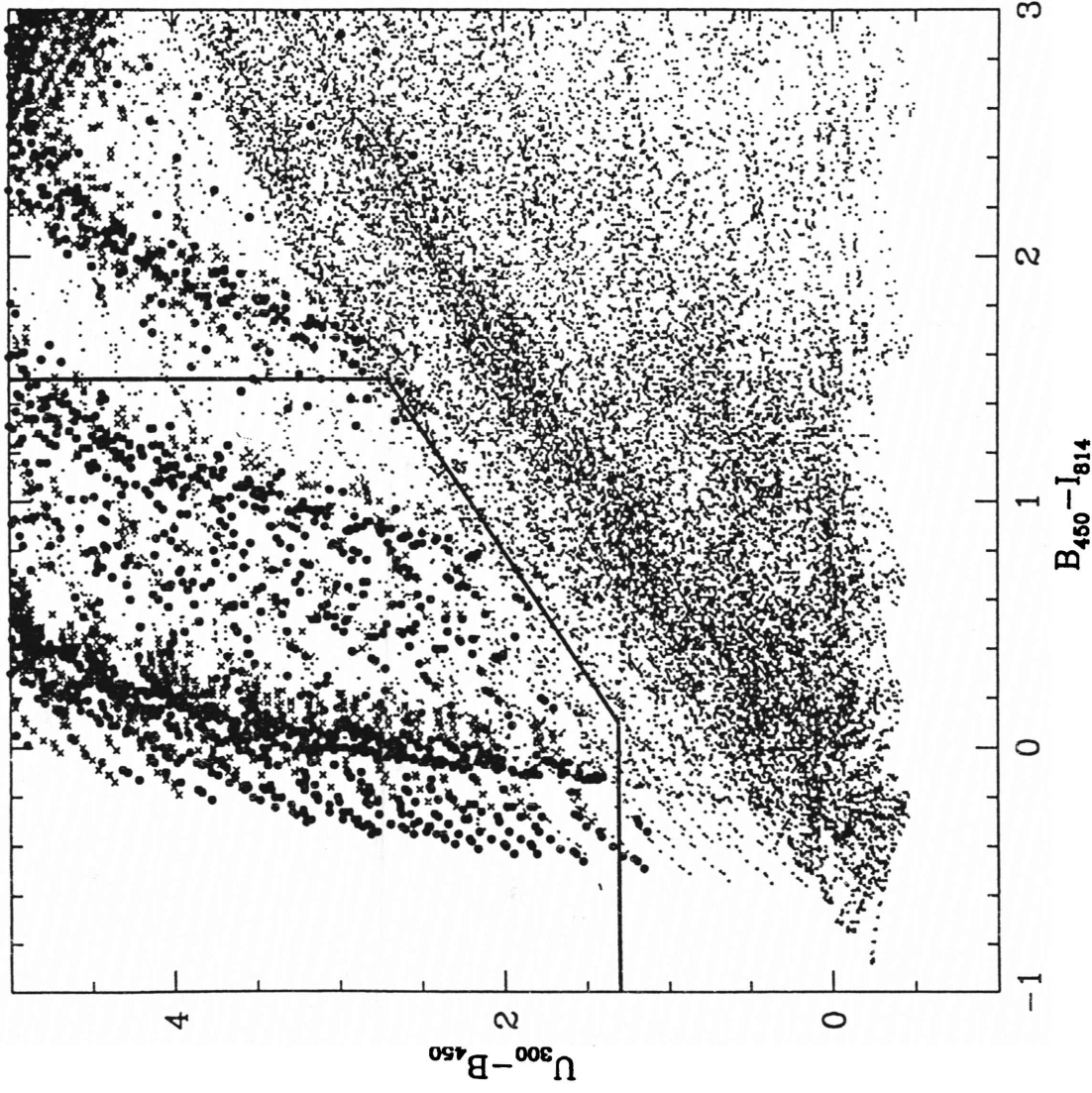
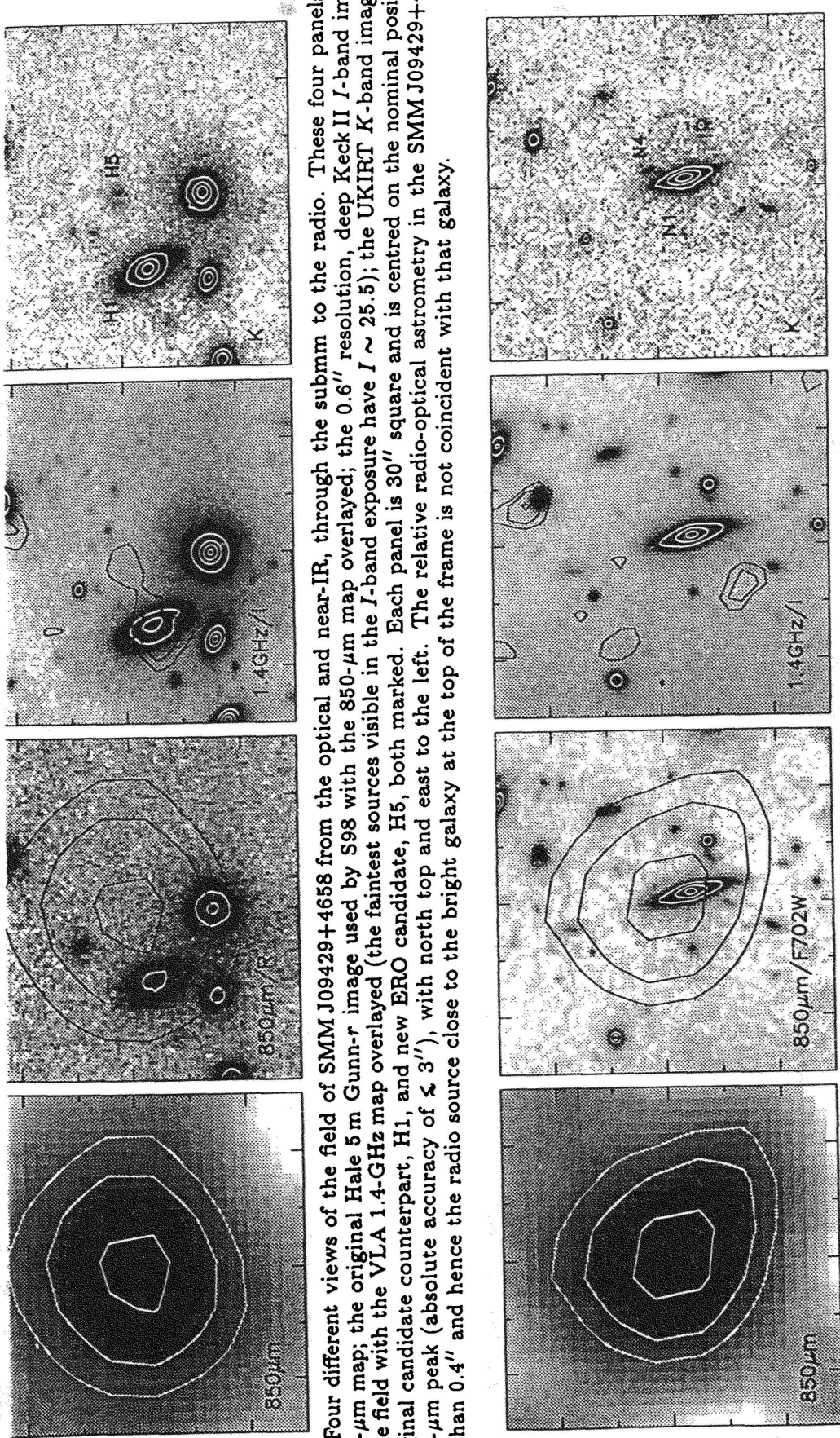


**Figure 3.**  $U_{300} - B_{450}$  versus  $B_{450} - I_{814}$  for model galaxies. A total of 103 879 synthetic spectra of galaxies representing a wide range of star formation histories, metallicities, dust contents and redshifts were folded through the *HDF* bandpasses. The galaxies shown are at redshifts of less than 2 or redshifts of greater than 3.5. Galaxies shown as solid circles are those in the redshift range 2 with ages of less than  $10^8$  yr and extinctions  $A_B < 1$ .  $\times$ s are galaxies in the same redshift range that have ages greater than  $10^8$  yr or  $A_B > 1$ . Our colour selection criteria are shown as the large polygon. Galaxies within the polygon in the *HDF* observations are selected as likely candidates for  $2 < z < 3.5$  objects. The selection criteria are  $U_{300} - B_{450} > 1.3$ ,  $U_{300} - B_{450} > B_{450} - I_{814} + 1.2$ , and  $B_{450} - I_{814} < 1$ .



# THE DISCOVERY OF ERO COUNTERPARTS TO FAINT SUBMM GALAXIES

IAN SMAIL,<sup>1</sup> R. J. IVISON,<sup>2</sup> J.-P. KNEIB,<sup>3</sup> L. L. COWIE,<sup>4</sup> A. W. BLAIN,<sup>5</sup>  
A. J. BARGER,<sup>4</sup> F. N. OWEN<sup>6</sup> & G. MORRISON<sup>6</sup>



1. Four different views of the field of SMM J09429+4658 from the optical and near-IR, through the submm to the radio. These four panels show 50-μm map; the original Hale 5 m Gunn-r image used by S98 with the 850-μm map overlaid; the 0.6'' resolution, deep Keck II *I*-band image of the same field with the VLA 1.4-GHz map overlaid (the faintest sources visible in the *I*-band exposure have  $I \sim 25.5$ ); the UKIRT *K*-band image with original candidate counterpart, H1, and new ERO candidate, H5, both marked. Each panel is 30'' square and is centred on the nominal position of 50-μm peak (absolute accuracy of  $\lesssim 3''$ ), with north top and east to the left. The relative radio-optical astrometry in the SMM J09429+4658 is  $r$  than 0.4'' and hence the radio source close to the bright galaxy at the top of the frame is not coincident with that galaxy.

2. The similar four views shown in Fig. 1, but here for the field of SMM J04433+0210. The four panels show from left to right, the 850-μm map; the original HST F702W identification image used by S98 with the 850-μm map overlaid; the deep Keck II *I*-band image of the same field with the 1.4-GHz map overlaid (the faintest sources visible in the *I*-band exposure have  $I \sim 26$ ); the UKIRT *K*-band image with the original candidate counterpart, N1, and new ERO candidate, N4, both marked. Faint emission coincident with N4 is just visible in the *I*/F702W images, however, aperture photometry does not confirm this as a formal detection and hence we have instead quoted a  $2\sigma$  upper limit for N4 in these passbands. Each panel is square and is centred on the nominal position of the 850-μm peak (absolute accuracy of  $\lesssim 3''$ ), with north top and east to the left.

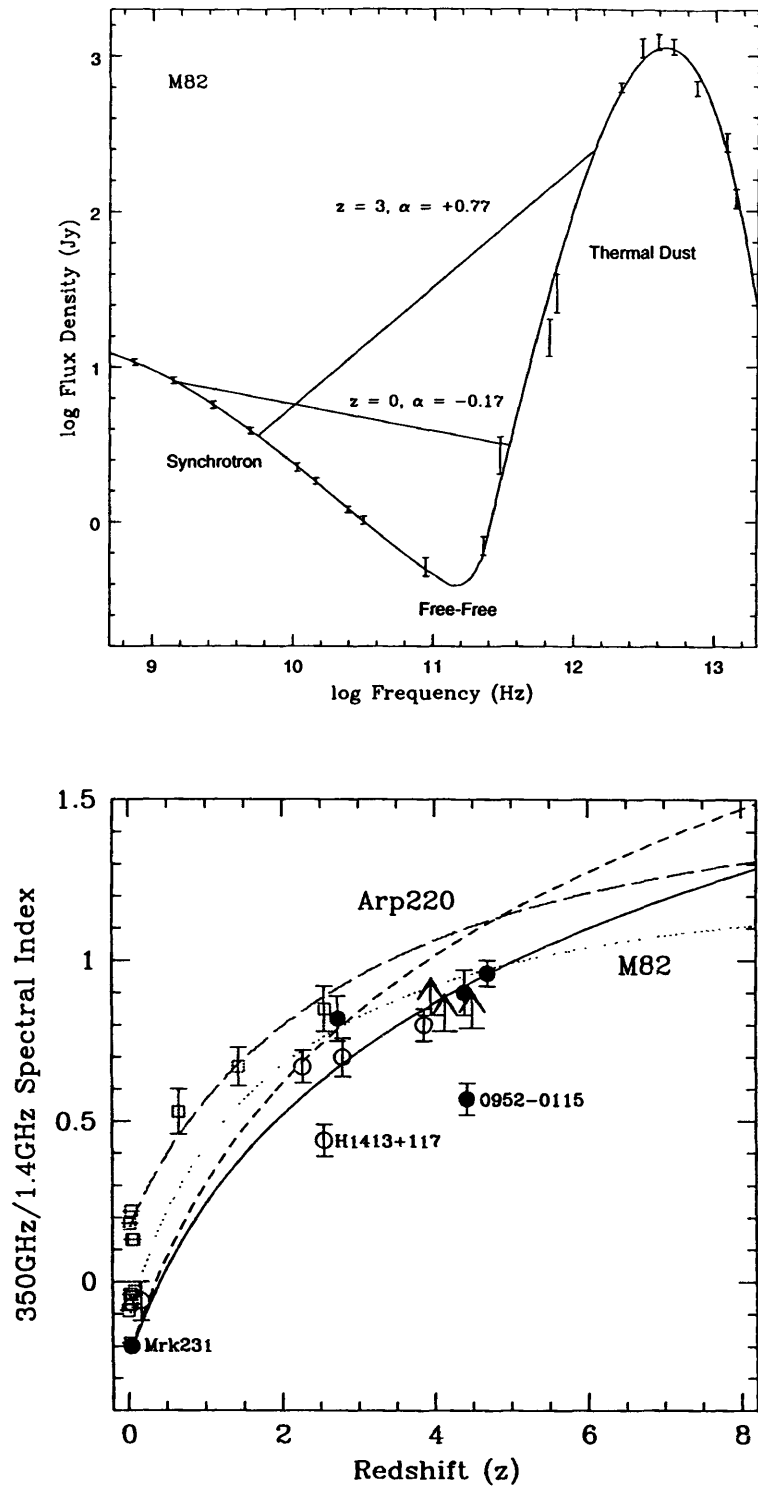


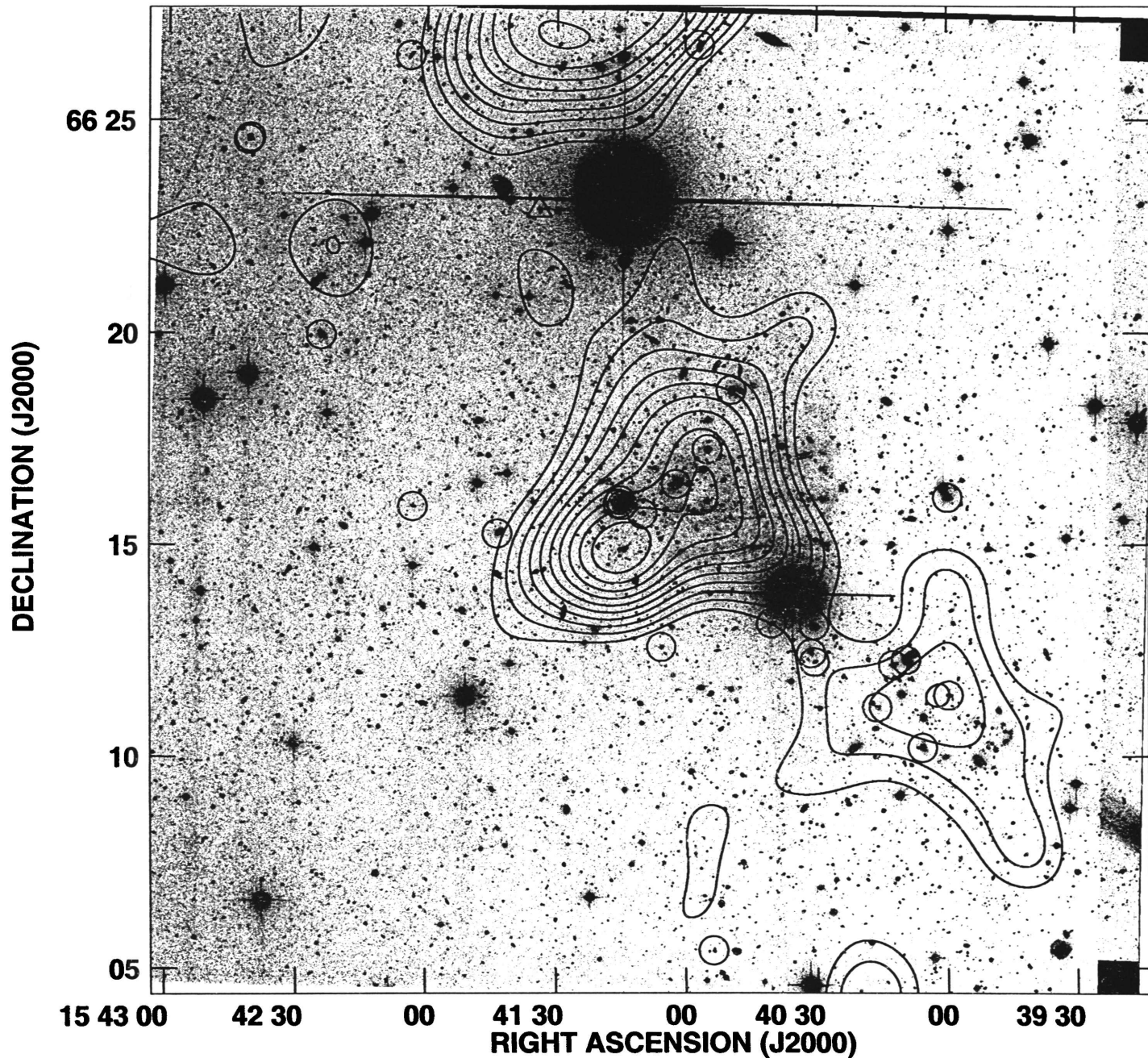
Figure 1: The upper panel shows the radio-thru-infrared SED of M82. The two straight lines show the change in observed spectral index between 1.4 GHz and 350 GHz for a source at  $z = 0$  and  $z = 3$ . The lower panel shows the behavior of the observed 1.4 GHz-to-350 GHz spectral index as a function of source redshift for star forming galaxies. The models are semi-analytic, based on equations in Condon (1992), and empirical models based on observations of Arp 220 and M82. The data points show the results for high redshift submm sources (see Carilli and Yun 1999, and Yun et al. 1999 for details).

Abell 2125 ( $z = .27$ )

<u>regime</u>		$\nu$	$\lambda$	<u>telescope</u>
Radio	L band	1.4 GHz	21 cm	VLA
IR	K band	140 THz	2.2 $\mu\text{m}$	KP 2.1m
optical	B filter	many Hz	4500 Å	HST
"	R filter	"	6500 Å	HST
sub mm		(240 GHz)	850 $\mu\text{m}$	SCUBA (or IRAM)
more IR	J band			KP 2.1 m

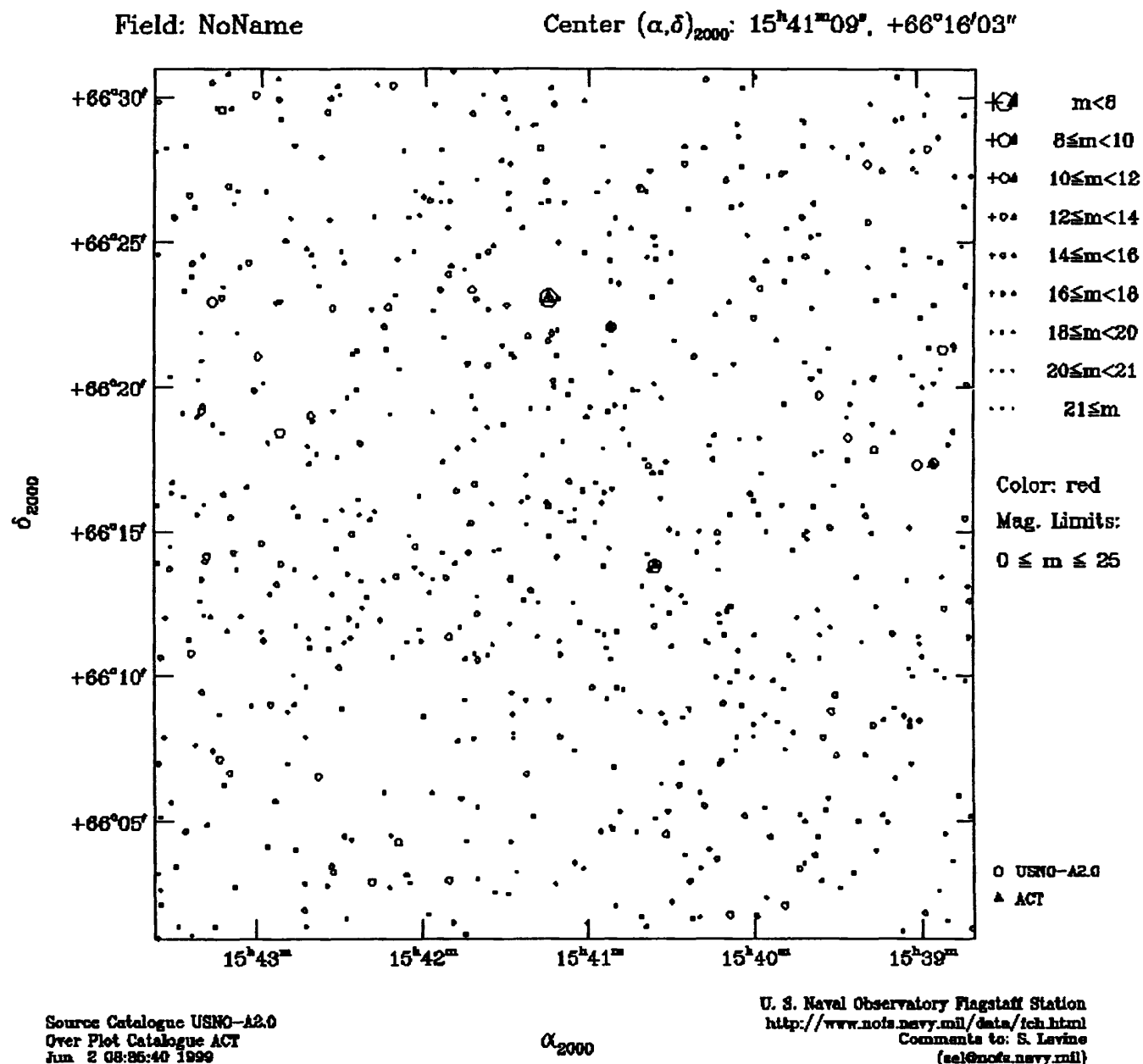


CONT: A2125 A2125XH.HGEOM.1  
GREY: A2125 - A2125R.XTRAN.1



Grey scale flux range= -1.00 30.00  
Cont peak flux = 1.0149E-02 CNTS/SEC  
Levs = 6.765E-04 \* (5, 6, 7, 8, 9, 10, 11, 12, 13,  
14, 15, 16)

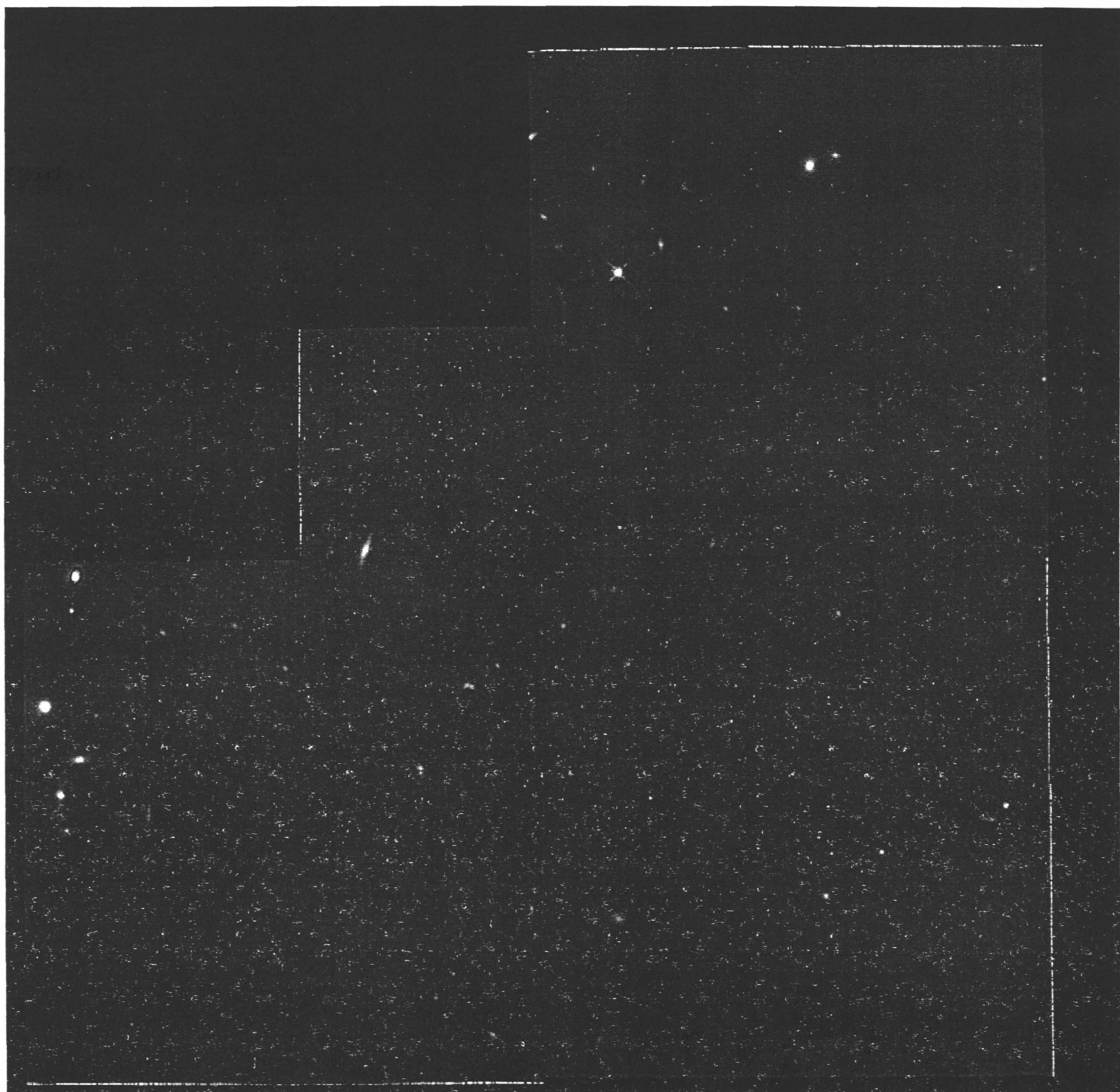
# USNO-A2.0 Search Results



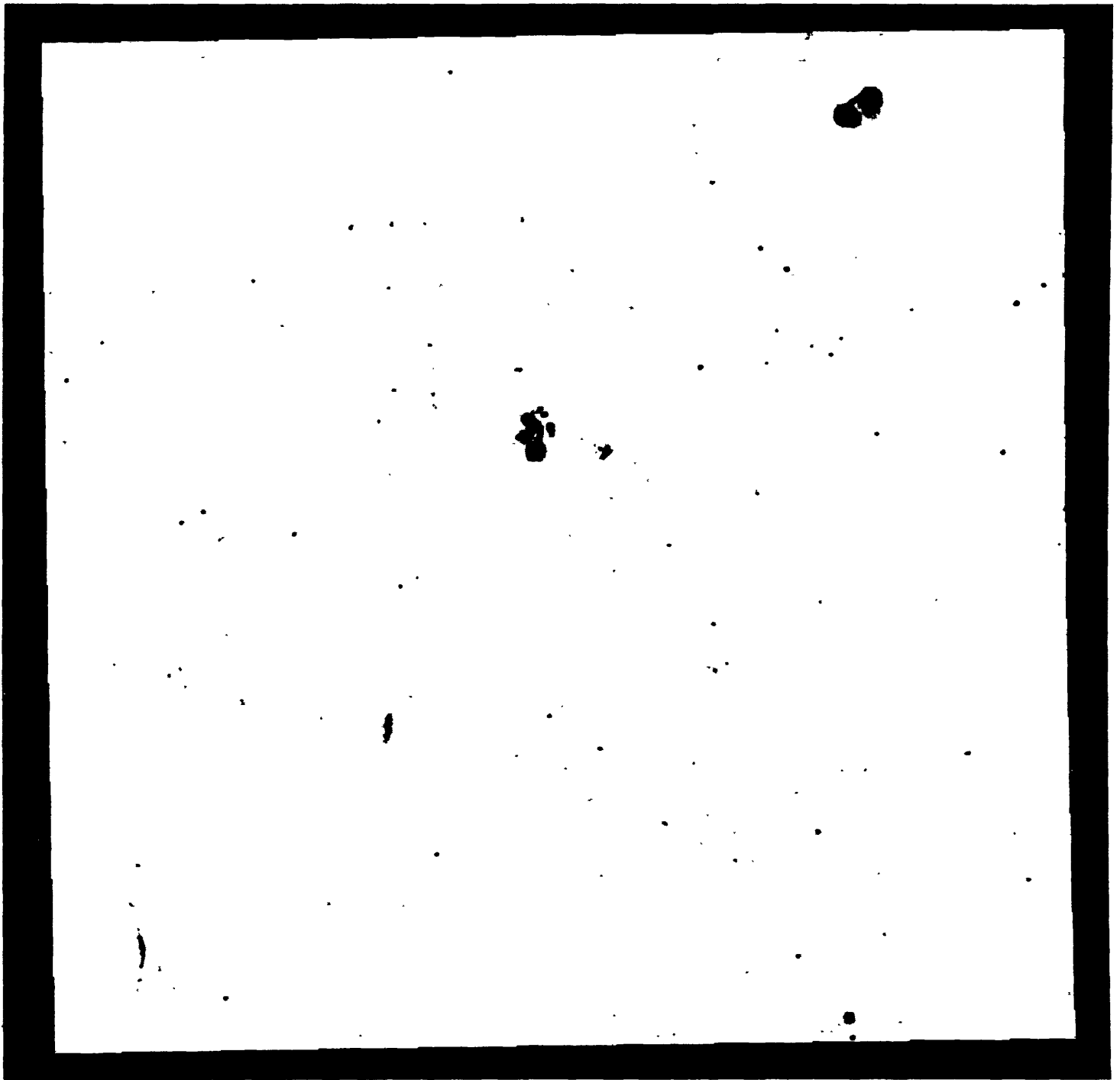
Total Number of objects from USNO-A: 714

Total Number of objects from ACT: 4

Star Chart: Postscript or GIF

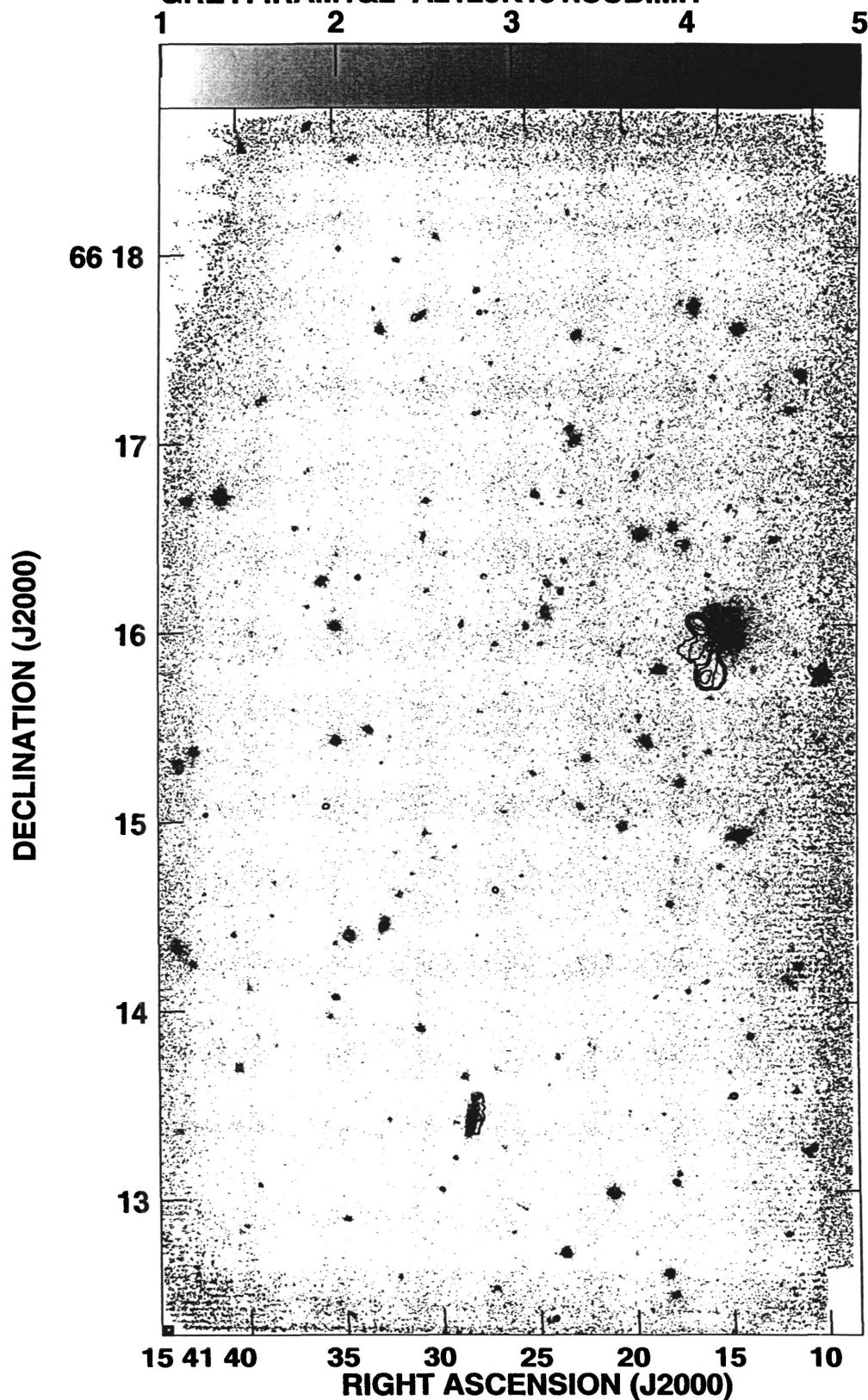


AIPS User 1802



AIPS User 1802

PLot file version 9 created 23-JUL-1999 13:53:26  
CONT: IRAM1&2 A1ONK131.OHGEO.1  
GREY: IRAM1&2 A2125K131.SUBIM.1



Grey scale flux range= 1.000 5.000

Cont peak flux = 2.1294E-02

Levs = 4.000E-05 \* (-1, 1, 2, 4, 8, 16, 32, 64,  
128, 256, 512, 1024, 2048, 4096)

Regime

# objects

coincidence

flux limit

IR

202

16

$1.0 \times 3 =$

3.0 Jy

radio

21

$7.3 \times 10^{-6} \times 3 =$

$2.2 \times 10^{-5}$  Jy

HST

33

9 obs

16

3 Jy



# N-Body Simulations of the Antennae

Chris Power

10th September, 1999

---

## Abstract

Collisions between galaxies can be dealt with analytically only in very specific cases. Unfortunately, the conditions that are prevalent in the bulk of galaxy interactions rarely satisfy these idealizations and so, when considering such situations, the researcher must make use of N-Body simulations to model the encounters. In general, pictorial representations of the time evolution of such encounters is desired.

In this report, I will discuss my work in this area; in particular I will concentrate on how I developed a means to convert observational and simulation data into a form that is readable by the interactive 3 dimensional visualisation tool, Geomview. I will also describe my work on the matching of simulation and observational data for the case of NGC 4038/9, the “Antennae”, as well as the motivation for such model matching and the characteristic features of a system that are particularly suited to such fitting.

As an interesting aside, I indulged myself and present brief discussions on **The History of Mergers** and previous attempts to model the “Antennae” in **Numerical Models of NGC 4038/9**.

---

## 1 Introduction

Until the early 1970’s, the exact nature of the tail- and bridge-like features observed in many peculiar galaxies was the cause of much debate. Indeed, analysis of the discussions at the 15th IAU Symposium, “Problems of Extragalactic Research” (1961) illustrates the then uncertain nature of the problem. Vorontsov-Vel’yaminov, well acquainted with peculiars as compiler of *The Atlas and Catalogue of Interacting Galaxies*, called for **new physics** to explain the bridges and tails he observed in his subjects; Thomas Gold advocated magnetic



forces, although he noted that they would be unable to restrain matter once it was in stellar form. Fritz Zwicky confirmed that the bridges are dynamically young but contain old stars, while the Lindblads postulated that “streams of matter” drawn by tidal forces may be responsible. Thus, whilst being a subject that stimulated much debate, there was little agreement over the cause of these bridges and tails.

At this time, P’fleiderer and Siedentopf were examining whether spiral patterns in galaxies might be excited by encounters with other passing galaxies. Although their results indicated that insufficient time had passed since galaxies were formed for the numbers of spirals observed to have been generated by such encounters, their research - using computers to model the encounters - would have important consequences for the problem of bridges and tails.

In 1972, at a time when much research was directed towards understanding how these characteristic features of interacting galaxies could have formed, two brothers, Alar and Juri Toomre published a paper that would revolutionise our understanding of how interacting galaxies form bridges and tails. In **Galactic Bridges and Tails**, the Toomres presented the a basic recipe for bridge and tail building based on the tidal interaction of two galaxies. They examined 4 well known systems with well defined bridges and tails. Although highly idealised - a galaxy was modeled as a central mass surrounded a disk of massless test particles - the model encounters were able to reproduce with varying degrees of success the characteristic features of the real systems. The results for the “Antennae”, one of the closest interacting systems sporting a symmetric pair of crossed tails, gave them particular pleasure.

Since then, Barnes (1988) and Bothun, Mihos and Richstone (1993) have engaged the problem of reproducing the characteristic features “Antennae”. This system has been called the “Rosetta Stone” of interacting galaxies; it would be fair to say that the general feeling is that if NGC 4038/9 can be successfully modeled, then a comprehensive theory of this class of galaxies is close at hand. If such a stage is to be reached, however, then the results of modeled encounters must match those of observations. In a recent review, Barnes (1998) outlined four key features of the “Antennae” which have thus far eluded attempts to model them. It should be clear that model matching, and in parallel, the visualisation of the results of simulations are of vital importance if a clear understanding of galaxy interactions is ever to be achieved. In this report, I shall outline the fruits of my Summer’s work in this particular area.

In section 2 I present a brief account of how our understanding of collisions between galaxies has evolved over the course of this century. From the earliest postulations of Lundmark and Lindblad to the ingenuity of Holmberg and the wild theorizing of Zwicky to the breakthrough computer experiments of the Toomre brothers, the history of the subject is both colourful and invigorating, and in my opinion, worthy of some discussion.

Section 3 deals with previous attempts to model NGC 4038/9 numerically; in particular, I consider the 1972 effort of Toomre and Toomre which relies on a

restricted 3 body code, and Barnes' 1988 attempt which utilises a 3 dimensional fully self consistent N-Body code. I also briefly discuss a recent paper by Mihos, Richstone and Bothun (1993) on star formation rates in NGC 4038/9, and indicate areas in which future models must improve.

Section 4 is concerned with model matching process. For any physical model of the Antennae to be considered plausible, it must reproduce the observed features of the system. I discuss the essential elements of any model matching scheme and part of my Summer's work.

Visualisation of Data, the topic of section 5, reflects the bulk of my Summer's work; in particular, it deals with the 3 dimensional representation of our data. After due consideration, the highly interactive 3D visualisation package **Geomview** was chosen as the viewing tool. I briefly discuss the development of software that processes both observational and simulation data into a form suitable for 3D viewing; the hopes for future development of this software; and the related topic of automating the model matching process in an efficient and flexible way.

## 2 A History of Mergers

Recent observations of the Hubble Deep Field (Abraham et al., 1996) have shown that the fraction of peculiar objects seen is significantly higher than it is among nearby galaxies. A sizable fraction of QSO hosts appear to be ongoing mergers, as originally envisioned. On a more fundamental level, mergers are thought to play an important role in structure formation in the early matter dominated epoch of the Universe.

However, mergers are not confined to exotic circumstances in history; if we look at the local Universe, there are numerous examples of disturbed galaxies that quite obviously point to galaxy interactions. Such a view was not always held; for many years, right up until the early 1970's, many held the opinion that simple *gravity* acting on stars could not produce the characteristic features - bridges and tails being the prime examples - of the class of peculiar galaxies.

### 2.1 The Hubble Sequence

In 1920, a Great Debate raged between Harlow Shapley and Heber Curtis; **what was the scale of the Universe?**. Considering the "spiral nebulae", what we now know to be external galaxies, Shapley argued that these were merely nearby gas clouds in a Universe that existed wholly within our own Galaxy. Curtis disagreed; he expounded the view that the Sun was but a member of a small Galaxy of which there were many.

The true nature of our Galaxy and the Universe was resolved by Edwin Hubble.

Using the 100 m Hooker telescope he was able to gauge the distance to Cepheids in M31, the Andromeda Galaxy; this distance was greater than that proposed by Shapley for the dimensions of our Galaxy and thus M31 must lie beyond its boundaries, a galaxy in its own right.

Hubble is perhaps better known for his observations which demonstrated that the Universe is expanding (borne out in the by now infamous Hubble Law), but he was also responsible for another important development of extragalactic astronomy - the **Hubble Sequence**. It should not be surprising that Hubble spent many years surveying thousands of galaxies, and during the course of his work, he noticed a trend - galaxies could be ordered into a sequence based on their morphology, the so called Hubble Sequence.

On the left hand side of the sequence, which is commonly called a Tuning Fork diagram, we have the ellipticals which range from E0 up to E7 based on their ellipticity. E0s are spherical and ball like while an E7 is shaped like a rugby ball. At the vertex we have the S0s, lenticulars - galaxies which have disks like spirals but unlike spirals are bulge dominated. Then we branch out into the spirals, Sa, Sb and Sc and the barred spirals, SBa, SBb and SBc.

The obvious question to ask is why the dichotomy of shapes among bulge dominated versus disk dominated galaxies? This was a problem of nature versus nurture - initial guidance was sought in the formation of galaxies, and indeed, the ELS (Eggen, Lynden-Bell, Sandage) hypothesis seemed to offer a solution. Stars in ellipticals formed far earlier and more quickly during the initial collapse of a primordial gas cloud than their counterparts in spirals. However, this now introduced the question, why should this be so? It is at this point that the importance of galaxy mergers becomes clear.

## 2.2 Early References to Mergers : Lundmark (1926) and Lindblad (1926)

The first studies of pairs of interacting galaxies was undertaken in the early 1920's. Knut Lundmark, then at Upsala Observatory in Sweden, carried out investigations of "double nebulae". (1920, 1926, 1927) Assuming that both of the galaxies are at the same distance from the observer, Lundmark deduced the relative properties such as size and luminosity of the different morphological types of nebulae. Based on this research, he was able to conclude that given the large sizes of the "nebulae" relative to their separations in space, "collisions or encounters must be rather common among these objects.

Lindblad (1926) further theorized that "sharp encounters between nebulae...must be considered as highly inelastic and must tend to convert translational (i.e. orbital) into rotational (i.e. internal) kinetic energy. An encounter of this kind may even lead to a fusion of the respective bodies."

### 2.3 Holmberg (1941)

Erik Holmberg was interested in the clustering tendencies of galaxies; galaxies arise in a variety of locations. A few percent can be found in clusters of hundreds; a still greater fraction can be found in groups of tens. Our own Galaxy and M31 are both part of a group of galaxies called the Local Group. In particular, Holmberg wanted to explain the origins of these groups and clusters, and the mechanism he had in mind was the mutual tidal capture of galaxies during initial hyperbolic passages. Initially the galaxies approach each other with sufficient energy to escape to infinity but lose energy during the encounter and thus become bound. By assuming a uniform distribution of galaxies, each with a peculiar velocity of a few hundred kilometers per second, Holmberg envisaged the gradual accumulation of galaxies into groups and clusters.

Unfortunately for Holmberg, there is a fundamental problem with this hypothesis; when the probability for an encounter is estimated, we find that only one galaxy in ten thousand will have had sufficient time to be tidally captured during the lifetime of the Universe, quite at odds with observations.

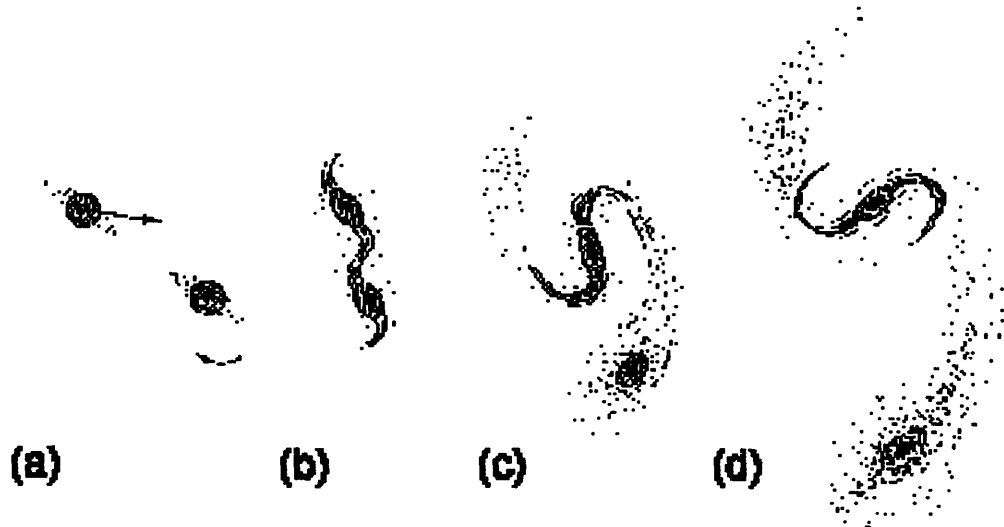
Despite this, it is interesting to follow Holmberg's experiments of tidal capture of galaxies during close encounters. These were numerical experiments in which each galaxy was modeled as 37 mass points arranged in concentric circles traveling around a common centre. What perhaps was most ingenious about this arrangement was that the mass points were represented by light bulbs! By using the inverse square behaviour of light, Holmberg had uncovered a method to mimic gravitational forces - this was the most computationally intensive part of the problem. Photocells were used to detect the magnitude and direction of the "gravitational force", i.e. the light, and so it was possible to map the trajectories of the mass points by graphical integration.

Holmberg simulated planar encounters between disk galaxies using this technique; he was able to estimate the efficiency of tidal capture for a variety of approach velocities, rotations and minimum separations. What's more he correctly noted that the maximum tidal distortion occurs *after* the passage of the interloper through pericenter. However, he did not report any problems with bar instabilities, something which should have plagued such a cold disk, and he also noted that tidal capture was most efficient during retrograde passages when the disks counter-rotated in an opposite sense to their orbital motion. As noted in Barnes (1996), this is "curious".

In addition to the hyperbolic passages, Holmberg did investigate parabolic encounters and used them to illustrate tidal deformations, but because of the number of mass points involved and the approximations made, felt that this was not sufficient for a detailed study of tidal response. Hence an opportunity was missed to uncover the tidal origins of bridges and tails.

## 2.4 Zwicky (1953,56)

Fritz Zwicky was the first to start systematically photographing peculiar galaxies using his 18 inch Schmidt camera at Palomar. Using these images, he quickly concluded that many of the narrow filaments that he observed must be due to tides stemming from gravitational interactions. In a 1953 issue of *Physics Today*, he described these filaments as tides and countertides and furthermore, correctly deduced that the narrowest of them must be sheets of matter seen edge on; furthermore, he emphasized that much of the visible matter in the bridges and tails must consist of stars. Shown below is one of his sketches - "the possible formation of an intergalactic bridge between two galaxies passing each other".



In the sketch, Zwicky considers the possible bridge formation between two interacting galaxies; the resulting configuration closely resembles Arp 96. Note that the lower galaxy in instances (a) and (b) becomes the upper galaxy in instances (c) and (d).

## 2.5 Vorontsov-Vel'yaminov (1959) and Arp (1966)

Vorontsov-Vel'yaminov published **The Atlas and Catalogue of Interacting Galaxies** in 1959. A compilation of interacting galaxies found in the Palomar Sky Survey and the Crimean Station of the Institute, *The Atlas...* was a record of fragmenting galaxies according to Vorontsov-Vel'yaminov, a theory proposed by Ambartsumyan in 1958.

Inspired by both Zwicky's sketches and faint images of peculiar and distorted galaxies, such as those of Vorontsov Velyaminov, Halton Arp spent four years photographing many such objects with the Palomar 200 inch. He believed that

”the peculiarities...represent perturbations, deformations and interactions which should enable us to analyze the nature of real galaxies which we observe and which are too remote to experiment on directly”. In 1966, he published his *Atlas of Peculiar Galaxies*, containing high resolution images of 338 systems .

## 2.6 Toomre and Toomre (1972)

During the 1960’s, Pfleiderer and Siedentopf investigated how spiral patterns in disk galaxies could be excited by gravitational interactions between disk galaxies and concluded that chance encounters between field galaxies are not sufficiently common enough to produce the observed population of spirals. However, they did produce, albeit in passing, the first plots of tail and bridge building.

This was followed in the early 1970’s by a spate of papers, but one in particular stands out. **Galactic Bridges and Tails** by Toomre and Toomre (1972) is seen as many as the seminal paper in the field of galaxy interactions and mergers. Although it was not unusual at this time for a paper to be published that dealt with computer modeling of interacting galaxies, the publication of TT’s paper was seen by many as a key turning point in the theory of interacting galaxies, triggering a true paradigm shift in the field. As will be highlighted in the next section, **Galactic Bridges and Tails** clearly established that bridges and tails - which for so long were the source of much heated debate and disagreement - were gravitational in nature. The paper comprehensively offered a very plausible and natural means to produce these characteristic features of interacting galaxies and indeed, through their discussion of related phenomena in the final section, the Toomres inspired a burst of new research. In particular, the discussion, *Stoking the Furnace*, preempted Larson&Tinsley’s 1978 paper which showed the connection between starbursts and the merging of galaxies.

## 3 Numerical Models of NGC4038/9

There have been several attempts to model the “Antennae” in the literature. I will, however, concentrate this discussion on Toomre and Toomre’s 1972 paper, **Galactic Bridges and Tails** and Barnes’ 1988 paper, **Encounters of Disk/Halo Galaxies**.

At the end of the main discussion, I will briefly discuss some of the observations that must be satisfied if the models are to be considered successful reconstructions.

Toomre and Toomre’s 1972 paper is seen by many as the seminal work in this field, triggering a paradigm shift and establishing mergers and tidal interactions as respectable subjects for theoretical inquiry. Although there were several papers in the literature dealing with interacting galaxies at that time and despite the fact that their modeling of galaxies as central masses surrounded by disks of test particles was hardly novel, there were many virtues to the Toomres’ work:

- their clear establishment of the necessary conditions for interactions to occur, in particular, an appreciation for the importance of bound encounters.
- their lucid descriptions of bridge and tail making
- their analysis and reconstruction of several well known interacting systems
- their discussion of merger related phenomena which preempted observations made several years later.

Barnes' paper, published 16 years after the Toomres' attempt, was the first to model interacting galaxies as fully 3 dimensional N-Body entities whose equations of motion were integrated in a self consistent manner. An important and telling addition to the simulation's armory was the presence of a massive dark halo; this would have an important effect on the evolution of the merger.

### 3.1 Toomre and Toomre, 1972

In **Galactic Bridges and Tails**, Toomre and Toomre (hereafter, TT) considered encounters between pairs of galaxies on parabolic orbits; each galaxy was idealized as just a disk of noninteracting test particles initially in orbit about a central mass points. As a result, all explicit self gravity of the disk was neglected; this was justified on two grounds:

- the self attraction of the outer part of a disk is, by definition, small. Hence, by neglecting self gravity the main qualitative conclusions are unlikely to be affected
- by relying on test particles as tracers it was hoped to make clear the kinematic nature of the observed filamentary structures.

TT modeled 4 interacting systems - Arp 295, M51, NGC 4676 and NGC 4038/9 - but it was their reconstruction of the "Antennae" which gave them "the most pleasure". This stemmed from prior concerns regarding whether "it was possible to obtain seemingly crossed tails from tidal interactions".

In section IV of TT, *Survey of Tails*, it is noted that "proper tail making in the sense of escape to infinity of particles from the antitidal side of a victim disk requires the perturbing mass to be at least comparable to the perturbed". Hence, if we observe an interacting system with two prominent tidal tails emanating from both disks of both galaxies then we can conclude that the masses involved were comparable and that the separation at periapse was small. With this assumption in mind, a mass ratio of exactly unity was assumed in the survey of 3 dimensional tails. This survey was of particular importance for analysis of NGC 4038/9, and in particular figure 18 of this section, shown below, plays a

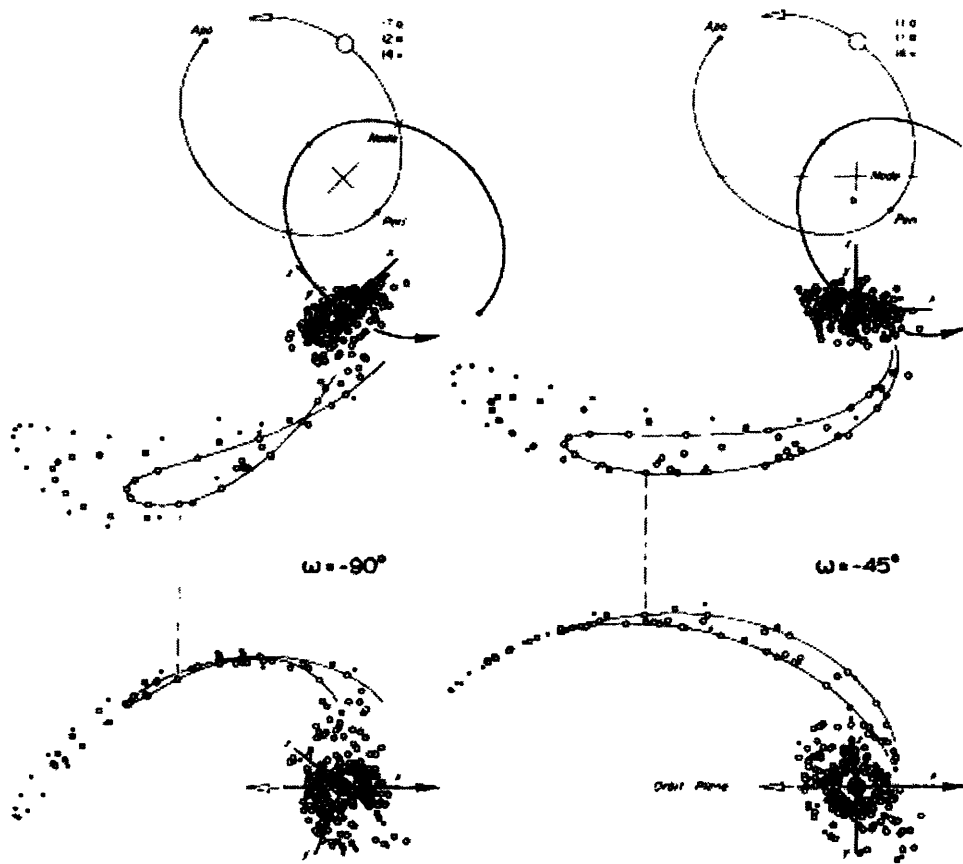


Figure 1: Figure 18 on page 623 of **Galactic Bridges and Tails**. This is part of the tail survey; in this case, the ellipticity was  $e \approx 0.6$  for equal mass passages of fixed inclination  $i = 60^\circ$  but with different orbital arguments of  $\omega = -90^\circ, -45^\circ, 0^\circ$  and  $45^\circ$ . The viewing time is  $t=6.086$  in their units, corresponding to  $135^\circ$  of orbit travel since pericenter. The viewing angles are normal and edge on to the orbit plane; in this case, the edge on views are from directions which exactly superpose the centers of victim and satellite.



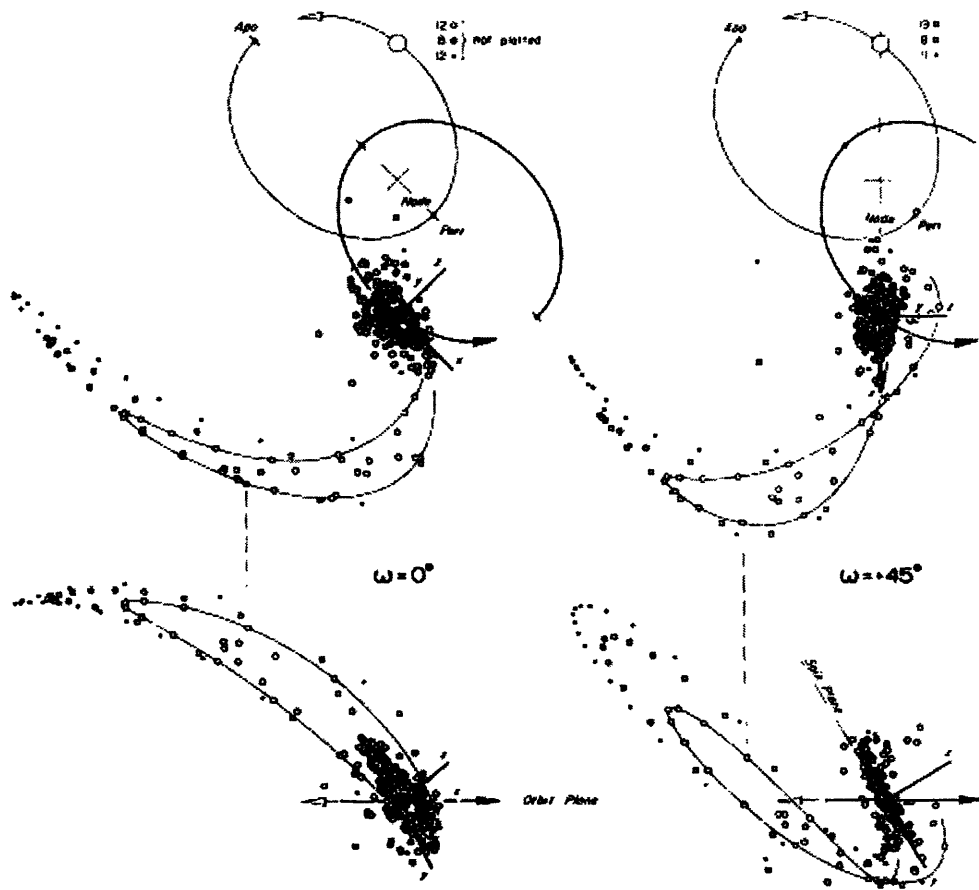


Figure 2: Figure 18 on page 624 of **Galactic Bridges and Tails**.

central theme.

TT observed that if every bare companion carried an  $i = 60^\circ$  tail of its own, chosen from amongst the four possibilities after a  $180^\circ$  visual rotation about the axis normal to the orbital plane, that no tail crossings were to be found in any view that was roughly perpendicular to the orbits. In addition to this, they were able to exclude all other views from near the great circle normal to the line connecting the masses; this was because of the precondition that no part of one tail could be much closer to the other than the distance between the hulks themselves.

Views from along the connecting line, however, produce a pair of crossed tails which TT compare to a “pair of symmetric gull wings”. In this case, they utilised the  $\omega = -45^\circ$  tail in figure 18 together with its identical twin attached to the perturbing mass. Similar results are possible for both the  $\omega = -90^\circ$  and  $\omega = 0^\circ$  cases, and almost the same for either case partnered with  $\omega = -45^\circ$  ribbon. The result is illustrated in figure 23 of TT, as shown.

TT chose the precise orbital parameters used in figure 23 to produce a result in accord with their 1971 NGC 4038/9 movie.

The forces from each massive body were softened gradually at close range by varying the potential at small radius as:

$$\Phi \approx -\frac{GM}{\sqrt{r^2 + a^2}}$$

where  $a = 0.2R_{min}$  as opposed to the standard  $\Phi = -GM/r$ . This gravity softening was essential in the mimicking of the mass distribution; if neglected, too many of the near side particles would have been extracted from both of the disks. In addition, this gravity softening facilitated further thinning of the tails. Whilst the models successfully reproduced the hallmark crossed tails of the “Antennae”, TT noted several deficiencies:

1. the real tails are unequal in length.
2. the actual NGC 4038 tail is more curved than in the model.
3. the rotation of the real hulks seem to be such that their adjacent ends approach and recede alike whereas the opposite holds true for the models.

In an attempt to remedy these shortcomings, TT made three suggestions:

- unequal tail length (objection 1) can be achieved by introducing slight inequalities in either the masses, inclinations or the initial outer radii.
- the second objection would seem to suggest that a second encounter will occur.

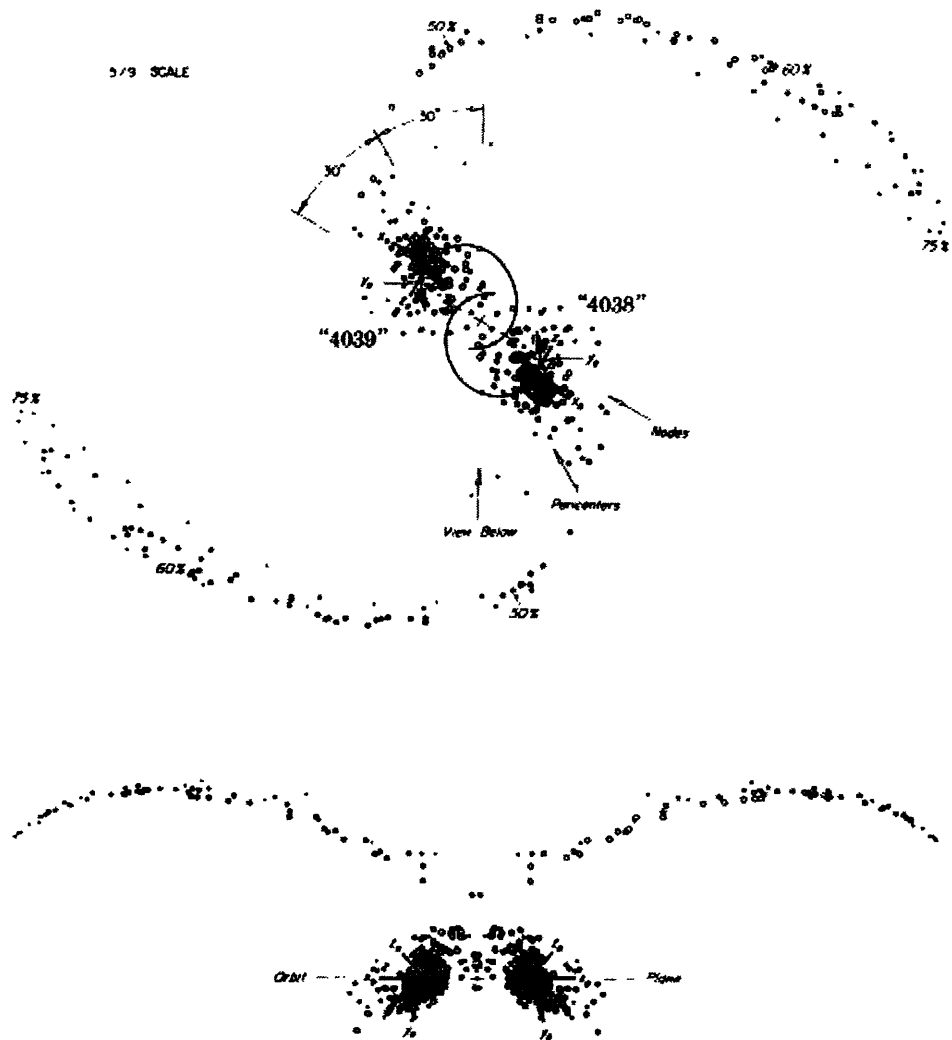


Figure 3: Figure 23 of **Galactic Bridges and Tails**. In this instance we see two identical disks of radius  $0.75 R_{min}$  which have undergone an  $e \approx 0.5$  encounter with orbit angles  $i_8 = i_9 = 60^\circ$  and argument at pericenter  $\omega_8 = \omega_9 = -30^\circ$  that appeared the same to both. The subscripts refer to the galaxies NGC 4038 and NGC 4039 respectively. The upper view is exactly normal to the orbit plane, while the lower view is edge on to the orbit plane with a viewing direction  $30^\circ$  from the line connecting the two pericenters. The viewing time is at  $t=15$  in their units, just slightly past apocenter.

- the third objection, by far the most serious, requires a substantial change of at least the argument  $\omega_\theta$  from  $-30^\circ \rightarrow -90^\circ$  as well as a further reduction in the longitude of viewing.

Despite the shortcomings, the Toomres captured the essence of the Antennae with a simplified 3-body model, and as they indicated, if further progress was to be made then a full N-Body self consistent code was necessary.

### 3.2 Barnes, 1988

In **Encounters between Disk/Halo Galaxies**, Barnes used prototype bulge/disk/halo model galaxies. These models consisted of a central bulge, a thin rotating disk and an optional spherical extended halo. The exact details of the simulated encounter which would produce the observed features of NGC 4038/9 followed those of Toomre and Toomre; the initial conditions corresponded closely to those used in **Galactic Bridges and Tails**, although some modifications were necessary to account for the presence of the massive dark halo.

The main characteristics of the model galaxies were as follows:

Mass Ratio of Components	1:3:16
Total Mass of Components	$M_B + M_D + M_H = 1.25$
Inverse Scale Length of Exponential Disk	$\alpha = 12$
Circular orbital period at radius $r = 3/\alpha$	$t_{orbit} = 0.93$

All these quantities were measured in arbitrary units with  $G = 1$ . Scaling to our galaxy, these numbers correspond to a length of 40 kpc, a time of 250 Myrs and a mass of  $2.2 \times 10^{11} M_\odot$ .

The galaxies were started on elliptical orbits with an eccentricity of  $e=0.5$ ; their pericentric separation was  $r_p = 0.5$  and the time to pericentre was  $t_p = 1.0$ . Both galaxies were inclined at  $i = 60^\circ$  to the orbital plane with a pericentric argument of  $\omega = -30^\circ$ .

These particular initial conditions will lead to a slow symmetric prograde encounter with the two disks inclined so as to sling tidal tails high above the orbital plane where they will eventually be seen in projection crossing each other. The configuration used is shown in figure 4.

Whereas Toomre and Toomre's test particle model galaxies followed Keplerian trajectories, the orbits of Barnes' self consistent model galaxies quickly decayed. The tidal coupling of orbital to internal motion was so effective that the relative orbit decayed in less than one initial orbital period. This was due to the presence of the massive dark halo which effectively soaked up the energy and angular momentum, as shown previously by van Albada and van Gorkum. Barnes noted that at the time when TT's model most closely matched observations, his models had already merged. However, his models do produce a configuration that

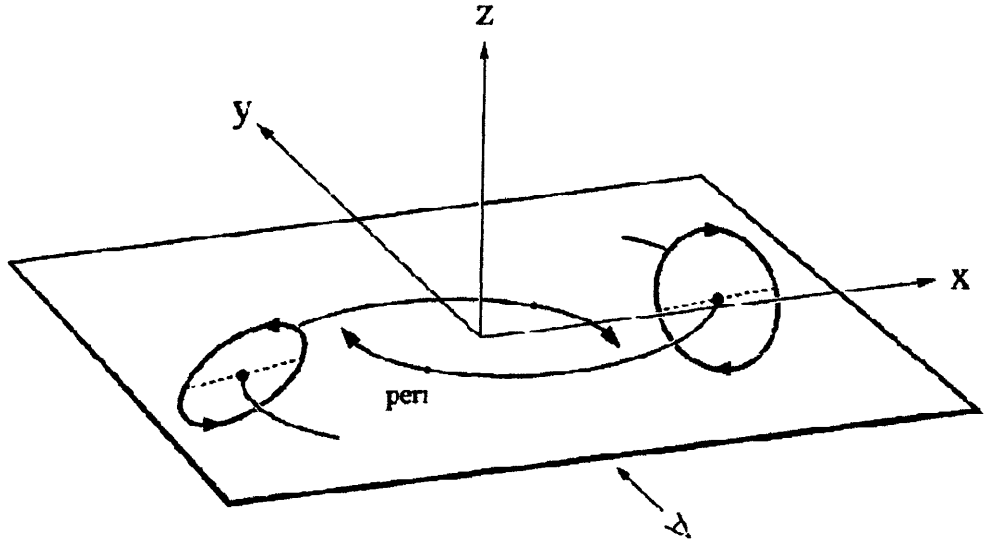


Figure 4: Figure 1 of **Encounters of Disk/Halo Galaxies**, illustrating the geometry of the encounter.

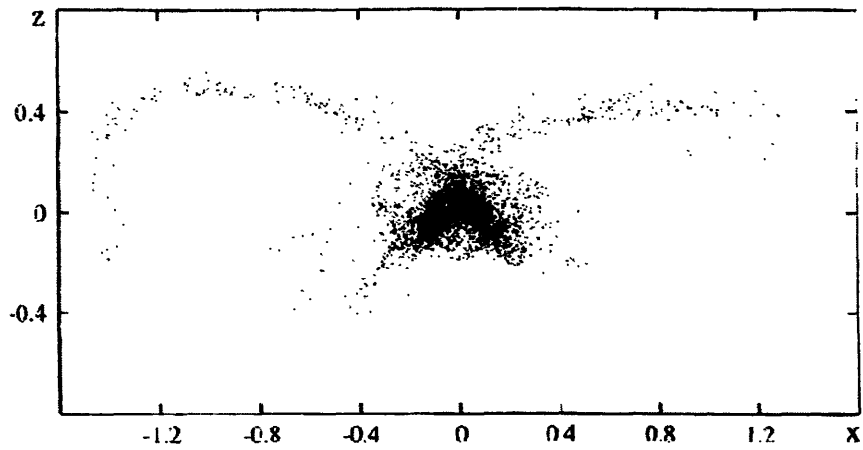


Figure 5: Figure 2 of **Encounters of Disk/Halo Galaxies**, showing the resulting configuration.

resembled observations but at a *much earlier time* -  $t=1.8$  in his arbitrary time units, corresponding to roughly one quarter of the initial orbital period after pericentre.

Further analysis of the encounter revealed several interesting features:

- the interaction slewed the inner galactic disks by  $\sim 70^\circ$  counterclockwise, almost edge on to our line of sight, indicating the presence of powerful torques on the disks during the encounter.
- distinct peaks in the dark matter distribution were observed to coincide with the luminous tails, “like a dark, distended body surrounding a luminous spine”.
- the visible tails were confined within the halo; this is a consequence of the dark matter, which initially shared phase space with the luminous matter, tagging along to the present stage.
- the more curving left hand tail of the model matches closely the appearance of the south western tail as revealed in both deep optical images (Schweizer, 1978) and high resolution HI mapping (Van der Hulst, 1979).
- Barnes was keen to stress that the asymmetry between the two tails was not due to any macroscopic asymmetry in the initial conditions <sup>1</sup> but was instead due to  $\sqrt{N}$  fluctuations in the galaxies which are swing amplified by the disk and sheared out by tidal forces during the encounter, thus further populating one of the resulting tidal arms.

Reviewing this particular simulation, Barnes considered both the positive and negative aspects of the result; the model encounter successfully reproduced:

- the narrowness of the tidal tails. This demonstrated the requirement for relatively cold disks. Previous attempts to self consistently model encounters of this kind, such as those of Negroponte (1987), produced stubby tails, clearly at odds with observation.
- the proximity of the hulks. This is a distinct improvement on TT’s model; although TT foresaw the importance of orbital decay due to tidal friction, they certainly could not have anticipated the rapidity of the decay. By following the bulges (which trace the dynamical centres of the galaxies) Barnes was able to observe that these bulges barely separated after pericentre, plunging back together after one third of an orbital revolution.

However, the model result was not without its shortcomings:

- The model galaxies, as shown in figure 5, are approaching one another along the line of sight with velocities comparable to the circular velocity

---

<sup>1</sup>Indeed, the encounter itself was symmetric.

of each disk. However, studies in HII (Rubin, Ford and D’Odorico, 1970) and HI (Mahony *et al*) indicate only a small line of sight difference -  $\sim 40 \text{ kms}^{-1}$ . Thus the model fails to match the observed kinematics of the main hulks.

- Conceptually there are problems associated with the very existence of this  $e=0.5$  orbit. The orbital period for such an encounter is *longer* than the Hubble time! Due consideration would seem to suggest that the galaxies experienced a close parabolic encounter - but such encounters do not result in configurations such as the one observed in the Antennae.

In conclusion, Barnes noted that the model of NGC 4038/9 came *subjectively* close to matching the appearance of the Antennae; based on this observation, it was felt, with some confidence, that the basic elements of the encounter were correct. He did caution, however, that the quality of the match was somewhat enhanced by the presence of *chance fluctuations* which could grow to macroscopic proportions at the right time and place to produce asymmetric tails - and so it would be **neither possible to infer precise properties of the progenitors nor to establish the uniqueness of a solution.**

### 3.3 Star Formation Rates in the “Antennae”

In their 1993 paper, Mihos, Richstone and Bothun considered models of NGC 4038/9 directly based on those used by Barnes in **Encounters of Disk/Halo Galaxies**, but with star formation rates in mind.. They tried to match the observed SFR with the model SFR by examining the spatial distribution of  $\text{H}\alpha$  and CO, but discovered that the models predicted that the nuclear regions should carry the majority of the star formation and ISM mass in the system. Based on observations, the model should have demonstrated the SFR and CO emission evenly divided between the nuclear and overlap regions.

### 3.4 Future Directions

As is clear from the previous discussions, while NGC 4038/9 has been modeled with some success, the simulated encounters have failed to reproduce some of the key characteristics of the system. In his 1998 review of galaxy interactions, Josh Barnes outlined four key elements that any improved model of the Antennae must include:

- Matching the observed velocity field - radial velocities of the two galaxies differ by only  $40 \text{ kms}^{-1}$ , much lower than those produced in previous models.
- Reconciling the adopted orbit with cosmological expectations - whereas previous simulations adopted elliptical ( $e \sim 0.6$ ) orbits, parabolic orbits would seem to be more plausible.

- Reproducing the gas rich ring in NGC 4038 - this ring is clearly visible in both the mid-IR and HI maps, and contains many young star clusters.
- Explaining the “overlap region” - this dusty region is brighter than either disk in mid-IR wavebands according to recent ISO observations. (Mirabel et al., 1998)

## 4 Model Matching

If a model is to be considered a successful representation of a physical system, it must reproduce the essential features of the system as gauged by observations. In the case of interacting galaxies, this reduces to matching the characteristic morphology and kinematics, but it is by no means a simple task.

As outlined in the previous section, there are several parameters which govern the evolution of an interacting pair of galaxies - the mass ratio of the pair, the inclination of their relative orbits, the pericentric argument, the ellipticity of the orbits and the viewing angle to name but a few. Subtle changes in a single parameter may have a significant effect on the morphology and kinematics of the observed pair. Furthermore, it is possible that no single set of initial conditions uniquely determine the final outcome (Barnes, 1988).

With these significant factors in mind, it is clear that model matching is a potentially daunting task. However, by making some plausible assumptions and deciding to work with carefully chosen characteristics of the system, it is possible to simplify the process somewhat.

When we set out to match tailed galaxies, our sample is already predefined - spiral galaxies which possess dynamically cold gas rich disks. As described above, Barnes noted in his 1988 paper that such dynamically cold disks are essential if the characteristic features of tidal interactions are to be reproduced. Furthermore, it is a well known observational fact that spirals have copious amounts of HI in their disks and that this neutral hydrogen extends out to approximately twice the luminous radius of a galaxy. This key fact coupled with the 21cm spectral line of HI which freely exhibits a Doppler shift in response to its motion offer us an effective **tracer**. Such a tracer reveals not only the spatial structure of bridges and tails but also the line of sight velocities. This information is vital.

In modeling encounters between galaxies, how the galaxy is represented can play a important role in how the interaction evolves. As Barnes (1988) noted, the inclusion of the massive dark halo in his fully N-body self consistent BDH encounter had a profound effect on the merging time when compared to Toomre and Toomre’s 3 body test particle encounter. (This demonstrates the importance of the dark halo for tidal friction and orbit decay.) Any *recipe* for model matching that is adopted must target characteristic features which are model independent.



For the model matching, I made extensive use of John's **Identikit** display package; this gives 3 separate projections - X-Y, Vz-Y and X-Vz- of the data under consideration, where X,Y and Z are the standard spatial coordinates and Vz is the line of sight velocity. The user can perform rotations about the spatial axes as well as scalings (both radial and velocity) of the model data compared to preloaded HI observational data.

During the early stages of the fitting process, I used alignment of the bulges as an initial guide towards a best fit; this seemed reasonable since the bulges track the dynamical centres of the galaxies. However, I soon revised the technique; the bulges **do** track the dynamical centres but their exact behaviour is uncertain under different kinds of galaxy models. Thus, I decided to simply concentrate on using the tails to guide the matching process.

Although I identified several lines of enquiry whose results would prove useful for future model fitting, both circumstances and time hampered any efforts to pursue them. In particular, I had hoped to investigate how the inclination of the disks during encounter affected results in terms of model dependency and also how changes in the respective orbital inclinations of the individual galaxies would change the results of the encounter.

Essentially, the primary purpose of my model matching efforts was not so much to identify a best fit - unlikely given the size of the parameter space - but to identify steps in the process which would lend themselves to automation. Discussion with John would seem to indicate that this primary goal was achieved.

## 5 Visualization of Data

### 5.1 Visualization and N-Body Simulations

One of the key aspects of my Summer's work was to develop software which would facilitate 3 dimensional visualisation of both model and observational data.

The very nature of the problem - modeling interactions between galaxies - is one played in a 7 dimensional parameter space of which only 3 of the dimensions - X, Y and Vz - are observable. What we observe is sensitive not only to the intrinsic physical parameters of the system, such as the mass ratio of the galaxies, but also to our viewing angle. Indeed Zwicky, in 1953, realised the importance of projection effects on what observe in his analysis of M51, noting that the narrowest of the filaments observed may be broad sheets of matter seen nearly edge on. It is not difficult to imagine a range of initial orbital parameters producing results which resemble the Antennae as we observe them today. This particular point was emphasized in **Encounters between Disk/Halo Galaxies**(Barnes, 1988).

Primarily, my intention was to build a programme that would allow the user to

view and manipulate, in effect, to get a physical picture of the data in a three dimensional form, before moving on to carry out more quantitative analyses using John's existing software.

Several options were considered - IDL, Java, VRML and the final choice, Geomview. Geomview is an interactive three dimensional visualisation tool that was developed by the now inactive Geometry Centre. As a means of visualisation, it is particularly user friendly and fulfilled all out criteria for processing speed and ease of use. The range of actions available to the user - rotations, translations, zoom in and out - are carried out by a simple point, click and drag. The object can be simultaneously viewed from several camera locations and the user may observe how the view changes from different perspectives.

The next task was to develop a programme which could take our existing data and convert it into a format which could be read by Geomview. I decided to use C for the writing of this programme because it is reasonable to expect that most users will have some proficiency in this particular language, thus allowing them to modify the programme if necessary, and also because I wished the programme to be integrated into existing software which is written in C.

The problem in hand reduced to reading in data which may exist in a variety of formats and writing this data to file in a form that would give a meaningful physical representation of the results. The first part of the problem was dealt with relative ease - given the structure of the data files which were to be read, I could simply tailor a specific function to read the required data from the file. The second part of the problem required a little more thought, but serendipity showed her hand and it was discovered that by using the OOGL VECT object file format, it was possible to get a particle representation of the data.

## 5.2 Sim2Oogl - A Snap, Zeno and P File Conversion Programme

With this information, writing the programme was quite straightforward; invoked from the command line, the programme which is called `sim2oogl` requires the name of the data file to be converted, the format of the data file and the type of output desired.

- the format of the file : this refers to the structure of the file - it can be SNAP/Tipsy, Zeno or P.
  - Tipsy files are readable by the Tipsy data visualisation package; this allows results of N-Body simulations to be quickly displayed and analysed.
  - Zeno files are produced by Josh Barnes Zeno N-Body simulation package.
  - P files are simple ascii data files

- the type of output desired : this rather self evidently refers to the form of Geomview readable output that is produced by the programme. The user can choose one of:
  - position coordinates (X-Y-Z)
  - velocity coordinates (Vx-Vy-Vz)
  - position (X-Y) with line of sight velocity (Vz)
  - position (X-Y-Z) with velocity vectors (Vx-Vy-Vz)
  - all of the above

Additional options are available - the user can define the number of particles in the disks and halo as well the number of galaxies involved. The default assumes two galaxies without halos and each disk containing  $N/2$  particles, where  $N$  is the total number of particles involved in the encounter.

Since Geomview is being used to display our data, I decided to further develop `sim2oogl` into an external module which can be used in tandem with the command line version of the programme. This module is called **Sim2Oogl** and it offers the user a GUI, built using the Tk/Tcl toolkit and scripting language, and invoked from within Geomview. The GUI extends the usability of `sim2oogl`, allowing the user to carry out a batch conversion of data files in addition to allowing files to be viewed once they have been converted.

The Tk GUI is built on top of the basic command line version of `sim2oogl`; the programme's function which handles input and output can be developed into a dynamically loadable extension that can be loaded into the Tcl interpreter using the `load` command. In principle, this is possible by working with Tk/Tcl's collection of C libraries, but a somewhat easier route was taken by using a programme called SWIG. SWIG requires an interface file in which the C functions to be used are declared as external objects; when invoked, SWIG then produces a wrapper file that is compiled and linked with the rest of the programme. In doing so, we get the dynamically loadable extension that can then be loaded into the Tcl script. Thus we have a means for exchanging information between the user interface and the basic conversion programme, as desired.

A comprehensive website - <http://www.cv.nrao.edu/~cpower/Sim2Oogl> - **Sim2Oogl1.0 in a Nutshell** was prepared (and mirrored in the packaged documentation) for user support. Further modifications of the programme will be posted to this website as they come to fruition.

### 5.3 Sim2Oogl as a Scientific Tool

Sim2Oogl was initially developed with aspirations of serious quantitative analysis in mind; however, after some time it was noted that it's main developer, Geometry Centre, has been inactive since early 1998 and thus active support is no longer available. Both John and myself had planned to contact groups using

Geomview for 3-D visualisation of N-Body data in the hope that their experiences would help guide our usage of Geomview. Could John's existing software, which displayed different aspects of the data in phase space, be superseded by a programme which used Geomview to display this information? This question was left unanswered, but my feeling is that it may be possible, but only if a significant portion of time is devoted to modifying the package as it stands. Despite this rather disheartening outcome, Sim2Oogl in its present form is a simple, robust programme which quickly and effectively converts data into a form which gives the researcher a "feeling" for the main qualitative features of the system being studied.

## 6 Conclusions

Barnes referred to the "Antennae" as the "Rosetta Stone" of interacting galaxies. Indeed, this particular system appears to hold a certain fascination for researchers in the field, starting with Toomre and Toomre's simple computer models in the early 1970s; (tenuous) parallels may be drawn between their attempts to decipher the crossed tails of NGC 4038/9 and the early efforts to unravel the secrets of the hieroglyphs. However, as should be clear from this report, a great body of research is concentrated on gaining a comprehensive understanding of the "Antennae". While previous modeled encounters have given promising results, there still exist basic discrepancies between model and observation which must be resolved before this comprehensive understanding can be claimed.

Although my contribution to this field was limited, I feel that my work on the 3D dimensional visualisation of data is of considerable use to researchers. Sim2Oogl is very user friendly and easily modified, a simple but effective tool. The fruits of model matching were less tangible, but I firmly believe that a level of sophistication is possible in automating our matching process which has been absent in other attempts.

## 7 With thanks to...

I don't think I can thank John Hibbard enough, but I can say that he has played a major part in making my Summer at NRAO one of the most positive experiences I have ever had. He has been a great influence to me over the last few months and has taught me a great deal about the path in life I've decided to take. I want to thank Juan Uson and Jack Gallimore for taking the time to indulge my interests over the course of the Summer; and Tracy Efland and Pat Murphy for making playful computers an altogether less stressful affair.

I'd also like to thank NRAO for giving me the opportunity to partake in the Graduate Research Programme as well as for their financial support this Summer; and Prof. Werner Blau, the Department of Physics and the Alice Barklie fund, all of Trinity College, Dublin for providing for my international travel expenses.

## 8 References

Note: The following references are listed in terms of decreasing usage - some references were purely of historical interest while others played a major role in developing my understanding of the subject. This is particularly true in the case of the first section.

- **Galaxies : Interactions and Induced Star Formation, Saas-Fee Advanced Course 26**, Springer. Edited by Kennicutt, R.C., Schweizer, F. and Barnes, J.E. - Essential Reading
- **Galactic Dynamics**, Binney, J. and Tremaine, S. Princeton University Press, 1987 - Yet more essential reading!
- **Galactic Bridges and Tails**, Toomre, A. and Toomre, J. 1972, ApJ, 172, 623.
- **Encounters of Disk/Halo Galaxies**, Barnes, J. 1988, ApJ, 331, 699
- **Dynamical Modeling of NGC 7252 and the Return of Tidal Material**, Hibbard, J. and Mihos, C. 1995, AJ, 110, 140

These references were used more for general or historical interest.

- **A Morphological Catalog of Galaxies in the Hubble deep Field**, Van den Bergh, S., Abraham, R.G., Ellis, R.S., Tanvir, N.R., Santiago, B.X. and Glazebrook, K.G. 1996, AJ, 112, 359.
- **Star Formation Rates in Normal and Peculiar Galaxies**, Larson, R. and Tinsley, B. 1978, ApJ, vol. 219, p. 46.
- **Evidence from the motions of old stars that the Galaxy collapsed**. Eggen, O.J., Lynden-Bell, D. and Sandage, A. 1962, ApJ 136, 748.
- **On the Clustering Tendencies among the Nebulae. II. A Study of Encounters between Laboratory Models of Stellar Systems by a New Integration Procedure**, Holmberg, E. 1941, ApJ, vol. 94, p. 385.
- Zwicky, F., Physics Today. 1953, 6, 7.
- Zwicky, F., Ergebnisse d. exakten Naturw. 1956, 29, 344.

- **The Atlas and Catalogue of Interacting Galaxies.** Vorontsov-Velyaminov, B.A. 1959
- **Extragalactic Astronomy,** Vorontsov-Velyaminov, B.A. Harwood Academic Publishers, 1987
- **Atlas Of Peculiar Galaxies.** Arp, H. 1966
- Pfeiderer, J. and Siedentopf, H. Zs. f. Ap, 51, 201. 1961
- Pfeiderer, J. Zs. f. Ap, 58, 12. 1963



# NRAO Summer Project Report

## Ionized Gas in Starburst Galaxies : A Study Using Radio Recombination Lines

Niruj Mohan Ramanujam  
(RAMAN RESEARCH INSTITUTE, INDIA)



- **Background**

I have been working on Radio Recombination Lines from Starburst galaxies for my graduate thesis in India, using the VLA. We had been scheduled a total of 54 hours for three different proposals on the VLA this summer. We were involved in the data reduction and analysis during this period.

Most galaxies have ongoing star formation. This usually proceeds at a steady rate of about  $\leq 1 M_{\odot}/yr$  over the whole disk galaxy with an efficiency of  $\leq 5\%$ , the efficiency being a measure of the fraction of molecular gas which gets converted to stars. The star formation rate depends on the surface density of the gas in the region which does not vary too much across galaxies.

There are a few galaxies (roughly 10% of all galaxies at small redshifts) where star formation proceeds at a rate 10-1000 times larger than normal galaxies. For example, in Starburst Nuclear Galaxies, one sees a rate of  $1-10 M_{\odot}/yr$  in a region which is less than a kpc in size. Star formation rates of a few  $1000 M_{\odot}/yr$  are seen in Ultra Luminous InfraRed Galaxies (ULIRGs). Star formation efficiency is also correspondingly higher in these galaxies (20-50%). These imply a high gas surface density which has been confirmed observationally. To increase the gas density by a factor of 10-100, an efficient way to dispose of the angular momentum of the gas has to be involved. Galaxy mergers and interactions are thought to be the major causes of gas inflow to the potential well. The presence of strong bars in interacting galaxies seems to enhance the gas inflow to the centre. The cause of the increased star formation efficiency is not well understood but overpressure due to the high intercloud gas density is believed to play an important role. Given the high rates of star formation and the total amount of gas found in these regions, it can be calculated that all the gas will be exhausted in a time much less than Hubble time and hence the galaxy will not be able to sustain this high star formation throughout its lifetime. Hence it is believed that galaxies are usually systems like our galaxy, producing stars at a small but steady rate and at some point of time, might have a burst of star formation due to interactions or mergers which lasts for a few tens of million years after which it gets back to normal. These galaxies, therefore, are called Starburst Galaxies.

Starburst regions are dominated by massive stars. These are responsible for the ultraviolet light from these starbursts. It is known that starbursts have huge amounts of dust in them. This dust absorbs most of the ultraviolet light and reradiates it in the infrared which peaks at roughly  $60 \mu m$ . In fact, the luminosity of starburst galaxies peaks in the infra-red and the IR luminosity is close to the total bolometric luminosity. Due to the large number of massive stars, we expect a large amount of ionized gas, which can be seen using optical and NIR Hydrogen recombination lines and NIR fine structure lines of heavy elements. The radio continuum, on the other hand is predominantly synchrotron and the thermal brehmstrahlung is a minor component. As the amount of dust mixed, and in front of these ionized HII regions is quite large, the extinction towards these regions, estimated from optical and NIR line ratios ranges from 1 to 30 magnitudes. A new tool has emerged in the past few years, to study the ionized gas, namely, by using Radio Recombination Lines (RRL), This has been possible due to new receivers on the VLA which are better than the older ones by a significant amount.

- **Present Work** We have been granted time on the VLA this summer on three different projects which are extensions of past work done with the VLA. They are :

a. Searching for RRLs from pc scale compact sources in the nucleus of *NGC 253* at 15 GHz using the VLA A configuration, based on the spectral indices and fluxes of these sources from Ulvestad and Antonucci (1997).

b. 15 GHz observations of RRLs from *NGC 3628 and IC 690/NGC 3690* in the D configuration as a follow-up to 8.3 GHz and 1.4 GHz observations of these galaxies with the VLA.

c. Searching for RRLs towards 6 new galaxies at 8.3 GHz using the VLA, in both the C and D configurations. We had been awarded a total of 48 hours, 4 hours per source per configuration. The six new galaxies, selected on the basis of their Br $\gamma$  fluxes are *NGC 5253, NGC 4038/4039, NGC 7552, NGC 1808, Henize 2-10 and VV 114*.

These observations were done this summer. Most of the data has been reduced and a few of the galaxies have been modelled to constrain the physical properties of these starburst regions.

#### **a. RRLs from compact sources in NGC 253**

Ulvestad and Antonucci have observed NGC 253 with the VLA in multiconfigurations and multi frequencies in the continuum. They detect over 50 compact sources with varying spectral indices. Some of these sources seem to contain a good fraction of thermal gas whereas most of the others are dominated by synchrotron emission. These sources are typically a few 10s of mJys in strength and are a few parsecs in diameter or less. We had estimated the RRL flux expected from a few of them which have a significant amount of thermal gas and results indicated that these could be detected by the VLA at 15 GHz. If so, this would prove our results from low resolution observations that the RRLs in the cm are emitted by compact HII regions.

We observed NGC 253 in the A array at 15 GHz for a total of 10 hours. We detect lines from a few of the compact sources. The line strengths are much less than expected. We will be modelling the line strengths in detail to estimate physical conditions. The reason for the lower line strength could be either non-unity values of filling factor in these sources or densities vastly different from those estimated from the continuum fluxes. Since this regions is crowded with lots of compact sources and quite a bit of extended emission as well, Ulvestad and Antonucci state that their flux determination and hence the spectral indices could have larger errors than quoted. If that is so, and the thermal component is much smaller than estimated, that would also lead to a lesser RRL flux.

We also have A array 8.3 GHz data on this galaxy, taken with the VLA this summer. This has a slightly larger beam and hence we would not lose any extended RRL flux as we might have done in the 15 GHz maps. We shall therefore compare the line maps of the 15 and 8.3 GHz data to constrain the properties of these thermal compact sources further and to verify if this is the population which emits the RRLs we see in low resolution VLA maps in the cm wavelength.

#### **b. 15 GHz band RRLs from NGC 3690 and NGC 3628**

Anantha et al (1993) had imaged the two starburst galaxies NGC 3628 and NGC 3690/IC 694 in recombination lines at 8.3 GHz. Modelling these lines based on a collection of HII regions as the line emitting source gave two classes of model which were degenerate to the 8

GHz line and continuum data. One class was that of high density ( $\geq 10^4 \text{cc}^{-1}$ ) compact (size  $\leq 1 \text{ pc}$ ) HII regions and the other was that of lower density ( $\leq 10^3 \text{cc}^{-1}$ ) bigger ( $\geq 5 \text{ pc}$ ) HII regions. The models predicted different line fluxes for these two classes of models at 1.4 GHz. We observed these two galaxies at 1.4 GHz with VLA and failed to detect a line at a 3 sigma level of 0.3 mJy. This rules out the low density models. In order to confirm the high density picture, we observed the galaxies at 15 GHz this summer with the VLA in the D configuration. Lines were detected in both these galaxies, with a strength consistent with high density gas. Further detailed modelling is being done.

### c. Searching for RRLs at 8.3 GHz from 6 new starbursts

More than a dozen galaxies have been detected in Radio Recombination Lines, mainly at 8.3 GHz using the VLA over the last decade. We wanted to expand this list and applied for time to search for lines towards 6 new galaxies and were granted a total of 48 hours. We selected NGC 5253, NGC 7552, NGC 4038/4039, Henize 2-10, VV 114 and NGC 1808 based on their high Br $\gamma$  flux and radio continuum flux. We observed each galaxy at 8.3 GHz in both the C and D configurations, for 4 hours per source per configuration this summer.

We have analysed the data for all the galaxies except for NGC 7552. Lines were detected in NGC 5253, Henize 2-10 and NGC 1808. We have a possible detection for NGC 4038/4039 and no lines were seen in VV 114. We have done detailed modelling of the lines from NGC 5253 and He 2-10 which we shall describe below.

#### *Modelling and physical parameters of the ionized gas in NGC 5253 and He 2-10*

Modelling was based on the unresolved emission line strength and the continuum from the same area. The basic features of the models were similar to previous ones (AZGV, ZAGV). The first model which was tried out was a uniform screen of ionized gas in front of the synchrotron radiation. As before, the only valid solutions which would reproduce the observed line and continuum data corresponded to electron temperatures of about 2500 K which are unphysical, especially since these two galaxies are of subsolar metallicities.

The next model which was tried out, which has been shown to work for all the starburst galaxies seen in RRLs so far is a collection of HII regions. A grid of models is set up - the free parameters being the electron density ( $n_e$ ), electron temperature ( $T_e$ ) and the size of the HII region ( $l$ ). The grid values assumed are :

$n_e$  : 0.01, 0.05, 0.1, 0.5, 1.0, 5.0, 10, 50, 100, 500, 1000, 5000, 10000, 50000, 100000, 500000 and 1000000  $\text{cc}^{-1}$ ,

$T_e$  : 2500, 5000, 7500, 10000 and 12500 K and

$l$  : 0.001, 0.005, 0.01, 0.05, 0.1, 0.5, 1.0, 5.0, 10, 20, 40, 60, 80, 100, 500 and 1000 pc.

The line and continuum fluxes for HII regions of each combination of parameters is calculated and from the total observed line flux, the number of HII regions needed for each model is calculated. The thermal continuum from this collection of HII regions is estimated and is checked for consistency with the observed total continuum and the estimated thermal flux. The following constraints are imposed to select the good models :

1. The calculated thermal continuum flux from the collection of HII regions is less than the estimated thermal flux (from [NeII] or IR recombination lines).
2. A minimum number of HII regions is required to account for the line width inside each beam.

3. The number of HII regions has to be greater than unity.
4. The volume filling factor of these HII regions has to be less than unity and
5. The number of O stars per HII region is calculated from the estimated ionizing photon flux and this number has to be greater than unity.

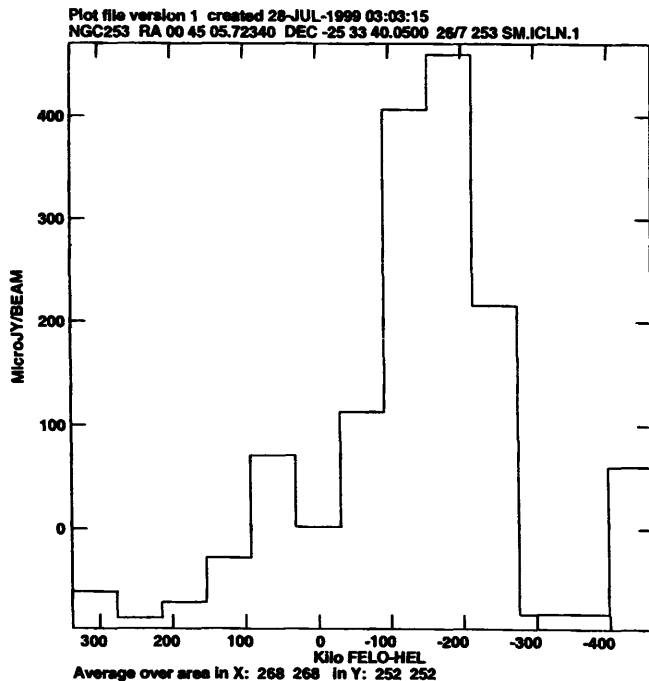
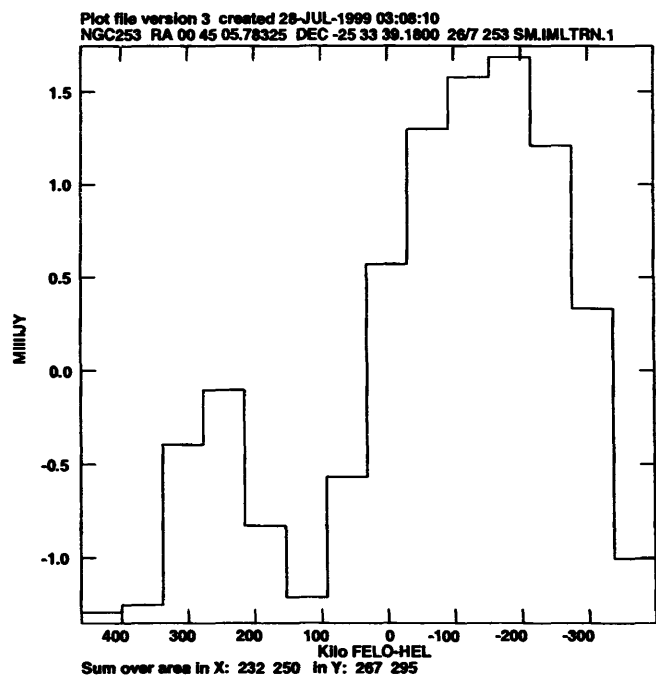
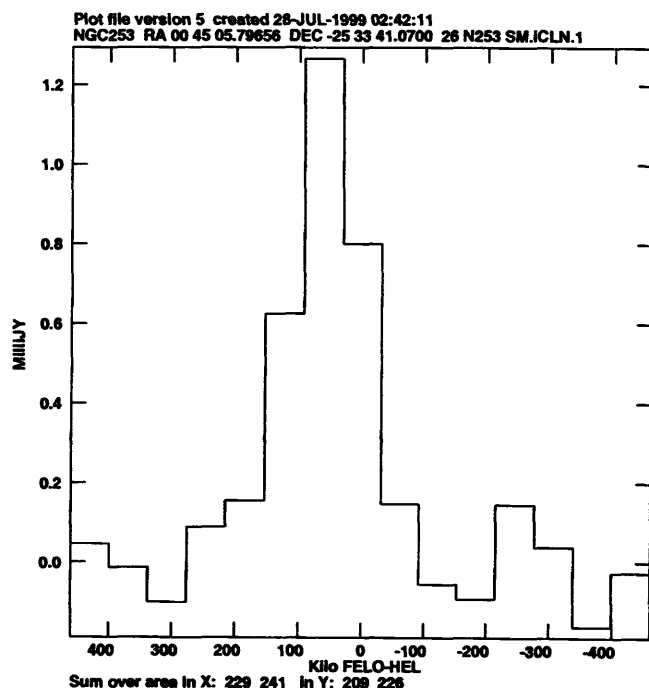
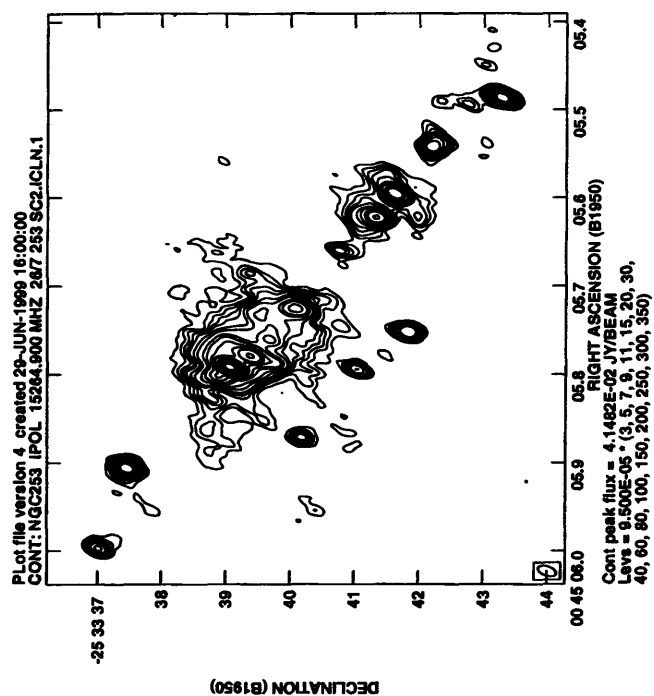
We then calculate the Lyman continuum photon flux, expected Br $\gamma$  flux, the total ionized gas mass, etc for the good models. We summarize the range of allowed parameters for these two galaxies below. All the models in this range are consistent with the observed line and continuum fluxes and multiwavelength observations are needed to distinguish between these. Due to their low metallicities, we present models corresponding to  $T_e \geq 10000$  K.

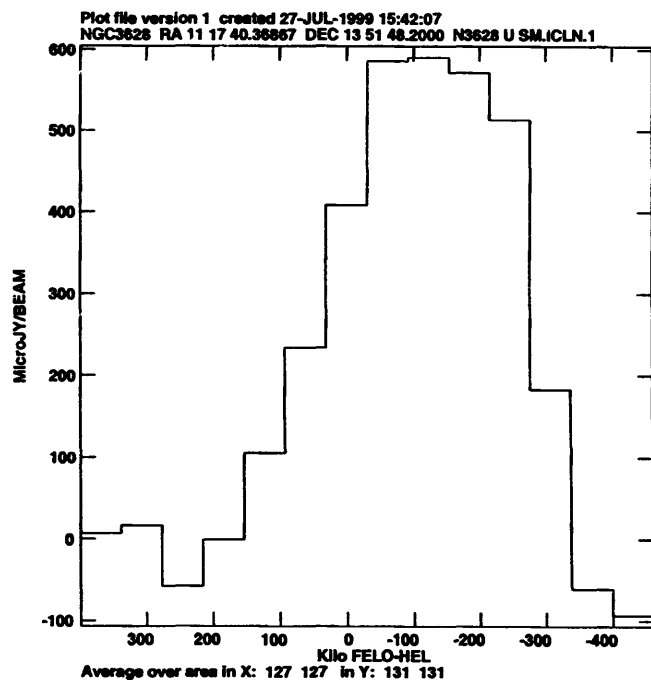
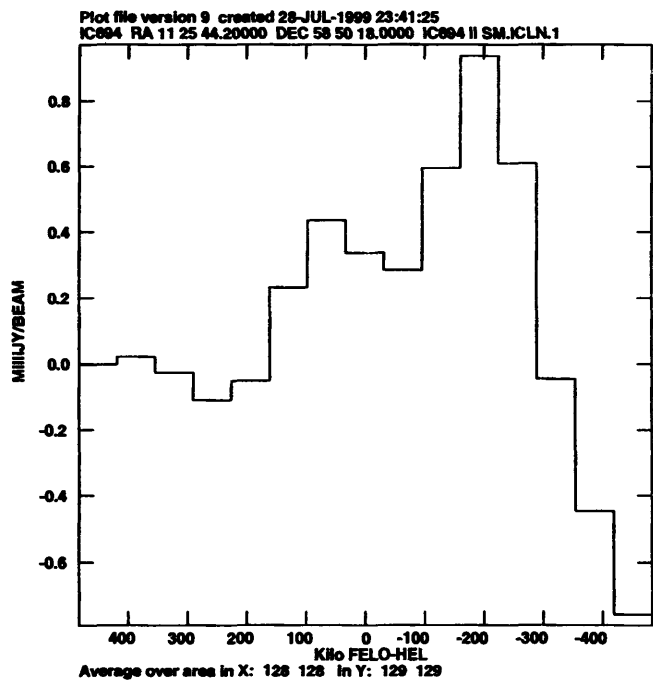
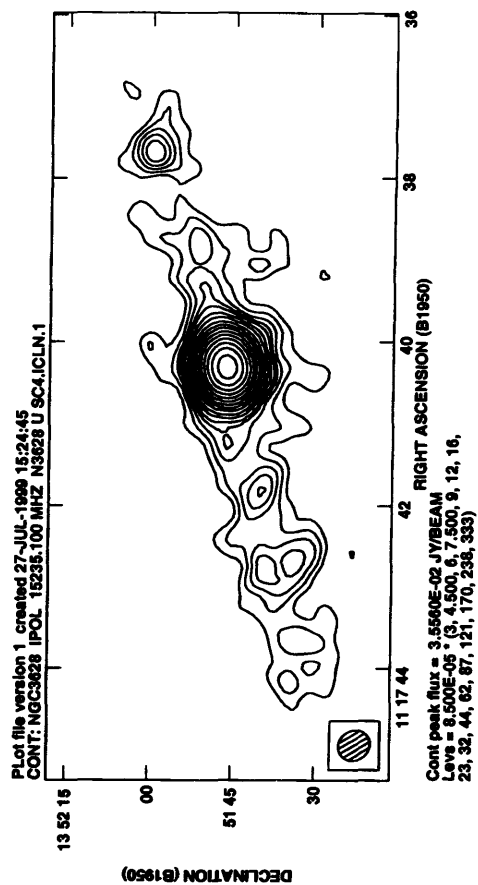
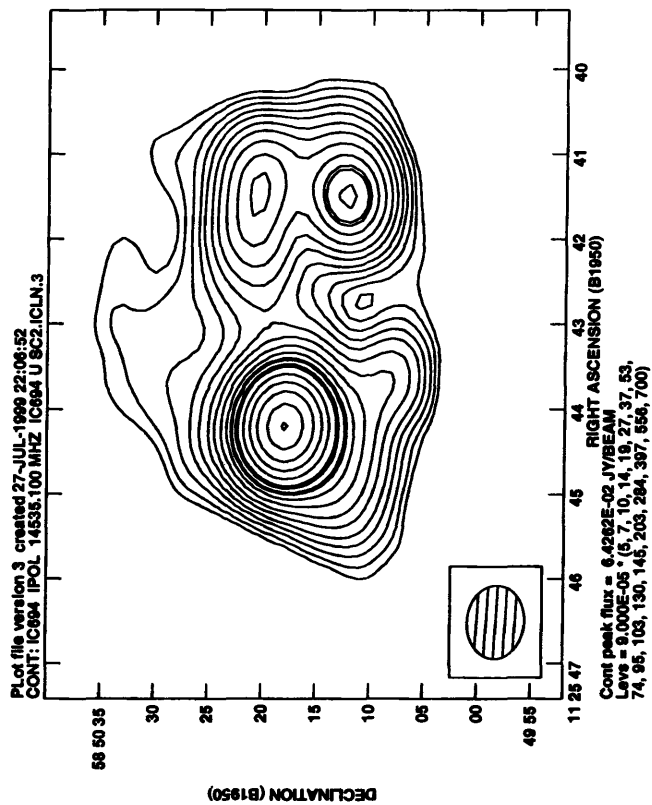
**Table 1: Parameters of galaxies**

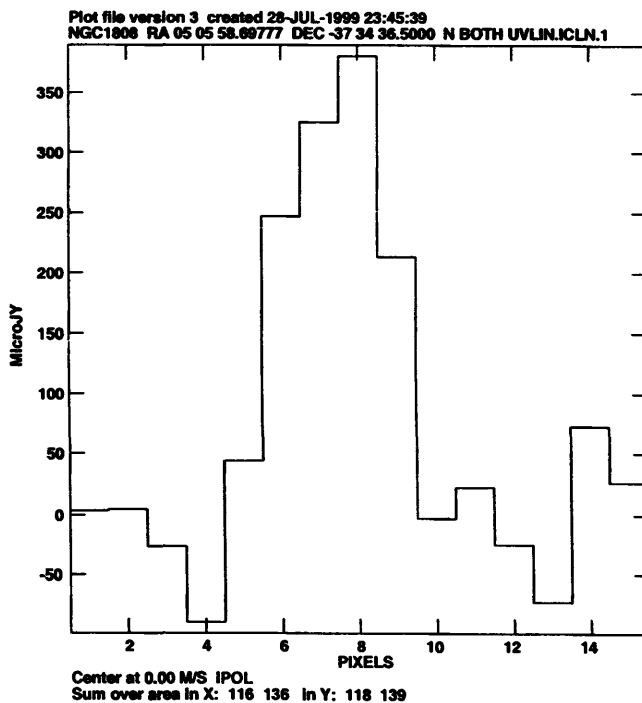
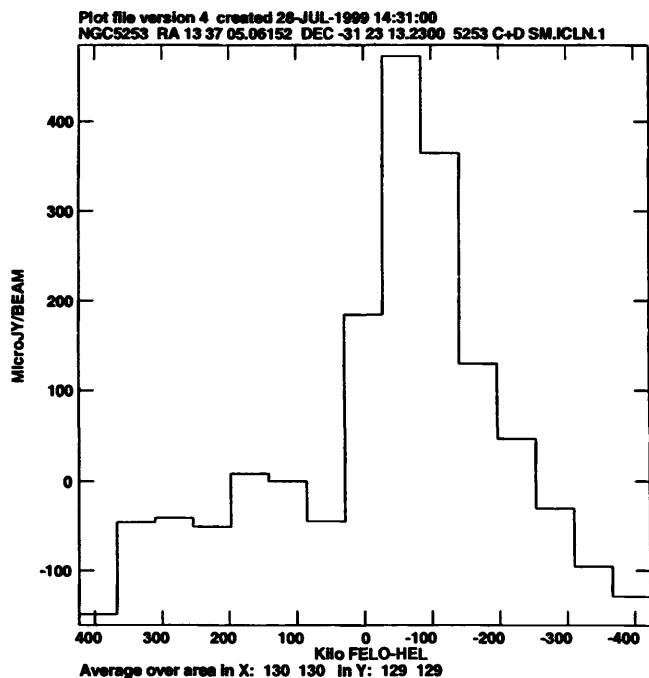
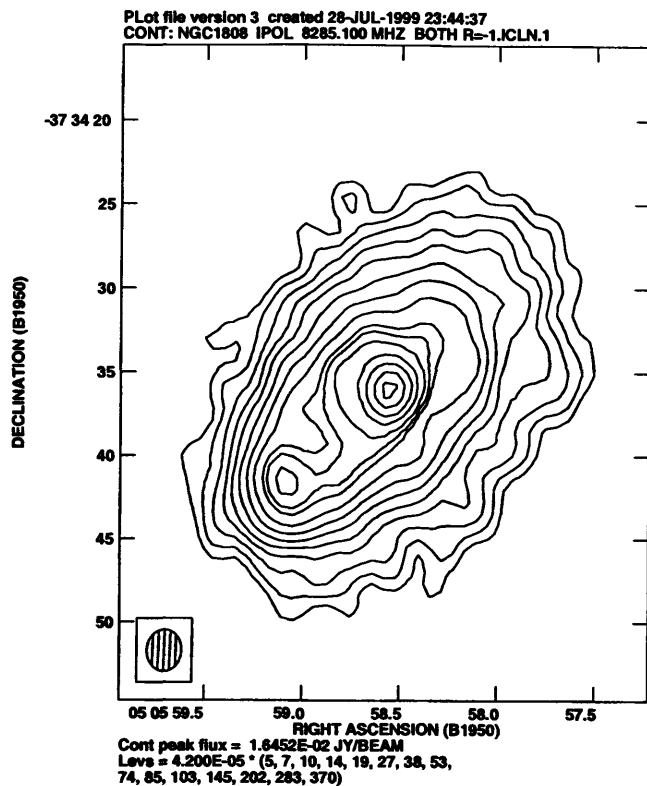
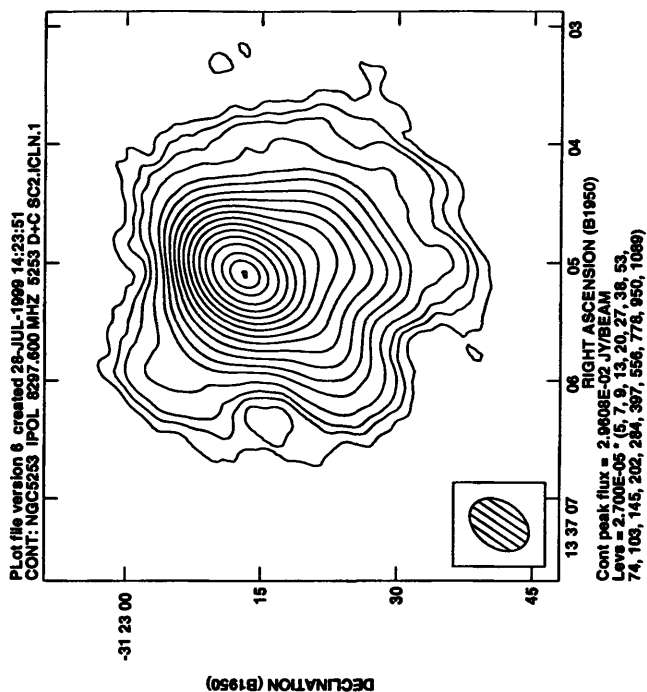
Parameter	NGC 5253	Henize 2-10
$n_e$	$10^4 - 10^5 \text{ cc}^{-1}$	$10^4 - 10^5 \text{ cc}^{-1}$
$l$	0.1 - 1.0 pc	0.1 - 1.0 pc
# of HII regions	20 - 1000	10 - 50
Vol. filling factor	$10^{-5} - 10^{-7}$	$\sim 10^{-5}$
$N_{Lyc}$	$10^{53.5-55.0}$	$10^{53.0-54.5}$
# of O stars	$\sim 3 \times 10^5$	$10^4 - 10^5$
O stars/HII reg.	30-30000	300-30000
$M_{HII}$	5000-100000 $M_\odot$	1000-10000 $M_\odot$

#### *Conclusions from NGC 5253 and Henize 2-10 models*

1. We have detected compact high density HII regions. These objects have been well studied in our own galaxy but nothing is known about these objects in other galaxies partly because of their small size and partly because these regions tend to be heavily obscured. Centimetre wavelength recombination lines seem to be the only way of directly detecting these objects, as has been shown for other starbursts as well. If this is true, then we are seeing the youngest stars in the burst region and hence accessing the most recent star formation which is unique. This is because it is known that in our galaxy, compact HII regions are less than a few times  $10^5$  years old.
2. Some of the models which have a large number of O stars in a 1 pc region correspond to Super Star Clusters which are believed to be the progenitors of the present day globular clusters. We cannot claim detection of SSCs but they turn out to be one of the possible solutions to our data. Further multifrequency RRL observations are needed to determine if SSCs are what we are seeing.
3. If we calculate the Lyman continuum photon flux, or equivalently, the expected Br $\gamma$  flux from these HII regions for each acceptable model, we find that the lowest  $N_{Lyc}$  we obtain, is a factor of 5 or so higher than the observed value. Thus we are led to either of two conclusions - RRLs and IR lines sample the same ionized gas but the extinction towards these objects is much much more than what is thought to be the case. If that is so, then we shall have to explain the ensuing anomalous Br $\alpha$  to Br $\gamma$  ratio. The other possibility is that RRLs and IR recombination lines come from totally different components in which case, we shall have to add the  $N_{Lyc}$  from RRLs and IR lines to get the total star formation rate which would increase by a factor of 5 to 10. Further observations should shed light on this question.







# Measuring Proper Motions in M84

C. Schwartz<sup>1,2,3</sup>

J.M. Wrobel, R.C. Walker

National Radio Astronomy Observatory, P.O. Box O, Socorro, NM 87801

## 1. Introduction

M84 is one of the larger galaxies in the nearby (17 Mpc) Virgo Cluster. At optical wavelengths it appears to be an elliptical with a dusty nucleus in the heart of the cluster. Radio wavelength observations tell another story: M84 is a low-luminosity, core-brightened, double-plumed galaxy extending over  $\sim 14$  kpc, cataloged as a Fanaroff-Riley morphological class I (FRI) galaxy. From radio-optical alignments we find the initial radio jet direction to be roughly perpendicular to kpc-scale dust distributions. HST images of NeII and V-band light from Verdoes et al. (1999) are available for comparison to the radio data, and indicate that the greatest radio elongation is closer to the minor axis of the galactic light.

Two epochs of VLA A-configuration data are available for study, both at 5 GHz (C-band, 6 cm), from 1980 and 1988. Additionally, C-configuration data are available from 1981. The A-configuration data readily probes the structure of the jets, resolving out the more diffuse lobes, which the C-configuration data details. Our goal is to create very high-dynamic-range images of two epochs of VLA data to determine the range of speeds seen within different components of the jet. By combining the data sets from A- and C-configuration for each epoch, we can obtain well-defined images of both the jets and the lobes. Moreover, addition of the C-configuration data raises the signal-to-noise ratio of the region. Imaging the A-configuration data alone results in the presence of a negative "bowl" surrounding the core, due to the lack of short spacings in that. By adding in the C-configuration data, we are able to obtain the short spacings needed to eliminate this negative bowl. B-configuration was not chosen because this configuration also would have issues with resolution of the lobe structure, and the shortest spacings available would not as small as was desired. Additionally, this configuration would possibly affect the feature positions too much, whereas C-configuration would provide less resolution and look at the

---

<sup>1</sup>NRAO Summer Student, 1999

<sup>2</sup>Present address: Broida Hall, Dept. of Physics, University of California, Santa Barbara, CA 93106

<sup>3</sup>E-mail: cschwartz@aoc.nrao.edu



larger picture. B-configuration is available for the first epoch of data, however, but not for the second.

Once high-dynamic range images were created, we were able to use various tools to compare the two epochs. Variations in the jet components were quantified and have produced preliminary results, which strongly warrant a further epoch of observations, both in A- and C-configurations.

## 2. Observations

M84 (Right Ascension = 12 22 31.450, Declination = 13 09 49.60, B1950) was observed with the NRAO Very Large Array (VLA), twice in A-configuration and once in C-configuration. The first epoch of data was taken 9 November 1980 in one 50 MHz band at 4.8851 GHz in all four Stokes parameters. The observations spanned eleven hours, with regular interruptions for scans on calibrators. The second epoch was taken 23 November 1988 in two contiguous 50 MHz bands centered on 4.8351 and 4.8851 GHz. Using the VLA in C-configuration on 17 November 1981, M84 was observed in one 50 MHz band at 4.8551 GHz.

Because the 1988 observation was made in two IFs it was necessary to split the data set into two, one for each IF, in order to combine this with the single-IF C-configuration data set. Based on the assumption that in further processing *AIPS* will know how to deal with the different frequencies, we then recombined the two data sets using the task *DBCON*. Thus, we ultimately combined three full data sets, one in C-configuration and two in A-configuration. All references to the 1988 A-configuration data set will refer to the 1-IF data set (post-*DBCON*) unless otherwise noted.

## 3. Self-Calibration and Imaging

The data sets were combined using the *AIPS* task *DBCON*. Both the 1980 and 1988 A-configuration data sets (hereafter 1980A and 1988A) were combined with the 1981 C-configuration data set (hereafter 1981C). However, since the flux density of the core varied over the 8-year period in question, we removed 10.2 mJy from the 1981C data set before adding it to the 1988A data. This is important because if no flux density was removed, the joint self calibration of the two epochs would fail. The flux adjustment was made to the lower resolution C-configuration data in an effort to minimize any possible impact on the position of the core.

After the images were combined, they were self-calibrated using an iterative process consisting of CALIB and IMAGR. Using scripts to automate the process, we self-calibrated both combined data sets, 1980A/1981C and 1988A/1981C. The first self-calibration involved phase calibrations and was based on a point-source model for the core. The second self-calibration was again a phase calibration, based on the image produced from the first self-calibration. The third was a amplitude and phase calibration based on the image produced in the second self-calibration.

The third and final self-calibrated data set was imaged using the *AIPS* task IMAGR and using the CLEAN algorithm to clean deeply. The resultant dynamic ranges (peak/rms) were 4200:1 for the 1980A/1981C data set, and 4300:1 for the 1988A/1981C data set. The final images are shown in figure 1. Additionally, we used the *AIPS* task COMB to subtract the second image from the first. This is shown as the third image in figure 1. The darker spots are those in which the first image (1980A/1981C) was brighter than the second, while light spots show where the second image (1988A/1981C) was brighter than the first. Therefore, a feature shifts from darker to lighter in the difference image. The difference image suggests an overall shift to the east. It is not yet clear if this is real or evidence of problems with the image fidelity. This will be an interesting topic for further study.

Initially, this project had a goal of finding the proper motion of the one bright knot previously known to be about 400 pc from the core of M84. However, upon deep cleaning of the images from each epoch, we discovered that 2 or possibly 4 knots were obvious. From south to north, we named these features A, B, C and D. Knot B is the feature we had originally planned on finding the motion of, as the primary example in this region of the jet. However, it has become possible to measure the motion of not one but four knots.

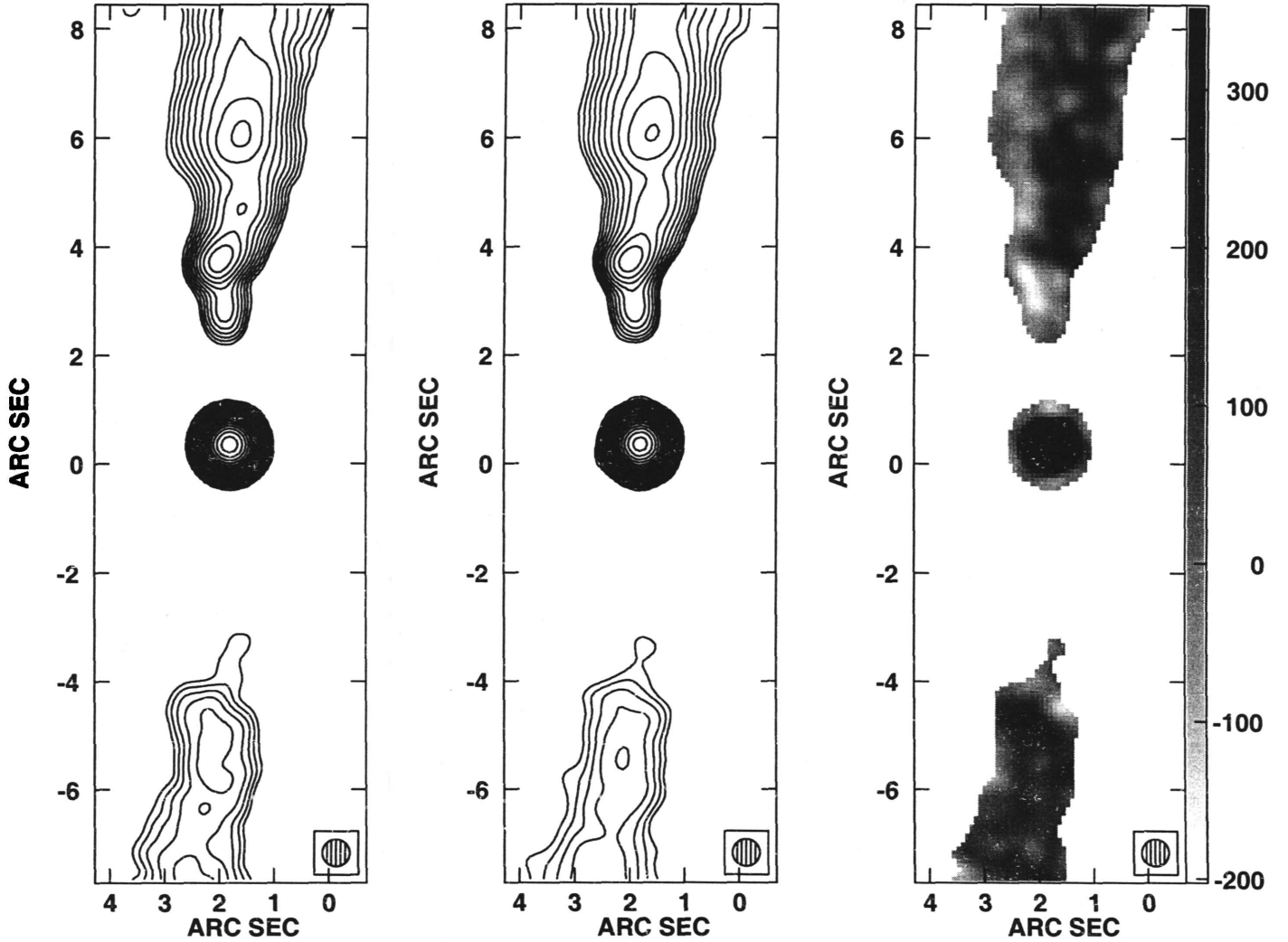


Fig. 1.— Contoured sub-images of M84's central region from 1980A/1981C and 1988A/1981C, with contours starting at 200  $\mu\text{Jy}$  and increasing by factors of  $2^{1/2}$ . The rightmost image is a difference image of 1988A/1981C subtracted from 1980A/1981C, where the darker spots are brighter in 1980 and the lighter spots are brighter in 1988. The scale to the right is in  $\mu\text{Jy}$ .

#### 4. Proper Motion Measurements

Because the data sets were both self-calibrated, we were not able to get absolute positions for the features within the jet. However, by using a FORTRAN program "*xycor*" created by R.C. Walker, we are able to obtain motions relative to the core for each epoch. The program uses output from the *AIPS* task PRTIM as its input, and measures the motion of the feature using both a least squares fit and a cross-correlation analysis. Table 1 shows the least squares fit results from *xycor*.

Feature	Approx. Core Distance	Distance: X	Error	Distance: Y	Error
A	234	-15.45	3.26	37.23	8.36
B	297	-10.98	1.83	-14.88	1.96
C	375	-11.51	4.98	4.92	8.93
D	476	-1.53	2.57	25.04	3.54

Table 1. Results from proper motion measurement program *xycor*. Approximate distance from core is given in parsecs. Distances and errors in both X and Y are given in milliarcseconds. For comparison, the angular resolution is 500 milliarcseconds, or 39 pc.

While the motions reported for features B and D are credible, features A and C are less reliable. Knot A does not appear to be a self-contained knot, it is more of a "peninsula" off the inner edge of the jet, so it is quite likely that *xycor* is not able to handle this feature when measuring its motion. C is also a very weak feature, appearing as a globule of higher brightness within the jet, but not quite a full knot. For these reasons, *xycor* could have serious problems in dealing with features A and C. Hence, the measurements given for the proper motions of features A and C are unreliable.

Conversely, we are fairly confident in the motions obtained for the motions of knots B and D. Because these knots are both clearly defined within the image with steep brightness gradients surrounding them, it is simple for *xycor* to find the proper motion. The overall motion over the eight year period for knot B is  $\sim 18.5$  mas, corresponding to a speed of  $\sim 0.58c \pm 0.06c$ . For knot D, the feature shifted  $\sim 25$  mas over eight years, corresponding to a speed of  $\sim 0.80c \pm 0.14c$ . These motions, while highly relativistic, are most surprising because we find knot B is moving *towards* the core. This is a unique situation, and it will be interesting to investigate this result.

## 5. Preliminary Results and Future Work

- The method we used for eliminating the negative bowl around the galactic core works quite well. There is no further evidence for negative structures above the noise limit, and both images show strong jet structure with the lobes fading into the noise.
- The motion of the features within the intermediate jet have been imaged for the first time and a new nomenclature has been adopted for the four features detected (A, B, C and D).
- We expect the proper motions of the features to be sub-luminal, as super-luminal motion occurs when the a relativistic jet is projected close to the line of sight. M84 is seen almost completely from the side, and so all motions are sub-luminal as expected. However, the speeds obtained for each of the features are still relativistic.
- The errors given by the program *xycor* will be investigated, since they may be unrealistically small, and do not account for image fidelity problems.
- We will propose to observe M84 once again in both A- and C-configurations. While we have missed the eight-year epoch (which would have been in 1996), we will still greatly improve the imaging and proper motions if another epoch is added.
- R.A. Laing (U. of Oxford) and A.H. Bridle (NRAO) will be looking into the polarization and Faraday Rotation measures of M84 using the data previously obtained in A-, B-, and C-configurations.

# Bi-directional Motions in the Radio Galaxy 1946+708

Hanna G. Smith  
Smith College

## 1. Introduction

Compact symmetric objects (CSOs) are a family of extra galactic radiosources comprising roughly 5% of flux-limited samples selected at high frequencies (Readhead et al. 1996; Taylor, Readhead, & Pearson 1996a). Their defining characteristic is the presence of high luminosity radio components on both sides of a central engine on sub-kiloparsec scales with little or no extended emission present. CSOs typically exhibit terminal hotspots which show no evidence of superluminal motion. The primary jets are much brighter than the counterjets; however both are essentially free of relativistic beaming effects (Wilkinson et al. 1994). They exhibit weak radio variability, have low radio polarization and low core luminosities. Parent objects are elliptical galaxies (Readhead, et al. 1994).

Taylor & Vermeulen (1997) asserted that CSOs provide a unique opportunity to determine the Hubble constant directly. Their analysis stemmed from the fact that a direct measure of the distance to an object can be obtained by observing angular motion in it, if the intrinsic linear velocity can be ascertained independently. Based on five epochs of observations of the CSO 1946+708 at 5 GHz Taylor & Vermeulen placed a lower limit on  $H_0$ . I spent the larger part of the summer reducing data from four subsequent epochs performed at 8.4 and 15 GHz. The primary goal of my project was to establish better constraints on the Hubble constant based on these data and to write a scientific paper discussing the results.

## 2. Observations

The four 8.4 and 15 GHz epochs were performed on 1995 March 22, 1996 July 07, 1998 February 06 and 1999 July 11. (The date of the last epoch caused some consternation, since, due to dynamic scheduling of VLBA observations, it was unclear whether epoch four would be observed during my time in Socorro.) Epochs one and three were observed using the ten element VLBA; due to problems at the St. Croix and North Liberty stations, epochs two and four were performed using nine antennas each. Both right and left circular polarizations were recorded using 2 bit sampling across a bandwidth of 8MHz. The VLBA correlator produced 16 frequency channels across each IF during every 2s integration.

Amplitude calibration for each antenna was derived from measurements of antenna gain and system temperatures during each run. Delays between the stations' clocks were determined using the AIPS task FRING (Schwab&Cotton 1983). Global fring fitting was performed using the same task. Calibration was applied when splitting the multi-source data set immediately prior to preliminary editing, imaging, deconvolution and self-calibration in DIFMAP (Shepherd, Pearson,&Taylor). Multiple iterations of phase self-calibration and imaging were applied to each source before any attempt at amplitude self-calibration was made. The preliminary models developed in DIFMAP were subsequently applied in AIPS to make phase corrections, to determine the leakage terms between the RCP and LCP feeds and to correct for residual phase differences between polarizations. Final imaging and self-calibration were performed in DIFMAP.

<b>Epochs</b>	<b>Frequency</b>	<b>Bandwidth</b>	<b>Polarization</b>
–	(GHz)	(MHz)	–
95mar22	15.3612	15	LL
–	8.42143	16	RR
96jul07	15.3495	32	LL
–	8.40549	32	RR
98feb06	15.3535	32	Dual
–	8.40946	32	Dual
99jul11	15.3535	32	Dual
–	8.40946	32	Dual
<b>Int. Time</b>	<b># Antennas</b>	<b>Scans</b>	<b>Sourcetime</b>
(s)	–	–	(s)
30	10	11	5440
20	10	19	15280
20	9	7	4700
20	9	14	19580
20	10	14	8680
20	10	15	16800
20	8	9	5580
20	9	17	9880

**Table 1.** General Information for Epochs 1-4

Model fitting of Gaussian components to the self-calibrated visibility data was also

performed in DIFMAP. The shapes of the components were fixed after fitting to the third epoch; in the first, second and fourth epochs each component was allowed only to move and to vary in flux density in order to fit the independently self-calibrated visibility data.

### 3. Preliminary Results and Discussion

#### 3.1. Velocities of the Inner Jet Components

Figure 1 shows the positions of the Gaussian model components fitted to the 8.4 GHz data in addition to the locations of components fitted to five previous epochs at 4.9 GHz by Taylor & Vermeulen (1997). Figure 1 also shows the displacements of the 8.4 GHz components from the core as a function of time for the inner jet components N5 and S5. The slopes of these plots represent the velocities of the jet components. Using this method we have calculated velocities of 0.145 mas/yr, 0.062 mas/yr, 0.061 mas/yr and 0.044 mas/yr for the each of the jet components N5, S5, N2, and S2 respectively. However, we have not yet quantified errors for these values.

#### 3.2. Constraints on the Hubble Constant

We are currently in the process of placing constraints on the Hubble constant using the procedure outlined by Taylor & Vermeulen (1997). Using the velocity, arm-length and flux ratios obtained from the 8.4 GHz data we have calculated a range of possible values for  $\beta \cos \theta$ . All arm-length and flux ratio calculations performed to date have yielded values between 0.10 and 0.16, for both the N5-S5 and N2-S2 pairs. The value of  $\beta \cos \theta$  obtained from the N2-S2 velocity ratio also fell in this range. This is consistent with values obtained previously from the 4.9 GHz data. However, the N5-S5 velocity ratio yielded an abnormally high value of 0.40. This could be the result of acceleration of the components N5 and S5 along the line of sight.

We should expect to see a comparably high  $\beta \cos \theta$  derived from the N5-S5 flux ratio if this is the case, which, thus far, we have not. Further calculations of  $\beta \cos \theta$  for both the N5-S5 and N2-S2 pairs are necessary to determine the best values to use in subsequent analysis.



### 3.3. Polarimetry

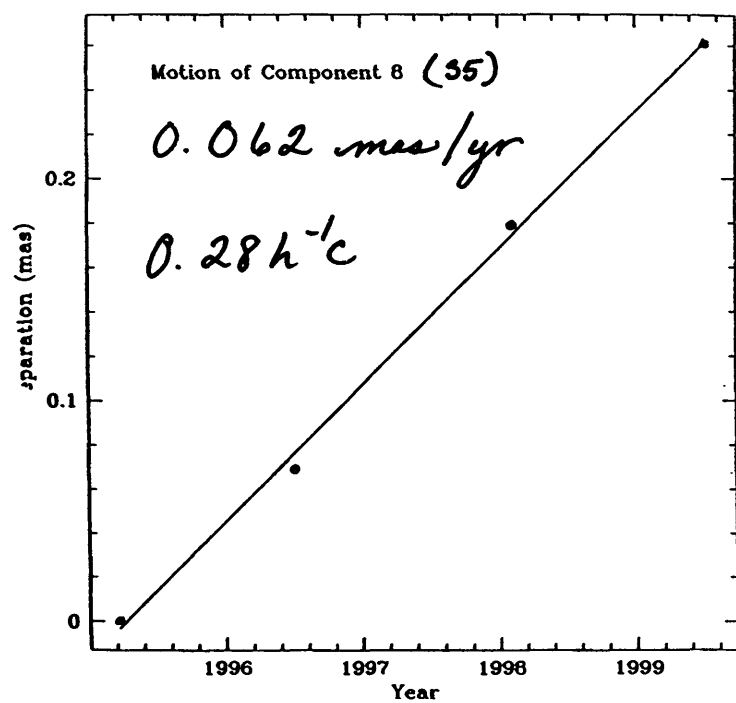
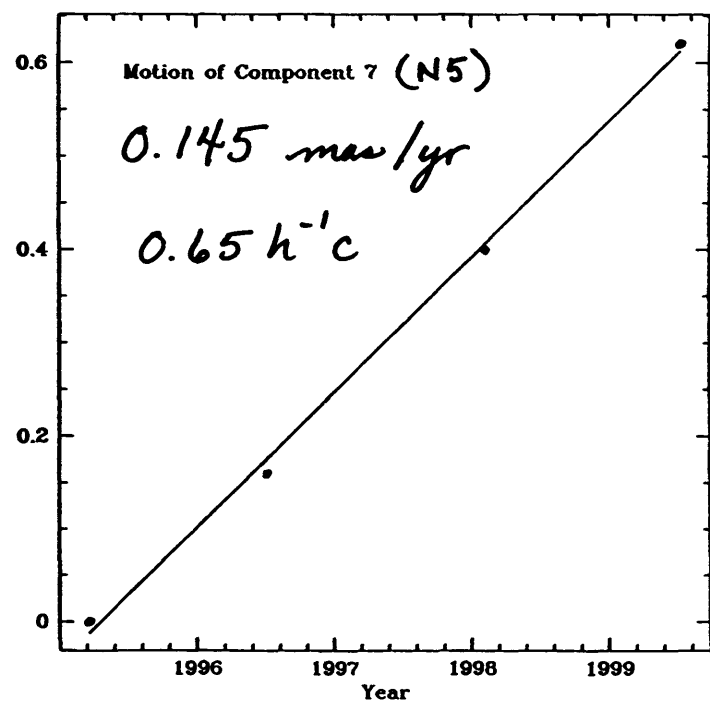
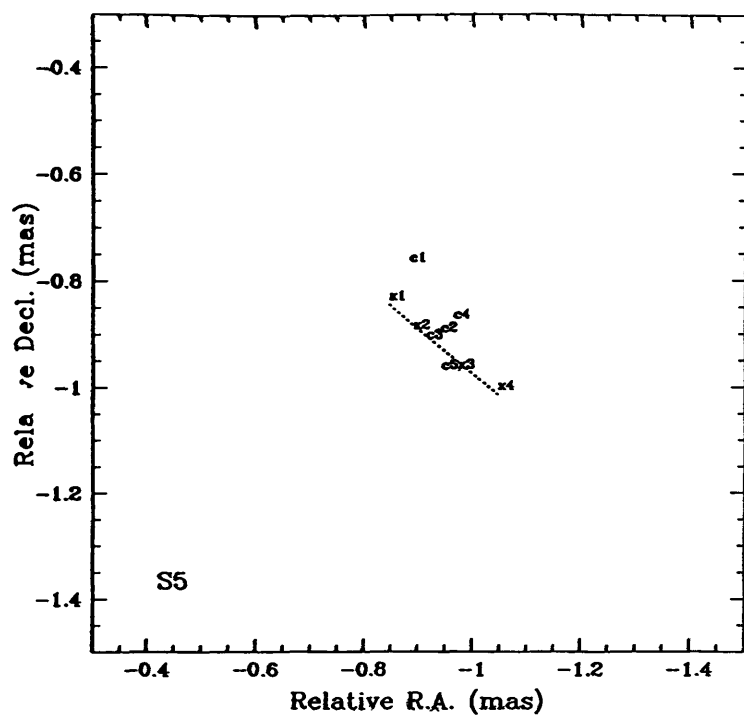
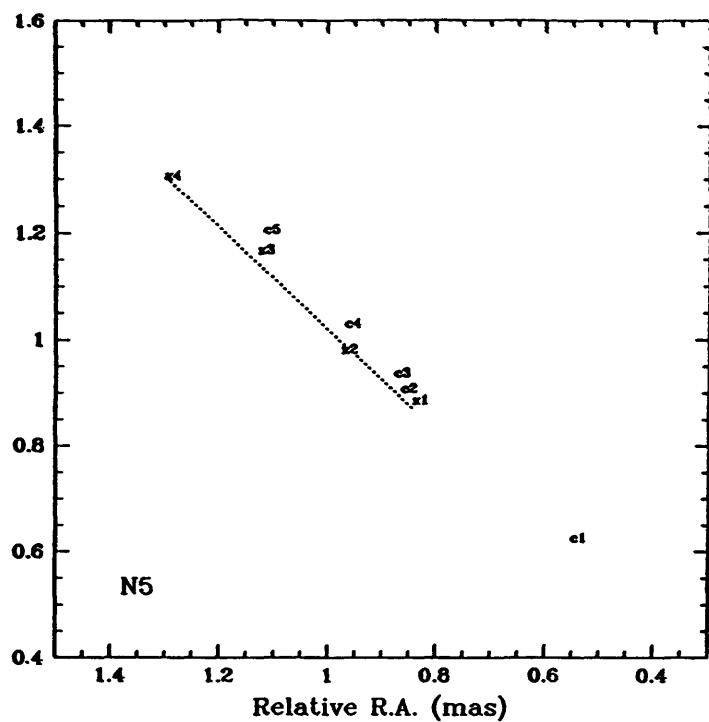
CSOs typically exhibit low radio polarization (Readhead et al. 1996). The dearth of polarized flux associated with CSOs is probably the result of Faraday rotation induced by an obscuring torus of gas, which the observer views edge on. Consistent with our expectations, we detected a negligible amount of polarized flux at both 8.4 and 15 GHz – 0.1% for bright jet components and 1% for the weakest components.

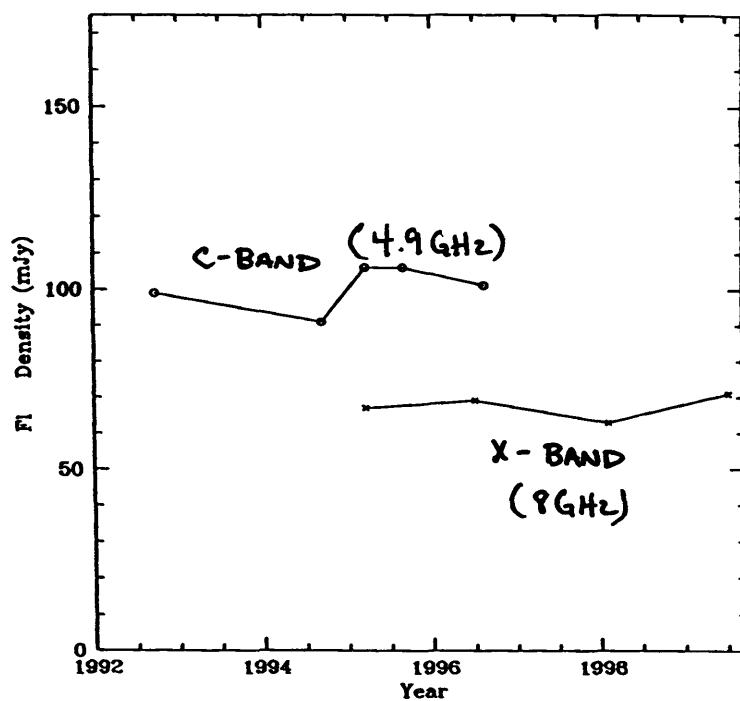
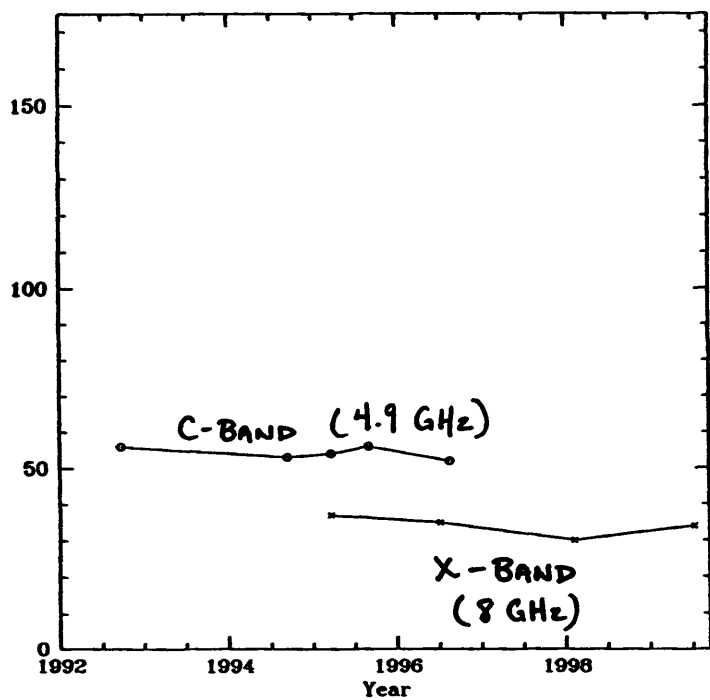
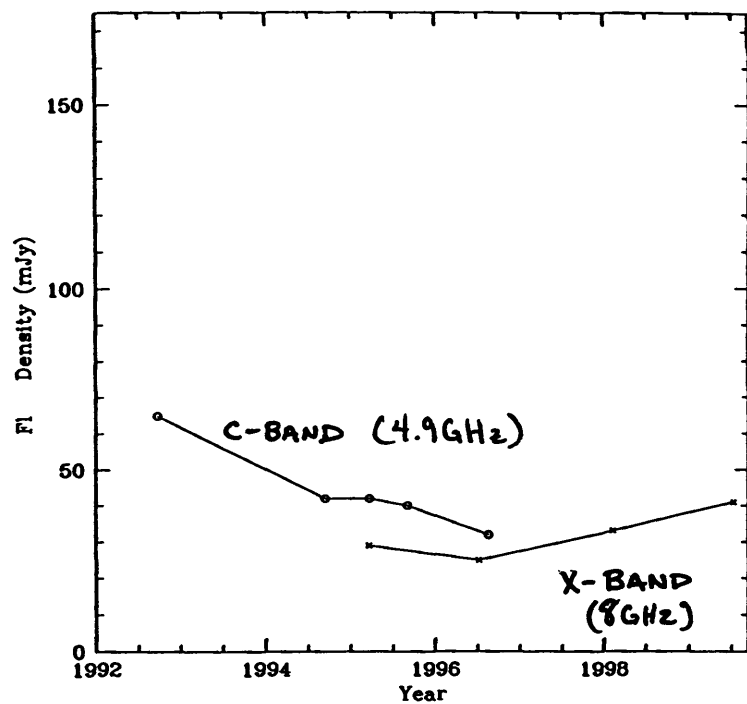
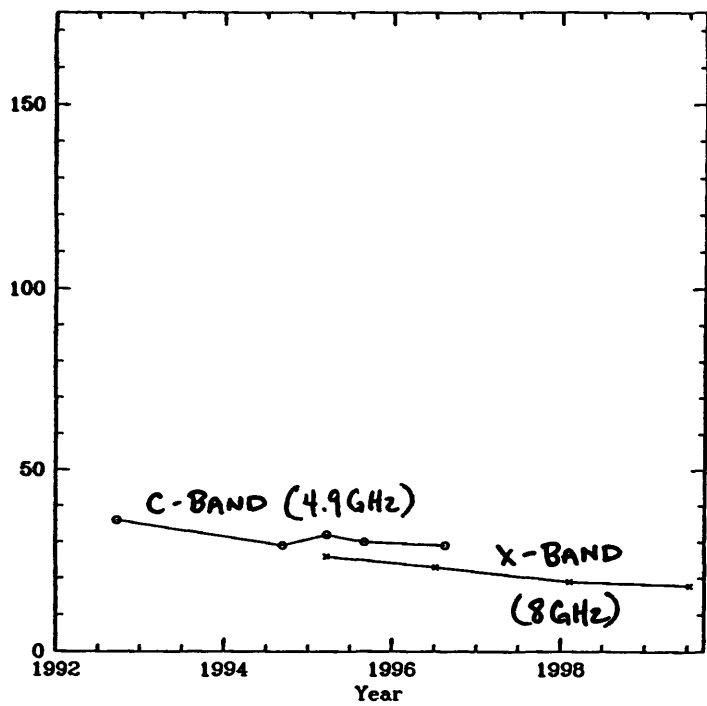
### 3.4. Light Curves

Figures 2-3 show light curves for the jet components N5, S5, N2, S2 and C respectively. N5 and S5 show dimming and brightening which could be indicative of a component bending first away from and then toward the line of sight, in the case of N5, or a component bending continuously away from the line of sight, in the case of S5. The fluxes associated with N2 and S2 stay fairly consistent in time, perhaps indicating that these components are not along the line of sight. A helical model of the jets' motions would need to be developed to determine if these are reasonable interpretations of the flux variations. The core component, C, brightens steadily over the course of the five 4.9 GHz epochs and the four 8.4 GHz. This is probably due to an intrinsic brightening of the source and is not indicative of three dimensional motions.

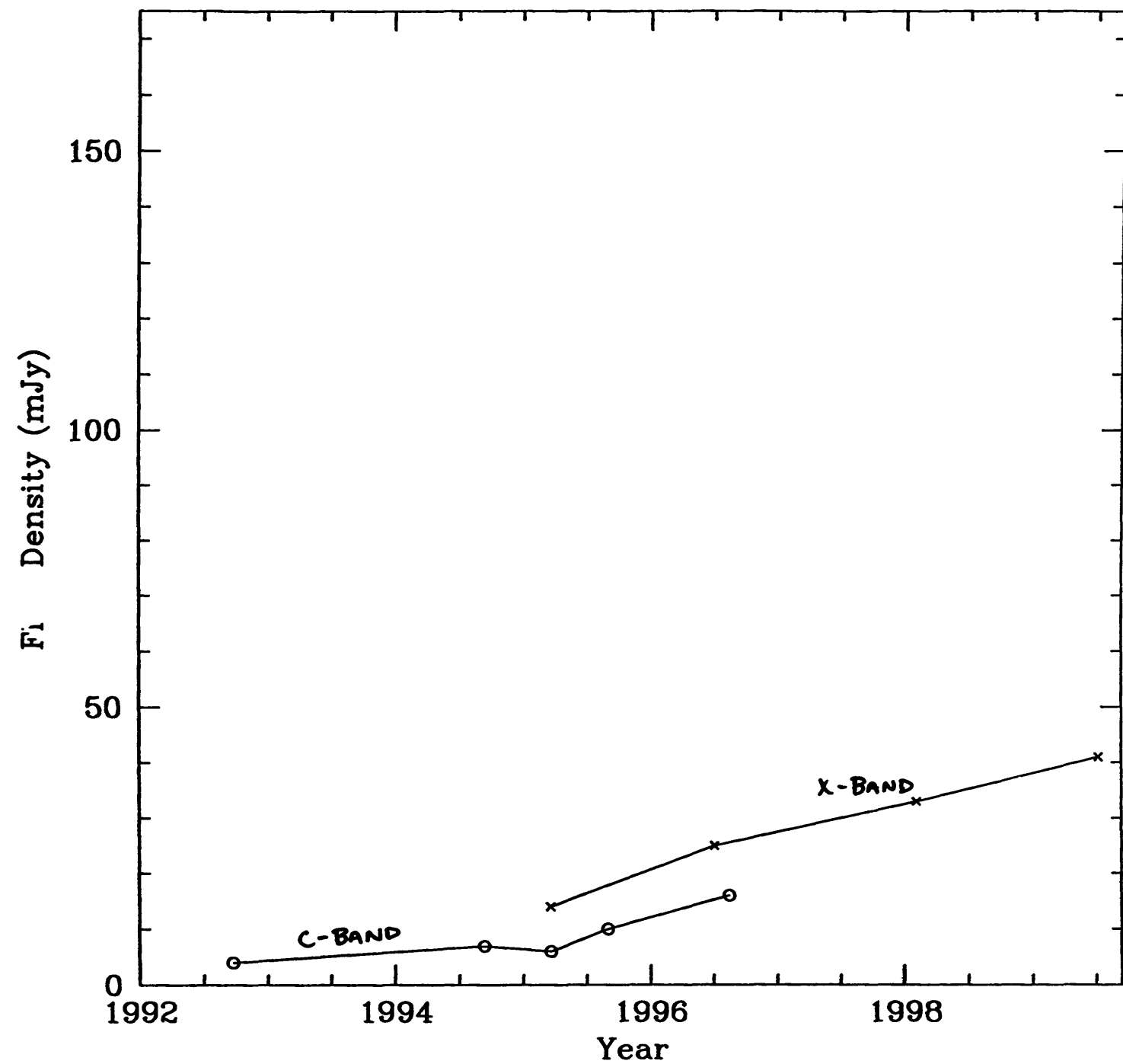
## 4. Conclusions

Since our analysis of all nine epochs of data is still in progress, we cannot yet set constraints on  $H_0$ . Our polarimetry results and jet velocities are consistent with expectations. We have also seen indications of more complex jet behavior. There will be more interesting results to report in the coming weeks.

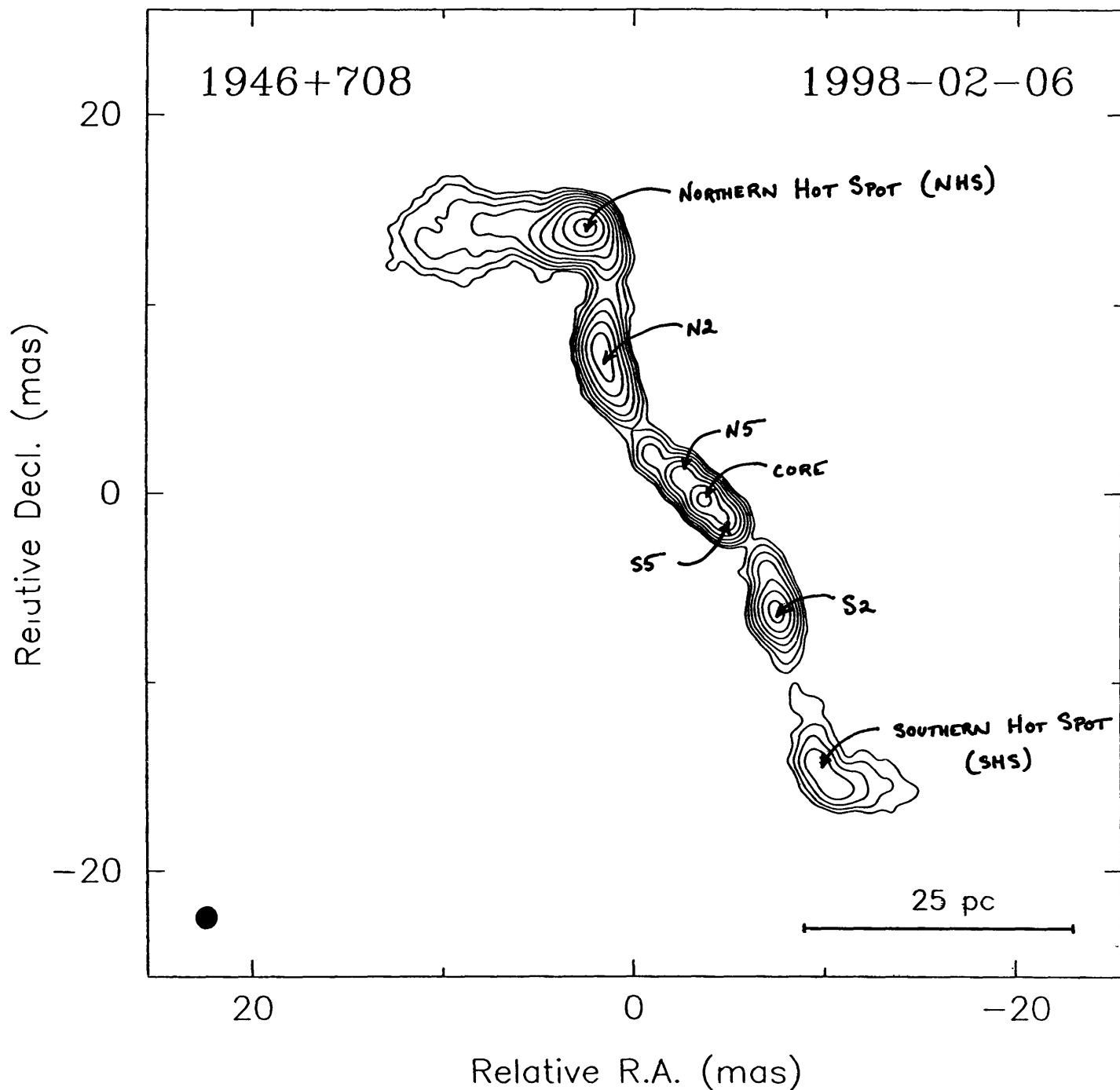




CORE



Frequency: 8.409 GHz, sigma=1.026888



Maximum: 6.8709E-02 JY/BEAM

Contours (%): 0.29 0.58 1.16 2.33 4.66 9.31 18.63 37.26 74.52

Beam: FWHM 1.15 × 1.08 mas, p.a. -10.6°

File: 1946+708 fits (14-Jul-1999 10:32)

# Radio Observations of Gamma-Ray Bursts: Summer, 1999

C. H. Young<sup>1,2</sup>

NRAO Summer Intern/REU Program 1999

D.A. Frail

National Radio Astronomy Observatory, P.O. Box 0, Socorro, NM 87801

## ABSTRACT

Gamma-ray bursts (GRBs) have eluded scientists and astronomers ever since their discovery by the Vela satellites during the Cold War. However, current advances in theory and technique have given us the knowledge to probe these events with great insight. Specifically, radio astronomy has provided a convenient window through which to view these magnificent bursts of energy.

We will present the results of observations conducted at the Very Large Array (VLA). Three GRBs (GRB 990520, GRB 990527, and GRB 990704) occurred in Summer 1999, which were monitored by the VLA. These bursts, observational techniques, and results obtained will be discussed in the first two sections of this paper. Also, the results of long-term monitoring, results, and conclusions for two additional bursts (GRB 980329 and GRB 980519) will be presented.

The study of GRBs is an intense science which is often teetering on the edge of technical capability. For this and other reasons which are unknown to astronomers, we often do not successfully observe the afterglows, radio or optical, which are associated with GRBs. As is the case with several of the GRBs discussed here. However, the methods of observation are worthwhile, and the lack of detection could hold significance within itself.

## 1. Introduction

Radio astronomy provides a well-adapted method for observing the afterglows associated with GRBs. The burst event only lasts for seconds, and the x-ray counterpart is

---

<sup>1</sup>Department of Physics and Astronomy, Mississippi State University, Starkville, MS 39760

<sup>2</sup>E-mail: chy1@ra.msstate.edu

not much longer. The optical afterglow can last for hours or days, but very few telescopes can respond in real-time to observe the temporal evolution of GRBs. However, the radio afterglow is extended over many months, so one can feasibly monitor the gradual rise and decline in flux of these afterglow events. The study of these radio counterparts is revealing new information about these elusive events.

## **2. Current Gamma Ray Bursts: Summer 1999**

### **2.1. GRB 990520**

On 20.1 May 1999, the Wide-Field Cameras (WFC) aboard the Beppo Sax satellite detected a fast x-ray transient which was initially named 1SAX J0835.9+5118 by the Beppo Sax team (Piro 1999). This transient event lasted for only ten seconds, had no associated detection on the Gamma-Ray Burst Monitor (GRBM), and was localized within an error circle of 3' (Piro 1999). No previously known x-ray sources were known within this error box, so the possibility of it being a GRB was significant.

Only  $\sim 16$  hours later (May 20.69), observations were conducted at the VLA at 1.4 GHz (Frail et al. 1999a). One radio source was found within the error circle provided by the Beppo Sax team. This radio source had not been previously detected by the NRAO VLA Sky Survey (NVSS) which was conducted in D-configuration, the same configuration of the radio observations of GRB 990520.

On May 20.93 follow-up observations were conducted at the VLA. We observed at 1.4 GHz, 4.8 GHz, and 8.5 GHz and found the previously mentioned radio source to be unchanging in flux (Frail et al. 1999b). Further investigations showed the source, although weak, to have been detected by the VLA FIRST Survey. With no other candidates for radio counterparts to GRB 990520, our observations concluded here. However, further reports confirmed that this fast x-ray transient was most likely a GRB (Kippen et al. 1999). Nonetheless, afterglow observations produced no significant results.

### **2.2. GRB 990527 and GRB 990704**

The observations of these two GRBs will not be discussed in detail here because the results were really of no great interest except for the lack of results. Statistically, only about one-third of all GRBs studied have a detectable radio counterpart, so the lack of a radio counterpart in the three current events listed here is no surprise.

### 3. Long-Term Monitoring of Gamma-Ray Bursts

#### 3.1. GRB 980329

On 29.16 March 1998, GRB 980329 was detected by the Beppo Sax GRBM and WFC (Frontera et al. 1998). Optical observations yielded no afterglow until further work by Taylor et al. at the Very Large Array showed a variable radio source within the error circle. This allowed a more detailed analysis of optical data from previous dates and the eventual report of an optical afterglow. Taylor et al. postulated that this initial obscuration of the optical counterpart was due to high dust content in the region where the burst originated while others have claimed that the burst occurred at a redshift of  $\sim 5$  (Fruchter et al. 1999).

We have conducted follow-up radio observations made with the VLA at 8.46 GHz, 4.86 GHz, and 1.43 GHz from which Taylor et al. published the results after a month of monitoring the afterglow. A long-term monitoring campaign, from which a more detailed analysis will be soon published, was continued for up to  $\sim 500$  days after the burst. Results from this campaign are shown in Table 1.

Radio afterglows of GRBs have a very elongated response time as compared to x-ray and optical counterparts. In figure 1, we have plotted the x-ray (in 't Zand et al. 1998), optical (Reichart et al. 1999), and our radio fluxes as a function of time. The well-tested models for afterglows (e.g. Sari et al. 1998) and observations (e.g. Frail et al. 1999c) of GRBs all conclude that the characteristics of the afterglow evolution are the same for all wavelengths. This characteristic allows for the long-term monitoring of GRBs which is an unparalleled tool in the study of GRBs.

#### 3.2. GRB 980519

The unfurling of the temporal evolution of GRB 980519 sparks excitement. Shortly after the burst, two models emerged from theorists who had based their predictions on preliminary data. Sari et al. (1999) proposed the jet model—a collimated outflow from some central engine. Their prediction was not completely obscene. The  $t^{-2}$  decay observed in the x-ray and optical fluxes (see figure 2) was almost exclusively indicative of the proposed jet model. However, the three radio data points obtained did not fit this model (see Frail et al. 1999c). Nonetheless, the steep decay at other wavelengths was convincing enough.

Chevalier and Li (1999) also produced a possible scenario from which the observed afterglows could have emerged. The circumstellar wind model called for a shell, expanding into a medium which has been shaped by a circumstellar wind. This model accounted for



the steep decay in x-ray and optical, but it also provided for the gradually, sloping light curve depicted in the radio observations.

Frail et al (1999c) continued radio observations of this GRB for months after the event. Final analysis of the data revealed interesting aspects of this GRB: (1) the circumstellar wind model accurately predicted the behavior of the radio afterglow and (2) interstellar scintillation (ISS) caused the seemingly sporadic spread of data points even at late times. The latter of these two will not be discussed here, and, for the first, it should be noted how radio observations provide a very convenient window through which to observe GRBs.

#### 4. Conclusions

We have presented here a broad overview of the GRBs from the summer of 1999 as well as a brief summary of the campaigns for long-term monitoring of GRBs 980329 and 980519. The material presented herein is, by no means, complete, so other resources should be consulted for a more detailed history (see, e.g., Frail et al. 1999c and Frail et al. 1999d).

#### Acknowledgements

Many thanks to D. A. Frail for his patience and help. Also, thanks go to NRAO and the REU Program for 1999.

Table 1. VLA Observations of GRB 980329

Epoch (UT)	$\Delta t$ (days)	$S_{8.46} \pm \sigma$ ( $\mu\text{Jy}$ )	$S_{4.86} \pm \sigma$ ( $\mu\text{Jy}$ )	$S_{1.43} \pm \sigma$ ( $\mu\text{Jy}$ )	( $\mu\text{Jy}$ )
1998 Mar. 30.23	1.07	166 $\pm$ 50			
1998 Apr. 01.13	2.97	256 $\pm$ 16			
1998 Apr. 02.15	3.99	84 $\pm$ 23			
1998 Apr. 03.14	4.98	109 $\pm$ 47			
1998 Apr. 04.11	5.95	135 $\pm$ 21			
1998 Apr. 05.12	6.96	194 $\pm$ 26			
1998 Apr. 06.89	8.73	58 $\pm$ 37	22 $\pm$ 37		
1998 Apr. 08.06	9.90	179 $\pm$ 41	146 $\pm$ 49		
1998 Apr. 11.09	12.93	274 $\pm$ 34	143 $\pm$ 45		
1998 Apr. 18.04	19.88	227 $\pm$ 22	107 $\pm$ 25		
1998 Apr. 19.00	20.84	205 $\pm$ 17	42 $\pm$ 21		
1998 Apr. 20.27	22.11	88 $\pm$ 21	52 $\pm$ 31		
1998 Apr. 21.91	23.75	291 $\pm$ 17	54 $\pm$ 20		
1998 Apr. 23.10	24.94	245 $\pm$ 37	65 $\pm$ 43		
1998 Apr. 27.02	28.86	465 $\pm$ 90	128 $\pm$ 42		
1998 Apr. 30.10	31.94	299 $\pm$ 51	85 $\pm$ 44		
1998 May 04.92	36.76	219 $\pm$ 32			
1998 May 08.01	39.85	321 $\pm$ 43	291 $\pm$ 57	47 $\pm$ 39	
1998 May 08.84	40.68	210 $\pm$ 45	60 $\pm$ 41		
1998 May 21.97	53.81	167 $\pm$ 38			
1998 May 24.96	56.80	248 $\pm$ 25	209 $\pm$ 33	42 $\pm$ 34	
1998 May 31.98	63.82	200 $\pm$ 23	76 $\pm$ 34		
1998 Jun. 06.84	69.68	167 $\pm$ 46	241 $\pm$ 44	0.464 $\pm$ 49	
1998 Jun. 12.98	75.82	169 $\pm$ 33	108 $\pm$ 51		
1998 Jun. 21.77	84.61	108 $\pm$ 36	191 $\pm$ 46		
1998 Jul. 20.70	113.54	151 $\pm$ 35	217 $\pm$ 49	134 $\pm$ 43	
1998 Jul. 28.43	121.27	157 $\pm$ 47	112 $\pm$ 56	16 $\pm$ 42	
1998 Aug. 06.68	130.52		132 $\pm$ 37	-39 $\pm$ 45	
1998 Aug. 10.58	134.42		71 $\pm$ 33	-17 $\pm$ 39	
1999 Aug. 03.60	492.44	40 $\pm$ 23			
1999 Aug. 06.68	495.52				

Note. — The columns are (left to right), (1) UT date of the start of each observation, (2) time elapsed since the GRB 980519 event, (3) 8.46 GHz flux density of the radio transient (RT), with the error given as the root mean square flux density, (5) 4.86 GHz flux density of the RT, and (6) 1.43 GHz flux density of the RT.

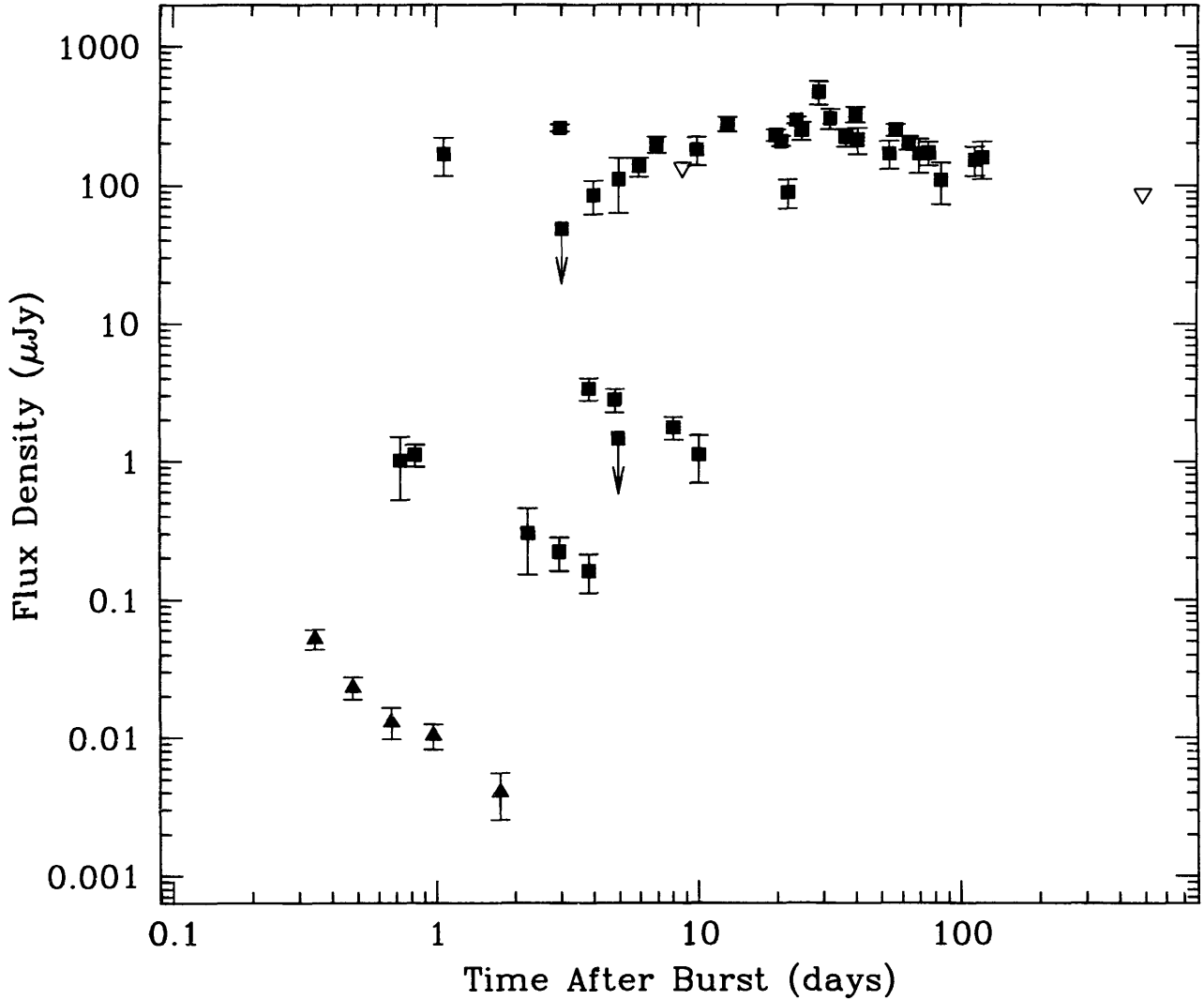


Fig. 1.— A broadband view of the afterglow associated with GRB 980329: the represented regimes are optical, x-ray, and radio. The green triangles represent x-ray observations, and the red and blue filled squares above these represent R- and I-band observations, respectively. Finally, the radio data (represented by purple, filled squares) spans across the top of the plot. This view of the time evolution of GRB 980329 depicts how the radio afterglow is much elongated in response as compared to the x-ray and optical counterparts.

Table 2. VLA Observations of GRB 980519

Epoch (UT)	$\Delta t$ (days)	TOS (min)	$S_{8.46} \pm \sigma$ ( $\mu\text{Jy}$ )	$S_{4.86} \pm \sigma$ ( $\mu\text{Jy}$ )	$S_{field} \pm \sigma$ ( $\mu\text{Jy}$ )	$S_{1.43} \pm \sigma$ ( $\mu\text{Jy}$ )
1998 May 19.81	0.30	99	49 $\pm$ 28			
1998 May 20.59	1.08	54	64 $\pm$ 27			
1998 May 22.35	2.84	112	103 $\pm$ 19			
1998 May 24.96	5.45	112	127 $\pm$ 20			
1998 May 31.54	12.03	132	40 $\pm$ 25	25 $\pm$ 27	591 $\pm$ 80	
1998 Jun. 02.56	14.05	125	142 $\pm$ 29	292 $\pm$ 41	607 $\pm$ 100	
1998 Jun. 05.14	16.63	106	230 $\pm$ 31	16 $\pm$ 33	596 $\pm$ 80	
1998 Jun. 07.43	18.92	183	1.2 $\pm$ 32	–13 $\pm$ 37	493 $\pm$ 82	–4.5 $\pm$ 34
1998 Jun. 11.94	23.43	69	82 $\pm$ 40	215 $\pm$ 44	537 $\pm$ 90	
1998 Jun. 18.58	30.07	78	66 $\pm$ 23	5 $\pm$ 31	676 $\pm$ 70	
1998 Jul. 07.26	48.75	100	78 $\pm$ 27	133 $\pm$ 42	480 $\pm$ 71	
1998 Jul. 20.23	61.72	124	0.9 $\pm$ 30	190 $\pm$ 40	356 $\pm$ 73	15 $\pm$ 42
1998 Jul. 21.25	62.74	94	42 $\pm$ 32	57 $\pm$ 45	480 $\pm$ 79	–35 $\pm$ 58

Note. — The columns are (left to right), (1) UT date of the start of each observation, (2) time elapsed since the GRB 980519 event, (3) total duration of the observing run, (4) 8.46 GHz flux density of the radio transient (RT), with the error given as the root mean square flux density, (5) 4.86 GHz flux density of the RT, (6) The integrated 4.86 GHz flux density of J232137.6+7715.0, a field source 2.5' from the GRB, and (7) 1.43 GHz flux density of the RT.

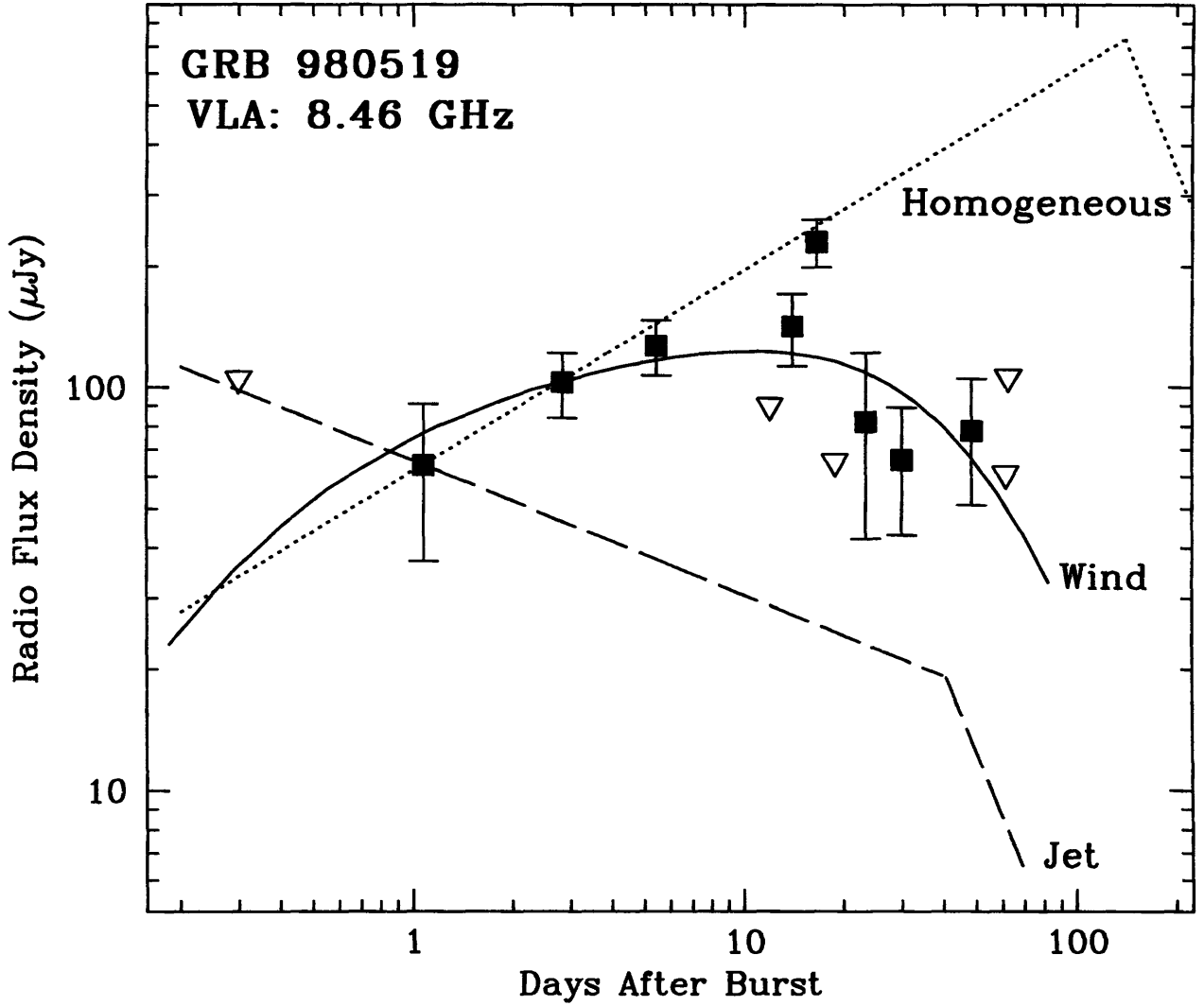


Fig. 2.— Observed and model lightcurves at 8.46 GHz. Detections are indicated by the filled squares. Upper limits for the non-detections (open triangles), are plotted as the peak brightnesses at the position of the radio transient plus two times the rms noise. Three different model predictions are plotted. The circumstellar model “Wind” is taken directly from Chevalier & Li (1999) with no modifications. The basic adiabatic, forward shock-model with spherical expansion into a homogeneous medium is indicated as “Homogeneous”. The predicted behavior for the jet model of Sari et al. (1999) is given by “Jet”. See text for additional details.

## REFERENCES

- Chevalier, R., Li, Z., 1999, ApJLetters, in press
- Frail, D., Kulkarni, S., Young, C. 1999a, GCN Circ. 334
- Frail, D., Kulkarni, S., Young, C., and Taylor, G. 1999b, GCN Circ. 337
- Frail, D., Kulkarni, S., Taylor, G., Shepherd, D. Bloom, J., Young, C., Nicastro, L., and Masetti, N. 1999c, submitted ApJ
- Frail, D., et al. 1999d, in prep.
- Frontera, F., Costa, E., Piro, L., et al. 1998, IAU Circ. 6853
- Fruchter, A. 1999, ApJ, 512, L1
- in 't Zand, J., Amati, L., Antonelli, L., et al., 1998, ApJ, 505, L119
- Kippen, R., et al. 1999, GCN Circ. 344
- Piro et al. 1999, GCN Circ. 333
- Reichart, D., Lamb, D., Metzger, M., et al., 1999, ApJ, 517, 692
- Sari, R., Piran, T., and Narayan, R. 1998, ApJ, 497, L17
- Sari, R., Piran, T., and Halpern, J. 1999, ApJ, 519, L17



**The 40FT. Telescope Controller**  
**National Radio Astronomy Observatory**  
**Green Bank, West Virginia**

**Scott A. Zemerick**  
**West Virginia University**  
**August 10, 1999**



## **Project Overview**

The 40 FT. Telescope at Green Bank serves as an educational tool that introduces radio astronomy to various educational groups. Since the telescope is operated manually without a computer, telescope observations require two or more people to perform. *The 40 FT. Telescope Controller* will allow a single person to plan observations in advance and have the telescope perform those observations unattended.

The *40 FT. Controller* will not completely replace the manual operations of the telescope, because these operations are part of the learning process for visiting educational groups. Instead, the *40 FT Controller* will allow a supervisor to accept observations from people off-site and have the telescope perform those observations unattended. This way, observations can be performed by those off-site who wish to continue their radio astronomy education.

## **Project Description**

The *40 FT. Controller* is composed of five applications:

1. ***System Diagnostics*** – Allows supervisor to check and configure various telescope operations.
2. ***Manual Controller*** – Controls telescope movement and data recording.
3. ***Remote Observer*** – Off-site creation of Observing Files that define those observations to be performed.
4. ***Automated Controller*** – Controls timing and all telescope operations so that observations can be performed unattended.

**5. *Task File Manager (Not Yet Created)* – Will allow easy management of Observation Files and easy creation of Task Files**

Graduates of Beaver College in Pennsylvania created and tested the *System Diagnostics and Manual Controller* in 1998. Picking up where they left off, I developed the *Remote Observer* and *Automated Controller*.

**The Remote Observer**

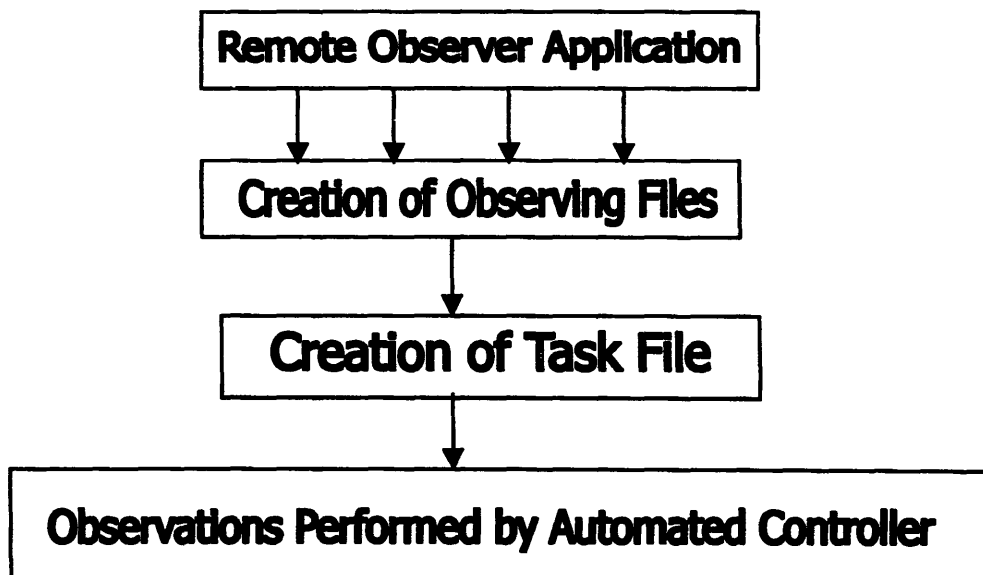
*The Remote Observer* is the application that easily generates Observation (OBS) Files containing specific observations to be performed on the 40FT. Telescope at some future time. People offsite who wish to use the telescope would first download *The Remote Observer* from NRAO and install it on their personal computer. The program then leads the user through several screens where specific options such as Start Right Ascension and Start Declination can be chosen. When the user is finished creating observations, *The Remote Observer* creates an ASCII OBS file that is then e-mailed to NRAO. This ASCII OBS file contains all the user's observations they wish to perform.

Currently, *The Remote Observer* will run only on the Microsoft Windows platform. For those users who do not have access to a PC or run other operating systems, it is possible for them to create an OBS file manually with any ASCII text editor. A standard OBS format has been created that allows for easy, manual creation of files. Below is an example of an OBS file. Note: Due to limited space, the entire file is not shown.

OBSERVER:	Scott Zemerick				
MODE:	LINE				
CHANNELS:	1 2				
COORDSYSTEM:	APPARENT				
DATE:	ASAP				
FREQUENCY:	1420.4508				
Seq	Type	Source	StartRA	StartDec	...
1	CAL	Start	12:13:4.3	10:34:45	...
-Line Comment for Number 1					
2	DRIFT	oriona	12:13:4.3	10:34:45	...
-Line Comment for Number 2					

## The Automated Controller

Once an Observing File has been created, a Task File is generated for the *Automated Controller*. A Task File is an ASCII file that contains a list of observations to be performed by the 40FT. Telescope. This list of observations is generated from existing Observing Files. The following chart illustrates the process of creating an observation for the *Automated Controller* to perform.

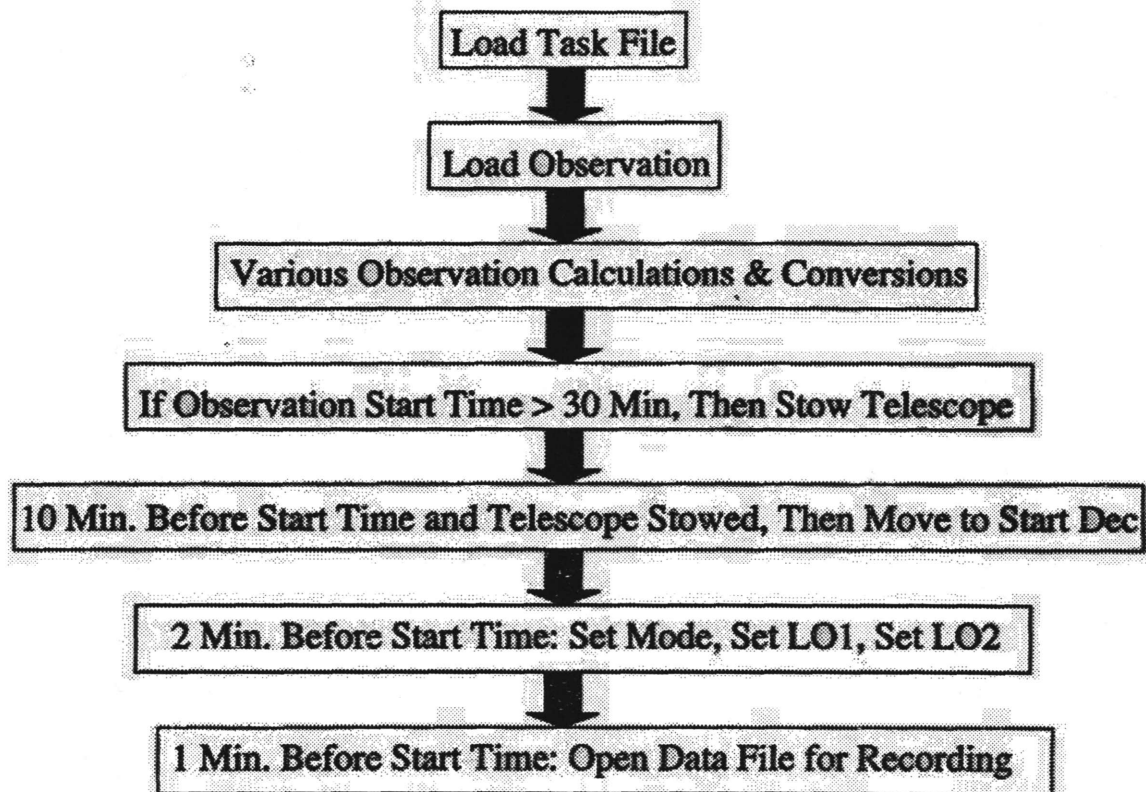


Once a Task File has been created and loaded, the *Automated Controller* then performs all observations specified. The *Automated Controller* is responsible for all telescope operations such as movement, frequency setting of the local oscillators, data recording, and timed calibrations. The *Automated Controller* is also able to perform all observation types such as *Continuum Calibration, Drift and Map* as well as *Spectral Line Calibration, Drift, and Spec*.

Since the *Automated Controller* requires an accurate timing of observations, a high-resolution Windows multimedia timer was used. This timer provides stable, accurate firings every 100 milliseconds. This way, recorded data is guaranteed to be precise and reliable.

The following chart illustrates the sequence of events the *Automated Controller* performs when an observation is loaded.

## **Automated Controller - Sequence of Events**



This sequence of events is performed for every observation found in the Task File. The *Automated Controller* is designed to run attended for a period of time until all observations in the Task File have completed. Once observations have finished, the supervisor will manage the data files created and distribute them electronically to those who were performing off-site observations.

## **Project Testing and Conclusion**

### **The Remote Observer**

Since *The Remote Observer* is a Windows application, testing has been performed on several personal computers. *The Remote Observer* successfully creates ASCII Observing Files with options specified by the user. It is recommended that *The Remote Observer* be released to a small number of off-site observers for final testing.

### **The Automated Controller**

*The Automated Controller* was first developed on a personal computer not connected to the 40FT. Telescope. As the development neared the end, testing of the *Automated Controller* was performed on the computer while connected to the 40FT. Telescope. The following telescope operations were successful during testing:

- Calibrations
- Telescope Direction Changing (North/South)
- Motor Control and Movement to a Particular Declination (including Stow)
- Observation Timing
- Frequency Setting the Local Oscillators
- Continuum and Spectral Line Observation Modes

The last remaining item to be tested at the telescope is the *Continuum Map Observation Mode* that involves data sampling while the telescope is in motion. While being

developed in the lab, a simulator was used to program and test the *Continuum Map Observation*. Using the simulator, successful Map Observations were performed in the lab. Due to time constraints, actual testing without the simulator was not possible. It is recommended that more testing of the *Continuum Map Observation* be performed at the telescope.

### The Task File Manager

The *Task File Manager*, the last application left to be developed, will provide an easy method of creating Task Files for the *Automated Controller*. Currently, Task Files are created manually using an ASCII text editor. The *Task File Manager* will provide the supervisor a list of observations (located in Observing Files) that can be chosen via a graphical user interface. Then, the *Task File Manager* will create an ASCII Task File which will be loaded by the *Automated Controller*.

# **Comet 1999/H1 Lee: Measurement of Hydroxyl**

**Porter Mason, Cristina Murray, Dustin Bambic, Jonathan Durbin and Alwyn Wootten  
National Radio Astronomy Observatory**

**This is a Report of Observations only and should not be circulated**

**August 6, 1999**





## 1. Introduction

Water is the significant constituent of cometary atmospheres. Whenever a new, fairly bright comet appears, the water abundance may be usefully estimated by observations of the hydroxyl lines at 18 cm.

We report observations of the 18cm lines of hydroxyl in C/1998 H1 (Lee).

## 2. Observations

Observations were made during 1999 May 25 at the 43m telescope of the National Radio Astronomy Observatory in Green Bank, West Virginia. The observed spectra are shown in Figure 1.

### 2.1. Instrumental Details

The 18 cm lines of OH were observed with the 43m telescope of the NRAO at Green Bank, WV, tuned to frequencies of 1667.3590 MHz and 1665.4018 MHz, respectively. Orthogonal linear polarizations of each line were sent to the correlator. The cooled HFET amplifiers provided a measured  $T_{sys}$  of 22 K under clear, cool conditions. Pointing was checked on strong sources and found to be excellent. The data was calibrated through measurement of a noise tube, which had been calibrated in the Jansky Lab by comparison to liquid nitrogen loads, and through observations of 3C286 (assumed flux  $S_{1.667MHz} = Jy$ , measured  $T_A = 3.87K$ ). Absolute calibration is believed to be accurate to 10%. The 1024 channel Mark IV autocorrelator provided a resolution of  $\sim 0.22 \text{ km s}^{-1}$ , which was divided into four 256 channel sections to sample the output of each polarization at each frequency. The data were taken using a frequency-switched mode, switching by 1.25 MHz, while tracking the topocentric velocity of the comet. Pointing was good under clear cold skies. The telescope tracked the ephemeris (JPL No. 17) for Green Bank extremely closely, as calculated from the JPL Horizons Ephemeris Generator.

The two polarizations were averaged to produce the final spectra. The beamwidth of the 43m telescope is  $18'$  at 1.667 GHz (corresponding to  $4 \times 10^5 \text{ km}$  at the comet's 0.89 AU distance at the time of these observations). Line intensities are measured in units of antenna temperature,  $T_A$  and corrected to an estimate of the true source brightness temperature  $T_R$  via  $T_R = T_A / \eta_A$ . The surface accuracy of the 43m telescope is  $0.114 \pm 0.005 \text{ cm}$ , as measured in recent holographic experiments (Maddalena, 1986). The low frequency aperture efficiency of the telescope is  $\eta_A 0.55 \pm 0.02$  (Maddalena 1986) but falls toward higher frequency. At 18cm, the beam is larger than the source for Comet C/1999 H1 (Lee). The efficiency measured on the moon ( $\eta_{f,s}$ ) at 14.8 GHz is 0.63 (Loren, Evans and Knapp 1979).

Table 1: Observed OH Line Intensities in Comet Lee

Transition (MHz)	$T_A$ (K)	$\sigma$ (K)	Velocity (MHz)	$\Delta V$ (km/s)	Integrated Intensity (K km/s)
1665	0.013	0.005	32.6	1.8	0.025 (0.008)
1667	0.032	0.005	32.6	1.8	0.062 (0.007)

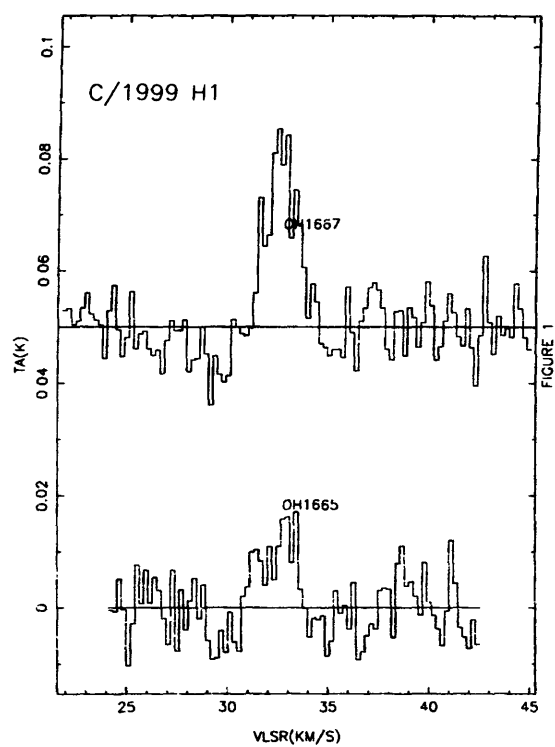


Fig. 1.— Figure 1. Spectra of the 1665 MHz (top) and 1667 MHz (bottom) transitions of hydroxyl observed with the NRAO43m telescope towards C/1999 H1 (Lee) during 1999 May 25.

## 2.2. Analysis

To interpret the observed line intensities, we assume a beam-averaged projected density of OH summed over all levels ( $N_{total}$ ), and that the excitation from the ground state  $\Delta$  doublet  $X^2\Pi_{3/2}, J = 3/2$  occurs via ultraviolet pumping of the  $A^2\Sigma^+(v = 0, 1)$  states by solar radiation. The inversion of the ground state population then depends upon the heliocentric radial velocity of the comet,  $V_{hel} = -24.4$  at the time of our observations. A numerical correction factor was applied to correct for this effect. We estimate this factor to be 0.34 for the  $-24.4 \text{ km s}^{-1}$  velocity of the comet relative to the sun, from the graph in Despois (1981) and the table in Schloerb and Gerard (1985).

To determine linestrength from the production rate of OH, one must also estimate the fraction of OH in the the beam, and assume lifetime and an outflow velocity. A simple preliminary estimate is that OH lies in a uniform density sphere of radius one photo-disassociation scalelength,  $\lambda$ . The scale length is given by an outflow velocity,  $v_{out}$  (assumed to be 1 km/s, from these observations) and the photo-disassociation lifetime,  $\tau$  (assumed to be  $1.1 \times 10^5$  second at 1 AU which corresponds to 110000 km). At the time of our observations, the comet was 1.2 AU from the Sun. For the beamsize of our observations, the radius of the emission region is significantly smaller than the telescope beam. We are thus insensitive to the details of how the OH is distributed within the beam. The total production rate of OH molecules can be derived from the two emission lines which we observe through modeling the excitation of OH. The OH production rate for a given transition is given by:

$$Q_{OH} = \frac{8(\pi\Delta\theta)^2 k\nu_{ij}^2 T_R dV}{4\ln 2 hc^3 \tau_{OH} A_{ij}}$$

Here,  $\Delta = 0.885 \text{ AU}$  is distance from Earth to the comet,  $\theta$  is the beamsize of the telescope,  $\tau_{OH}$  is the hydroxyl lifetime, and  $A_{ij}$  is the Einstein coefficient for the transition observed.

This can also be written:

$$Q_{OH} = \frac{N_0 T_R dV \pi R^2}{\tau_{OH} f}$$

where  $N_0$  is the column density of the appropriate transition of OH which gives rise to a 1 K  $\text{km s}^{-1}$  line, taking into account solar radiative pumping,  $R$  is the beamsize in km, and  $f$  is the fraction of OH molecules within the beam ( $f=1$  in the present case). We evaluate  $N_0(1667)=1.37 \times 10^{14} \text{ cm}^{-2} \text{ K}^{-1} \text{ km s}^{-1}$  and  $N_0(1667)=2.15 \times 10^{14} \text{ cm}^{-2} \text{ K}^{-1} \text{ km s}^{-1}$  for conditions appropriate to C/1999 H1 (Lee).

The OH production rate which we measure is  $Q_{OH,Tot} = 5.5 \times 10^{28} \text{ mols}^{-1}$ . Finally, we infer a value of  $Q_{H_2O}=5.5 \times 10^{28} \text{ mols}^{-1}$  assuming that each  $\text{H}_2\text{O}$  photodissociation event gives rise to one OH molecule.

We acknowledge support from the National Science Foundation under the Research Experiences for Undergraduate program. We appreciate the timeliness of the Green Bank staff in scheduling this experiment at late notice.

## REFERENCES

- Despois, D. *et al.* 1981 *Astron. Astrophys.* 99, 320.  
 Loren, R., Evans, N. and Knapp, G. 1979 *Ap. J.* 234, 932.  
 Maddalena, R. 1986, private communication.  
 Schloerb, P., and Gerard, E. 1985 *AJ* 90, 1117.

---

This manuscript was prepared with the AAS L<sup>A</sup>T<sub>E</sub>Xmacros v3.0.

**Table 2: Derived Water Production Rate**

Quantity	Value
$Q_{OH}$	$5.5 \times 10^{28}$
$Q_{H_2O}^1$	$5.5 \times 10^{28} \text{ s}^{-1}$

# **H I Absorption in the Luminous QSO, PDS 456: A NRAO Summer Student Project**

C. Young<sup>1</sup>, C. Brogan, C. Cheung, B. Jones, M. Lystrup, E. McGrath, N. Mohan, D. Osgood, A. Petric, C. Schwartz, H. Smith  
NRAO Summer Intern/REU Program 1999

M. Yun

National Radio Astronomy Observatory, P.O. Box 0, Socorro, NM 87801

## **ABSTRACT**

We present results from the Summer Student Project at the Very Large Array (VLA) in Socorro, NM for 1999. We chose to observe a quasar which was recently discovered in the Pico dos Dias survey (Torres et al. 1997). This object, also an IRAS source, has a relatively high inferred dust content and is also the most luminous quasar in our nearby universe with a redshift of  $\sim 0.18$  (Simpson et al. 1998; Torres et al. 1997). We chose to observe this object at  $\sim 1200$  MHz in the hopes that H I gas might be present around this quasi-stellar object (QSO) and, thus, exhibit H I absorption.

## **1. Introduction**

PDS 456 ( $\alpha = 17^h 28^m 19^s.7966 = -14^\circ 15' 55''.87$ ) is of interest in the study of QSO formation because it is relatively bright in both the infrared and optical regimes. We hope to reveal the nature of the gas surrounding PDS 456 by searching for H I absorption towards this object. The detection of H I in absorption could show a number of possible features. For example, if the H I were part of a cold quiescent halo around PDS 456, we would expect to see absorption at the systemic velocity of the galaxy. If the H I were being expelled as a result of the QSO shedding its outer layers, the absorption should appear at blueshifted velocities. A third possibility is that H I is accreting onto the central engine, in which case we should detect redshifted H I absorption (see for example van Gorkom et al. 1989).

---

<sup>1</sup>E-mail: chyl@ra.msstate.edu

## 2. Observations

We observed PDS 456 on 16 July, 1999 with the VLA in A-configuration. The source 3C48 has a well-known flux density and was observed once for flux calibration (Perley et al. 1998). Also, 1733-130 (J2000) was observed intermittently to bracket PDS 456 and provide adequate phase calibration. This phase calibrator had a high flux density (5.2 Jy) and was used, along with 3C48, for bandpass calibration.

We observed in the spectral line mode of the VLA and opted to use online Hanning smoothing to overcome the effects of an interference source at 1200 MHz. Basing our choice of observing mode on optimal bandwidth and velocity resolution, we observed in 4IF mode with 32 channels in each band. This mode provided a total bandwidth of 6.25 MHz (1563 km/s), and a velocity resolution of 24.4 km/s.

The rest frequency of H I absorption is 1420.406 MHz. However, the expected frequency for H I absorption toward PDS 456 is 1199.667 MHz due to its estimated redshift of  $\sim 0.18$  (Simpson et al. 1998). Unfortunately, several factors degrade VLA observations at this frequency: (1) a strong source of radio frequency interference (RFI) is present at  $\nu = 1200$  MHz, (2) the system temperature is increased at this frequency compared to the standard 1.4 GHz, and (3) the ground becomes a significant source of noise at these low frequencies. The latter two of these factors must be accepted, but we took measures to decrease the interference caused by the RFI at 1200 MHz.

Ideally, all recorded channels should be reliable, but the outer channels are often degraded due to imperfect electronics. For this reason, these outermost channels are usually discarded. We took advantage of this fact and chose our two IFs such that the two 32-channel bands overlapped at exactly 1200 MHz, the frequency of the RFI. By this arrangement the data is least affected by the interference.

## 3. Data Reduction

We used the standard procedure for reducing spectral line data (see the VLA Spectral Line Users Guide). The initial appearance of a weak detection prompted us to take extra measures to ensure its reliability. Due to the 1200 MHz continuum strength of PDS 456, we were able to self-calibrate the phases of the continuum map and apply these corrections to the line data. Also, the maps were CLEANed such that all sources within 30' of the phase center and with a flux density greater than 5 mJy (as detected by the NVSS) were cleaned separately to improve map quality (Condon et al. 1998). Even after many different combinations of self-calibration and the aforementioned CLEANing process, the weak

detection remained constant. We also imaged the RCP and LCP line data separately and determined that the apparent detection was evident in both polarizations.

#### 4. Results

PDS 456 has been observed before by the VLA. The NVSS found this source to have a flux density of 22.7 mJy at 1.46 GHz, and other observations at 8.4 GHz and 4.6 GHz verify that this source is an unresolved steep spectrum source (Simpson et al. 1998; Yun 1998, private communication). However, no one has ever attempted to search for HI absorption toward PDS 456, probably because of the difficult nature of the observations. Fortunately, our project was intended to be a tool of instruction rather than discovery, so we were allowed to proceed with this observation despite reasonable doubt of its success.

As alluded to before, we did detect what appears to be an HI absorption line. However, preliminary data reduction confirms our detection at only about the 2 1/2 sigma level, where one sigma is equal to the root mean square (RMS) noise. The measured RMS noise in our maps is  $\sim 1.4$  mJy which agrees with the theoretical value calculated by considering time on source, declination of the source, and system imperfections at the observing frequency.

The smoothed spectrum (see figure 1) which seems to depict a  $\sim 5$  sigma detection is actually somewhat misleading. The unsmoothed spectrum (see figure 2), however, exhibits the  $\sim 2.5$  sigma detection previously mentioned. We are confident that this one-channel detection is not an artifact created during data reduction for two reasons: (1) the detection has remained constant despite numerous attempts to remove it through methods of calibration and CLEANing, (2) the second IF does not exhibit the same artifact (see figure 3), and (3) the spectrum of a field source of  $\sim 50$  mJy does not exhibit the same structure in IF1 (see figure 4).

We have submitted a proposal for an additional 3-4 hours of VLA time to verify this weak detection. Publication of the results from these tentative observations will follow in a timely manner.

#### 5. Discussion

Assuming that the HI absorption is real and associated with PDS 456, we can speculate on the origin and nature of this gas. Our initial hypothesis, which prompted these observations, was that PDS 456 is in a transition period from a dust-enshrouded (i.e. ultraluminous infrared galaxy) to naked QSO. This claim was made because PDS 456 is an



IR-bright source, but it is also very bright optically with a magnitude of  $B = 14.69$  (Torres et al. 1998). However, in this scenario we would expect to see H I at velocities ranging from 0 km/s to  $\sim 300$  km/s. Since we observe infalling H I at a velocity of about 200 km/s instead, our view of this source has changed. Now we postulate that we have detected the infall of H I gas onto PDS 456. Considerable work has been conducted in this field of H I astronomy (see, for example, van Gorkom et al. 1989 for a good review), and the infall of cold gas into galaxies has been suggested by observations. In these studies no blue-shifted H I has been detected; likewise, we have detected no blueshifted H I absorption in PDS 456. This lack of detection could be a result of the source being unresolved by the VLA. The detection of emission lines from this source might provide further insight about the nature of the surrounding gas.

## REFERENCES

- Condon, J. J., Cotton, W. D., Greisen, E. W., Yin, Q. F., Perley, R. A., Taylor, G. B., Broderick, J. J. 1998, *AJ*, 115, 1693
- Perley, R. A. and Taylor, G. B. 1998, *VLA Calibration Manual*
- Simpson, C., Ward, M., O’Brien, P., Reeves, J. 1998, *MNRAS*, 303, L23
- Torres, C. A. O., Quast, G. R., Coziol, R., Jablonski, F., de la Reza, R., Lepine, and Gregorio-Hetem, J. 1998, *ApJ*, 488, L19
- van Gorkom, J. H., Knapp, G. R., Ekers, R. D., Ekers, D. D., Laing, R. A., and Polk, K.S. 1989, *AJ*, 97, 708

## 6. Acknowledgements

We thank NRAO for granting observing time to this group of undergraduate and graduate students. Also, our gratitude is extended to Greg Taylor, Liese van Zee, and Chris Fassnacht, directors of the 1999 REU summer program at NRAO, Socorro.

NRAO is operated by Associated Universities, Inc., under a cooperative agreement with the National Science Foundation.

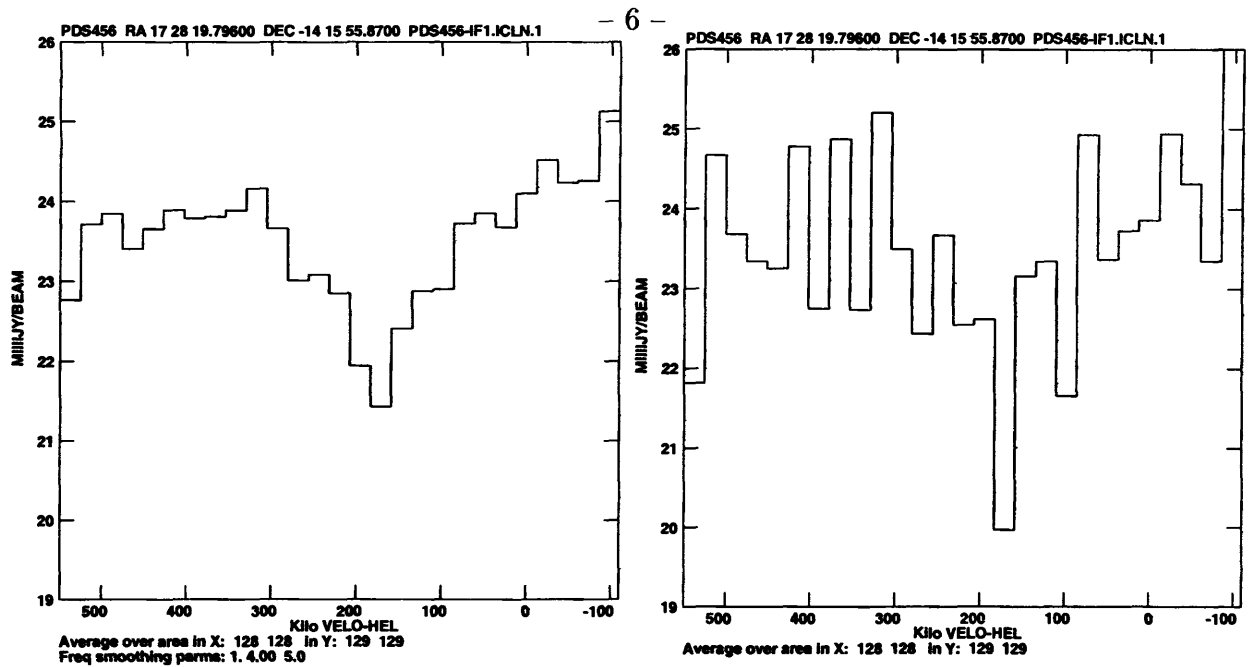


Fig. 1: [LEFT] Smoothed IF1 H I spectrum at the continuum peak of PDS 456.

Fig. 2: [RIGHT] Unsmoothed IF1 H I spectrum at the continuum peak of PDS 456.

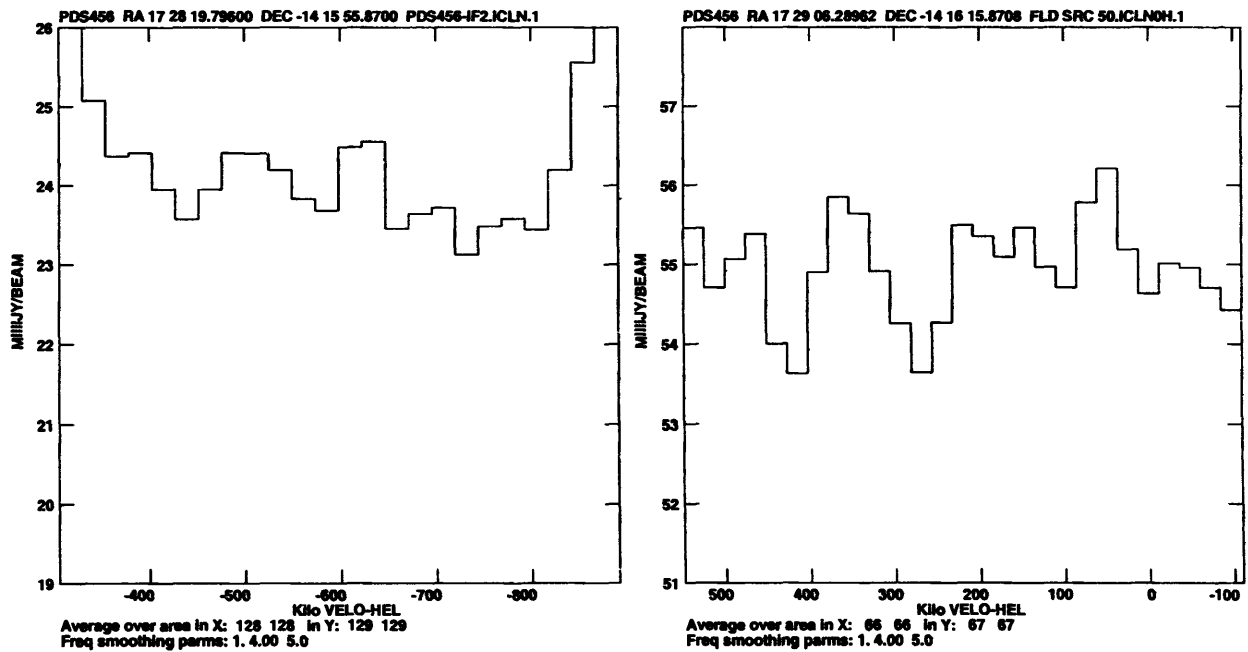


Fig. 3: [LEFT] Smoothed IF2 H I spectrum at the continuum peak of PDS 456.

Fig. 4: [RIGHT] Smoothed IF1 H I spectrum from a nearby field source.

**Student Questionnaires 1999  
(AOC and CV Students)**





# NATIONAL RADIO ASTRONOMY OBSERVATORY

520 Edgemont Road, Charlottesville, VA 22903-2475

(804) 296-0211

(804) 296-0278

## MEMORANDUM

DATE: August 4, 1999  
TO: Summer Students  
FROM: Al Wootten  
SUBJECT: Questionnaire

Before you leave us we would appreciate you filling out and returning to me the following questionnaire. We will use your response to improve the program for next year. Feel free to use the back of this sheet if you need more room for your responses. Thanks!

- How did you find out about the NRAO-REU program?

Surfing the net

- What is your overall reaction to the program?

I couldn't ask for a better experience

- How have your career decisions been influenced by your experiences at NRAO?

I'm more confident in my decision to pursue an astronomy career.

- Have you previously been an REU student at another institution? If so, how do your NRAO experiences compare with your experiences elsewhere?

NO

- In what ways could we improve your stay at NRAO?

A house for us all to stay in together would have been nice.

- What changes would you like to see in the NRAO-REU program?

Just the house as said above

- Do you and your mentor plan to publish results of your summer research, or to present the results at a professional meeting (the REU program can pay most of your costs)?

I plan to present a poster paper in Jan at the AAS meeting.



# NATIONAL RADIO ASTRONOMY OBSERVATORY

520 Edgemont Road, Charlottesville, VA 22903-2475

(804) 296-0211

(804) 296-0278

## MEMORANDUM

DATE: August 4, 1999  
TO: Summer Students  
FROM: Al Wootten  
SUBJECT: Questionnaire

Before you leave us we would appreciate you filling out and returning to me the following questionnaire. We will use your response to improve the program for next year. Feel free to use the back of this sheet if you need more room for your responses. Thanks!

- **How did you find out about the NRAO-REU program?**  
Off the web, not NRAO's page, but through the NSF site somehow.
- **What is your overall reaction to the program?**  
I really enjoyed it. I learned a great deal and met some great people.
- **How have your career decisions been influenced by your experiences at NRAO?**  
Quite a bit. I plan to focus more toward astronomy than I had planned. Mostly because in talking to people this summer I realize I am with my background. (I've always wanted to)
- **Have you previously been an REU student at another institution? If so, how do your NRAO experiences compare with your experiences elsewhere?**  
I was an REU at Duke for chemistry. I enjoyed the research and interaction with faculty (the fact that there was interaction) more here. I also found my research more interesting.
- **In what ways could we improve your stay at NRAO?**  
Making housing easier to deal with. Perhaps offering a house where all the REU's could live. I just ended up spending a lot more \$ than I thought I would've on housing.
- **What changes would you like to see in the NRAO-REU program?**  
Maybe more observing projects? Don't know if that's possible.  
More field trips?  
Overall, I was satisfied though.
- **Do you and your mentor plan to publish results of your summer research, or to present the results at a professional meeting (the REU program can pay most of your costs)?**  
My web stuff will somehow be acknowledged, not sure how just yet. At this time I don't plan on going to AAS or anything. But we'll see.



# NATIONAL RADIO ASTRONOMY OBSERVATORY

520 Edgemont Road, Charlottesville, VA 22903-2475

(804) 296-0211

(804) 296-0278

## MEMORANDUM

DATE: August 4, 1999  
TO: Summer Students  
FROM: Al Wootten  
SUBJECT: Questionnaire

Before you leave us we would appreciate you filling out and returning to me the following questionnaire. We will use your response to improve the program for next year. Feel free to use the back of this sheet if you need more room for your responses. Thanks!

- How did you find out about the NRAO-REU program?

*The Internet*

- What is your overall reaction to the program?

*Positive. It has been an invaluable summer for me*

- How have your career decisions been influenced by your experiences at NRAO?

*yes - now I have a much better idea of what kind of jobs I can get and I have a new-found interest in radio astronomy*

- Have you previously been an REU student at another institution? If so, how do your NRAO experiences compare with your experiences elsewhere? *No*

- In what ways could we improve your stay at NRAO? *Perhaps an advance on our paychecks when we first get here to help cover expenses. It was very expensive for me to come here and I had to take out a loan.*

- What changes would you like to see in the NRAO-REU program? *I think we should be made aware of computer/printer policies when we first get here so we don't run into the problems we did - we need to be told early on which printers can handle post script files, etc.*

- Do you and your mentor plan to publish results of your summer research, or to present the results at a professional meeting (the REU program can pay most of your costs)? *yes. We plan to publish and present the results at the AAS meeting in January, 2000.*





**InterOffice**

# **National Radio Astronomy Observatory**

**Socorro, New Mexico**

**16 February 1999**

**From: Miller Goss**  
**To: Distribution**  
**Subject: Summer Student Program**

Attached are notes taken at the meeting of September 14, 1999. The discussion on the summer student program was productive. Many ideas and suggestions were brought up. The resulting action items will improve the process. Especially important is to have one central coordinator for the 2000 Summer Student program. Copies of all next year's summer student correspondence, beginning with offer letters/acceptance of employment are to be channelled to Terry Romero.

The 1999 Summer Student program at the AOC was a great success. My sincere thanks to all of you.

/tr  
attachment



InterOffice

## National Radio Astronomy Observatory

Socorro, New Mexico

16 February 1999

From: T. Romero  
To: Distribution  
Subject: Notes on Post Mortem Summer Student Meeting

The meeting on September 14, 1999, reflected on a successful summer student program. Overall, the student evaluations were quite positive. Discussion of the concerns brought up by students resulted in solutions for some and ideas and possible solutions for others. These points are divided into are two categories. Those which can be addressed locally and those which have a solution in the early stages of advertizing and recruitment and are handled through Charlottesville.

Please note the third and last category listing of **ACTION ITEMS** and who is responsible for carry through.

### **SOCORRO ISSUES:**

**Housing:** Students seemed to find the exercise of settling on housing prior to their arrival, as a futile exercise. Ideas and suggestions:

- a) Have all students stay at the Guest House when they arrive with an allowance of more than two days. This does not necessarily have to be free for the entire number of days. Almost all of this years' students found housing after and not before their arrival.
- b) Look into New Mexico Tech married student housing; availability, pricing and probability of reserving for the summer?
- c) Have an NRAO representative look over available housing in Socorro. Interested students could take up the offer based on what they are told by NRAO Representative. This apparently has been done in the past with a degree of success.

**Furnishings:** The furnishing used by students this year seemed to be pretty worn. Miller discovered one of the VSQs at the site (# 3), having quite a bit of furniture stored which could be cycled for summer student use. Skip was going to look into this and into obtaining furniture which is in better condition, to make available for next years' students.

**Student Observing:** The time allocated for the student observing was too late in the summer. Mid to late June would be preferable and a single block of five observing hours is preferred rather than the two short blocks received this time.

**Evaluations:** It was decided to have student evaluation made anonymous. Greg thought this was straight forward using Web based submissions.

**Work Stations and Office cubicles:** Both of these should be assigned to students prior

## **InterOffice**

to arrival. Workstations should be well prepared with clean disks and AIPS environment set up. There was some confusion this year when students attempted to work on a computer which was not useable. AIPS numbers should also be assigned ahead of time.

**Local Contact:** It was decided information to and from students should be through one person. Terry Romero will be the clearing house once the offer letters are sent and until students arrive in Socorro.

## **CHARLOTTESVILLE ISSUES:**

**Graduate Student definition:** Clarification and clearer definitions for recruitment of graduate students should be addressed. The information on the NRAO Web page needs to be updated. The students found the current information confusing. The regular REU program only accepts undergrads but NRAO recruitment includes graduate students, funded outside the REU program. Local consensus was that it was beneficial to have the mix of graduate and undergraduate students working in the summer student program. In the future, more effort will go into recruitment of graduating seniors and first and second year grad students.

**Employment date:** Students were sent information telling them a Monday had to be the first day of employment. This does not seem to be the case. Personnel was happy for them to begin on any day. This information should be updated in the offer letter.

**VLA Tours:** It should be made known to students ahead of time, that they are expected to participate in providing weekend tours at the VLA site, for two days sometime in the summer. Perhaps this can be posted along with the recruitment information or in the offer letter.

## **ACTION ITEMS:**

### **for Skip Lagoyda:**

1. In 2000, all students are booked into the Guest House and are given a minimum of up to one week's stay, free of charge, while locating housing in Socorro. The maximum stay at the Guest House would be two weeks and students would be charged for the second week.
2. Get rid of unusable furniture immediately. Organize a complete inventory listing on what is available and useable for next year, including furniture found in VSQ. Add to inventory, items necessary to bring the inventory up to par for students' needs.
3. Maintain inventory of furniture status (loans, returns and condition).

### **for Allen Lewis:**

1. Follow up with New Mexico Tech on married student housing (availability and pricing).
2. Have available leads on local housing and contact information and provide to students, upon arrival/check-in.

## **InterOffice**

### **for Greg Taylor:**

1. Greg will place a request in April 2000, to Barry Clark, for scheduling a single block of five hours observing for summer students.
2. Greg will set up anonymous evaluation on the Web and have it available for next years' program.
3. Greg has already contacted Al Wootten on the issues which are listed in the under Charlottesville. Greg will follow up with Al, on resolving these points.

### **for Chris Fassnacht:**

1. Gustaaf van Moorsel should be given a list showing where each student will work. All workstations should be set up and completely ready to use by at least one week prior to the first student arrival. Chris will follow up on this with Gustaaf.

### **for Terry Romero**

1. Once employment offers are accepted, Terry will coordinate all local mailings, collate and distribute pertinent information. She will be the central point of contact for the summer students before and up to their arrival.

### **Distribution:**

Chris Fassnacht, Miller Goss, Skip Lagoyda, Allen Lewis, Terry Romero, Greg Taylor,  
Liese van Zee



# NATIONAL RADIO ASTRONOMY OBSERVATORY

520 Edgemont Road, Charlottesville, VA 22903-2475

(804) 296-0211

(804) 296-0278

## MEMORANDUM

DATE: August 4, 1999  
TO: Summer Students  
FROM: Al Wootten  
SUBJECT: Questionnaire

Before you leave us we would appreciate you filling out and returning to me the following questionnaire. We will use your response to improve the program for next year. Feel free to use the back of this sheet if you need more room for your responses. Thanks!

- How did you find out about the NRAO-REU program?

*A college professor referred me to the web page.*

- What is your overall reaction to the program?

*It's a great way to gain experience.*

- How have your career decisions been influenced by your experiences at NRAO?

*I'm still a little undecided as to what I want to do, but NRAO has helped out some.*

- Have you previously been an REU student at another institution? If so, how do your NRAO experiences compare with your experiences elsewhere?

*No.*

- In what ways could we improve your stay at NRAO?

*I didn't have a problem, but I did hear others talk about housing being a difficult part of the summer.*

- What changes would you like to see in the NRAO-REU program?

*I think it would have been nice to play some social events for the students.*

- Do you and your mentor plan to publish results of your summer research, or to present the results at a professional meeting (the REU program can pay most of your costs)?

*I don't think so.*

**1998 Summer Research Symposium  
Program  
(Charlottesville)**



## **Summer Student Research Seminar**

**Tuesday, August 3, 1999**

**12:00**

**Edgemont Road Conference Room**

**Christina Murray**

**U. New Mexico**

**“Milliarcsecond Structures of Seyfert Galaxies:  
A VLBA Snapshot Survey”**

**Porter Mason**

**Duke University**

**“The 2mm Spectral Survey”**

**Dustin Bambic**

**Western Kentucky University**

**“NGC 7331: Characterizing the contribution of spiral  
density waves in flocculent galaxies”**

**Jonathan Durbin**

**Valdosta State University**

**“A Low-Noise Element for the Array Feed”**

QB 61 . R47 1999